

PALEOCLIMATIC CONDITIONS  
DURING THE LAST  
DEGLACIATION INFERRED FROM  
COMBINED ANALYSIS OF  
PLUVIAL AND GLACIAL RECORDS

A PALEOHYDROLOGY STUDY OF THE OWENS VALLEY, CALIFORNIA

Submitted in partial fulfillment of a Ph.D in Earth and Environmental Science at the  
New Mexico Institute of Mining and Technology

## ABSTRACT

Late Pleistocene glacial and lacustrine fluctuations preserved some of the best and most dramatic evidence of climate change on the continents. Unfortunately, paleoclimatic interpretation of those records has long been hampered by the mutual dependence of both hydrologic systems on temperature and precipitation, that is – glaciers and closed-basin lakes increase in size in response to decreased temperature as well as increased precipitation. Researchers have therefore typically relied on uncertain assumptions about one of these variables in order to infer changes in the other. In this study we show that reconciliation of glacial and lacustrine records by itself provides a means of constraining both temperature and precipitation. This is possible because each system has different relative sensitivity to those primary climatic variables. To convert the geologic record of changes in the glacial and lacustrine records to paleoclimatic constraints, we used physically-based models of the glacial and lacustrine systems to identify combinations of climatic conditions that could reproduce the changes preserved in the geologic record. The glacier model is a spatially distributed snow- and energy-balance model loosely coupled to a vertically integrated 2-D glacier flow model. It specifically addresses the need for a model that can reproduce not only the larger, easily estimated shapes of the last glacial maximum, but also the much more complex ice distributions of the latest Pleistocene. We used a Thornthwaite water balance model to estimate the sensitivity of the lacustrine system to climate change, as it is dominated by climatically induced changes in evapotranspiration and runoff. Applying this dual-system modeling approach to the glacial-pluvial record in the Owens Valley, we find that temperatures were  $\sim 6^{\circ}\text{C}$  colder during the last glacial maximum (LGM) but had warmed by about  $4^{\circ}\text{C}$  from that low by  $\sim 13$  ka, well before the onset of the Holocene. More significantly, we conclude that LGM precipitation was probably no more than 25 to 50% greater than today and that the increased precipitation continued, with intermittent dry periods, until the end of the Pleistocene.

## ACKNOWLEDGEMENTS

First, I thank, beyond measure, my wife, Cathy, and children, Sara and Megan, for their patience and support through the too-many years of this project. At New Mexico Tech, I have greatly enjoyed working with Dr. Fred Phillips on this effort, and many others, and I thank him in particular for his never-flagging enthusiasm for this research, and hydrology and paleoclimatology research in general. Many thanks also to all the members of my research committee for their excellent comments and suggestions along the way. In particular, Eric Small has been highly valued for his many suggestions and comments regarding surface energy balance dynamics as well as heart-rate training and cycling fitness. I learned more from John Wilson's extremely thorough review of this manuscript than I care to admit and I thank him sincerely for his efforts. No muddled, ambiguous, or incoherent sections were left unaddressed in his review and I only hope I was able to correct most of them, without further obfuscation, in my revisions. Though not officially a member of my research committee, I heartily thank Steve Schaffer, who was singularly helpful in proposing a simple and effective means of constructing the glacier flow model. I am also grateful to Terry Thomas for his care and skill in processing virtually all of the  $^{36}\text{Cl}$  samples discussed in this report, and for modifying and retyping the rock processing procedures presented in Appendix B. Finally, thanks to all our friends in Socorro for their friendship, generosity and kindness during my years at NMT; without them, our stay might have seemed overly long.

Financial support for this project was provided by the NASA Earth System Science Fellowship Program and the National Science Foundation.

## TABLE OF CONTENTS

<i>Chapter 1 - Introduction .....</i>	<i>1-1</i>
<i>Chapter 2 - Lacustrine Chronology Development.....</i>	<i>2-1</i>
Pluvial records in the Owens Valley .....	2-2
Owens Lake .....	2-2
Searles Lake .....	2-3
Interpretation of stable isotope records .....	2-8
Owens lake.....	2-13
Searles Lake .....	2-16
Lake level chronology overview.....	2-18
<i>Chapter 3 - Closed Basin Lake Sensitivity to Climate Change.....</i>	<i>3-1</i>
Sensitivity of lake evaporation to temperature .....	3-1
Basin runoff sensitivity to climate change .....	3-6
Water balance and climatic sensitivity of the Owens Valley .....	3-18
Modeled runoff and lake response .....	3-26
Lumped-parameter, regional water balance approach .....	3-27
Thornthwaite water balance model .....	3-29
Spatially distributed application of the Langbein relationship .....	3-41
Summary .....	3-43
<i>Chapter 4 - Glacial Chronology.....</i>	<i>4-1</i>
Cosmogenic chronology .....	4-1
Sampling .....	4-2
Processing and analysis.....	4-2
Results.....	4-9
Terminus position chronology .....	4-21
<i>Chapter 5 - Glacier Modeling.....</i>	<i>5-1</i>
Snow/ice energy and mass balance.....	5-1
Estimation of monthly meteorological variables .....	5-2
Energy balance calculations.....	5-13
Intermediate grid examples.....	5-33
Glacier flow model .....	5-35
General continuity equation.....	5-40
Finite difference form and solution.....	5-41
Flow parameters.....	5-46
<i>Chapter 6 - Paleoclimatic Interpretation of Changes in Glacial Extent Using 2-D Models of Snow/Energy Balance and Ice Flow .....</i>	<i>6-1</i>



Accumulation area ratio (AAR) method and lapse-rate estimates of temperature depression	6-1
Application of the 2-D snow and energy balance model to the relationship between glaciers and climate.....	6-4
Climatic sensitivity of ELA .....	6-5
Surface-integrated water balance .....	6-13
Climatic sensitivity of AAR.....	6-16
The 2-D snow/ice energy and mass balance model coupled to a 2-D flow model .....	6-18
Model domain and example simulations .....	6-19
Simulated glacier distribution under modern climate .....	6-22
Simulated large glaciers – faithfulness to field evidence.....	6-26
Simulated glacier distribution under altered climate .....	6-28
Accumulation area ratios of simulated glaciers .....	6-38
Transient response of the flow model .....	6-41
Terrain alteration to match simulated glaciers to field evidence .....	6-44
Interbasin comparison – Bishop Creek and Horton Creek.....	6-45
Sensitivity to modeling assumptions and uncertain parameters .....	6-48
Potential applications of the 2-D glacier model .....	6-66
<i>Chapter 7 - Combined Analysis of Glacial and Lacustrine Records .....</i>	<i>7-1</i>
<i>Chapter 8 - Implications and Discussion.....</i>	<i>8-1</i>
<i>Chapter 9 - Conclusions .....</i>	<i>9-1</i>
Recommendations for further research .....	9-1
 <i>Appendices</i>	
Transient Isotope Calculations Worksheet .....	A-1
Rock Sample Processing for <sup>36</sup> Cl Analysis .....	B-1
Observed and Estimated Meteorological Data.....	C-1
Solar Angles Calculation Worksheet .....	D-1
Snow and Energy Balance Model Calculation Worksheet .....	E-1
Glacier Flow Model Code.....	F-1

---

## LIST OF FIGURES

---

- Figure 1-1. Map showing location of the Owens Valley, and the drainage basins of Bishop Creek, Horton Creek and McGee Creek. Figure modified from that in the USGS groundwater study of Danskin [1998]. Outer black line is the Owens Valley drainage basin boundary. Buff-colored inner region is the ground-water basin for Owens, Round, Chalfant, Hammil, and Benton Valleys – areas outside the ground-water basin include bedrock, the Volcanic Tableland, Long Valley, and isolated unconsolidated deposits. Thin white line is geologic contact. .... 1-5
- Figure 2-1. Oxygen isotope record of core OL-90 Owens Lake, California for the last 55 ka. Left ordinate axis is composition of carbonate; right-hand ordinate is inferred composition of the water from which the carbonates precipitated, assuming a water temperature of 15°C. Modified from Benson et al. [1996]. .... 2-3
- Figure 2-2. (A) The Searles Lake chronology of Smith [1987] shown with the radiocarbon dates of Lin et al. [1998] for Poison Canyon Units B and C (circles) and tufa at the spill level (square). The radiocarbon dates indicate that the last high stand of Searles Lake occurred at ~12 to 13 ka. (B) The Owens Lake stable isotope record of Benson et al. [1996]. .... 2-5
- Figure 2-3. Inferred lake level changes in Searles Lake for the late Pleistocene. Squares represent radiocarbon-dated samples of layered lacustrine sediments found in the southern end of Searles Valley [Smith, 1987; Benson et al., 1990]. Corresponding interpretations of lake-level fluctuations based on sediment type and stratigraphy are shown with symbols. .... 2-6
- Figure 2-4. Stable isotope composition records of carbonates in Owens Lake (black line) and Searles Lake (circles and gray line)..... 2-7
- Figure 2-5. Lake isotopic composition over time (top row) and lake surface area over time (bottom row) for three hypothetical scenarios in which the inflow to the lake is doubled, halved, then doubled again via a step function with a 100-yr timestep. In scenario A the lake is closed at all times. In scenario B the lake is closed under the lower inflow rate but overflows when the inflow is doubled. In scenario C the lake is always overflowing. In each scenario the lower flow rate is the higher flow rate of the previous scenario. Upper dashed line in lower row is lake surface area at overflow; lower line is modern, pre-irrigation area. Circles represent calculated composition for hypothetical continuous sampling of the lake where each sample averages approximately 25 years. .... 2-12
- Figure 2-6. Calculated steady-state composition of Owens Lake as a function of relative average annual inflow (normalized to modern inflow). .... 2-14
- Figure 2-7. Inferred relative inflow history for Owens Lake (upper graph) and combined lake surface area history (lower graph) for the Owens Valley lake system based on the Owens Lake  $\delta^{18}\text{O}$  record of Benson et al. [1996]. Black lines assume an 8°C decrease in temperature and a 2‰ decrease in

$\delta^{18}\text{O}$  for precipitation and runoff. Gray lines assume a 4°C decrease in temperature and a 1‰ decrease in  $\delta^{18}\text{O}$  for precipitation and runoff. Dotted lines in lower graph show cumulative lake surface area when China Lake (lower line) and Searles Lake (upper line) are at their sill levels. ....2-16

Figure 2-8. Calculated steady-state isotopic composition of carbonate in lakes downstream from Owens Lake as a function of relative inflow rate to Owens Lake (inflow rate normalized to modern inflow rate). Evaporation rate and isotopic composition of precipitation and local inflow to each lake are assumed to be the same as at present. Runoff from basins below Owens Lake is assumed negligible. ....2-17

Figure 2-9. (A) Oxygen isotope composition of carbonate from Owens Lake core OL90 [Benson et al. 1996]; Dotted line indicates the assumed dividing line for a closed versus overflowing Owens Lake; (B) oxygen isotope record for dolomite from Searles Lake core KM-3 [Phillips et al., 1992]; (C) calculated composition for dolomite in Searles Lake based on the inferred inflow history for Owens Lake (Figure 2-7) and (D) same as C but with the assumption that the diagenetic processes that produced dolomite did not alter the original calcium carbonate isotope signal. ....2-19

Figure 2-10. Comparison of lake level indicators in the lake system of the ancestral Owens River: (A) oxygen isotope records from Searles Lake, (B) elevations of marls and tufa deposits dated by Lin et al. [1998], (C) estimated combined lake surface area history inferred from (D) the Owens Lake isotope record. The hiatus in the Owens Lake record and periods of closure are also shown in C. Thick gray lines indicate our interpretation of the last wet episode in each record. ....2-20

Figure 3-1. Saturation vapor pressure curve for water. Reduction in the evaporation rate due to decreased temperature can be estimated from the coincident decrease in the saturation vapor pressure. Upper dotted line indicates vapor pressure at the mean annual air temperature at Owens Lake. Lower dotted line indicates the reduction in vapor pressure corresponding to a 5°C decrease in temperature. ....3-2

Figure 3-2. Relative change in evaporation rate as a function of temperature changes from a water surface initially at 15°C. Heavy black solid line reflects no temperature contrast between air and water temperatures. Dotted lines represent conditions where air temperature is 5°C warmer than water temperature and RH is 33% (upper dotted line) or 66% (lower dotted line). Dadot lines represent conditions where air temperature is 5°C cooler than water temperature and RH is 33% (upper dadot line) or 66% (lower dadot line, masked by black line). When the air is cooler than the water and RH is relatively high (lower dotted line), changes in temperature can make the vapor densities of the two bodies approach the same value. Under those conditions, very small temperature changes can lead to large reductions in evaporation rate as the evaporation rate approaches zero. ....3-4

Figure 3-3. Regressions of basin-wide mean annual precipitation, basin-wide mean annual runoff and basin-wide mean annual temperature (time-weighted by amount of precipitation) from runoff measurements throughout the United States. Dotted lines and question marks indicate where the data were extrapolated beyond the measurements. {From Mifflin & Wheat, 1979 [modified after Langbein, 1949]} ....3-7

Figure 3-4. Runoff response curves for the four areas studied by Flaschka et al. [1987]. Modeled runoff is plotted as a function of changes in temperature and precipitation. Solid lines show result of scenarios in which only precipitation was changed. Dashed lines include temperature, where a +2.0°C change was used in conjunction with a decrease in precipitation, and a -2.0°C change was used with increases in precipitation. ....3-9

Figure 3-5. Simulated stream flow responses to uniform change scenarios in the N. Fork American River Basin (sub-basin of the Sacramento River), showing percent streamflow change as a function of changes in mean temperature and mean precipitation. Simulations are for climate runs with the PRMS model. [Jeton et al., 1996].....	3-10
Figure 3-6. Runoff response (% change) to changes in mean annual precipitation and temperature based on Duell's [1994] regression models of the historical record. ....	3-11
Figure 3-7. Contour plot of percentage streamflow change as a function of percentage precipitation change and temperature departure for the Sacramento Basin. Changes are with respect to the long-term means, calculated from annual means for streamflow and precipitation, and from winter means for temperature. From Risbey and Entekhabi [1996]. ....	3-12
Figure 3-8. Relative amount of runoff (normalized to initial runoff) as a function of initial runoff coefficient with no change in evapotranspiration but an increase in precipitation of 10% (dotted line), 20% (dashed line), 30% (dashed line). Solid line shows effect of a 10% decrease in precipitation.....	3-15
Figure 3-9. Comparison of Duell's regression-model contours of percent change in runoff (left) with those for a simple runoff response calculation using the equation described in the text (right). The latter calculation assumes that evapotranspiration increases by ~2.5% per degree C and is proportional to precipitation by a factor of ~0.8. ....	3-16
Figure 3-10. Hypothetical response of runoff in a closed basin to changes in precipitation ( $P_0$ =modern precipitation rate) and temperature. Contours are runoff normalized to present-day runoff. Initial runoff coefficient is 0.14. Figure A illustrates relative change in runoff assuming that ET increases equal precipitation increases. Figure B illustrates response assuming that ET responds only to temperature. ....	3-19
Figure 3-11. Elevation map of the Owens Valley based on the USGS GLOBE digital elevation model dataset (left) and subdivisions of the basin (right) separated by water-balance characteristics. The alluvial valley area is as defined by the USGS study of the groundwater system of the valley [Danskin, 1998].....	3-20
Figure 3-12. Increase in runoff as a function of increased precipitation (assuming no change in evapotranspiration) for a basin with an initial runoff ratio of 15% (solid line) and one with an initial runoff ratio of 30% (dotted line).....	3-25
Figure 3-13. Cumulative lake surface area contours for the Owens Valley ( $10^8 \text{ m}^2$ ) as a function of changes in mean annual temperature and precipitation. Plot A assumes that evapotranspiration is directly proportional to precipitation and proportional to temperature in a manner predicted by the saturated vapor pressure curve. Plot B assumes the same conditions except for in the Sierra Nevada and riparian area of the Owens River where evapotranspiration increases are only half of the corresponding precipitation increase. ....	3-29
Figure 3-14. Mean annual climatic datasets and soil moisture storage capacity map used in the Thornthwaite water balance model. Annual average precipitation in the Owens Valley is from the PRISM dataset [Daly et al., 1994]; mean annual temperature is based on the regression of temperature records from the Owens Valley. Land cover data is from the USGS Land Use Land Cover dataset. ....	3-32

Figure 3-15. Combinations of temperature and precipitation for which the Thornthwaite water balance model was used to simulate basin evapotranspiration and runoff response in the Owens Valley.....	3-37
Figure 3-16. Modeled runoff response of the Owens Valley to changes in temperature and precipitation in contours of (top) relative runoff (normalized to present-day value) and (bottom) relative runoff coefficient .....	3-38
Figure 3-17. Lake surface area ( $10^8 \text{ m}^2$ ) as a function of temperature and precipitation changes in the Owens Valley and the resultant runoff as calculated using a Thornthwaite water balance model. ....	3-40
Figure 3-18. Contours of constant runoff coefficient, as a function of mean annual precipitation and temperature, from (A) the Langbein [1949, 1962] summary of runoff in the U.S. and (B) application of the Thornthwaite water balance model of the Owens Valley for a wide range of climatic conditions. Figure A was derived by multiple non-linear regression of data interpolated from the Mifflin and Wheat plot of the original Langbein [1949] curves. ....	3-41
Figure 3-19. Comparison of the runoff coefficient contours generated from (A) the Langbein summary of runoff in the U.S., (B) results of a spatially distributed application of the Langbein precipitation-temperature-runoff relationship, and (C) the Thornthwaite water balance model of the Owens Valley. ....	3-42
Figure 4-1. Map of Bishop Creek and the surrounding area showing locations of other creeks and drainage basins referenced in the text. Digital elevation data is from USGS 7.5-min STDS DEMs. The striping apparent in portions of the surface is an artifact of errors in the USGS digitization that have since been corrected. ....	4-3
Figure 4-2. Oblique aerial photo of Bishop Creek terminal moraine complex showing several Tahoe and Tioga lateral and terminal moraines. ....	4-4
Figure 4-3. Oblique aerial photo of Horton Creek showing several Tahoe- and Tioga-stade moraines. ....	4-5
Figure 4-4. Oblique aerial photo of the moraines below McGee Creek with Tioga and Tahoe moraines indicated. ....	4-5
Figure 4-5. Locations of moraine boulders, polished or striated bedrock, and erratics sampled and analyzed in the Bishop Creek basin and in Humphreys Basin. ....	4-6
Figure 4-6. Locations of moraine boulders, polished or striated bedrock, and erratics sampled and analyzed in the Horton Creek (HL-series, circles) and McGee Creek (LMC-series, crossed circles) basins. Contour interval is 100 meters. ....	4-7
Figure 4-7. Ages from the most recently dated features in Bishop Creek and Horton Creek. Uncertainties shown are the standard deviation of the AMS analysis. ....	4-12
Figure 4-8. Summary of $^{36}\text{Cl}$ ages of samples from the Bishop Creek basin. Different symbols represent ages assuming different erosion rates. Groupings indicate locations of the sampled moraines and deposit types. Age ranges are our estimates of uncertainty based on the range and spread of ages associated with each deposit. Error bars give the one sigma standard deviation in age given by the uncertainty in the AMS measurement. ....	4-14

Figure 4-9. Three-dimensional view looking eastward across Humphreys basin through Piute Pass into North Fork, Bishop Creek. ....	4-16
Figure 4-10. Map of paleo iceflow indicators above Piute Pass at the head of the north fork of Bishop Creek. Dashed line shows inferred location of the ice divide during the last glacial maximum. ....	4-17
Figure 4-11 Summary of $^{36}\text{Cl}$ ages of samples from the Horton Creek basin. Different symbols represent ages assuming different erosion rates. Groupings indicate locations of the sampled moraines and deposit types. Age ranges are our estimates of uncertainty based on the range and spread of ages associated with each deposit. Error bars show 1-sigma standard deviation in age due only to the uncertainty in the AMS measurements. ....	4-18
Figure 4-12. Summary of $^{36}\text{Cl}$ ages of samples from the McGee Creek. Different symbols represent ages assuming different erosion rates. Groupings indicate locations of the sampled moraines and deposit types. Age ranges are our estimates of uncertainty based on the range and spread of ages associated with each deposit. Error bars give the one sigma standard deviation in age given by the uncertainty in the AMS measurement. ....	4-20
Figure 4-13. Terminal position elevations of glaciers in the Bishop Creek area. Lines are creek profiles within each basin. ....	4-23
Figure 5-1. Precipitation data used to estimate monthly precipitation as a function of elevation for the Bishop Creek area. Sites included in the regression were South Lake, Lake Sabrina, Bishop Creek and Bishop Airport. ....	5-5
Figure 5-2. Precipitation as a function of elevation in February (left) and July (right). ....	5-5
Figure 5-3. Mean annual precipitation versus elevation regression used in this study (solid red line) and Danskin's [1998] linear regression for the west side of the Owens Valley. ....	5-6
Figure 5-4. Hypsometry of Bishop Creek and several nearby basins. ....	5-7
Figure 5-5. Hypsometric integral curves for Bishop Creek and nearby basins. ....	5-8
Figure 5-6. Total precipitation, snowfall and rainfall as a function of elevation in Bishop Creek under modern climatic conditions. ....	5-10
Figure 5-7. Calculated monthly precipitation for Bishop Creek partitioned into snow and rain for an elevation of (left) 2000 m and (right) 3000 m. ....	5-11
Figure 5-8. Average wind speed at Bishop, CA and – for comparison - Reno, NV. Values of zero represent gaps in the data. ....	5-12
Figure 5-9. Summary of mean monthly meteorological, energy-balance and snow-balance measurements of Marks et al. [1992] and Marks and Dozier [1992] at the 'Lake site' in the Emerald Basin during 1988 and 1989. The vertical dashed line indicates the first month for which there is significant melting. This corresponds to the first month for which the average temperature is considerably above zero. ....	5-17
Figure 5-10. Relative optical path length for the first day of the year (circles) and the middle day of the year (squares). ....	5-20

Figure 5-11. Atmospheric transmissivity coefficient dependence on temperature at different zenith angles as calculated in this model (solid lines) and using the polynomial expression of Klein [1948].5-21

Figure 5-12. Oerlemans approximation for the effect of cloud-cover on the atmospheric shortwave radiation transmission coefficient at 1500 m (dashed red line) and at 4000 m (dashed blue line). The approximation of Barashkova [Kondratyev, 1969] (thin black dotted line) is shown for comparison.5-23

Figure 5-13. Shortwave radiation albedos for a range of snow and ice conditions. From Paterson, 1994.....5-25

Figure 5-14. Simulated daily average solar radiation on a horizontal plane at an elevation 1300 m with random cloudiness (left) compared with daily average solar radiation measurements made during 1984 and 1985 at a site in the northern Owens Valley [Duell, 1990]. .....5-26

Figure 5-15. Error caused by calculating atmospheric longwave radiation from a mean temperature instead of integrating over the diurnal temperature cycle. ....5-29

Figure 5-16. Monthly sensible heat (H) values from the Emerald Basin [Marks and Dozier, 1992] plotted against the product of mean temperature and wind speed. Box shows the equation and  $R^2$  value for a linear regression (dotted line) of the data.....5-31

Figure 5-17. Examples of calculated monthly energy flux via shortwave radiation (1<sup>st</sup> column), sensible heat transfer (2<sup>nd</sup> column) and latent heat transfer (3<sup>rd</sup> column) from the mass and energy balance model applied to the Bishop Creek drainage. Upper row are grids for July, lower row is October. Energy fluxes are mean monthly values ( $\text{watts m}^{-2}$ ).....5-34

Figure 5-18. Hypothetical glacier cross-section (longitudinal slice) illustrating the driving stress for a parallel-sided (top and bottom sides, that is) slab of ice on an inclined plane.....5-37

Figure 5-19. Five-point finite difference star used to calculate ice-flow velocities. ....5-43

Figure 5-20. Log ice flux ( $\text{m}^3/\text{yr}$  per unit width) contours as a function of ice thickness (m) and ice-surface gradient. Flow parameter,  $f$ , equals 0.5 (i.e. equal weights are assigned to the sliding and deformation terms of the ice flow equation). Arrow indicates that at a surface slope of  $\sim 2\%$ , and initial ice thickness of 120 m, a tripling in ice flux from  $\sim 900 \text{ m}^3/\text{yr}$  to  $\sim 2700 \text{ m}^3/\text{yr}$  (per unit width) requires an increase in thickness of  $\sim 55 \text{ m}$ .....5-47

Figure 6-1. USGS Digital elevation model (DEM) for the area of the Bishop Creek drainage basin with stream and stream diversions from the USGS hydrography digital line graph map. Drainage basin for Bishop Creek above Coyote Creek is shown in white. Black outline (A) is the Tioga maximum ice extent as inferred from field mapping of glacial features. Right-hand figure shows the areas used for calculating integrated surface balance for the Tioga maximum glacier (blue outline) and the Tioga IV glacier (red outline) in Bishop Creek.....6-3

Figure 6-2. Hypsometric curves for the areas defined in the polygons shown in Figure 6-1. Solid line is hypsometric curve for the Tioga I glacier area, dashed line is for the Tioga IV glacier. Dashed vertical lines indicate elevations that would describe an accumulation area ratio of 0.65. The ELA of the modern glaciers, approximately 3700 meters, is shown for comparison. ....6-3

Figure 6-3. Modeled net annual accumulation of snow (mm of snow water equivalent) in the Bishop Creek basin for modern climatic conditions. Blue indicates areas of positive net accumulation. Red

indicates areas of negative net accumulation (ablation). Grid is universal transverse mercator projection showing northing and easting in meters. ....	6-6
Figure 6-4. Enlarged view of a portion of Figure 6-3 shown as shaded relief. Color-coding for net annual accumulation of snow (mm of snow water equivalent) is only approximate due to relief shading. Areas outside the Bishop Creek drainage basin are color-coded by elevation, not snow accumulation. ....	6-7
Figure 6-5. Comparison of annual average energy fluxes at South Lake in the South Fork of Bishop Creek for (left) modern climatic conditions and (right) a temperature decrease of 4°C and no change in precipitation. Bars are, left-to-right, the average annual energy used for melting, and average annual shortwave, longwave, sensible, and latent energy fluxes. ....	6-7
Figure 6-6. Simulated net annual snow (water equivalent) accumulation in Bishop Creek for four different climatic conditions. Climatic changes are indicated by the difference in temperature from modern (°C) and the rate of precipitation relative to modern conditions (i.e. 5.0*P = five times the modern precipitation rate). The region between the two black polygons illustrates the area that, based on geological evidence, we considered the likely contributing area for the Bishop Creek glacier during the last glacial maximum. Thin blue line is the 3300-m elevation contour. ....	6-8
Figure 6-7. Contours of equilibrium line altitude (ELA) derived from application of the spatially distributed snow and energy balance model. The local ELA includes shading and shadowing effects of the terrain. Circles indicate simulations on which the contours were kriged. ....	6-10
Figure 6-8. Regional ELA as a function of changes in temperature and precipitation from the modern climate. Circles indicate simulations for which ELA was calculated. Calculations are as shown in Appendix E. ....	6-11
Figure 6-9. Comparison of regional ELA contours (dashed red curves) and 'local ELA' contours (blue curves). ....	6-13
Figure 6-10. Simulated net annual accumulation distribution in Bishop Creek assuming a temperature depression of (A) 6°C and (B) 5°C. The net accumulation patterns produce near-zero surface integrated water balances for the Tioga maximum glacier (A) and the Confluence glacier (Tioga IV) (B). Yellow polygons indicate the areas over which the water balance was integrated (excluding area within inner polygon in A). Thin blue lines are the 3000-m and 3100-m contours, respectively, corresponding to an AAR of 0.65. Px1 indicates precipitation rate is 100% of modern. ....	6-15
Figure 6-11. Curves representing zero integrated net accumulation for the Tioga II (solid line) and Tioga IV glacier (dashed line) in Bishop Creek. Integrated balance is over the polygon areas shown in Figure 6-1. ....	6-16
Figure 6-12. Accumulation area ratio versus average annual snow accumulation in the polygons shown in Figure 6-10 for the Tioga II (gray circles) and Tioga IV (open circles) glaciers. The average water balance is zero for distributions that produce a steady-state glacier. Area of symbols is proportional to precipitation rate. ....	6-17
Figure 6-13. Shaded relief image of the area of used for modeling glacier snow/ice energy and mass balance and glacier flow in Bishop Creek. Black line is the watershed boundary. ....	6-19



- Figure 6-14. Simulated glacier output for the Bishop Creek basin for (left) modern precipitation rate and temperature and (right) a decrease in temperature of 1°C and no change in precipitation. ....6-20
- Figure 6-15. Simulated glacier output for the Bishop Creek basin assuming no change in precipitation and a decrease in temperature of (left) 2°C, (right) 3°C. ....6-21
- Figure 6-16. Simulated glacier distribution in the Bishop Creek area under modern climate. Boxes show locations of glaciers in following plate. Simulated glaciers (grey and blue shaded areas) are overlain by the USGS topographic maps of the area.....6-23
- Figure 6-17. Comparison of simulated glacier distribution under modern climate with the USGS-mapped glaciers and permanent snowfields for the area below Mt Humphreys at the head of McGee Creek. Simulated glaciers (grey and blue shaded areas) are overlain by the USGS topographic maps of the area. Existing glaciers are mapped in white with blue contour lines.....6-24
- Figure 6-18. Comparison of simulated glacier distribution under modern climate with the USGS-mapped glaciers and permanent snowfields for the area above Upper Lamarck Lake in the north fork of Bishop Creek. Simulated glaciers (grey and blue shaded areas) are overlain by the USGS topographic maps of the area. Existing glaciers are mapped in white with blue contour lines. ....6-25
- Figure 6-19. Comparison of simulated glacier distribution under modern climate with the USGS-mapped glaciers and permanent snowfields for the area near the Powell Glacier in the middle fork of Bishop Creek. Simulated glaciers (grey and blue shaded areas) are overlain by the USGS topographic maps of the area. Existing glaciers are mapped in white with blue contour lines. ....6-26
- Figure 6-20. Comparison of a simulated Tioga maximum glacier (produced by a 5°C temperature depression and a 50% increase in precipitation) with our estimate of the glacier's shape (black line) based on field mapping of glacial trimlines and other glaciomorphologic features. ....6-29
- Figure 6-21. Ice velocity vector map for a simulated Tioga maximum glacier in Bishop Creek, overlain on a digital relief image of the terrain. Area shown is just below the confluence of the South and Middle Forks. The plot shows a cross-section of the terrain and glacier at A-B. ....6-30
- Figure 6-22. Comparison of simulated-glacier velocity vectors (yellow arrows) for a Tioga maximum glacier in Bishop Creek with mapped flow indicators (bold black arrows). Area shown includes Piute Pass and part of Humphrey's Basin above the North Fork of Bishop Creek and the mapped flow indicators are those shown in Figure 4-10. Red-shaded area shows relief; gray and blue colors indicate ice-flow velocity. ....6-31
- Figure 6-23. Simulated glaciers in Bishop Creek under four different combinations of temperature and precipitation. Upper simulations both match glaciomorphologic evidence of ~Tioga II glaciers. Upper left represents temperature 3°C colder and precipitation 260% greater than modern; upper right represents a change due only to temperature depression (-6°C). Lower left simulation matches the Tioga IV glacial advance and lower right the Recess Peak advance. ....6-32
- Figure 6-24. Terminus elevation along an arbitrary reference flowpath versus total ice-covered area at the end of each simulation. Different symbols correspond to different grid resolutions. ....6-33
- Figure 6-25. Contours of glacier terminus position, as meters elevation, for simulated Bishop Creek glaciers under different climatic conditions. Contours were developed by kriging the results of the simulations indicated by the symbols. ....6-34

- Figure 6-26. Contours of glacier terminus position, as meters elevation, for simulated Horton Creek glaciers under different climatic conditions. Contours were developed by kriging the results of the simulations indicated by the symbols. ....6-34
- Figure 6-27. Changes in terminus position (m elevation) of glaciers in Bishop Creek glacier as a function of (A) temperature and (B) precipitation. ....6-35
- Figure 6-28. Total ice-covered area of simulated glaciers (symbols) versus ELA compared to hypsometric curve (dashed curve) – the fraction of total basin area below each elevation.....6-36
- Figure 6-29. Simulated glaciers for climatic conditions that provide near-zero surface integrated water balance within the presumed polygonal areas that describe (A) the Tioga II glacier's extent and (B) the Tioga IV glacier's extent. Both examples illustrate the difficulties in reconstructing the shape of even relatively large glaciers solely from field evidence. The extent of the Tioga IV glacier, for example, depends significantly on the degree of contribution from South Fork, where little evidence of that advance remains. ....6-39
- Figure 6-30. Shaded relief image of the confluence area showing (left) the descending left and right lateral moraines extending from the Middle Fork of Bishop Creek. The simulated glacier for a temperature depression of 4°C and 30% precipitation increase (right) provides an excellent match to the morainal evidence.....6-40
- Figure 6-31. Accumulation area ratios of simulated glaciers as a function of total glacier surface area. Symbol size is proportional to equilibrium line altitude. Different symbols correspond to different grid resolutions. ....6-40
- Figure 6-32. Terminus elevations of simulated glaciers plotted against the glacier's integrated surface balance error at steady state.....6-41
- Figure 6-33. Simulated glacier growth in the Bishop Creek basin. Initial ice thickness is zero; final steady state simulates Tioga-maximum conditions. Parameters shown are (A) integrated surface balance, (B) maximum ice thickness and (C) lowest elevation with ice.....6-42
- Figure 6-34. Estimated time to reach steady state versus terminus elevation. Vertical collections of points reflect the fact that many simulations were run to a rough estimate of the minimum time required.....6-43
- Figure 6-35. Examples of simulated glaciers in Horton and McGee Creeks under a 5°C temperature depression. (A) The Horton Creek glacier, flowing on the existing topography leaves Horton Creek at the terminal moraine complex and two lobes of ice flow to the southeast. (B) Simulated glaciers on a modified surface, excavated to allow the ice to flow along Horton Creek. Contour interval is 100 meters.....6-47
- Figure 6-36. Terminus elevation (m) contours of glaciers in Bishop Creek (heavy gray lines) and Horton Creek (black lines) assuming that mean annual precipitation in Horton Creek is ~14% less than in Bishop Creek. Temperature difference and  $P_0$  refer to modern climatic conditions. ....6-48
- Figure 6-37. Profiles of three simulated glaciers along a streamline of the existing topography (black region). Accompanying glacier thickness map shows reference path with the glacier produced using the “best-fit” conductance values of this study. ....6-52

Figure 6-38. Differences in a simulated steady-state Tioga-maximum glacier in Bishop Creek as the sliding and deformation coefficients are varied from those of the (A) base-case simulation by (B) a decrease of one order of magnitude, and (C) an increase of an order of magnitude. Climatic adjustment is a 5°C decrease in temperature and a 150% increase in precipitation. ....6-53

Figure 6-39. Mean monthly shortwave, longwave and net energy fluxes to the glacier surface at South Lake in the South Fork of Bishop Creek under climatic conditions of -5°C and 1.5 times precipitation assuming (left) modern cloudiness conditions, (center) a doubling in cloudiness and (right) cloudiness distribution shifted by 6 months. Only months where temperature is above zero are shown; first month in each series is June. ....6-58

Figure 6-40. (A) Net accumulation map for a 5°C temperature depression and 50% precipitation increase and (B) the change in net accumulation induced by calculating the snow/ice energy and mass balance on the surface of the Tioga maximum glacier rather than the modern ground surface. ....6-59

Figure 6-41. Change in net accumulation induced by (A) a doubling in wind speed and (B) calculating the snow/ice energy and mass balance over two, rather than one, annual cycle. ....6-60

Figure 6-42. Change in net accumulation induced by (A) a doubling in cloudiness and (B) a shift in monthly cloudiness by six months (winter to summer).....6-61

Figure 6-43. Histogram of increases- over the base-case model estimates - in temperature depression needed to sustain a given glacier at steady state.....6-65

Figure 6-44. End-member net accumulation maps for the Tioga II glacier in Bishop Creek. DT = temperature difference from modern climate. Prel = precipitation rate normalized to that of the modern climate.....6-69

Figure 6-45. Simulated glaciers developed from the net accumulation maps in Figure 6-44. DT = temperature difference from modern climate. Prel = precipitation rate normalized to that of the modern climate.....6-69

Figure 7-1. Overlay of the Bishop Creek glacier response surface (thin black, subhorizontal, contours of equal terminus elevation (m)) and the Owens Valley lake system response surface (thick gray contours of cumulative lake surface area ( $10^8 \text{ m}^2$ )). Temperature and precipitation reference ( $P_0$ ) conditions refer to modern climate.....7-2

Figure 7-2. Estimated history of changes in the glacial and terminal lake system in the Owens Valley for the past ~20 kyr. Curved line (left ordinate) is cumulative surface area for the Owens Valley lake system. Dotted lines indicate lake surface area at lake sills. Bars (right ordinate) represent elevations of glacial termini during advances or relatively stable glacial periods in Bishop Creek.....7-4

Figure 7-3. Overlay of the Bishop Creek glacier terminus position response surface (thin black, subhorizontal, contour lines labeled with terminus elevation in meters) and the Owens Valley lake system response surface (cumulative lake surface area contours (thick gray lines). Heavy black dashed lines indicate cumulative lake surface areas at sills of Owens, China and Searles Lakes. Temperature and precipitation reference ( $P_0$ ) conditions refer to modern climate. ....7-5

Figure 7-4. Total lake surface area contours (dashed lines) corresponding to various sills in the system, and glacier terminus elevation contours (solid lines) corresponding to four of the last five recorded advances in Bishop Creek. The latter have been adjusted to account for systematic errors in

the glacier model. Circles and corresponding ages indicate the intersections of contours describing contemporaneous events in the lake-surface area and glacial chronologies. They therefore describe the temperature and precipitation combinations that could satisfy both constraints. Error bars represent one sigma errors in the temperature and precipitation estimates derived from the glacier model. ....7-7

---

## LIST OF TABLES

---

Table 2-1. Estimates of modern values for various parameters needed to calculate the water balance and isotope balance of Owens Lake. The references list sources for the estimated values.....	2-13
Table 3-1. Summary of precipitation and discharge data for the Owens Valley and subbasins considered in this study. †The runoff coefficient shown for the riparian area is calculated differently than for the other subbasins; its precipitation term includes discharge from the other subbasins. ...	3-21
Table 3-2. Soil moisture storage capacity associated with the land cover types shown in Figure 3-14.	3-33
Table 4-1. Terminal position elevations (meters above mean sea level) of glaciers in the Bishop Creek area. ....	4-22
Table 5-1. Summary of basin precipitation (P), temperature (T) and runoff coefficients ( $\alpha$ ) used or calculated in the estimation of precipitation differences among basins in the Bishop area. ....	5-9
Table 5-2. Sensible heat transfer coefficients from the literature. The value for Oerlemans is calculated from the published bulk transfer coefficient and an assumed average wind speed of 6 m/sec. ....	5-32
Table 5-3. Empirically determined coefficients for glacier ice flow due to deformation ( $k_1$ ) and sliding ( $k_2$ ). Row G shows the average of many values reported in the literature, and row H provides the ratio of the largest of the values to the smallest. Row I shows the values used by Pfeffer et al. [1997] that assumes a slightly different form of the sliding velocity term than those studies listed in rows A through F. Values used in this study are shown in row J. ....	5-46
Table 6-1. Changes in terminus position as a result of various sensitivity tests described in the text. $\Delta Z$ and $\Delta X$ are, respectively, the vertical and horizontal changes in terminus position. $\Delta Z_{\text{frac}}$ and $\Delta X_{\text{frac}}$ are the fractional changes in the decrease in elevation (1950 m) represented by the base case, and the total length (27.5 km) of the base-case glacier. Note that item C also corrects for the effect of initial conditions described by simulation G. ....	6-63
Table 6-2. Estimated paleoclimatic uncertainties associated with various errors and uncertainties in the modeling process. Effects of the uncertainties are described in terms of the difference in temperature depression ( $\Delta T$ ), and the difference in the relative precipitation rate ( $\Delta P/P_0$ ) that would be required to produce the Tioga maximum glacier relative to the base case simulation. Items A and B are considered systematic errors. Estimated uncertainties are based on (C) a factor of 5 uncertainty in both flow constants, (D) an ~40% error in the albedo of ice, (E) a factor of 2 difference in cloudiness, (F) a factor of 2 difference in windiness, (G) a factor of 2 difference in turbulent transfer coefficients, and (H) a 20% difference in precipitation. ....	6-63

Table 6-3. Parameter changes included in the logic tree uncertainty analysis, estimated probabilities, and the difference in temperature from the temperature predicted using the base-case model. ....6-64

---

## CHAPTER 1 - INTRODUCTION

---

The ability to predict changes in global climate requires a thorough understanding of the fundamental processes that control it. Our knowledge of these processes is based in part on our ability to understand what has driven past changes in climate, and our ability to understand those changes is, in turn, based largely on our ability to reconstruct, from geological records, the histories of the numerous climatic variables that attend, reflect and control climate change.

The late Quaternary is of particular interest to those studying how the global climate system behaves because high-resolution proxy records of climate are available for much of that period and because it contains many dramatic changes in global climate, including the transition from the last glacial maximum (LGM), at ~18 ka, to the dramatically warmer, and relatively stable, present-day interstadial. Temperature is clearly one of the primary variables of climate change and the spatial distribution of changes in it is one of the primary clues to the mechanisms behind climate changes of the past. Proxies in ice-sheet cores and sea sediments provide excellent high-resolution temperature histories for much of the late Quaternary for the poles and certain ocean areas. Continental records of climate change, by comparison, are generally less accurate (Stute *et al.*, 1992) and typically of lower resolution. Precipitation and temperature reconstructions for continents, for example, have been based on packrat middens, pollen data, beetle and land snail data, soil carbonates, cave deposits, tree rings and noble-gas paleothermometry in groundwater (Stute *et al.*, 1992).

Two sources of geologic evidence that are of widespread interest as continental paleoclimate records in North America are (1) the lacustrine deposits of the large pluvial lakes and (2) the glacial deposits of the more extensive alpine glaciers that once existed in parts of the Great Basin of the southwestern United States. During what is commonly termed the glacial-pluvial period, vast lakes existed in many of the closed basins of the Great Basin that now contain only ephemeral lakes or playas. At the same time, glaciers in many of the mountain ranges of the Great Basin extended many

kilometers beyond where the present-day cirque glaciers are active. Incomplete yet remarkable histories of the changes in the lakes are preserved in exposed shorelines, wave-cut terraces, beach bars and thick lacustrine mud deposits. Similar glacial histories are preserved in abandoned glacial trim-lines, lateral moraines and sequences of terminal moraine loops. Many geologists have examined these deposits and described their stratigraphy, chronology and relationship to other paleoclimatic records. Typically, the deposits are summarized using a parameter that reflects the system's response to climatic change. For glacial deposits, this is generally the glacier's equilibrium line altitude (ELA). It represents the position on a glacier above which there is net annual accumulation and below which there is net ablation. The ELA is therefore similar to the regional snowline in that it is clearly responsive to changes in the primary climatic variables - temperature and precipitation. The position of the ELA of a paleoglacier, however, is not directly preserved in glacial deposits. It must be inferred based on assumptions about the accumulation area - ablation area ratio of typical glaciers and the presumed 2-D extent of the former glacier. Moreover, because it responds quite strongly and similarly to changes in both temperature and precipitation, paleo-ELAs can suggest ranges of combinations of those variables that may have existed in the past but cannot be used to reconstruct the specific histories of either variable independently. For the purposes of understanding the mechanisms behind climate change however, it is the specific changes that we desire.

Those studying the pluvial lakes confront a similar problem. The Great Basin is characterized by a large number of internally drained basins. The terminal lakes in these basins collect groundwater and runoff<sup>1</sup> from the surrounding landscape and achieve water balance by adjusting their surface area so that net annual evaporation equals the net annual inflow. Today most of the lakes are small and ephemeral but during the pluvial high stand, lake surface areas were as much as ten times the area of the modern lakes [Benson *et al.*, 1990]. The parameter that best describes the response of these

---

<sup>1</sup> Defined here as the discharge of water in surface streams, excluding artificial storage and diversion effects [Langbein, 1949].



closed basin lakes to climate change is the combined lake surface area (LSA) of the water bodies providing the evaporation outflow that balances groundwater and surface water inflow. This parameter is sensitive to both temperature and precipitation changes because temperature affects evaporation and transpiration, and precipitation affects the rate of inflow to the lake. As such it provides a constraint on the combinations of precipitation and temperature changes that would have been required to produce the greatly expanded lakes but does not by itself define the specific degree of change in each.

Within a basin that contains, or once contained, both alpine glaciers and closed-basin lakes we can often assume that temperature and precipitation changes are relatively uniform. Consequently both the lakes and the glaciers in the basin respond to essentially the same climate forcing. The response of these systems to changes in the primary climatic variables, however, is likely to be quite different. This is fundamentally a result of the difference in how the two systems attain water balance. At steady state, glaciers achieve water balance by moving snow accumulated at high elevations to lower elevations where it can melt. Evaporation and sublimation play a much smaller role in controlling the mass balance of most alpine glaciers. Steady state in a closed-basin lake system, on the other hand, represents a balance between basin-wide precipitation and evapotranspiration. Because the energy required for melting is roughly only one eighth of that required for evaporation, glaciers should be much more sensitive than closed-basin lakes to changes in temperature.

These differences in the response of the two systems to the primary climatic variables provide us with a potentially powerful means of interpreting their geologic record. Each system by itself can be considered to define a temperature vs. precipitation response curve for each glacial or lacustrine extent. For the reasons discussed above, the slopes of these curves should be sufficiently different that, given knowledge of the extent of both systems at a particular time, we can use the constraints imposed by their intersecting response curves to determine the climatic conditions that could

reproduce each system at the observed state. This paper describes the implementation of that concept, demonstrated in an attempt to determine the paleoclimatic conditions that existed in the Owens Valley (Figure 1-1) during the last deglaciation.

A particularly difficult aspect of determining the response of lacustrine systems to climate change lies in estimation of the response of basin-wide evapotranspiration and runoff. For this reason, previous attempts to reconcile the lacustrine and glacial records have typically used independent estimates of LGM temperature and precipitation changes to determine what basin-scale climatic changes would have been required to accommodate the recorded changes in each system. Brakenridge [1978] and Hostetler and Benson [1990], for example, both considered the response of lacustrine systems in the Great Basin to an assumed temperature depression of 7° to 8°C with little or no corresponding increase in precipitation. Those estimates of the paleoclimate of the LGM were based on independent analyses of regional snowline depression in the Great Basin. Regional snowline depression is assumed to reflect primarily a decrease in temperature when the latitudinal gradient of the snowline index is similar to that under modern conditions. Based on evidence of the lower limit of small glaciers in Nevada, Arizona and New Mexico, Brakenridge [1978] concluded that the similarity in the latitudinal gradient of their distribution with that of the modern snowline and mean annual -6°C isotherm required only a temperature depression of 7° to 8°C. Dohrenwend however, in his review of previous estimates of paleoclimatic conditions in the Great Basin, indicated that Brakenridge's estimate was based on an overgeneralized model of temperature distribution:

*"This temperature model, derived from climatic data collected in Arizona and southwestern Utah, was applied to the distribution of modern glaciers in Montana, Wyoming, and northern Colorado in order to estimate the mean annual temperature of the modern cirque-glacier ELA in Arizona" [Dohrenwend, 1984].*

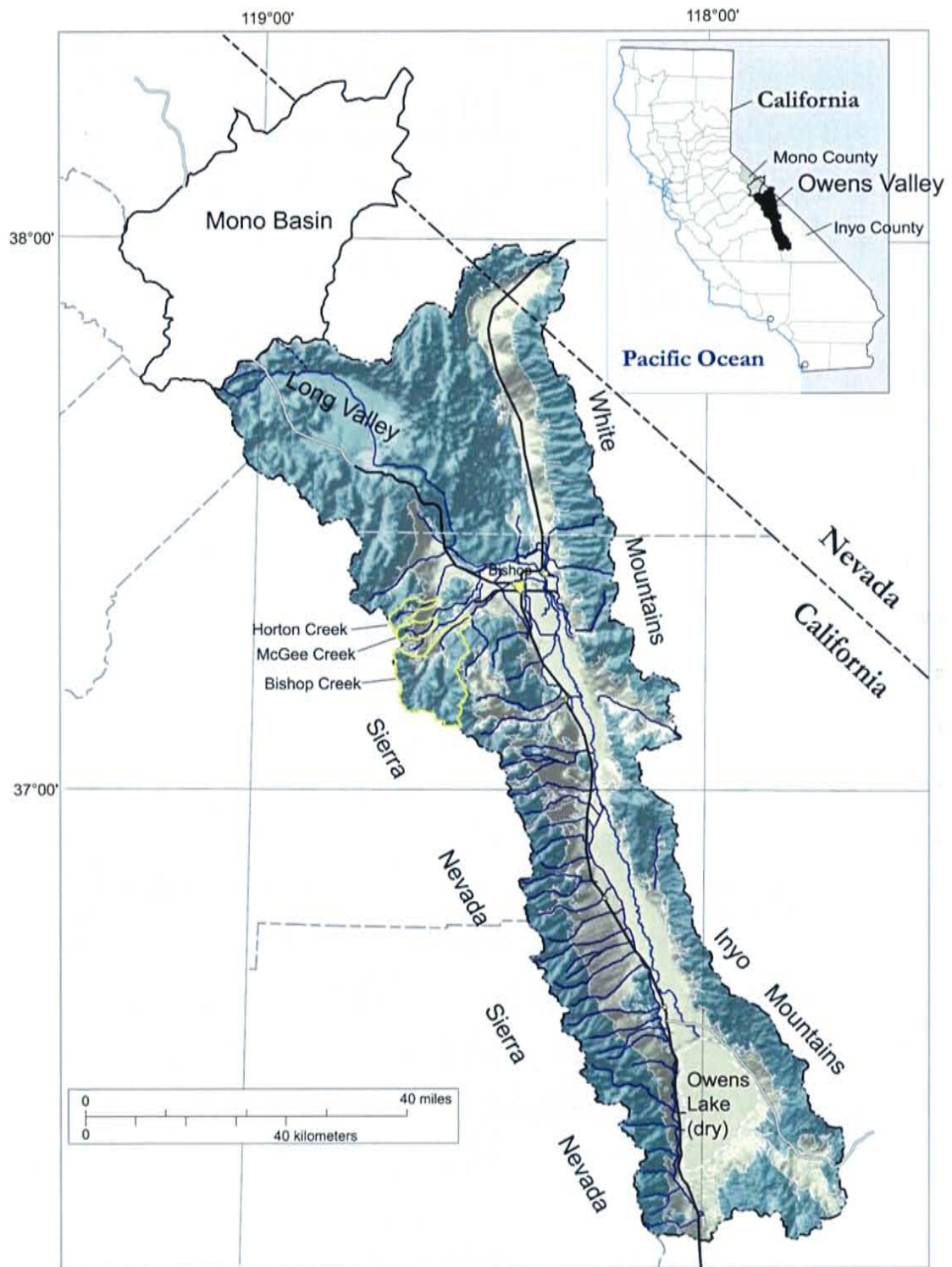


Figure 1-1. Map showing location of the Owens Valley, and the drainage basins of Bishop Creek, Horton Creek and McGee Creek. Figure modified from that in the USGS groundwater study of Danskin [1998]. Outer black line is the Owens Valley drainage basin boundary. Buff-colored inner region is the ground-water basin for Owens, Round, Chalfant, Hammil, and Benton Valleys – areas outside the ground-water basin include bedrock, the Volcanic Tableland, Long Valley, and isolated unconsolidated deposits. Thin white line is geologic contact.

Dohrenwend conducted a more careful analysis of full-glacial cirque-floor ELAs and nivation (frost-action derived changes in slope) threshold altitudes with modern ELAs but came to a similar conclusion: (1) mean annual temperature in the Great Basin during the last glacial maximum was approximately 7°C colder than at present and (2) precipitation rates were probably similar to modern. From his comparison of latitudinal gradients of modern versus full glacial snowline proxies, Dohrenwend also concluded that the full glacial climate of the Great Basin was characterized “by either a steeper north-to-south temperature gradient or a steeper south-to-north accumulation-season precipitation gradient than exists today.” His estimates of temperature and precipitation differences during the LGM may therefore not apply as far south as the Owens Valley.

Reconstruction of both temperature and precipitation changes from latitudinal gradients in temperature and snowline indicators requires accurate regional scale mapping of a large number of modern- and paleo-snowline indicators as well as detailed knowledge of the spatial and altitudinal distribution of temperature and precipitation. Unfortunately, sufficiently detailed climatic data are often lacking for many individual basins that may be included in such an analysis. Climatic data for upland areas of the Great Basin are, for example, extremely limited. “Only three long-term weather observations exist and the proximity of these stations to the Sierra Nevada limits their usefulness as representative indicators of climatic conditions in the Great Basin” [Dohrenwend, 1984]. Moreover, climatic parameters are often highly variable not only from basin to basin but even across a single basin. Regional scale interpretations of glacial evidence are therefore typically based on, at best, mean annual climatic norms that tend to smooth out temporal differences in precipitation and temperature cycles that may have a large impact on the relevant energy and mass balances.

To avoid the large-scale averaging of climatic parameters necessitated by regional analyses, we here attempt to use the combined constraints imposed by (1) a single closed basin and associated terminal lake system and (2) an individual glacier or glaciers within the same basin for which relatively

detailed climatologic information is available. Specifically, we apply this combined constraints approach to the Owens Valley (Figure 1-1), at the southwestern boundary of the Great Basin. The lacustrine system is the closed basin lake chain that begins with Owens Lake and extends, at wettest times, to Death Valley. The glacial counterpart we consider is the glacial record of one of the largest tributaries of the eastern Sierra Nevada, Bishop Creek, as well as several smaller tributaries to the Owens River.

Application of the combined constraints approach to reconstructing paleoclimate requires

1. chronologies of the changes in each system so that contemporaneous states of each are known for at least one time period and
2. an assessment of the sensitivity of each system to a large range of changes in the primary climatic variables as well as to changes in other, second-order, climatic variables which may have been different in the past.

We apply a number of different methods to recover the history of changes in the glaciers and lakes in the Owens Valley during the last ~25 kyr. The lakes of the Owens Valley have been studied in detail for many years and we rely on results from many of these studies for our lacustrine chronology. Detailed chronologies of glacial advances are considerably more difficult to establish. Although many researchers [Birman, 1964; Sharp, 1969; Clark and Gillespie, 1997] have mapped the moraines throughout much of the eastern Sierra Nevada using the glacial succession first described by Blackwelder [1931] (or elaborations thereon), relatively few absolute dates are available to constrain the timing of the associated advances. This is because relatively few methods are available to reliably date glacial deposits and some of these are only recent developments. The most detailed geologic records of the Sierra Nevada's glacial history are the large lateral and terminal moraines extending out of the mouths of many of the canyons of the eastern side of the range. Radiocarbon

dates can be obtained in rare instances where organic materials contemporary with the moraines can be obtained. Clark and Gillespie [1997] managed, for example, to date organic deposits in several alpine lakes behind mapped Recess Peak moraines in the Sierra Nevada. In recent years cosmogenic exposure dating methods have greatly improved our ability to date glacial features, including moraines, erratics, and glacially polished or abraded rock surfaces [Gosse and Phillips, 2001]. The limits of this method appear to be primarily in its application to very old moraines – approximately 50 ka and up – where the scatter of boulder ages is greatly increased because of the greater variance in the weathering histories of surface boulders as erosion of the finer moraine materials continuously exhumes ‘new’ boulders. Even here, however, there have been recent advances in our ability to constrain moraine ages through statistical analysis of the distribution of sample ages [Shanahan *et al.*, 2000] and modeling of the erosive processes.

The most detailed chronology of glacial advances in the eastern Sierra Nevada is that developed by Phillips and Plummer [Plummer and Phillips, 1996; Phillips and Plummer, in preparation] for Bishop Creek, Horton Creek, and McGee Creek near Bishop, California, where nearly 200 cosmogenic exposure ages have been obtained on Tahoe and Tioga [Blackwelder, 1931] and younger moraines. We therefore use the glacial record of the Bishop Creek area as the basis for our glacial chronology of the Owens Valley.

A variety of methods have been used to estimate the sensitivity of closed-system lakes and glaciers to climate change. For this study, we developed a relatively high-resolution two-dimensional numerical glacier model to determine how glaciers in the various basins would respond to changes in climate. The model combines a monthly calculation of mass and energy balance, to estimate net annual snow accumulation distribution, with a transient 2-D, in-the-plane, ice-flow model to determine actual shape and extent of the resultant glaciers. Because the primary geologic evidence of the extent of the glaciers at different times is terminus position, we used terminal elevation as the

criteria for evaluating glacier response (elevation and downvalley distance are essentially linearly related and therefore equally useful as terminus position indicators). To analyze the sensitivity of the closed basin lake chain to climate change, we used a Thornthwaite water balance model [Dingman, 1993] to estimate changes in evapotranspiration and runoff from the basin, a simple steady-state lake water balance model to determine the resultant change in lake surface area and a steady-state isotopic composition model to relate the lake water balance to isotopic records of isotopic composition of the lakes in the basin. We use the total lake surface area within the basin as a primary measure of basin response.

Paleoclimate studies of the Great Basin have generally focused on the geologic record of either the glaciers or the lakes. Because of that dichotomy, we discuss some of the previous estimates of the glacial-pluvial conditions in the Great Basin, as well as the Owens Valley, in the following subsections that deal specifically with the geologic records of each of these systems. The following sections of this dissertation thus discuss, sequentially, (1) the chronology of lacustrine changes in the Owens Valley, (2) sensitivity of the lake system to changes in the climate and estimation of a response curve in terms of lake surface area as a function of changes in the primary climatic variables – temperature and precipitation, (3) the chronology of glacial advances in Bishop Creek and nearby adjacent creeks, and (4) sensitivity of the glaciers to climate change. Finally, we illustrate how the combined response curves help to narrow the range of climatic conditions that must have existed at several different times during the last deglaciation and how those changes relate to other evidence of climate change in the western United States.

---

## CHAPTER 2 - LACUSTRINE CHRONOLOGY DEVELOPMENT

---

The lacustrine chronology that we wish to interpret in terms of changes in temperature and precipitation is that of the Owens Valley in southern California. This section describes that drainage system, the lakes that provide evaporative outflow from it, and the evidence that we have used to construct a chronology of changes in the lakes that accompanied the close of the last glacial period.

The Owens Valley (Figure 1-1) is an approximately 8,550-km<sup>2</sup> basin that occupies the southwestern part of the Great Basin section of the Basin and Range physiographic province [Danskin, 1998]. The basin is delimited to the west by the crest of the Sierra Nevada and to the east by the crest of the Inyo-White Mountains. It is approximately 30 to 70 km wide and 200 km long and elevations range from 1050 m at Owens Lake, now dry due to artificial diversions, to 4300 m at Mount Whitney, the highest point in the Sierra Nevada. The natural discharge point for groundwater and surface water runoff in the Owens Valley is Owens Lake, at the extreme south end of the valley. Until the lower Owens River was diverted from the valley to Los Angeles in 1912, Owens Lake was approximately 250 km<sup>2</sup> in area and about 9 m deep. Evaporation at the lake currently exceeds inflow and the lake is a playa. During the glacial-pluvial period however, Owens Lake often reached its maximum depth of ~68 m and flowed over its sill at the southwestern end of the Coso Mountains. The overflow from Owens Lake entered Indian Wells Valley to form China Lake. When China Lake reached a depth of ~8 m it spilled into Searles Valley to form Searles Lake. Searles Lake coalesced with China Lake upon reaching a depth of ~180 m and at a depth of ~200 m overflowed into Panamint Valley to form Panamint Lake. During periods of extreme wetness, Panamint Lake overflowed to form Lake Manly in Death Valley, the ultimate sink for the Owens Valley drainage, as well as that from the Amargosa and Mojave River paleolake systems.



## PLUVIAL RECORDS IN THE OWENS VALLEY

### *OWENS LAKE*

In the early 1990's the USGS obtained several core samples from the bed of Owens Lake. Data from core OL-92, spanning ~800,000 years, were published in GSA Special Paper 317. Subsequently Benson *et al.* [1996] conducted continuous high-resolution sampling of cores OL84B, OL90-1 and OL90-2, each approximately 30-m long. Physical and chemical data obtained from those cores included total organic and inorganic carbon, magnetic susceptibility, and carbon and oxygen isotope composition. The cores span the period from 12.5 to 55 thousand radiocarbon years before present and each 5- to 6-cm long sample represents from about 10 to 40 years of sediment deposition, depending on the sediment accumulation rate. The  $\delta^{18}\text{O}$  of the carbonate precipitated in the lake (Figure 2-1) is essentially a record of the isotopic composition of the water over time (fractionation during the precipitation process is approximately 30‰ [Benson *et al.*, 1996] and only weakly sensitive to temperature). The  $\delta^{18}\text{O}$  record of the lake provides an indirect measure of the 'relative wetness' of the Lake. It represents a balance between the liquid inputs and outputs to the lake and their composition and evaporative enrichment of the heavier isotopes. During periods of closure, evaporation plays a dominant role in the water balance of the lake and the lake becomes highly enriched in the heavier isotopes. In contrast, when the lake is overflowing the lake tends toward lighter  $\delta^{18}\text{O}$  values.

The Owens Lake record presents a clear history of a long relatively wet period, with  $\delta^{18}\text{O}$  in the range of ~18 to 25‰, followed by a period of closure beginning at ~10,000 radiocarbon years B.P. and continuing to the present. Within the overflow period are numerous semi-cyclic variations in composition with periods of one thousand to several thousand years and a magnitude generally less than 4‰. The variation appears to be smaller during the closed period but as the duration of that record is much shorter, this observation is uncertain. Relatively continuous high-frequency changes

in composition exist throughout the record, with a magnitude of up to 6‰, and the magnitude of these changes appears larger in the earlier, wetter, part of the record. An approximately 1,800-year hiatus in the record begins slightly before 15,500 radiocarbon years B.P. and ends at ~13,700 radiocarbon years B.P. Clearly the lake level receded below the level of the core site during that time and Benson [1996] suggests that the entire lake desiccated during that period. The hiatus is followed by an abrupt and dramatic increase in wetness beginning at ~13,300 radiocarbon years B.P. and essentially continuing until the onset of the Holocene at ~10,000 radiocarbon years B.P.

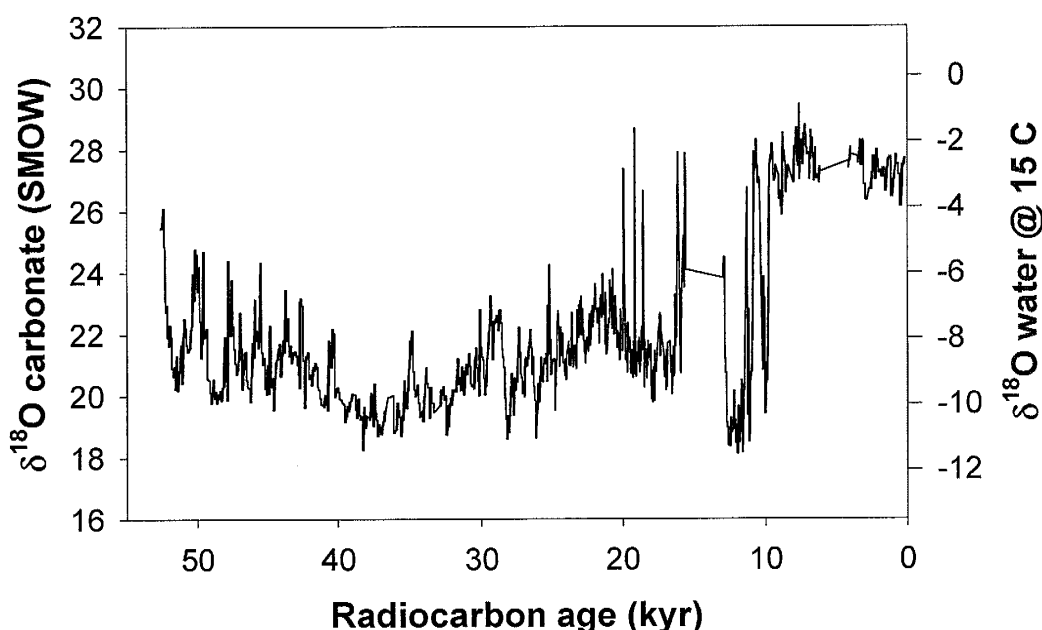


Figure 2-1. Oxygen isotope record of core OL-90 Owens Lake, California for the last 55 ka. Left ordinate axis is composition of carbonate; right-hand ordinate is inferred composition of the water from which the carbonates precipitated, assuming a water temperature of 15°C. Modified from Benson et al. [1996].

#### SEARLES LAKE

Throughout most of the Pleistocene, Searles Lake was the terminal basin for the ancestral Owens River [Smith and Street-Perrott, 1983], and although Searles Lake overflowed several times during the last ~130,000 years, the downstream lake in Panamint Valley never expanded to much more than a fraction of its maximum area [Smith, 1987]. Numerous studies have examined the

layered marls and salt deposits that were deposited during repeated filling and evaporation cycles in Searles Lake, and the stratigraphy of the lakebed deposits is summarized elsewhere [eg Stuiver and Smith, 1979; Smith, 1987]. Lacustrine deposits dating from the last ~25 ka include, from the top down, the Overburden Mud, Upper Salt, and Parting Mud. The latter two units represent a relatively deep lake that subsequently evaporated, while the Overburden Mud appears to have been formed by sediment washing in from the sides of the basin. Radiocarbon ages on the deposits generally indicate that the latest full period in Searles Lake began about 23,000 years B.P. and ceased about 10,000 years ago [Benson *et al.*, 1990]. The Upper Salt unit represents only a small fraction of that time, having been precipitated in as little as 100 years, and the Overburden Mud was deposited after ~9700 years B.P., by a series of shallow, intermittent lakes produced by local runoff [Benson *et al.*, 1990]. Additional information about the chronology of Searles Lake is drawn from tufa samples from the shoreline at the Searles Lake spill-over level (~695 m elevation) and from lacustrine sediments exposed at Poison Canyon, on the western edge the lake, that correlate to the Parting Mud unit. Based primarily on that correlation, Smith [1987] summarized the chronology of lake level fluctuations in Searles Lake as shown in Figure 2-2A. Recently Lin *et al.* [1998] obtained new radiocarbon dates and U-Th isochron dates for the Poison Canyon outcrop and shoreline tufa deposits. Of the dates presented in that paper, we consider the pre-reservoir-corrected radiocarbon ages the most reliable (Lin *et al.*, 1998 - Table 1). These dates, shown with the original Smith [1987] chronology in Figure 2-2A, suggest that the last high stand in Searles Lake (Poison Canyon Unit C) occurred at approximately 12-13 ka radiocarbon. This is roughly consistent with the timing of the last period of very light stable isotope ratios in Owens Lake (Figure 2-2B). Based on the new radiocarbon dates of Lin *et al.*, [1998] and the sedimentology of Poison Canyon Units B and C, we present Figure 2-3 as an appropriately revised version of Smith's [1987] radiocarbon chronology of lake level fluctuations in Searles Lake.

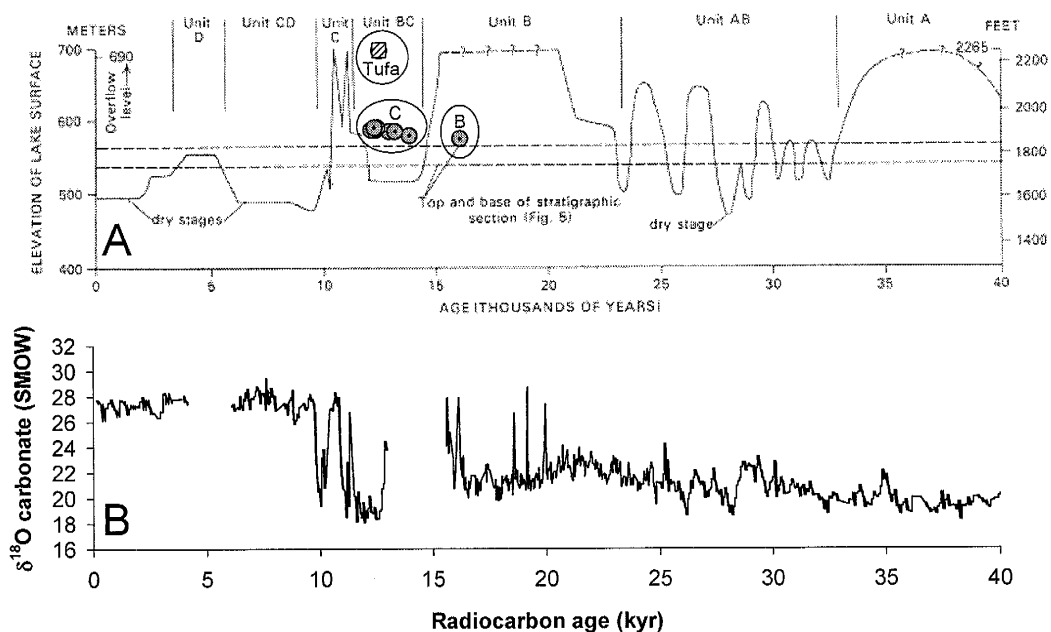


Figure 2-2. (A) The Searles Lake chronology of Smith [1987] shown with the radiocarbon dates of Lin et al. [1998] for Poison Canyon Units B and C (circles) and tufa at the spill level (square). The radiocarbon dates indicate that the last high stand of Searles Lake occurred at ~12 to 13 ka. (B) The Owens Lake stable isotope record of Benson et al. [1996].

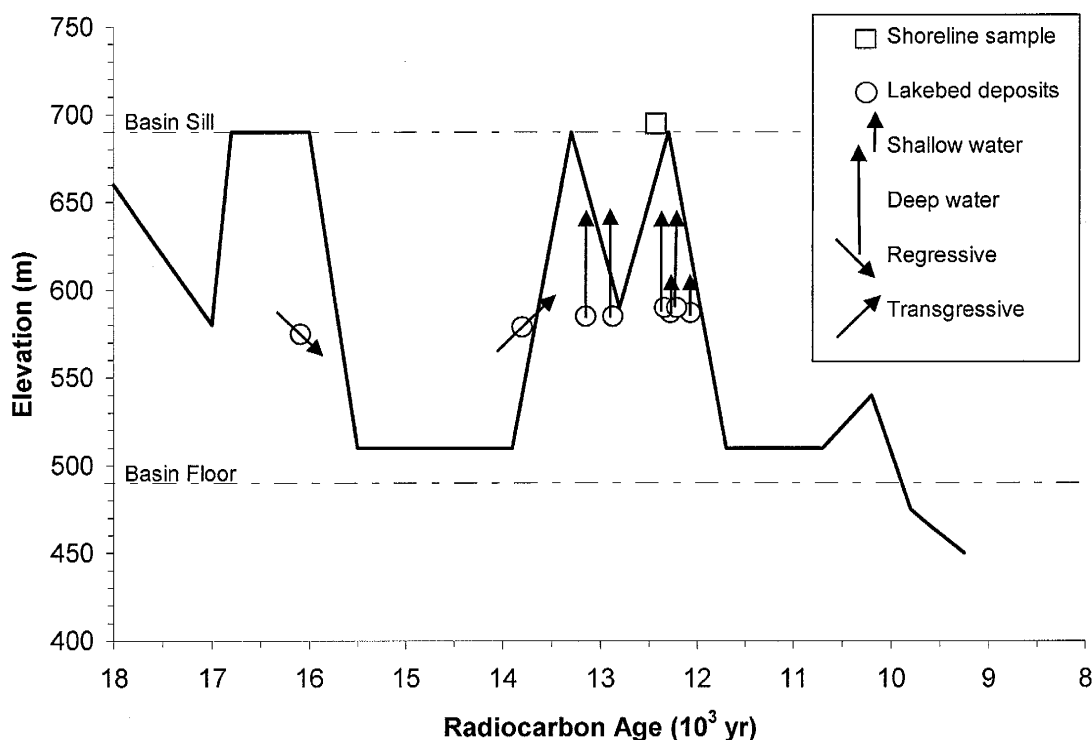


Figure 2-3. Inferred lake level changes in Searles Lake for the late Pleistocene. Squares represent radiocarbon-dated samples of layered lacustrine sediments found in the southern end of Searles Valley [Smith, 1987; Benson *et al.*, 1990]. Corresponding interpretations of lake-level fluctuations based on sediment type and stratigraphy are shown with symbols.

Although of lower resolution than the Owens Lake record, an oxygen isotope record has also been obtained from Searles Lake. Phillips *et al.* [1992] measured isotopic composition of a set of discontinuous samples from the 693-m section of core KM-3 of Searles Lake bed. The core was sampled at one- to two-foot intervals in an attempt to yield a sampling frequency of approximately one sample every one to two thousand years. The period of that record corresponding to the high-resolution Owens Lake record is shown with the Owens Lake data in Figure 2-4. Because sample ages in this portion of the Searles record are only poorly constrained, direct comparison of specific features of the two records is probably not warranted. Comparing their overall features, the most striking difference between them is that the Searles  $\delta^{18}\text{O}$  values are virtually all about 15‰ more enriched than the Owens Lake values. This is a consequence of the sequential enrichment process that occurs in the lake chain as the total lake surface area expands to accommodate ‘wetter’ climate.

Precipitation rates are extremely low and potential evapotranspiration rates very high in the extremely arid region to the south of Owens Lake. As a consequence the downstream lakes receive virtually no runoff from their drainage basins, even under significantly colder or wetter climate [Smith and Street-Perrott, 1983]. Inflow to those lakes therefore occurs only when the closest lake upstream overflows. Inflow to China/Searles Lake is therefore primarily overflow from Owens Lake, which is enriched by evaporation to some degree even when the lake is overflowing. The enrichment process in Searles Lake therefore begins with more enriched water and in turn, when it overflows, provides a more enriched starting point for Panamint Lake.

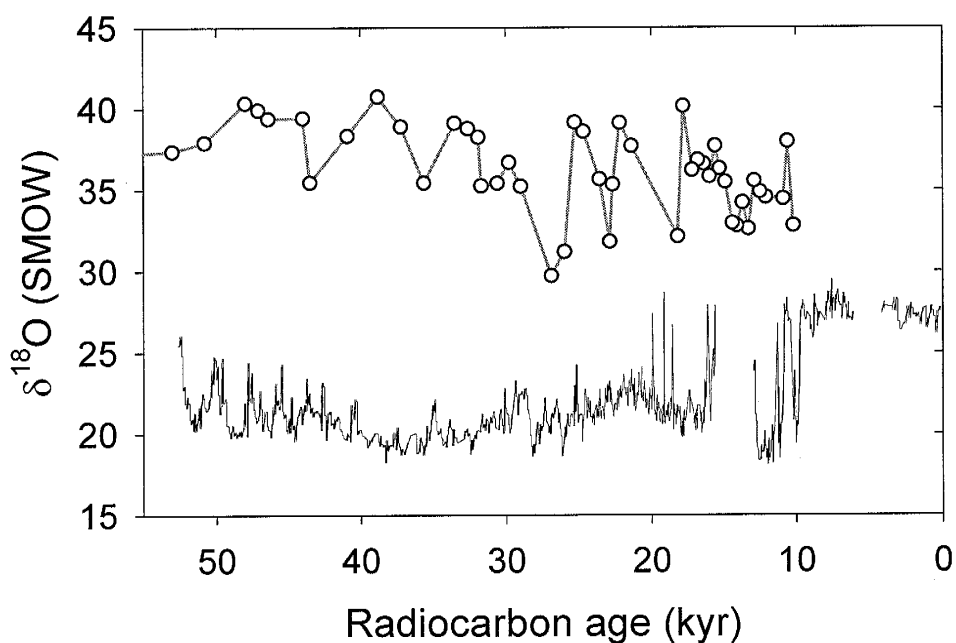


Figure 2-4. Stable isotope composition records of carbonates in Owens Lake (black line) and Searles Lake (circles and gray line).

## INTERPRETATION OF STABLE ISOTOPE RECORDS

The stable isotope records of the lakes can be used to infer lake surface area histories if suitable equations relating the inputs and outputs to the lake and their composition can be solved for inflow and evaporation rate. This requires solution of the coupled, time-dependent, water-balance and isotope-balance equations.

The water balance of a closed basin lake can be described symbolically as

$$\frac{dV}{dt} = (P_L - E_L)A_L(z) + (P_B - E_B)A_B(z) - Q_{out} + (G_I - G_O), \quad \text{Eq. 2-1}$$

where  $V$  = lake volume,

$t$  = time,

$P_L$  = Precipitation rate over lake surface,

$P_B$  = Precipitation rate over drainage basin,

$E_L$  = Evaporation rate from lake surface,

$E_B$  = Evapotranspiration rate from drainage basin,

$A_L$  = Area of lake surface at elevation  $z$ ,

$A_B$  = Area of drainage basin when lake surface is at elevation  $z$ ,

$G_I$  = Groundwater flow into lake,

$G_O$  = Groundwater outflow from lake and

$Q_{out}$  = Outflow over sill.

If the groundwater contribution is minor, equation 2-1 can be simplified to

$$\frac{dV}{dt} = (P_L - E_L)A_L(z) + (P_B - E_B)A_B(z) - Q_{out}. \quad \text{Eq. 2-2}$$

The differential equation describing the isotope balance of a closed-basin lake, neglecting the groundwater contribution, is

$$\frac{d\delta_L}{dt} = Q_{in} \cdot \delta_{in} + (P_L \cdot \delta_P - E_L \cdot \delta_E)A_L(z) - Q_{out} \cdot \delta_L, \quad \text{Eq. 2-3}$$

where  $Q_{in}$  = rate of inflow to the lake from the basin, i.e.  $(P_B - E_B) \cdot A_B$ ,

$\delta_{in}$  = isotopic composition of inflow from basin,

$P_L$  = precipitation rate over lake surface,

$\delta_P$  = isotopic composition of precipitation,

$E_L$  = evaporation rate from lake surface,

$\delta_E$  = isotopic composition of evaporating water,

$A_L$  = area of lake surface,

$Q_{out}$  = rate of outflow over sill and  
 $\delta_L$  = isotopic composition of lake water.

The equations describing the isotopic composition of water removed from the lake via evaporation were described by Craig and Gordon [1965]. Their equation for the composition of lake evaporate, adapted to include a term representing the degree to which air over the lake is modified by evaporation from the lake itself [Hostetler and Benson, 1994; Gat, 1995], is

$$\delta_E = \frac{\alpha\delta_L - hf\delta_{air} - (\varepsilon^* + \Delta\varepsilon)}{(1 - fh) + \Delta\varepsilon}, \quad \text{Eq. 2-4}$$

where  $\delta_E$  = isotopic composition of evaporating water,  
 $\alpha$  = equilibrium isotopic enrichment factor,  
 $\delta_L$  = isotopic composition of lake,  
 $h$  = relative humidity of ambient air,  
 $f$  = fraction of air over water coming from beyond lake surface,  
 $\delta_{air}$  = isotopic composition of water vapor in ambient air,  
 $\varepsilon^*$  = equilibrium isotopic enrichment factor, and  
 $\Delta\varepsilon$  = kinetic isotopic enrichment factor.

Solution of the coupled water balance and isotope balance equations is simplified if the observations of isotopic composition can be assumed to represent steady states or near-steady states of the system. This can be assumed if both the response time for isotopic changes in the system and the sampling interval are both much less than the variations in the forcing function. Otherwise a transient analysis of the data may be necessary.

The response time for changes in isotopic composition depends, in part, on whether the lake is closed or overflowing. When the lake is closed, the response time for volume changes also determines the isotope balance response time and can be determined from the water balance equations. The analytic solution to equation 2-2, assuming no outflow from the lake and written in terms of maximum lake depth,  $z$ , is [Hostetler, 1995]

$$z(t) = z_{ss}(t)(1 - e^{-kt}), \quad \text{Eq. 2-5}$$



where  $k = \frac{\partial A / \partial z}{A} E_{net}$ ,  $E_{net}$  is the net evaporation rate from the lake surface ( $E_L - P_L$ ), and  $\partial A / \partial z$  is the relationship between surface area, depth, and lake volume determined by the geometry of the lake basin. The time constant for this exponential equation is  $1/k$ , or  $\frac{A}{\partial A / \partial z} \frac{1}{E_{net}}$ . The rate of response of the lake to changes in the water balance is thus a function of the surface evaporation rate and the shape of the lake basin. The response time is inversely proportional to the ‘shallowness’ of the lake basin; steeper-walled basins require larger changes in storage to produce a given change in surface area and thus respond more slowly to a change in water balance. Response time is also inversely proportional to the evaporation rate. For a given surface area at steady state, a low evaporation rate implies a low inflow rate. As the filling time for a given change in volume is a function of the magnitude of the imbalance between inflow and evaporation, the time required for the same relative increase in lake surface area is greater when the evaporation rate is low.

For all practical purposes, changes in lake volume occur only when the lake is not overflowing. Evaporation rates in Owens Lake and the downstream lakes during periods in which lake volume was changing would likely have been similar to those today,  $\sim 1.3 - 2 \text{ m yr}^{-1}$  [Phillips *et al.*, 1992]. Lakes in the Owens Valley system are typically very shallow; the historic, pre-irrigation depth in Owens Lake was  $\sim 9 \text{ m}$  and at periods of overflow the lake was approximately  $68 \text{ m}$  deep [Gale, 1914]. Based on the above analysis, these evaporation rates and area-depth data from Phillips *et al.* [1992], the response times for the lakes in the Owens Valley are on the order of 50 years or less, even with a 50% decrease in the net evaporation rate. This is only slightly larger than both the sampling interval and the period represented by each sample of the Owens Lake record of Benson *et al.* [1996].

We estimate the response time for isotopic balance adjustments via a finite-difference lumped parameter model of the coupled water and isotope balance equations (Appendix A). A hypothetical step-function perturbation of the lake inflow rate is input to the model for a single lake and the

response of the lake surface area and isotopic composition observed through time. The model was parameterized using topographic and isotopic data from the Owens Valley. Figure 2-5 illustrates the response of the lake for three scenarios in which inflow to the lake is doubled. The response time for changes in isotopic composition is essentially the same as that for adjustments in the lake water balance, less than 50 years in these scenarios. This is consistent with <100-yr isotope response times observed by Hostetler and Benson [1994] in simulations of Pyramid Lake using a one-dimensional thermal, water and isotope balance model. The changes in  $\delta^{18}\text{O}$  associated with transients in the lake water balance are all of similar magnitude in these examples, approximately 4‰ to 6‰. The response for a lake that remains closed is, however, only a temporary change in the  $\delta^{18}\text{O}$  of the lake, reflecting the temporary change in the ratio of evaporation to inflow. The other perturbations result in asymptotic approaches to new steady states.

The response time for isotope balance in the Owens Lake suggests that a steady-state solution to the coupled water balance and isotope balance equations is reasonable when the period of changes in  $\delta^{18}\text{O}$  is greater than 200 years. As most changes in the Owens Lake record appear to have a period of at least 1000 years, we used a steady-state analysis to estimate changes in inflow rate to Owens Lake from the record.

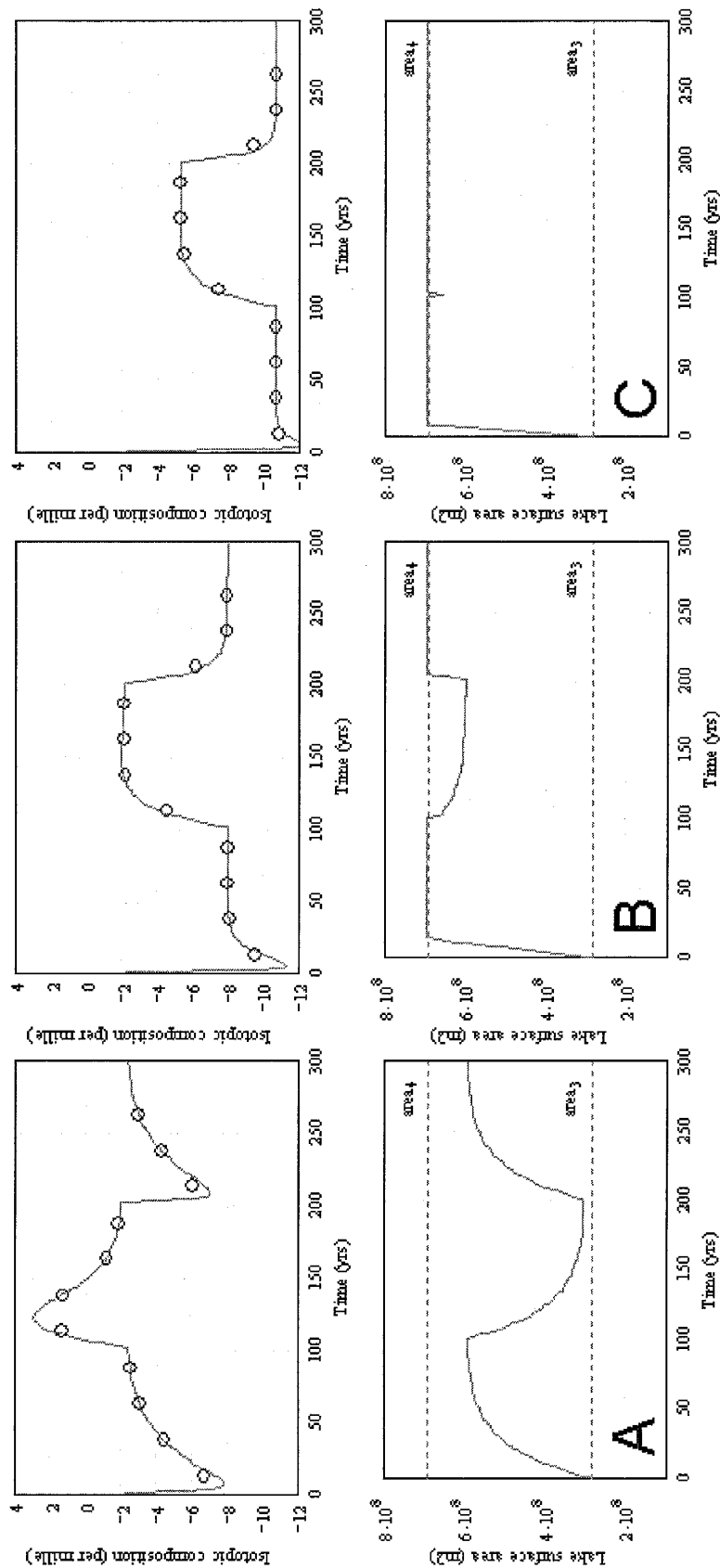


Figure 2-5. Lake isotopic composition over time (top row) and lake surface area over time (bottom row) for three hypothetical scenarios in which the inflow to the lake is doubled, halved, then doubled again via a step function with a 100-yr timestep. In scenario A the lake is closed at all times. In scenario B the lake is closed under the lower inflow rate but overflows when the inflow is doubled. In scenario C the lake is always overflowing. In each scenario the lower flow rate is the higher flow rate of the previous scenario. Upper dashed line in lower row is lake surface area at overflow; lower line is modern, pre-irrigation area. Circles represent calculated composition for hypothetical continuous sampling of the lake where each sample averages approximately 25 years.

## OWENS LAKE

Parameters required for solution of the steady-state isotope balance equations in terms of inflow rate include the average relative humidity, evaporation rate and sensitivity of evaporation to temperature, and the isotopic composition of lake precipitation, basin runoff and vapor in the ambient air. Our estimates of the modern values of the various model input parameters, and the corresponding data sources, are summarized in Table 2-1. We estimated that the isotopic composition of the corresponding vapor would be within  $\sim 2\%$  of regional precipitation. Because of the low relative humidity, however, the model is quite insensitive to the latter parameter.

Parameter	Value	Source
Precipitation $\delta^{18}\text{O}$	$\sim -12\%$	Friedman <i>et al.</i> , 1992
Inflow $\delta^{18}\text{O}$	$\sim -16\%$	Williams and Rodoni, 1997
dE/dT	10 cm ( $^{\circ}\text{C} \cdot \text{yr}^{-1}$ )	Smith and Street Perrott, 1984
Relative Humidity	20% – 30%	Duell [1990] and Nat'l Weather Service
Ambient vapor $\delta^{18}\text{O}$	$\sim -18\%$ to $-14\%$	

Table 2-1. Estimates of modern values for various parameters needed to calculate the water balance and isotope balance of Owens Lake. The references list sources for the estimated values.

The steady-state equations can be used to produce a curve of isotope composition as a function of inflow rate. Figure 2-6 illustrates the isotopic composition of Owens Lake as a function of the annual inflow rate to the lake, normalized to the estimated historical, pre-irrigation runoff rate. The relationship assumes a constant evaporation rate ( $\sim 1.3 \text{ m yr}^{-1}$ ) and inflow composition and a precipitation rate that is weakly proportional to changes in the inflow rate, reflecting an assumed amplification in the runoff response to precipitation [Wigley and Jones, 1985]. We also assume that the model parameters described in Table 2-1 remain constant, though changes in those parameters would attend large changes in the regional precipitation. For inflow rates for which the lake is closed, the steady state isotopic composition is essentially identical (close to  $-2\%$ ) because the balance between evaporative enrichment and replacement is roughly the same in each case (the slight differences in steady-state composition for the closed lake are the result of differences in the ratio of

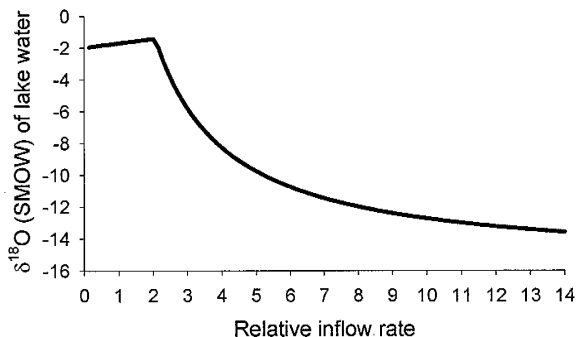


Figure 2-6. Calculated steady-state composition of Owens Lake as a function of relative average annual inflow (normalized to modern inflow).

overflowing, the composition is close to that of the closed-basin condition but highly sensitive to the inflow rate, as the relative importance of evaporative enrichment decreases with increasing flow rate. At extremely high inflow rates, the lake becomes essentially a wide spot in the river, its composition begins to approach that of the Owens River, about -16‰, and the relative sensitivity to inflow rate is greatly reduced.

Figure 2-6 demonstrates that the steady state model is relatively insensitive to changes in inflow when the lake is closed. This supports the idea that the high-frequency variations in the Holocene portion of the Owens Lake isotope record are the result of transient events in the lake's water balance. We therefore apply the steady-state model to infer past inflow rates only for the period before 10,000 radiocarbon years B.P., when the lake appeared to be nearly always overflowing.

Conversion of the steady-state isotopic composition of lake-precipitated carbonate to inflow rate requires some assumption about water temperature, evaporation rate and the relationship between precipitation and lake inflow for the period of interest. Here we assume evaporation is proportional to saturated vapor pressure of the ambient air and consider two different paleotemperature assumptions for interpretation of the pre-Holocene  $\delta^{18}\text{O}$  record. Assuming that temperatures during

the inflow to the net precipitation on the lake surface). When the lake is overflowing however, the steady-state isotopic composition is a non-linear function of the inflow rate. The curve is steepest when the overflow rate is close to zero and decreases asymptotically to approach the inflow composition. When the lake is barely

the glacial-pluvial period were probably on the order of 4 to 8 degrees colder, we considered two scenarios of uniform temperature decrease that bracket that range. Changes in isotopic composition are likely to have accompanied temperature changes in the basin. Winograd [1992] obtained an excellent record of changes in  $\delta^{18}\text{O}$  from calcite precipitated in a conduit supplying a spring in the Amargosa Desert, Nevada. That record, which covers the period from  $\sim 550$  to 50 ka, suggests that  $\delta^{18}\text{O}$  values were frequently about 2‰ lighter during glacial periods than during interstadials. We therefore assumed a maximal decrease of  $-2\text{‰}$  for the  $-8^{\circ}\text{C}$  scenario and half that change for the  $-4^{\circ}\text{C}$  scenario. In this preliminary analysis of the isotopic response of the lakes to climate change, we make no attempt to effect these changes to the system in a realistic way. Rather, we consider them more in terms of the overall sensitivity of the system, applying the changes uniformly across the entire  $\delta^{18}\text{O}$  record to examine the implications for the relative inflow inferred from it.

Using the steady-state isotope balance and the contemporaneous changes mentioned above, we inferred a relative inflow history for the lake from the isotope record of Benson *et al.* [1996] (Figure 2-7). Together with the hiatus in latter record, suggesting a desiccation event, the inferred inflow history suggests that rather large variations in the inflow rate have occurred over the last  $\sim 50,000$  years, ranging from less than the historic, pre-irrigation, rate (during desiccation) to 3 to 4 times that rate at about 12,000 radiocarbon years B.P. The relative inflow rate depends significantly on the assumed temperature of the calculations, as lower temperatures imply decreased evaporation in the model.

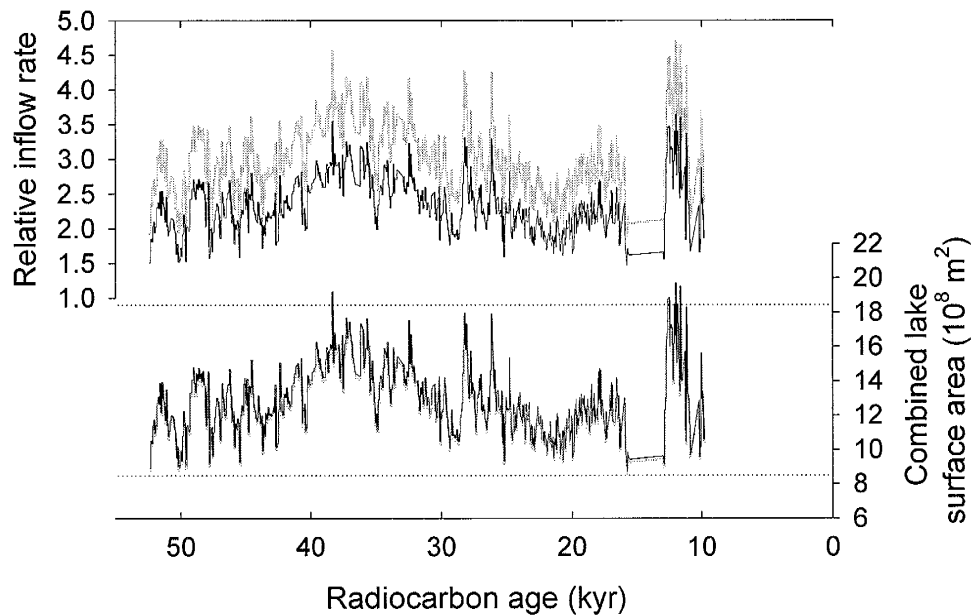


Figure 2-7. Inferred relative inflow history for Owens Lake (upper graph) and combined lake surface area history (lower graph) for the Owens Valley lake system based on the Owens Lake  $\delta^{18}\text{O}$  record of Benson et al. [1996]. Black lines assume an  $8^\circ\text{C}$  decrease in temperature and a  $2\text{‰}$  decrease in  $\delta^{18}\text{O}$  for precipitation and runoff. Gray lines assume a  $4^\circ\text{C}$  decrease in temperature and a  $1\text{‰}$  decrease in  $\delta^{18}\text{O}$  for precipitation and runoff. Dotted lines in lower graph show cumulative lake surface area when China Lake (lower line) and Searles Lake (upper line) are at their sill levels.

#### SEARLES LAKE

When inflow to and precipitation on Owens Lake exceeds the evaporative capacity of that basin, Owens Lake overflows and supplies flow to a series of downstream lakes. Each lake in the downstream chain thus receives more isotopically enriched inflow than its upstream lake, and isotopic composition is increasingly enriched with distance downstream. We can estimate the composition of a hypothetical calcium carbonate precipitate in each lake by assuming the whole system is effectively at steady state and including outflow from each lake in the inflow to the next lake downstream. The composition of the carbonate in the lakes is typically about  $30\text{‰}$  greater than that of the water, due to fractionation during the precipitation process. Figure 2-8 illustrates how the sequential enrichment process might affect the composition of carbonates in the lakes in the Owens Valley system as a function of runoff to Owens Lake. At lower inflow rates to Owens Lake, all of the

lakes are closed and each receives only local runoff. As runoff composition is assumed to be similar throughout the area, so is the closed-basin  $\delta^{18}\text{O}$  value for each system. When a lake receives only a small amount of overflow from an upstream lake, its composition reflects a mixture of that water and that of local precipitation on the small lake surface. The influence of the isotopic composition of rain on the lake is felt only at low inflow rates, however. At higher rates, when the lake is still closed, its  $\delta^{18}\text{O}$  reflects only evaporative enrichment of outflow from its upstream lake, which is lighter as flow rates increase in the system. The abrupt end to the China Lake curve indicates the level at which it coalesces with Searles Lake.

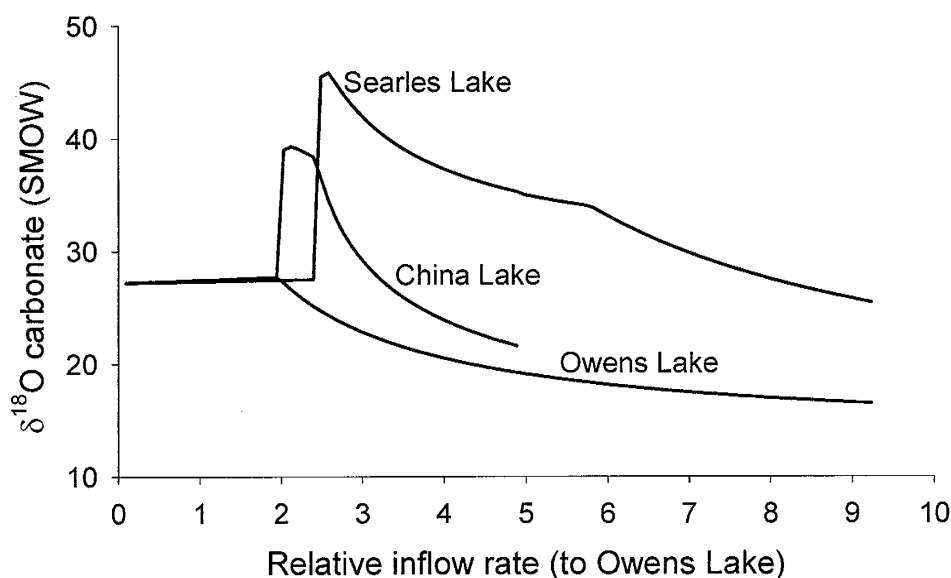


Figure 2-8. Calculated steady-state isotopic composition of carbonate in lakes downstream from Owens Lake as a function of relative inflow rate to Owens Lake (inflow rate normalized to modern inflow rate). Evaporation rate and isotopic composition of precipitation and local inflow to each lake are assumed to be the same as at present. Runoff from basins below Owens Lake is assumed negligible.

We can use the relationship between inflow at Owens Lake and composition of the downstream lakes to estimate the  $\delta^{18}\text{O}$  values of carbonates that would be precipitating in Searles Lake based on the inflow history we infer from the Owens Lake record. The Searles Lake  $\delta^{18}\text{O}$  data is from analysis



of dolomite and other precipitates (principally gaylussite) in core KM-3 and has been normalized to dolomite composition using a relative relationship established by analysis of both minerals. Dolomite is assumed to preserve the original  $\delta^{18}\text{O}$  signal of the lake, with  $\delta^{18}\text{O}$  levels enriched according to the mineral-water fractionation factor for precipitation of dolomite [Phillips *et al.*, 1992, 1994]. Applying that assumption to the steady state lake model however results in an inferred Searles Lake composition that is considerably heavier than the measured values. It may be that the dolomite preserved, unaltered, the signal of the calcium carbonate from which it is presumably derived. The inferred composition record based on that assumption is a relatively good fit to measured values from core KM-3 (Figure 2-9), although as mentioned previously, sample ages in the Searles Lake isotope record are only poorly constrained. The largest discrepancies between the two curves are a series of very light values (30 – 35‰) in the KM-3 record between ~28 and 18 ka. These anomalously light values do not correspond to an apparent increase in wetness in Owens Lake.

#### LAKE LEVEL CHRONOLOGY OVERVIEW

Figure 2-10 summarizes the available lake chronology data on a calendar age timescale using the radiocarbon correction data of Stuiver *et al.* [1998]. The most direct evidence of the lake surface area chronology is from radiocarbon dates on marls and tufa deposits from Poison Canyon [Lin *et al.*, 1998], while the best-dated record is the isotope record from Owens Lake [Benson *et al.*, 1996]. Our interpretation of the timing of the last major pluvial event, that appears to exist in each record, is based on the chronology of Benson *et al.* [1996] for Owens Lake.

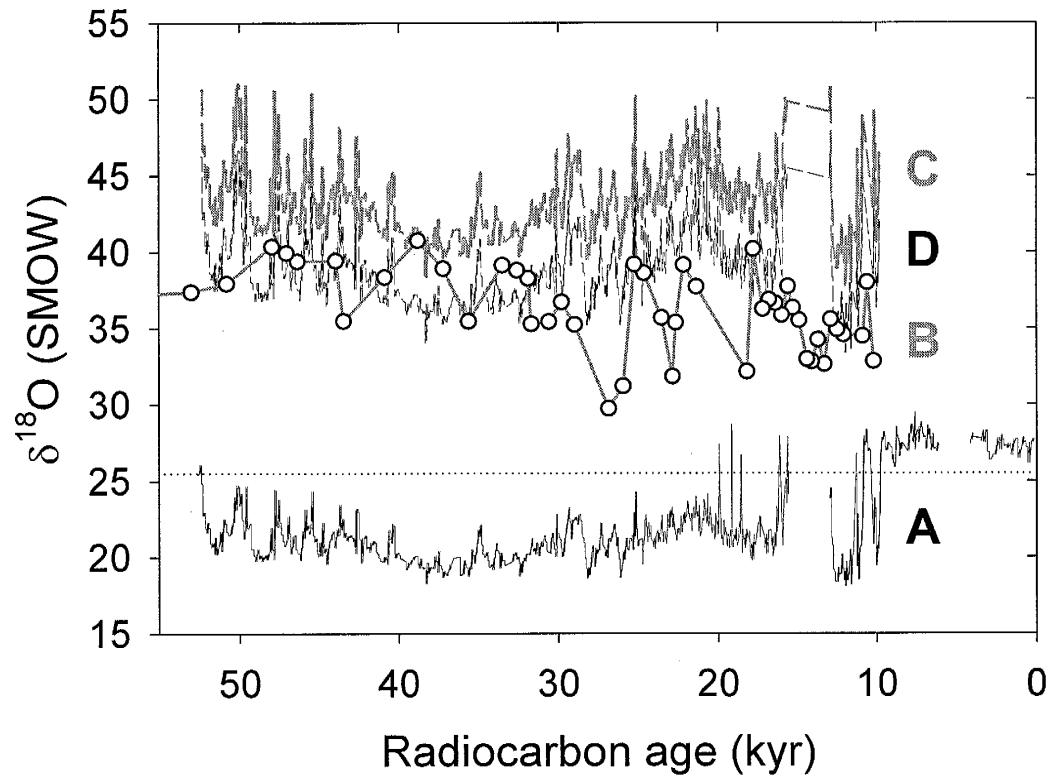


Figure 2-9. (A) Oxygen isotope composition of carbonate from Owens Lake core OL90 [Benson et al. 1996]; Dotted line indicates the assumed dividing line for a closed versus overflowing Owens Lake; (B) oxygen isotope record for dolomite from Searles Lake core KM-3 [Phillips et al., 1992]; (C) calculated composition for dolomite in Searles Lake based on the inferred inflow history for Owens Lake (Figure 2-7) and (D) same as C but with the assumption that the diagenetic processes that produced dolomite did not alter the original calcium carbonate isotope signal.

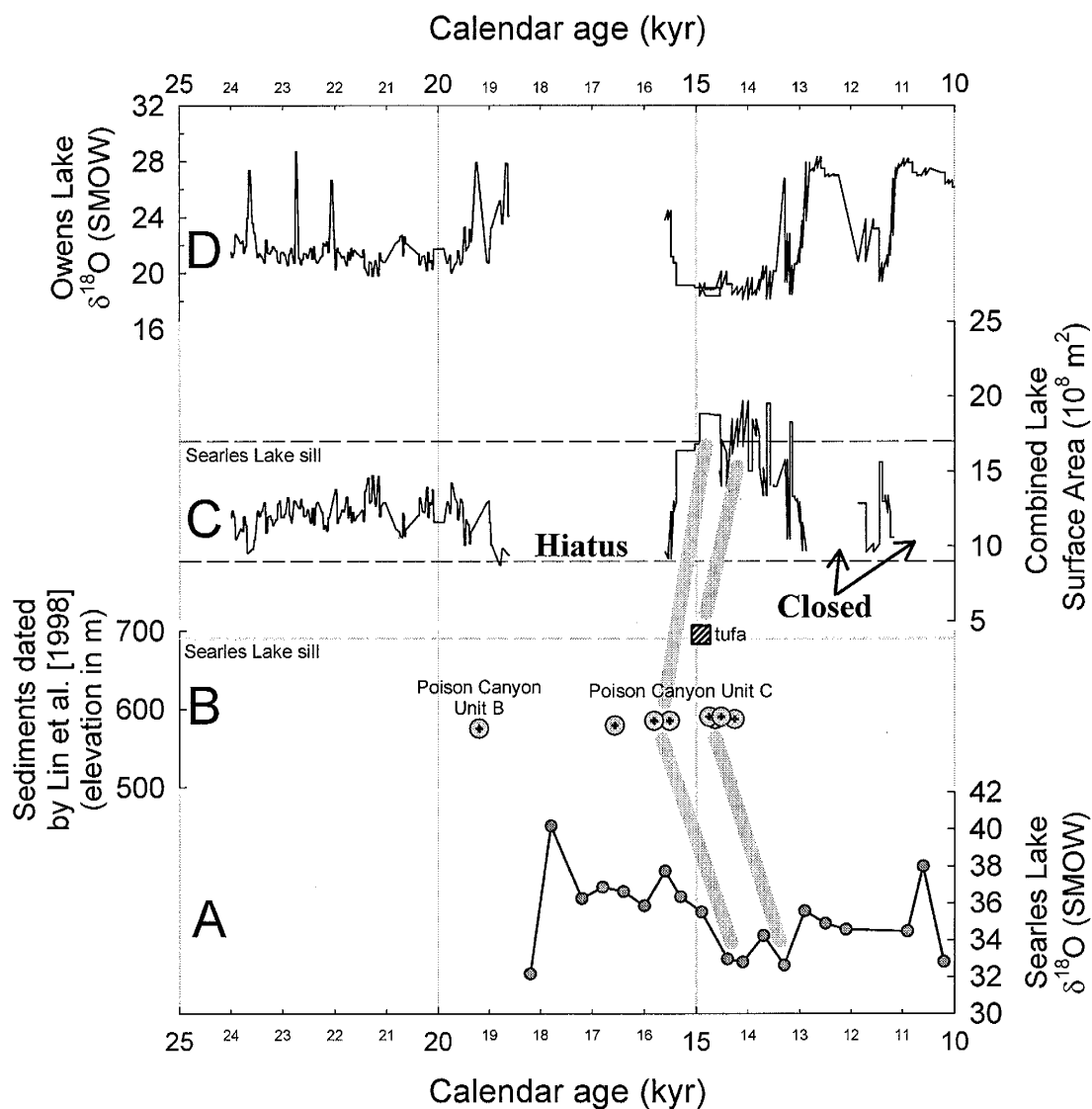


Figure 2-10. Comparison of lake level indicators in the lake system of the ancestral Owens River: (A) oxygen isotope records from Searles Lake, (B) elevations of marls and tufa deposits dated by Lin et al. [1998], (C) estimated combined lake surface area history inferred from (D) the Owens Lake isotope record. The hiatus in the Owens Lake record and periods of closure are also shown in C. Thick gray lines indicate our interpretation of the last wet episode in each record.

From these data and our reinterpretation of Smiths' [1987] radiocarbon chronology (Figure 2-3) we summarize the calendar-age fluctuations of the surface elevation of Searles Lake, which effectively mirrors the degree of overflow from Owens Lake, as follows. Alternating wet-dry conditions existed in Searles Lake throughout much of the late Quaternary, from at least 40,000 until about 16,000 years B.P. Marls from Poison Canyon unit B deposits indicate that Searles Lake was large but not near its sill at 19 ka, and Stuiver and Smith [1979] concluded that Searles was also periodically overflowing during and prior to the last glacial maximum. The hiatus in the Owens Lake record and age difference between units B and C at Poison Canyon indicates that a very dry period occurred sometime between the last glacial maximum, at ~18 ka, and the last major pluvial period in Searles Lake that began just after 16 ka and ended at ~13 ka. This last episode appears to have occurred in two pulses. In the second pulse, as evidenced by tufa preserved at the spill level, Searles Lake overflowed into Panamint Lake, though not enough to form a very extensive lake in that basin. At ~13 ka, following the last overflow period in Searles Lake, the water level in Searles Lake declined rapidly but the basin continued to contain a significant lake until ~10 ka. The presence of the Overburden Mud indicates that during at least the early Holocene, conditions were still significantly wetter than at present.

---

## CHAPTER 3 - CLOSED BASIN LAKE SENSITIVITY TO CLIMATE CHANGE

---

Having established a lake-surface area history in the Owens Valley, we now wish to relate that history to the climatic changes that may have attended it. We accomplish this using a model that describes how the various elements of the closed-basin water balance interact with climate. These interactions include changes in vegetation, runoff from the catchment area, soil and groundwater storage, and lake-atmosphere exchanges. In some areas, tectonic and other local, non-climatic factors may also effect changes in lake volume or surface area. For simplicity many previous studies in the Great Basin have focused primarily on the lake-atmosphere exchange, specifically the sensitivity of evaporation to temperature [Antevs, 1952; Galloway, 1970; Benson, 1986; Hosteteler and Benson, 1990; Hosteteler, 1992]. Others have incorporated climatic effects on runoff through non-physical models of the relationship between basin, climate and runoff [Mifflin and Wheat, 1979]. Physically-based approaches to estimating basin runoff response, such as those applied to African paleolakes Chad [Kutzbach, 1980] and Tanganyika [Bergonzini [1997], have generally been neglected in the Great Basin.

Because there are many potentially important interactions between climate and basin water balance parameters, it is not a simple task to sort out which are the first-order effects. In choosing a model, we first review those studies that bear on the relative importance of the various interactions. Due to its dominance in the literature, we consider first the sensitivity of lake evaporation to temperature.

### SENSITIVITY OF LAKE EVAPORATION TO TEMPERATURE

At steady state, net annual evaporation from the lake surface in a closed-basin equals the combined inflow from surface-water and groundwater discharge, and precipitation on the lake. Changes in the evaporation rate directly alter the water balance and require an adjustment in lake size

to restore steady state. Evaporation rate is a function of temperature, humidity, windspeed, cloudiness and possibly other climatic variables. Several authors have attempted to estimate the temperature change necessary to produce the large lakes of the pluvial period based primarily on the associated reductions in lake evaporation. The estimates vary widely, ranging “from as little as 4.5° F (Antevs, 1952) to as much as 20° F (Galloway, 1970)” [Mifflin and Wheat, 1979]. Using a lumped-parameter energy balance analysis of closed basin lakes, Benson [1986] concluded that this effect had been vastly overestimated:

*“In former studies (for example, Galloway, 1970), great emphasis has been placed on decrease of evaporation rate due to air-temperature reduction. However, the sensitivity analysis showed that evaporation rate does not change when both  $T_{air}$  and  $T_{lake}$  are reduced by equal amounts.”*

Different methods can be used to estimate the sensitivity of evaporation to changes in air

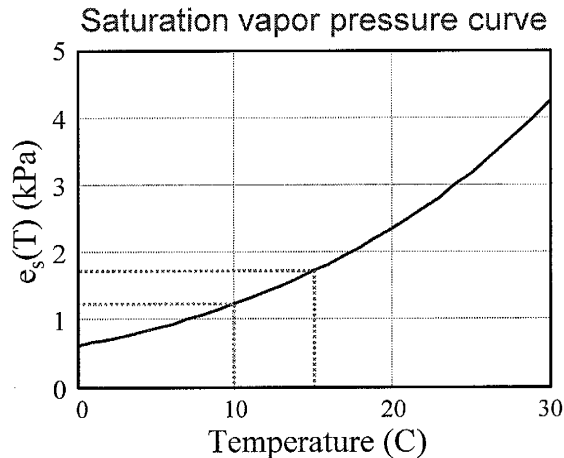


Figure 3-1. Saturation vapor pressure curve for water. Reduction in the evaporation rate due to decreased temperature can be estimated from the coincident decrease in the saturation vapor pressure. Upper dotted line indicates vapor pressure at the mean annual air temperature at Owens Lake. Lower dotted line indicates the reduction in vapor pressure corresponding to a 5°C decrease in temperature.

temperature. Consider the driving force for net evaporation - the vapor density gradient between the surface of the lake and the ambient air. The vapor density of the air at the lake surface can be assumed to be at the saturation vapor pressure for its surface temperature. The vapor density of the surrounding air can be calculated from its temperature and relative humidity (RH). If the air and water are at the same temperature, the difference in vapor pressure between the air and water at any

temperature is simply  $(1 - RH)$  multiplied by the saturation vapor pressure. For constant RH, the

vapor pressure difference is given by the slope of the saturation vapor pressure curve (Figure 3-1) times the change in temperature. The saturation vapor pressure at the average annual temperature at Owens Lake (approximately 15°C) is about 1.7 kPa and the slope of the saturation vapor pressure curve near that temperature is slightly less than 0.1 kPa K<sup>-1</sup>. Because of the shape of the saturation pressure curve (Figure 3-1), the reduction in the vapor pressure gradient (and, consequently, evaporation) is about 5.6 percent per degree C. Under these conditions, unless the vapor pressure gradient is negligible, equal changes in both air and water temperature always produce a change in evaporation rate. This suggests that Benson's [1986] conclusion that evaporation rate is unaffected when reductions in air and lake-surface temperature are equal is incorrect.

The above analysis assumes identical lake-surface and air temperatures, but there is usually a contrast between lake-surface temperature and air temperature, especially on a seasonal basis. However, if we assume that this contrast remains essentially constant then the change in evaporation rate due to a temperature change of the system is essentially the same as before (Figure 3-2). Only in cases where the combination of temperature contrast and temperature change tends to produce identical vapor densities in the ambient air and at the water surface does the lake-air temperature contrast increase the sensitivity of evaporation to temperature. In general, regardless of the temperature contrast between the two bodies, the change in evaporation as a function of temperature change is relatively constant, producing about a 28% decrease in evaporation for a 5°C decrease in temperature.

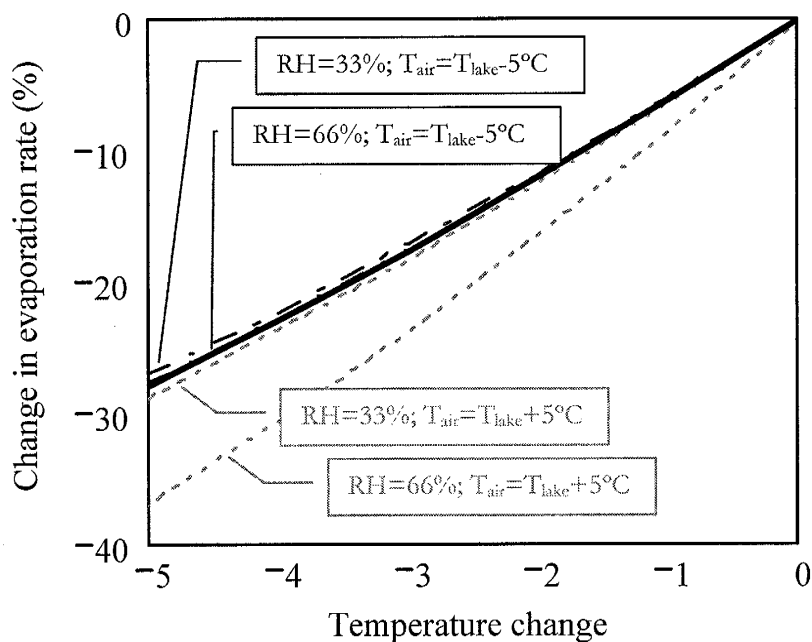


Figure 3-2. Relative change in evaporation rate as a function of temperature changes from a water surface initially at 15°C. Heavy black solid line reflects no temperature contrast between air and water temperatures. Dotted lines represent conditions where air temperature is 5°C warmer than water temperature and RH is 33% (upper dotted line) or 66% (lower dotted line). Dadot lines represent conditions where air temperature is 5°C cooler than water temperature and RH is 33% (upper dadot line) or 66% (lower dadot line, masked by black line). When the air is cooler than the water and RH is relatively high (lower dotted line), changes in temperature can make the vapor densities of the two bodies approach the same value. Under those conditions, very small temperature changes can lead to large reductions in evaporation rate as the evaporation rate approaches zero.

Another means of estimating the change in evaporation rate that might result from a change in temperature is from analysis of modern evaporation rates in closed-basin lakes at different temperatures. Mifflin and Wheat (1979) compared evaporation rates collected from studies of lakes throughout the Great Basin. These data “suggest no more than about 7.2 inches of variation in annual evaporation within a range of 6° latitude.” They attribute most of the variation to temperature variation associated with changes in altitude. Their data suggest that evaporation from a body of water at the elevation of Owens Lake (~1200 m) would decrease at a rate of approximately 13.7 % per 1,000 feet increase in altitude. Assuming a lapse rate of about 3.5° F per thousand feet, that is about a 4% change per degree F, or about 6%/°C - nearly identical to that calculated from simple physical principles. Benson [1986] also observed a relationship between temperature and evaporation



rate among lakes in the Great Basin but concluded that the relation was not a valid means of estimating sensitivity to temperature change because it did not include analysis of the total energy balance of those systems. Those data display a trend of about  $0.09 \text{ m yr}^{-1}$  change in evaporation rate per degree C. For Owens Lake, where the historical evaporation rate is approximately  $1.27 \text{ m yr}^{-1}$  [Smith and Street-Perrot, 1983] that is  $\sim 7\%$  per  $^{\circ}\text{C}$ , again quite similar to the estimate from both the simple physical approach and the regression analysis of Mifflin and Wheat [1979].

This simplistic analysis does not include the potential effects of changes in the cyclical variation of water and air temperature, nor possible changes in cloud cover, relative humidity, lake depth, ice cover and a number of other parameters. It is unlikely however that such effects would have led to substantially larger changes in evaporation rate. The available lake records indicate that the lakes in the Owens Basin, and in many other areas of the Great Basin expanded to at least 3 to 5 times their present surface areas during the pluvial period. Given that even a  $10^{\circ}\text{C}$  decrease in temperature would yield only about a doubling of lake surface area by depressing evaporation, it is likely that the larger part of the relative increase in wetness of the pluvial period was due to factors other than evaporation suppression associated with reduced temperatures.

Hostetler and Benson [1990] used a combined thermal and water balance model to examine the response of pluvial Lake Lahontan under the  $\sim 7^{\circ}\text{C}$  cooler climate suggested by Dohrenwend [1984]. In combination with the assumed temperature depression and a 43% increase in cloudiness inferred from global circulation models of the full glacial climate, they found that the mean annual surface temperature of the lake would be  $\sim 7^{\circ}\text{C}$  colder and lake evaporation in the basin would be reduced by approximately 43%. To produce the Lahontan highstand under such conditions would require a 380% increase in mean annual discharge to the lake. If seasonal ice-cover were to exist on the lake and further suppress evaporation, highstand conditions would still require a 260% increase in runoff [Hostetler, 1991]. These runoff increases are significantly larger than the calculated increases in lake

surface area that would result from evaporation suppression, and the needed runoff increases would be even larger if the temperature depression during the LGM was less than 7°C. Hostetler and Benson [1990] thus demonstrated that changes in basin runoff are likely the dominant mechanism for changes in lake surface area in the Great Basin, unless temperature reductions were much greater even than 7°C.

#### **BASIN RUNOFF SENSITIVITY TO CLIMATE CHANGE**

Mifflin and Wheat [1979], in a comprehensive study of the pluvial lakes and climate of Nevada, recognized the importance of runoff in contributing to the greater lake-surface area of the period, concluding “pluvial climatic conditions were clearly conducive to more runoff reaching the lower parts of many of the closed basins in Nevada.” They estimated pluvial period runoff using a summary of the relationship between basin-wide mean annual precipitation, temperature (time-weighted by amount of precipitation), and runoff. This relationship was originally described by Langbein [1965], based on measurements in ~25, arid to humid, basins in the United States (Figure 3-3). Extrapolating somewhat beyond the original data, they noted that in the modern Great Basin, where 15 inches of precipitation at 50°F (10°C) yields only 1 inch of runoff, a temperature decrease of 10°F (to 40°F) would lead to about 2.5 inches of runoff. That implies that a 6°C decrease in temperature could more than double runoff. The curves suggest that runoff is even more sensitive to precipitation; the same 250% increase in runoff (1” to 2.5”) would occur if basin-wide mean annual temperature remained constant (40°F) and the basin-wide mean annual precipitation increased from 15 inches to 20 inches.

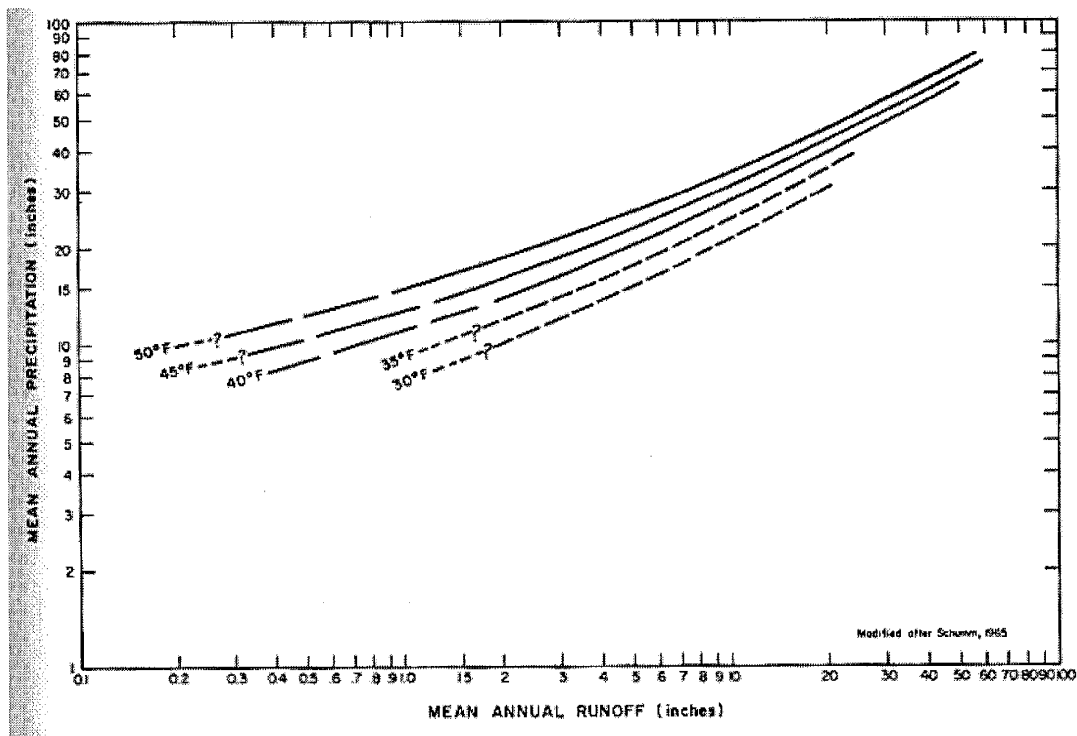


Figure 3-3. Regressions of basin-wide mean annual precipitation, basin-wide mean annual runoff and basin-wide mean annual temperature (time-weighted by amount of precipitation) from runoff measurements throughout the United States. Dotted lines and question marks indicate where the data were extrapolated beyond the measurements. {From Mifflin & Wheat, 1979 [modified after Langbein, 1949]}

The Langbein curves suggest that modest decreases in temperature and/or increases in precipitation can cause dramatic changes in runoff. This provides a possible explanation for the fact that the pluvial lakes were much larger than can readily be explained by suppression of lake evaporation. Although it is likely that changes in runoff played a dominant role in creating the much larger lakes of the pluvial period, the studies of Langbein [1949, 1962] and Mifflin and Wheat [1979] do not provide a compelling physical explanation for the assumed sensitivity to temperature and precipitation. In addition, while the curves may represent valid relationships between runoff, temperature and precipitation among modern basins, it is not clear that they represent a valid means of determining the likely response of runoff to climate change. The factors that create the observed relationship between temperature, precipitation and runoff under the existing climate may not have

any bearing on that relationship for an earlier climate, or even for a single basin under the existing climate.

A number of investigators have attempted to assess the potential impact of climate change on streamflow in the Great Basin. While these studies generally focused on the potential impact of climatic warming, their results can give us some insight into the processes that control runoff in arid basins, the likely direction of change resulting from changes in temperature and precipitation and possibly the relative magnitude of those changes.

Flaschka *et al.* [1987] applied a water-balance model similar to that described by Thornthwaite and Mather [1955] to four watersheds in Nevada and Utah to assess the effects of hypothetical climate change on streamflow in the Great Basin. They calibrated the precipitation and temperature sensitivity of their models using historical records of precipitation, temperature and streamflow, and then used the model to predict the effects of moderate changes in temperature and precipitation. Their results suggest that annual streamflow on the West Fork Carson River would increase by 40% if temperature declined by 2°C and precipitation increased by 25% (Figure 3-4). These results are similar to the analysis of Mifflin and Wheat in that they suggest that streamflow is very sensitive to both temperature and precipitation. The magnitude of the response predicted is, however, dramatically less than that described by Mifflin and Wheat, whose model suggests that a 33% increase in precipitation could result in a 250% increase in runoff in much of the Great Basin.

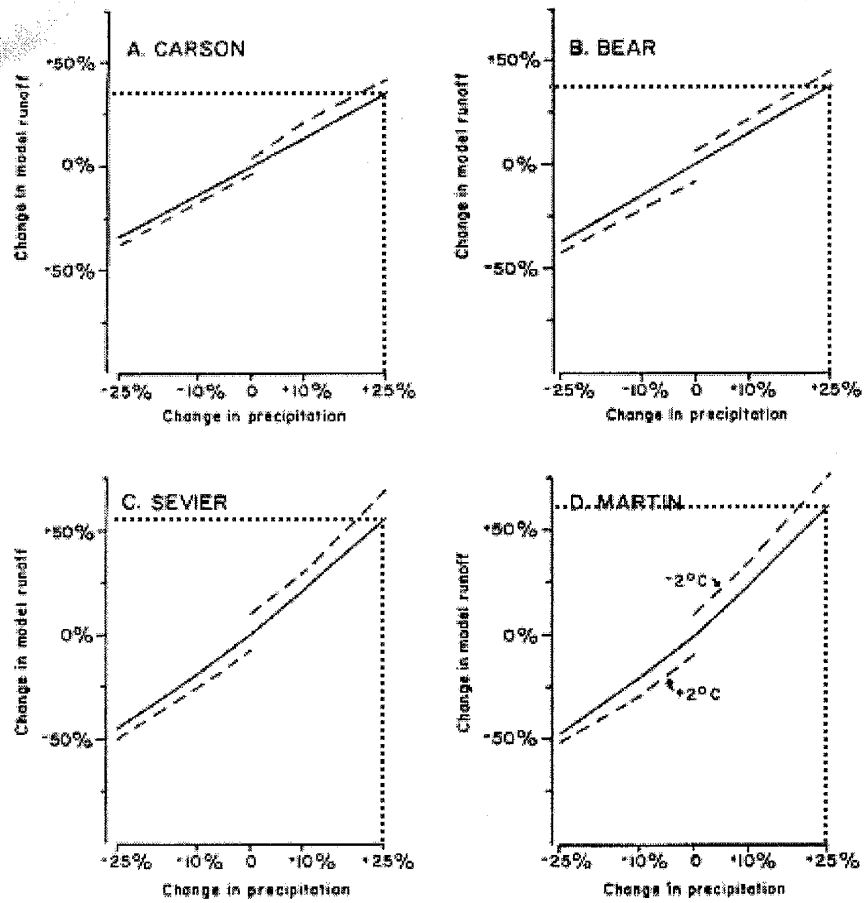


Figure 3-4. Runoff response curves for the four areas studied by Flaschka et al. [1987]. Modeled runoff is plotted as a function of changes in temperature and precipitation. Solid lines show result of scenarios in which only precipitation was changed. Dashed lines include temperature, where a +2.0°C change was used in conjunction with a decrease in precipitation, and a -2.0°C change was used with increases in precipitation.

Jeton and Smith [1996] used a process-oriented precipitation-runoff hydrological model, PRMS [Jeton and Smith, 1993], to estimate streamflow sensitivity to climate for the North Fork American River, a tributary of the Sacramento River. Seasonal distribution of precipitation there is similar to that in the Bishop Creek region. Their results (Figure 3-5) indicate that basin streamflow displays a

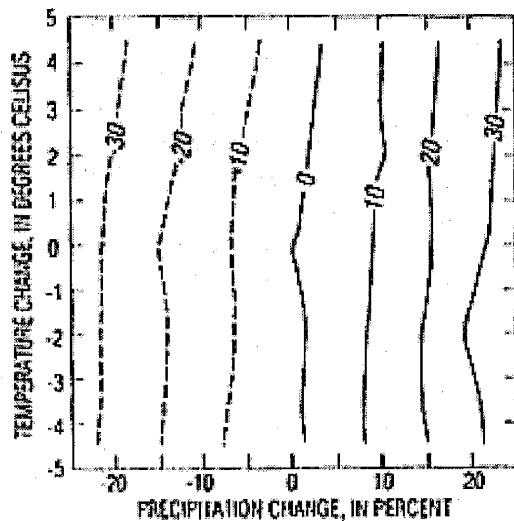


Figure 3-5. Simulated stream flow responses to uniform change scenarios in the N. Fork American River Basin (sub-basin of the Sacramento River), showing percent streamflow change as a function of changes in mean temperature and mean precipitation. Simulations are for climate runs with the PRMS model. [Jeton et al., 1996].

strong dependence on precipitation but virtually no dependence on temperature. They attribute the relative insensitivity to temperature to a buffering effect of the snowmelt process. Temperature affects streamflow primarily via changes in sublimation and evapotranspiration (SET). Under warmer conditions, potential SET is greater, but snowmelt-induced runoff occurs earlier in the year, when the energetic potential for ET is lower. Conversely, under cooler conditions, potential SET is lower but the spring snowmelt occurs when the energetic potential for ET is higher - closer to the annual maximum in

solar radiation, and the near-annual-maximum temperature, reached in June.

The magnitude of the PRMS-modeled streamflow response to precipitation was similar to that of Flaschka *et al.* [1987], with streamflow increasing only slightly more than precipitation. With no temperature change, a 20% increase in precipitation produced about a 30% increase in streamflow. In a review of this and other modeling studies of streamflow response in the Sacramento Basin, Risbey and Entekhabi [1996] concluded that the basin hydrological models generally indicate that while streamflow timing is sensitive to temperature, streamflow amount is sensitive only to precipitation.

Several studies have used annual regression models and historical data to estimate the sensitivity of streamflow to climate change. Duell [1994] developed models of streamflow response in the American, Carson and Truckee River basins, California and Nevada by regressing 1961-1991 streamflow data on temperature and precipitation. Those models demonstrate sensitivity of runoff to both temperature and precipitation, with the latter variable explaining at least 80% of streamflow

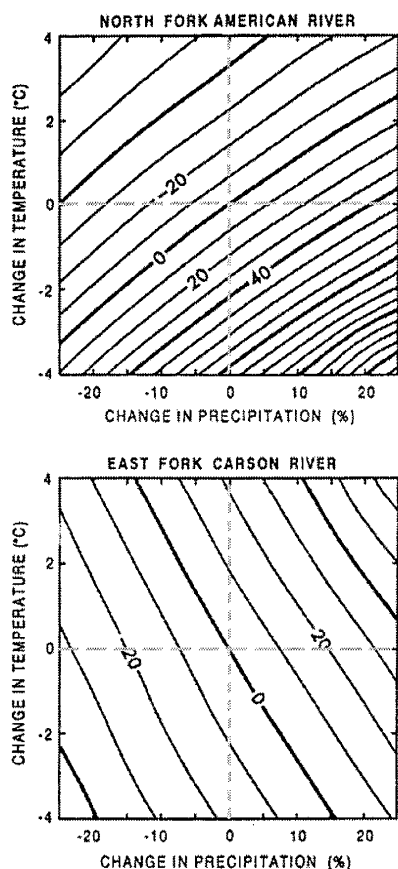


Figure 3-6. Runoff response (% change) to changes in mean annual precipitation and temperature based on Duell's [1994] regression models of the historical record.

variability. The magnitude and direction of the observed responses to temperature and precipitation are similar to those of Flaschka *et al.* [1987], but sensitivity for basins on the east side of the Sierra was lower than that for the North Fork American River, on the warmer, lower west side (Figure 3-6). With a 2°C decrease in temperature and a 25% increase in precipitation, streamflow increases 102% in the North Fork American River but only 22% in the East Fork of the Truckee River basin. Streamflow response to temperature is also different for east-side versus west-side basins. May mean temperature has a direct relation on annual streamflow for all the high-elevation basins and the significance of this relationship was greater than that between mean annual temperature and streamflow. In

addition, while runoff in the west-side basins decreased with temperature, it increased with temperature in the east-side

basins. Duell posited that high early-season temperatures

reduce sublimation and evapotranspiration by causing the snowpack to melt earlier, when the energetic potential for evapotranspiration is lower. Duell's regression also demonstrated that temperature was not a significant variable when only the coolest and wettest years were considered.

He suggested that this was in part due to the smaller variation in temperatures during those years and in part because evapotranspiration is small relative to runoff during the coolest and wettest years.

Risbey and Entekhabi [1996] performed a regression analysis of streamflow, temperature and

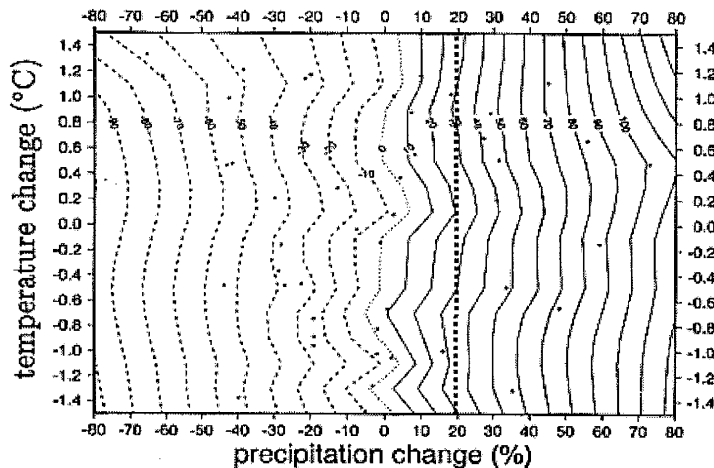


Figure 3-7. Contour plot of percentage streamflow change as a function of percentage precipitation change and temperature departure for the Sacramento Basin. Changes are with respect to the long-term means, calculated from annual means for streamflow and precipitation, and from winter means for temperature. From Risbey and Entekhabi [1996].

precipitation in the Sacramento Basin, California. Their analysis also showed a strong relationship between precipitation and streamflow but virtually no dependence on temperature<sup>2</sup>. They suggest that the regression model applied by Duell [1994] overestimates streamflow response to temperature. Risbey and Entekhabi [1996] also noted a non-

linear relationship between precipitation and streamflow; for larger precipitation increases, the increase in streamflow becomes larger than the increase in precipitation. They explain this nonlinearity as the result of changes in soil moisture storage. "A larger fraction of the precipitation becomes runoff in wet years when the ground is wetter and the snowpack volume is larger. As the saturated area of the basin increases in wet years, the amount of runoff relative to precipitation increases."

In summary, studies of the sensitivity of modern runoff to interannual changes in temperature and precipitation generally suggest greater sensitivity to the latter and a slight amplification of

<sup>2</sup> Although they used winter means as a temperature index, Risbey and Entekhabi [1996] noted that using annual mean temperatures would have made little difference in their results.



precipitation changes in runoff response. Response also seems to vary significantly with basin type and elevation. It is not clear, however, to what extent the magnitude of the runoff sensitivity observed in these studies would apply to larger and more permanent climatic changes. It seems likely that year-to-year changes in soil moisture storage may accommodate a significant fraction of the changes in recharge that occur over short timescales and around the mean value, as, for example, increases in recharge one year replace storage losses that occurred in a previous drought year. The climatic sensitivity that is displayed in interannual variations in runoff may thus be a significantly damped version of the sensitivity to more permanent changes in climate.

Basin runoff depends on type and distribution of vegetation; amount, timing and form of precipitation; soil type and thickness; depth to bedrock; surface slope and a host of other factors. These factors make the relationship between climate change and runoff a complicated one not easily subject to prediction. Nonetheless, as C.W. Thornthwaite recognized as early as 1948 [Thornthwaite, 1948], a fundamental control on runoff is the relationship between potential evapotranspiration and precipitation. We illustrate the importance of that relationship with two hypothetical examples.

If evapotranspiration within a basin is primarily water-limited rather than energy-limited, changes in precipitation may result in roughly proportional changes in evapotranspiration. Precipitation over desert areas, for example, is often small and the productivity of the xerophytic vegetation in those regions is typically limited by availability of water. Under these conditions, a small amount of runoff may occur, depending on geologic, topographic and other factors, but the plants use most of the precipitation that falls. An increase in precipitation might therefore result in only a very small increase in the annual runoff, as plant productivity increases might use as much of the additional water as they do of the base amount. If the fraction of the additional water used is the same as that of the base amount, the runoff coefficient (runoff divided by total precipitation in the basin) is unchanged and the increase in runoff is directly proportional to the increase in precipitation. If, on

the other hand, the dominant vegetation is energy-limited, then increases in evapotranspiration will likely not be proportional to increases in precipitation because insufficient energy is available to use the additional moisture. In that case, a larger fraction of the additional precipitation will exit the basin as runoff and the net increase in runoff will be greater than the increase in precipitation. In an analysis of the potential impact of increased atmospheric CO<sub>2</sub> on future runoff, Wigley and Jones [1985] explored the sensitivity of runoff to changes in evapotranspiration and precipitation mathematically. We review that analysis here to illustrate why runoff in arid basins such as the Owens Valley might be very sensitive to long-term changes in precipitation.

As Wigley and Jones [1985] point out, the relative increase in basin runoff due to a change in climate depends largely on the coincident changes in evapotranspiration. Evapotranspiration,  $ET$ , is a function of many not necessarily independent factors, including, for example, energy and moisture availability, area and type of vegetated cover, and atmospheric CO<sub>2</sub> concentration. In this analysis, we summarize these effects in a single equation that relates  $ET$  under the new climate to that under the initial climate,  $ET_0$ ;

$$ET = \beta(T, P)ET_0, \quad \text{Eq. 3-1}$$

where  $\beta(T, P)$  is a coefficient whose value is a function of the temperature and precipitation of the new climate. The ratio of the new annual runoff,  $R_I$ , relative to the initial runoff rate,  $R_0$ , is given by

$$R_I / R_0 = \frac{\alpha - \beta(1 - \gamma_0)}{\gamma_0}, \quad \text{Eq. 3-2}$$

where  $R_0$  = initial annual runoff amount,  
 $R_I$  = new annual runoff amount,  
 $\alpha$  = precipitation rate normalized by the modern rate,  
 $\beta$  = the coefficient  $\beta(T, P)$  normalizes  $ET$  by  $ET_0$ , and  
 $\gamma_0$  = the initial runoff coefficient.

Equation 3-2 illustrates that the relative runoff rate ( $R_I/R_0$ ) is greater than 1 only by the increase in

precipitation when the relative change in evapotranspiration equals the relative change in precipitation (i.e.  $\beta = \alpha$ ). At the other extreme we can consider increases in precipitation without increases in evapotranspiration. The sensitivity of runoff to precipitation is given by

$$\frac{\partial(R_1 / R_0)}{\partial \alpha} = \frac{1}{\gamma_0}.$$

Precipitation increases without corresponding increases in evapotranspiration are

thus amplified in runoff, particularly in basins where the initial runoff coefficient is small. With an initial runoff coefficient of 15%, similar to that of the Owens Valley, a 20% increase in precipitation can potentially increase runoff by 200% (Figure 3-8). Relative sensitivity to changes in precipitation and changes in  $ET$  is given by

$$\frac{\frac{\partial(R_1 / R_0)}{\partial \alpha}}{\frac{\partial(R_1 / R_0)}{\partial \beta}} = \frac{1}{1 - \gamma_0}.$$

Eq. 3-3

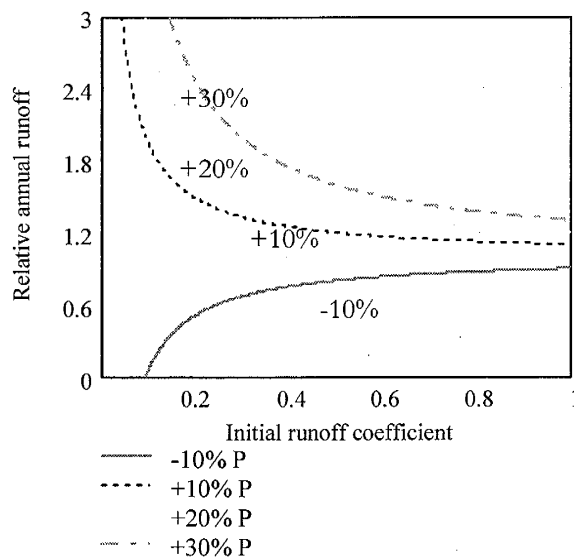


Figure 3-8. Relative amount of runoff (normalized to initial runoff) as a function of initial runoff coefficient with no change in evapotranspiration but an increase in precipitation of 10% (dotted line), 20% (dashed line), 30% (dash-dot line). Solid line shows effect of a 10% decrease in precipitation.

This shows that runoff is always more sensitive to precipitation and that relative sensitivity is greater for larger values of the initial runoff coefficient.

The equations of Wigley and Jones [1985] provide a simple relationship between runoff, runoff coefficient and changes in evapotranspiration. To examine Duell's [1994] data in these terms, we assumed that the following linear function adequately describes the changes in  $ET$  related to

interannual changes in temperature and precipitation:

$$\beta(\alpha, \Delta T) = (1 + a \cdot \Delta T)[1 + b(\alpha - 1)]. \quad \text{Eq. 3-4}$$

As before,  $\alpha$  is the average annual precipitation normalized to its present value,  $\Delta T$  is the difference from the modern mean annual temperature, and  $a$  and  $b$  are fitting parameters describing relative sensitivity to temperature and precipitation, respectively. Using this equation and the runoff relationships described by Wigley and Jones [1985], we used multivariate regression to find the parameters  $a$  and  $b$  that provided the best fit to the runoff-temperature-precipitation relationships observed by Duell [1994] (Figure 3-9).

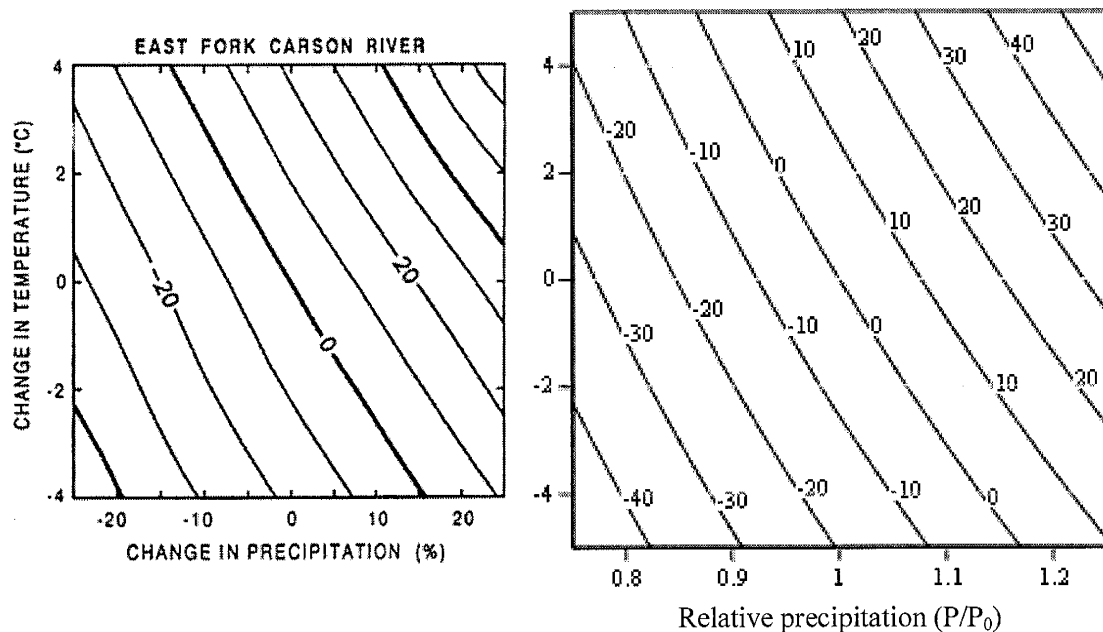


Figure 3-9. Comparison of Duell's regression-model contours of percent change in runoff (left) with those for a simple runoff response calculation using the equation described in the text (right). The latter calculation assumes that evapotranspiration increases by ~2.5% per degree C and is proportional to precipitation by a factor of ~0.8.

The best-fit values of the fitting parameters suggest that evapotranspiration in the East Fork Carson River basin increases by 2.5% per degree C and that it is proportional to precipitation by a factor of ~80%. This capacity to absorb increases in precipitation via ET is therefore significantly greater than the ability of the basin to evapotranspire precipitation incident on the basin; the basin's runoff

coefficient is about 40%<sup>3</sup>. A similar analysis of the modeling results of Jeton *et al.* [1996] for the N. Fork American River suggests that about 70% of increased precipitation is evapotranspired in that basin. The modern day runoff coefficient in that basin is about 60%<sup>2</sup>. Thus, at least for the range of precipitation changes seen in the historical record, evapotranspiration changes in both of these basins seem to nearly equal the year-to-year changes in precipitation.

Studies of modern precipitation – runoff relationships in the southwestern U.S. generally demonstrate that precipitation changes are magnified in runoff, even for the magnitude of changes seen at the interannual time-scale. Temperature and precipitation changes associated with significant climatic events are likely to be, if not larger, at least longer-lasting. In a very arid basin like the Owens Valley, such changes could significantly alter the basin's runoff coefficient. The mathematical relationships described by Wigley and Jones [1985] demonstrate that such changes could make the system very sensitive to climate, providing a possible physical explanation for the highly sensitive precipitation-temperature-runoff relationship described by Mifflin and Wheat [1979].

From the above analysis it is clear that accurately estimating the response of runoff to climate depends critically on correctly estimating the associated changes in evapotranspiration. The difficulty of that task is exacerbated by the fact that, even in a modern basin water balance, it is difficult to accurately determine the role of ET. The following paragraphs summarize details of the modern water balance in the Owens Valley and the changes in evapotranspiration that might accompany climate change.

---

<sup>3</sup> This figure is based on runoff and precipitation data presented in Duell [1994].

## ***WATER BLANCE AND CLIMATIC SENSITIVITY OF THE OWENS VALLEY***

The area of the Owens Valley is approximately 8550 km<sup>2</sup> and precipitation falling on the basin amounts to about 2900 million m<sup>3</sup> yr<sup>-1</sup>. Based on historical records of lake surface area and estimates of annual evaporation rate at the lake, the natural inflow rate to Owens Lake is estimated at ~410 million m<sup>3</sup> yr<sup>-1</sup> [Smith and Street-Perrott, 1983]. Data from the USGS indicate that modern outflow from the basin, including both aqueduct flow and river flow reaching Owens Lake (but not including water diverted from the Mono Lake basin) is ~414 million m<sup>3</sup> yr<sup>-1</sup>. Assuming the system is roughly at equilibrium under modern conditions, this suggests that evapotranspirative losses from the basin today are quite similar to those of the natural, preirrigation era. Dividing the net discharge from the basin by the observed total precipitation yields a valley-wide runoff coefficient of about 14%<sup>4</sup>.

Considering the basin as a whole, we can conservatively estimate the runoff increase due to an increase in precipitation by assuming that ET is directly proportional to precipitation but proportional to temperature only by 6% per degree, similar to that predicted for open water evaporation in the Owens Valley region [Benson, 1986]. The resultant relative runoff ( $R_1/R_0$ ) response contours (Figure 3-10A) display sensitivity to temperature and precipitation but without the precipitation amplification that is observed even in year-to-year runoff variations [Risbey and Entekhabi, 1996]. Evapotranspiration rate is, however, unlikely to be directly proportional to precipitation, particularly in the wetter portions of the basin where most of the precipitation is winter snowfall. Increases in precipitation in those areas would tend to greatly increase the spring runoff peak and provide little opportunity for the vegetation to use the additional moisture. As a high-end estimate of the potential runoff increase due to climate change, we might therefore assume that all ET in the basin is water-limited and fixed at its present annual rate. The resultant runoff response

---

<sup>4</sup> For comparison, the runoff coefficient for the Nile River, Egypt, is about 10% [Wigley and Jones, 1985].

curves for this scenario are shown in Figure 3-10B. Runoff increases in this scenario are highly amplified, with as little as 20% increase in precipitation resulting in a 500% increase in runoff.

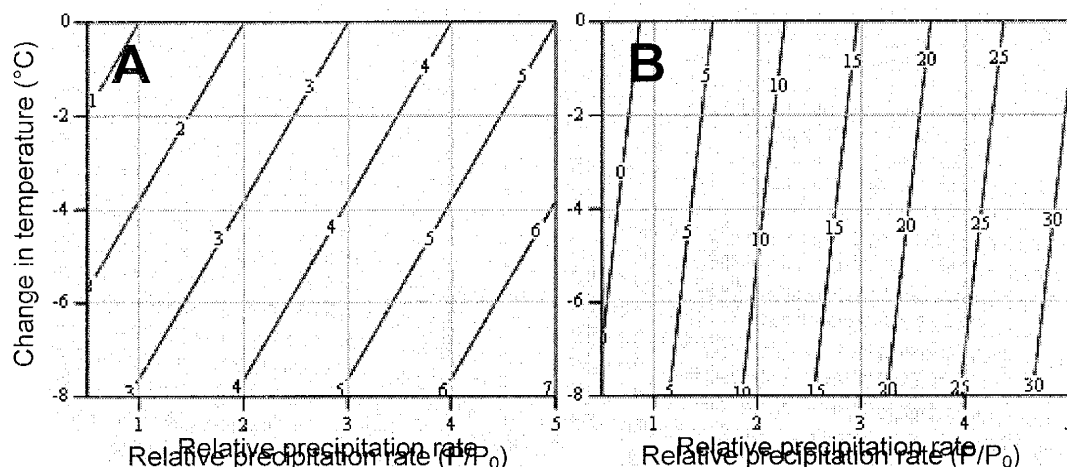


Figure 3-10. Hypothetical response of runoff in a closed basin to changes in precipitation ( $P_0$ =modern precipitation rate) and temperature. Contours are runoff normalized to present-day runoff. Initial runoff coefficient is 0.14. Figure A illustrates relative change in runoff assuming that ET increases equal precipitation increases. Figure B illustrates response assuming that ET responds only to temperature.

Clearly the problem with this simplistic analysis is that even if climate changed uniformly across the basin, it is highly unlikely that changes in ET would be uniform. In order to consider better the potential effects of climate change on the runoff that reaches Owens Lake, we subdivided the basin into regions that have substantially different characteristics and would be expected to respond differently to climate change (Figure 3-11). To simplify calculation of their water budgets, the areas generally correspond to regions described by the USGS in their study of the groundwater system of the Owens Valley [Danskin, 1998]. The four regions include the Owens Valley groundwater basin (as delineated by the USGS and shown in Figure 1-1), or alluvium; the Sierra Nevada mountains; the Inyo-White mountains; and the riparian area of the Owens River.

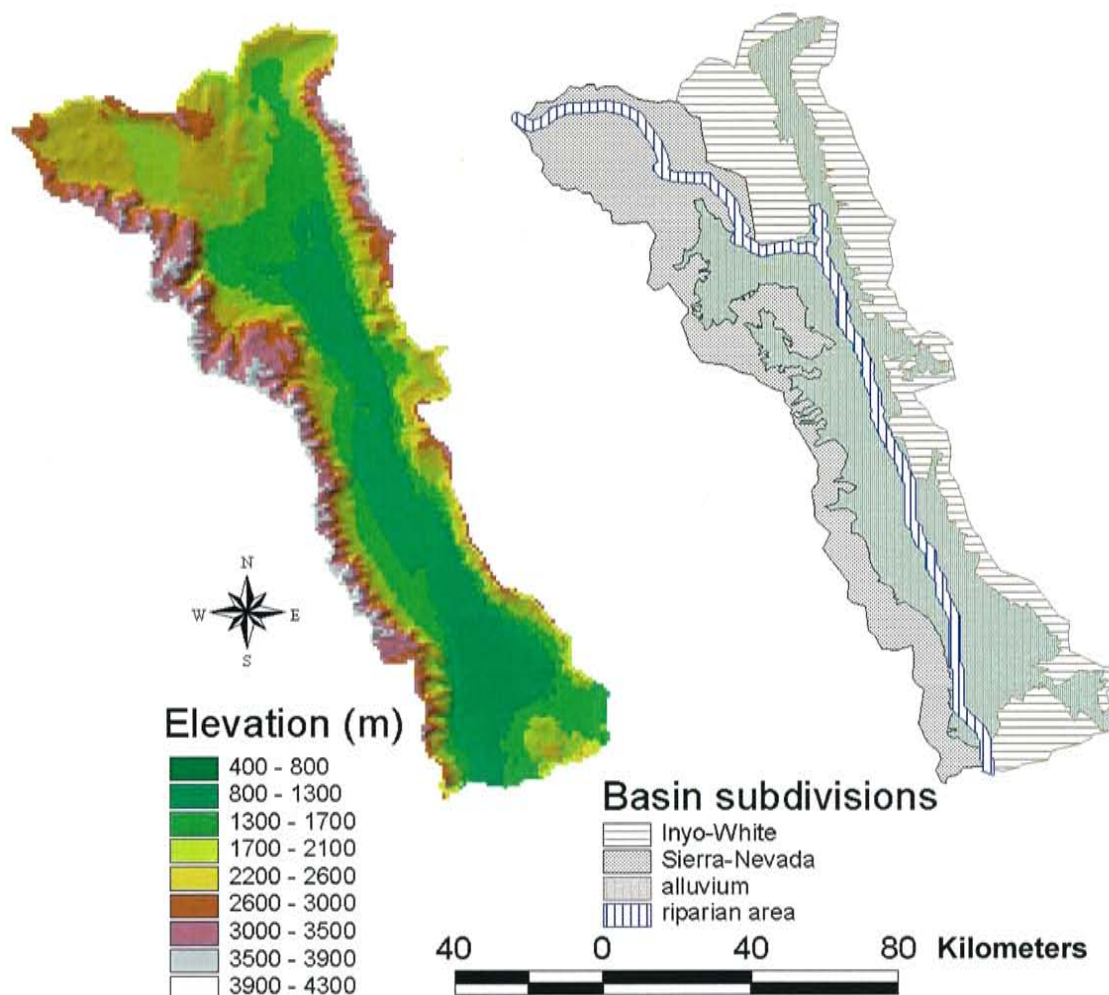


Figure 3-11. Elevation map of the Owens Valley based on the USGS GLOBE digital elevation model dataset (left) and subdivisions of the basin (right) separated by water-balance characteristics. The alluvial valley area is as defined by the USGS study of the groundwater system of the valley [Danskin, 1998].

We calculated runoff coefficients for the basin subdivisions, or subbasins, using a combination of (1) discharge measurements and estimates reported by Hollet *et al.* [1991], (2) PRISM<sup>5</sup> precipitation maps developed by Daly *et al.* [1994] and (3) GIS-based calculation of subbasin areas. Total precipitation and runoff estimates for the subbasins and the entire Owens Valley are summarized in Table 3-1.

<sup>5</sup> PRISM (Parameter-elevation Regressions on Independent Slopes Model) is an expert system that uses point data and a digital elevation model (DEM) to generate gridded estimates of climate parameters (Daly *et al.*, 1994).



	Area (km <sup>2</sup> )	Mean annual precipitation rate (cm yr <sup>-1</sup> )	Total precipitation or inflow (m <sup>3</sup> /yr)	Total discharge (m <sup>3</sup> /yr)	Runoff coefficient (%)
Sierra Nevada Mountains	2.64E+03	55.8	1.48E+09	5.71E+08	39
Inyo-White Mountains	2.39E+03	27.7	6.62E+08	1.32E+07	2
Alluvial basin	3.51E+03	19.5	6.85E+08	3.70E+06	1
<b>Subbasin Subtotal</b>	<b>8.55E+03</b>	<b>34.3</b>	<b>2.82E+09</b>	<b>5.88E+08</b>	<b>21</b>
Riparian area		~5.0†	5.88E+08†	4.10E+08	70
<b>Owens Valley</b>		<b>33.0</b>	<b>2.84E+09</b>	<b>4.10E+08</b>	<b>14.4</b>

Table 3-1. Summary of precipitation and discharge data for the Owens Valley and subbasins considered in this study. †The runoff coefficient shown for the riparian area is calculated differently than for the other subbasins; its precipitation term includes discharge from the other subbasins.

#### SIERRA NEVADA REGION

Runoff from the Sierra Nevada is the largest source of water for the Owens River. Total discharge from gaged and ungaged streams in the Sierra Nevada is about 571 million m<sup>3</sup> yr<sup>-1</sup>. Approximately 40% of that water recharges the groundwater system by infiltration through the alluvial fans after exiting the mountains [Danskin, 1998]. A small portion of the remainder evapotranspires from the riparian area along the streams between the mountains and the Owens River; the remainder recharges the Owens River directly. Total precipitation over the Sierra Nevada is approximately 1500 million m<sup>3</sup> yr<sup>-1</sup> and the runoff coefficient for the area is ~40%. Calculations for separate tributary basins in the region indicate that the runoff coefficient is quite variable in the mountains. Runoff coefficients for Bishop Creek and Horton Creek, for example, are relatively high - ~60% to 65% - while those in Coyote and Rawson Creeks, just east of the Bishop Creek drainage, are between 35% and 40%. Runoff from many of the other tributaries must therefore be considerably lower to offset higher values in large drainages such as Bishop Creek, which by itself provides nearly 30% of the total mountain runoff in the Owens Valley.

The Sierra Nevada provides most of the water that is discharged to Owens Lake. Estimates of basin-wide runoff response to climate change are thus most sensitive to its response. As Jeton *et al.* [1996] pointed out, there are competing effects in the response of runoff to climatic changes. Under

current conditions, a large fraction of the annual precipitation in the Sierra Nevada occurs as snowfall. Most of the water available for ET is therefore available only when the snow melts. As that tends to occur over a relatively short season, only a small fraction of the snowmelt is available to the local vegetation. Because the overall distribution of the average winter snowpack would not be significantly altered by changes in precipitation alone, increases in precipitation would probably not effect large increases in ET. The runoff coefficient for these areas would thus increase with precipitation.

The effect of decreased temperature is more difficult to estimate. Decreased temperature would tend to extend the winter snowpack to lower elevations. Under present conditions, most of the annual precipitation occurs in the winter even at the lower elevations where most of it is in the form of rain rather than snow. While many types of vegetation are dormant during the winter, coniferous forests may be capable of using a large amount of winter precipitation. Conversion of the rain in those areas to a seasonal snowpack would probably decrease the time over which the precipitation is available to plants and the seasonal snowmelt peak might also exceed the storage capacity of the thin mountain soils, thereby tending to maintain, rather than increase, the annual ET from those areas. At the same time however, temporary storage of that precipitation as snow might increase ET in the downstream riparian area, by making it available in the spring, when available energy is greater than in winter.

Growth of glaciers in the Sierra Nevada might also have a significant effect on ET in the mountain basins. The area occupied by glaciers in the Bishop Creek drainage during the LGM was substantial. Only a small fraction of the ice on the glacier itself reaches the atmosphere via sublimation and evaporation. The area occupied by glaciers would otherwise be occupied by riparian vegetation in the main stream channel and a combination of brush and trees on the slopes above the stream not occupied by bedrock. Glaciation of these areas would decrease ET and increase their

runoff coefficient considerably. The runoff coefficient in the Bishop Creek basin is today about 0.65 and the area of glaciers in the basin is an insignificant part of the total area. During the Tioga maximum, however, the Bishop Creek glacier occupied about 80% of the watershed. If the runoff coefficient for the glaciated portion of the basin is 90%, the runoff coefficient for the full drainage basin could have effectively increased to ~85% from the modern value of ~65%. Clearly this is a potentially important means of increasing the runoff coefficient in glaciated areas.

#### *INYO-WHITE SUBBASIN*

The Inyo-White mountains subbasin also includes the Volcanic Tableland, north of Bishop and the Inyo and White mountains that form the eastern boundary of the valley. Runoff from this area stands in marked contrast to the Sierra region. The total precipitation incident on the area is about 660 million  $\text{m}^3 \text{yr}^{-1}$  but the estimated runoff from its gaged and ungaged tributaries is only 13 million  $\text{m}^3 \text{yr}^{-1}$ , yielding a runoff coefficient of about 2%.

Precipitation in the Inyo-White range is considerably lower than the potential ET in the region and increases in precipitation would likely result in concomitant increases in ET. In contrast to the Sierra Nevada side of the basin, few perennial streams discharge from the Inyo-White range and field evidence suggests that the situation was not significantly different in the past. While snow does fall on the higher parts of the range during the winter, most of that either sublimates or melts off and infiltrates to be lost by evapotranspiration. Given the aridity of the region and the lack of evidence of significant stream drainage from the area in the past, it seems likely that ET changes in the region would be proportional to increases in precipitation. Since the runoff from this region is already extremely low, errors in estimating the response of this region should have little effect on the overall response of the basin.

#### ALLUVIAL VALLEY SUBBASIN

The alluvial basin includes the valley floor and areas of alluvium extending to the bedrock contact with the mountains. Hollet *et al.* [1991] report that precipitation slightly exceeds evapotranspiration over the alluvial basin, producing a small net recharge to groundwater through the alluvium and volcanic deposits. Total precipitation incident on the alluvium is approximately 690 million  $\text{m}^3 \text{yr}^{-1}$  and the USGS estimates that only a small portion of that, about 3.7 million  $\text{m}^3 \text{yr}^{-1}$ , reaches the water table. As very little precipitation and virtually no recharge occurs through the valley fill under present conditions, the overall water balance of the basin is not particularly sensitive to this contribution. Even a fairly substantial increase in the runoff coefficient for the area would provide only a very small increase in the amount of water reaching the Owens Lake.

#### OWENS RIVER AND RIPARIAN AREA

Both mountain ranges and the alluvial basin discharge, via surface water or groundwater, to the Owens River, and under natural conditions the only losses from the river are to evapotranspiration in the riparian area along the river, evaporation from Owens Lake, and groundwater underflow out of the basin to the south. Underflow is reportedly a small component of the overall basin water balance [Danskin, 1998], and underflow into the basin nearly balances underflow out of the basin. We ignore underflow in this analysis.

Total discharge of surface water and groundwater that should leave the system via the Owens River is approximately 590 million  $\text{m}^3 \text{yr}^{-1}$ . Of that, approximately 410 million  $\text{m}^3 \text{yr}^{-1}$  appear to have reached Owens Lake during historical times. This implies that about 180 million  $\text{m}^3 \text{yr}^{-1}$  are evapotranspired in the riparian area. Based on the evapotranspiration measurements of Duell [1990] and earlier lysimeter studies, Hollet *et al.* [1991] estimated that the evapotranspirative loss from the riparian area between Pleasant Valley Reservoir and the aqueduct intake below Tinemaha reservoir ( $\sim 37^\circ 00'$  N latitude) is about 140 million  $\text{m}^3 \text{yr}^{-1}$ . We assume that the difference in the residual-based estimate and the  $\sim 30\%$  lower direct estimate of evapotranspiration represents the loss that would occur in the area between the aqueduct intake and Owens Lake. A runoff coefficient for the valley floor (essentially the riparian area of the river), calculated as the ratio of annual river discharge to

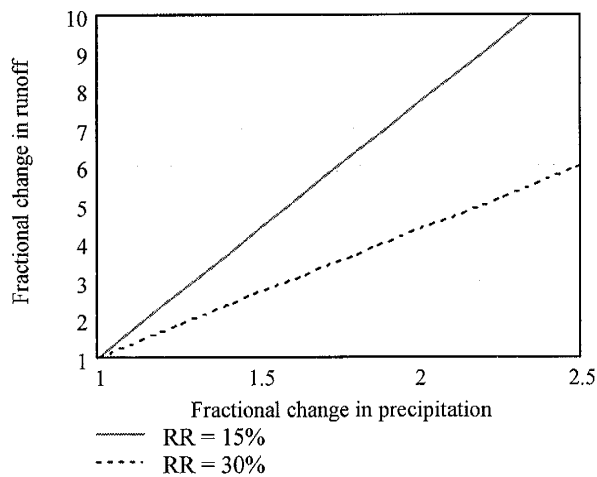


Figure 3-12. Increase in runoff as a function of increased precipitation (assuming no change in evapotranspiration) for a basin with an initial runoff ratio of 15% (solid line) and one with an initial runoff ratio of 30% (dotted line).

assumption that ET increases only slightly in response to increased precipitation might provide fairly reasonable estimates of the basin-wide runoff response.

Figure 3-12 illustrates runoff response to precipitation assuming no change in evapotranspiration for basins with runoff coefficients of 15% and 30%. The former value represents the actual basin-

total annual inflow (precipitation plus inflow from surrounding subbasins), is thus about 70%. Since the source for most of the water reaching the riparian area is the winter snowpack in the Sierra Nevada, the overall runoff coefficient for the Sierra Nevada might be better estimated as the product of the runoff coefficients for the two areas, approximately 30%. Use of this value for the initial runoff coefficient and the

wide runoff coefficient and the latter a coefficient for the Sierra Nevada and Owens River riparian area together, without the alluvial valley and Inyo-White Mountains. With the higher runoff coefficient, runoff increases of 2 to 5 times the existing runoff require precipitation increases of 30% and 220%, respectively. These changes are on the order of those described in Figure 3-3.

#### MODELED RUNOFF AND LAKE RESPONSE

Having established the importance of the climatic sensitivity of runoff to the water balance of closed-basin lakes, we used a variety of models to examine both basin-runoff and lake-evaporation effects on lake level response to climate change. In each, we limit our consideration of potential climate effects to changes in the primary climatic variables - precipitation and temperature. Several previous studies have considered the effects of cloudiness and other secondary climatic variables on lake evaporation and lake surface area in the Great Basin [Benson, 1986; Hostetler and Benson, 1990]. Results of those studies serve to emphasize the importance of runoff in producing the greatly increased lake surface area of the pluvial period. They have not, however, presented a plausible explanation for the dramatic increases in runoff that appear to have occurred throughout the Great Basin. In this study, we focus on exploring the basic nature of the relationship between climate and runoff, and how that relationship affects the sensitivity of the lakes along the ancestral Owens River. We recognize however, that secondary climatic variables like cloudiness and wind speed may have significant effects on any system involving a balance between inflow and evapotranspiration. If the models developed in this study provide a satisfactory explanation for the greatly increased lake surface area of the pluvial period, further studies will probably be required to incorporate secondary climatic effects.

In interpreting lake surface area variations with a steady-state lake evaporation and basin runoff response, we assume that changes in storage that might be effected by a perturbation in the water

balance are either negligible or that those changes occur more rapidly than the timescale of the changes of interest. In this study, it appears that lake levels often remained at relatively constant levels for hundreds to thousands of years. Evidence from the USGS's studies of the groundwater system in the Owens Valley indicates that both of these assumptions are probably valid for the timescale of interest here. This is primarily because groundwater in the Owens Valley is controlled to a large extent by springs, seeps, evapotranspiration, and surface water features [Danskin, 1998] that act as hydraulic buffers on groundwater levels in the unconfined aquifer. Danskin [1998] emphasizes the exceptional importance of these features in understanding the operation of the hydrologic system in the Owens Valley. "These buffers adjust the quantity of water exchanged with the aquifer system and effectively minimize variations in water-table altitude. The widespread presence of hydraulic buffers is the primary reason the water-table altitude beneath the valley floor has remained relatively constant since 1970 despite major changes in the type and location of ground-water discharge." Even where changes in the groundwater system are effected, the system appears to be capable of adjusting on a timescale of decades or less. In considering alternative water management options for the valley, including changes in groundwater pumping, Danskin [1998] notes that the "highly transmissive and narrow aquifer system will transmit the effects of pumping to other sensitive areas of the valley within a couple of years." We conclude that the Owens Valley hydraulic system does not introduce a significant time-constant issue in our analysis of the large-scale (in terms of both time and lake size) variations of the hydrologic changes in the glaciers and lakes during the last deglaciation.

#### ***LUMPED-PARAMETER, REGIONAL WATER BALANCE APPROACH***

As a first cut at estimating the sensitivity of the Owens Valley lake system to climate, we consider a simple, lumped-parameter annual water balance model, but with the several regions of the basin treated separately. Runoff from each region is calculated from mean precipitation, temperature and an estimated evapotranspiration response function. Evapotranspiration reduction via temperature

depression is assumed to be proportional to the corresponding reduction in the vapor pressure gradient, assuming constant relative humidity and a minor contrast between water and air temperature. Inflow to the riparian area includes runoff from the Sierra Nevada, Inyo-White range and groundwater basin. Direct precipitation in the riparian area is thus a minor component of its water balance.

As a conservative estimate of the increased runoff resulting from increased precipitation, we can assume that the runoff coefficient is constant and affected only by temperature. Increases in runoff are then directly proportional to changes in precipitation and the only additional runoff is that derived from suppression of evapotranspiration from the lake and basin. Figure 3-13A illustrates the response of lake surface area to changes in precipitation and temperature under this assumption. Searles Lake is believed to have been overflowing at  $\sim 18$  ka, which implies a corresponding cumulative lake surface area of  $\sim 17 \times 10^8$  m<sup>2</sup>. The lumped parameter model under these conditions of greater temperature sensitivity indicates that this would not happen without at least a doubling in precipitation unless temperature is depressed by at least 7°.

The assumption of a constant runoff coefficient does not appear reasonable for the Sierra Nevada. As an alternative, we consider the possibility that evapotranspiration in the Sierra Nevada uses only half of any increases in precipitation. We assume a similar ballpark estimate for the riparian area, where we posit two primary, and competing, effects on evapotranspiration. First, increases in discharge to the riparian area would, in part, simply create increased flow rates in the main trunk stream, which would allow little opportunity for vegetation to remove the additional water. Second, increased discharge might increase groundwater levels in the valley floor and thereby increase the width of the riparian areas, which would increase evapotranspiration. Figure 3-13B illustrates the lake surface area response under these assumptions. With only those two relatively minor and reasonable assumptions about the likely response of evapotranspiration to climate change, we



observe a rather dramatic change in predicted response of the closed basin lake system. The sensitivity to precipitation is greatly increased and now the minimum temperature depression that could yield a full Searles Lake with less than a doubling of precipitation is only 5°C. This again emphasizes the importance of the relationship between evapotranspiration and climate on the sensitivity of runoff and, in particular, the high sensitivity of runoff to precipitation in arid basins.

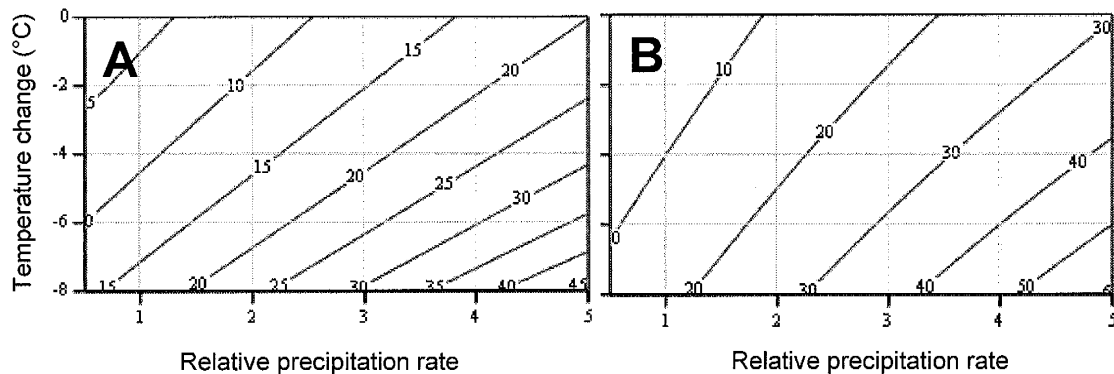


Figure 3-13. Cumulative lake surface area contours for the Owens Valley ( $10^8 \text{ m}^2$ ) as a function of changes in mean annual temperature and precipitation. Plot A assumes that evapotranspiration is directly proportional to precipitation and proportional to temperature in a manner predicted by the saturated vapor pressure curve. Plot B assumes the same conditions except for in the Sierra Nevada and riparian area of the Owens River where evapotranspiration increases are only half of the corresponding precipitation increase.

#### THORNTHWAITE WATER BALANCE MODEL

The lumped parameter model provides a reasonable means of illustrating the sensitivity of the system to different assumptions but may be of little use in evaluating the likelihood of those assumptions. The range in calculated lake surface areas demonstrated in these examples illustrates that lake surface area is highly sensitive to basin runoff and response of runoff to climate change. As an alternative means of estimating changes in runoff that might result from climate change we developed a Thornthwaite water balance model for the Owens Valley [Dingman, 1993; Thornthwaite and Mather, 1955]. The model is essentially a monthly accounting of the moisture available to the vegetative cover in the basin and the resultant amount evapotranspired, requiring monthly records of temperature, precipitation, potential evapotranspiration and soil moisture storage. Our formulation

of the model is based largely on that described by Alley [1984] and summarized by Dingman [1993]. Flaschka *et al.* [1987] applied a similar model in a study of runoff response to global warming in four basins in Nevada and Utah. They found it generally sufficient for predicting observed streamflow response to interannual temperature and precipitation changes.

Most of the runoff in the Owens Valley comes from snowfall in the Sierra Nevada, so changes in snowcover may strongly influence the annual water balance. Recognizing the potential importance of snowcover in the interannual variation of runoff, Flaschka *et al.* [1987] tested their model with and without a component that calculated the amount of snow in the basin. They found that inclusion of this effect had virtually no effect on how well the model fit the historical record. This suggests that the impact of interannual variations in snowcover on evapotranspiration is either too small to have an appreciable effect on annual ET or that streamflow response to that effect is averaged over a longer time-scale. On the other hand, large changes in the thickness and extent of seasonal and permanent snowcover will occur if the climate changes significantly. We therefore incorporated snowfall, snowmelt and snow evaporation in the model.

The monthly water balance is calculated for each cell in a gridded domain defined by the drainage basin of the Owens Valley. The nominal cell size of the digital elevation models used is approximately 930 meters. Temperatures were estimated using 2<sup>nd</sup> degree polynomial functions of elevation for each month, each determined via regression of temperature records from stations in Death Valley, Trona, Bishop, Lodgepole, and the White Mountain Research Station. We used the PRISM [Daly, 1994] 4-km resolution gridded data for the western U.S. for monthly precipitation amount and distribution. The spatial distribution of mean annual precipitation in those grids compared well with the mean annual precipitation contours of the basin mapped by the USGS [Danskin, 1998]. The spatial resolution of these maps is coarse compared to that of the base DEM, however, and further development of this model should include resampling of the PRISM data to the

scale of the base grid. Precipitation is apportioned between snow and rain based on the fraction of the month falling below a critical temperature of 2°C. The fraction of the month below the critical temperature is calculated assuming a normal temperature distribution using the mean monthly standard deviation of temperature at Bishop. Snowmelt is calculated using a simple temperature-based melt index, calculated from regression of the Marks and Dozier [1992] data for Emerald Basin. Melt occurs only when temperature is above a critical temperature (0.5°C) and then at a rate of 40 cm month<sup>-1</sup> °C<sup>-1</sup> above the critical temperature. This rate is within the range of values recommended by Rango and Martinec [1995] in their evaluation of the degree-day method of computing snowmelt.

Accurate determination of potential evapotranspiration generally requires estimates of net solar radiation, relative humidity, wind speed and temperature. Of those parameters, the distribution of solar radiation and temperature can be estimated reasonably well. Only rough, basin-wide approximations could be assumed for the remaining variables, and net radiation is only decreased markedly in the rugged terrain near the mountain crests, a small fraction of the whole. For that reason we used a simple temperature-based approach to estimate potential evapotranspiration, a slightly modified form of the method proposed by Malmstrom [1969]. Malmstrom claimed improved climate classification using a simplified form of the original Thornthwaite equation for potential evapotranspiration that requires only calculation of the saturation vapor pressure at the monthly average air temperature. Malmstrom provided a coefficient for the calculation that yields 2.5 cm monthly PET at 0°C. We adjusted this coefficient to yield, at the elevation of Owens Lake, the estimated annual evaporation rate of 127 cm yr<sup>-1</sup> [Smith and Street-Perrot, 1983]. Soil moisture storage capacity varies significantly across the basin, depending on geology, topography, soil type, rooting depth and a host of other factors. To distinguish areas of different soil moisture storage capacity, we used the land use - land cover data available from the USGS (Figure 3-14). The land cover types present in the Owens Valley and the soil moisture storage capacity that we assigned to

each are shown in Table 3-2.

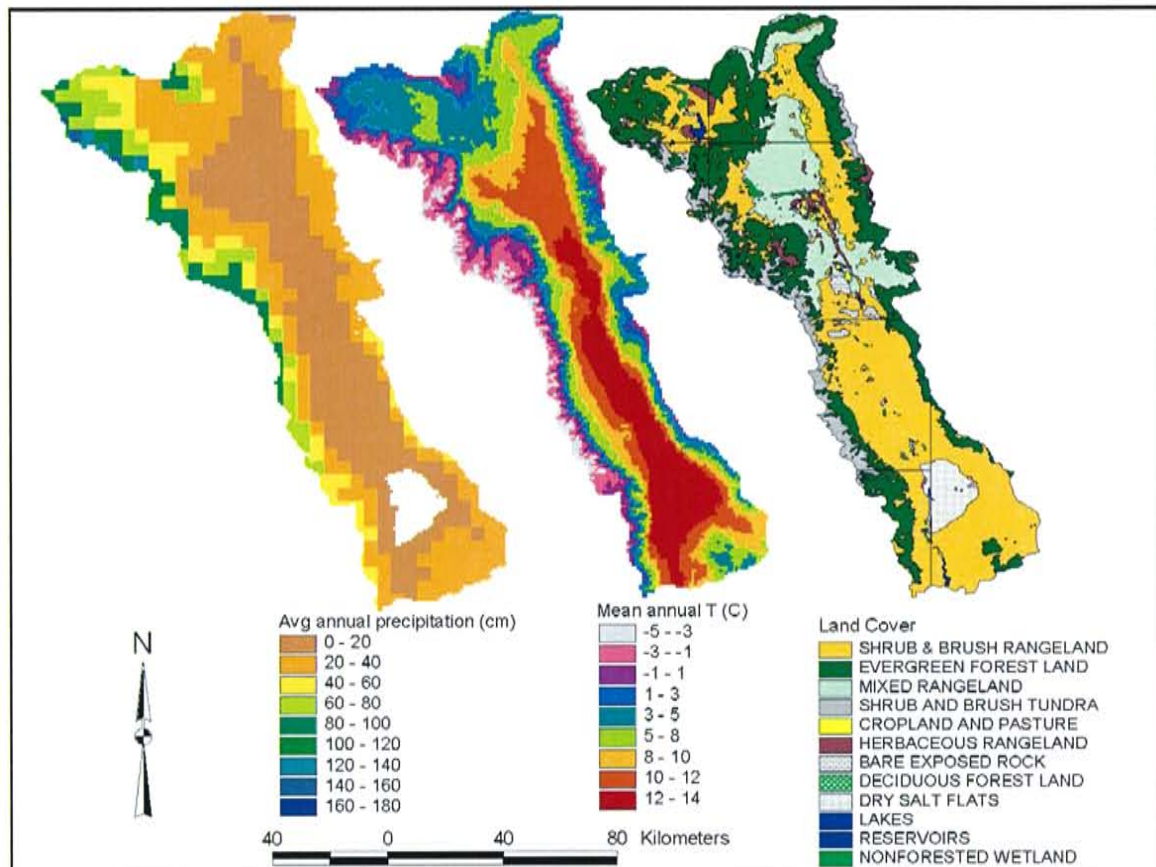


Figure 3-14. Mean annual climatic datasets and soil moisture storage capacity map used in the Thornthwaite water balance model. Annual average precipitation in the Owens Valley is from the PRISM dataset [Daly et al., 1994]; mean annual temperature is based on the regression of temperature records from the Owens Valley. Land cover data is from the USGS Land Use Land Cover dataset.

Land Cover Type	Soil moisture storage capacity (cm)
Lakes and reservoirs	100
Non-forested wetland	50
Evergreen forest land	20
Shrub & brush rangeland	12
Cropland and pasture, Deciduous forest land, Herbaceous rangeland, Mixed rangeland	10
Shrub and brush tundra	1
Bare exposed rock	0.5
Dry salt flats	NULL

Table 3-2. Soil moisture storage capacity associated with the land cover types shown in Figure 3-14.

Evaporation from snow is calculated using a mass transfer coefficient, estimated wind speed, the saturated vapor pressure at the temperature of the snow and the vapor pressure of the ambient air. Estimates of the importance of snow evaporation and sublimation on the overall water balance of the seasonal snowpack have had an interesting history of conflicting opinions. In 1934, Matthes concluded from observations of snow surfaces in the high Sierra that virtually all of the snowfields above 12,000 feet “waste away during the summer without contributing a drop of water to the streams in the valleys below.” Matthes thus implied that virtually all of the snow at high elevations is lost to the atmosphere through sublimation and evaporation. Seeking to test that conclusion, Sharp [1951] conducted a study of the water balance of a small snow bank at an elevation of 12,200 feet in the middle fork of Bishop Creek. Based on careful surveys of snow bank thickness and density and by periodic measurements of snowmelt using a weir set on bedrock below the snow bank, Sharp observed that 99% of the wastage during an approximately two-week period in July ran off through the weir. He thereby concluded, contrary to Matthes’ statement, that evaporation plays a relatively insignificant role in ablation. Making note of the spectacular difference of opinions on the subject, Beaty [1975] attempted to determine the fraction of snow lost by evaporation in the White Mountains on the east side of the Owens Valley. Beaty’s observations suggested that Matthes was largely correct, and measurements of runoff from several small blocks of snow in May, 1970 indeed

indicated that 50 to 80% of the losses occurring during a 2 to 3-day period were due to sublimation. These studies were quite informal in nature and were conducted over only very short periods of the melt season. The large differences in the conclusions of those studies suggest that a much more detailed set of measurements would be required to resolve the question more definitively. Several detailed mass and energy balance studies of snow cover in the Sierra Nevada have since attempted to resolve the issue. Anderson [1976], using mean-profile methods at the Central Sierra Snow Laboratory near Lake Tahoe, California, calculated average evaporation rates of only 2 mm per month during the accumulation season and 4 mm per month during the snowmelt season. In contrast, Marks and Dozier's [1992] mass and energy balance calculations at two sites in the Emerald Basin indicated that snowpack losses via evaporation during 1986 were ~20% at the outlet of Emerald Lake and 25% at an exposed ridge, with approximately even distribution of the loss between the accumulation and snowmelt seasons. Kattleman and Elder [1991] calculated the total snow evaporation in that basin for the years 1986 and 1987 as 18% and 33%, respectively. These fractions represent several centimeters of water loss via evaporation. Leydecker and Melack [1999] summarized these calculations in a recent study that focused directly on the measurement of evaporation from snow in the Central Sierra Nevada. They used the mean-profile method to calculate snow evaporation at eight locations, analyzing four to six years of data at most of the sites. Their analysis indicated that annual evaporation from the snowpack at those sites, which included both Emerald Basin and the Central Sierra Snow Laboratory, varied from 12 to 156 mm. In attempting to explain the disparity between their results and those of Marks and Dozier [1992], they concluded that the difference was due, first, to the anomalously high wind speeds (~averages of 7.5 m/sec and 5.0 m/sec at the lake and ridge sites respectively) measured by Marks and Dozier [1992] and, second, to differences in the method used to determine the temperature of the snow layer from which evaporation/sublimation occurs. Their data indicate that average wind speed in the Sierra Nevada is on the order of ~2 m/sec.

Based on the analysis of Leydecker and Melack [1999], which appears to be the most comprehensive study of evaporation from snow to date, we incorporated a  $-2^{\circ}\text{C}$  temperature adjustment for calculation of snow temperature from ambient air temperature, and used a uniform wind speed of  $2 \text{ m sec}^{-1}$  in the calculation of snow sublimation. Having initially used the data of Marks and Dozier [1992] to estimate a dimensionless bulk turbulent heat transfer coefficient of 0.0019 [Paterson, 1994], we reduced that value to 0.0010 to better reflect the aerodynamic conditions that would exist under the calmer conditions that Leydecker and Melack [1999] suggest is typical in the region. Under this parameterization, snow evaporation in the model amounts to approximately 8% of the annual snowfall. Leydecker and Melack [1999] estimated that about 7% of the annual snowpack in the Sierra Nevada is lost via sublimation and evaporation.

Evapotranspiration in the model occurs at the potential evapotranspiration rate when sufficient water is available from precipitation. Otherwise it occurs at a rate dependent on the amount of water available from direct precipitation, snowmelt, and a change in soil moisture storage. Soil moisture storage each month is calculated according to the equation [Dingman, 1993]

$$S_m = S_{m-1} \exp \left[ \frac{-(PET_m - W_m)}{S_{\max}} \right], \quad \text{Eq. 3-5}$$

where  $m$  is month of the water year,  $S$  is soil moisture storage,  $PET$  is potential evapotranspiration,  $W$  is available water, including rainfall and snowmelt, and  $S_{\max}$  is soil moisture storage capacity.

Evapotranspiration where snowcover exists was handled in a somewhat ad-hoc manner. We allowed evapotranspiration beneath snowcover only when the temperature was above a critical temperature ( $^{\circ}\text{C}$ ). Below that temperature, only sublimation/evaporation is allowed to occur. Above it, evaporation from snow and evapotranspiration of the melting snow and incident rainfall occur simultaneously.

The model performs monthly accounting of the available water for evapotranspiration and tracks the amount of water contained in soil moisture storage and snowpack throughout the year to determine a steady state condition under a given set of climatic inputs. At the end of each year, the model starts over but retains the soil moisture storage grid from the end of the just-completed year. The model is thus run until the monthly quantities converge to constant values.

In areas where annual snow evaporation and melting is less than the annual snowfall there is net accumulation of snow. Under dramatically reduced temperatures, this can occur throughout much of the higher elevations in the basin. Net annual snow accumulation leads to the development of glaciers, which also modify the landscape and affect the water balance. Alpine glaciers accumulate snow at high elevations and move it to lower elevations where it is removed primarily by melting. The accumulation areas may produce significant annual snowmelt in the melting season and no modification of the model is required to incorporate that contribution. The ablation areas, however, effectively displace areas of vegetation-dominated evapotranspiration with areas where losses to the atmosphere are limited to sublimation and evaporation, thereby increasing net runoff from the basin. In this analysis we consider only steady-state glaciers, in which the annual snowmelt is equal to the annual snow accumulation. To simulate the effect of the presence of steady-state glaciers in the basin, the remaining snowpack at the end of every year is simply added to the basin runoff.

In the Owens Valley, a considerable fraction of water that runs off from the high elevations in the Sierra Nevada reaches the Owens Valley floor only to be lost via evapotranspiration in the riparian area of the Owens River. Because the water balance model provides no 'routing' component to reproduce that effect, we incorporated it by establishing a separate 3-km wide Owens River riparian area in which evapotranspiration could exceed annual precipitation. Evapotranspiration of the riparian area was adjusted to a fraction of the mean annual PET (0.75) that provided a good match to the historical inflow for Owens Lake.



## RESULTS

Most of the runoff in the Owens Valley is derived from snowmelt in the Sierra Nevada. As discussed previously, the runoff coefficient for the Sierra Nevada region, as determined from USGS discharge measurements, is approximately 40%. In the initial parameterization of the model, soil moisture storage capacity in all but the high tundra areas was given a value of 10 cm, the value used by Flaschka *et al.* [1987] for all regions in their model and one that would also be within the range suggested by Roberts *et al.* [1993] for the areas given their soil type, slope, and mineralogy. After establishing initial estimates for the parameters in the model we simulated the existing climate with the water balance model and examined the runoff data for the Sierra Nevada region. The runoff coefficient for that area was ~48%, slightly higher than that calculated using the PRISM precipitation data and the USGS discharge data. To allow slightly larger evapotranspiration from the region, we increased soil moisture storage capacity within the evergreen areas to 20 cm, a value still well within the range suggested in the parameterization recommended by Roberts *et al.* [1993]. Small adjustments in the magnitude of the monthly snowmelt index and critical temperatures for evapotranspiration were also tested but these changes had little effect on the runoff from the area and the initial values

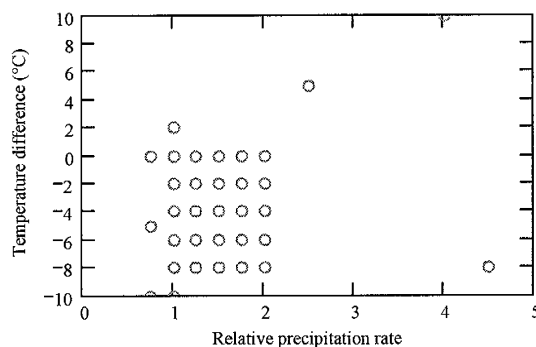


Figure 3-15. Combinations of temperature and precipitation for which the Thornthwaite water balance model was used to simulate basin evapotranspiration and runoff response in the Owens Valley.

were reinstated for the final simulations. After calibration, the runoff coefficient for the Sierra Nevada area was ~45%, still larger than that determined independently for the area but certainly within range of values that would include the uncertainty associated with its calculation.

## SENSITIVITY

Following minor calibration adjustments and correction to provide the historic inflow to Owens Lake we ran the model for a wide range of temperature and precipitation combinations (Figure 3-15) to examine the response in, and beyond, the likely range of reasonable applicability. As illustrated by

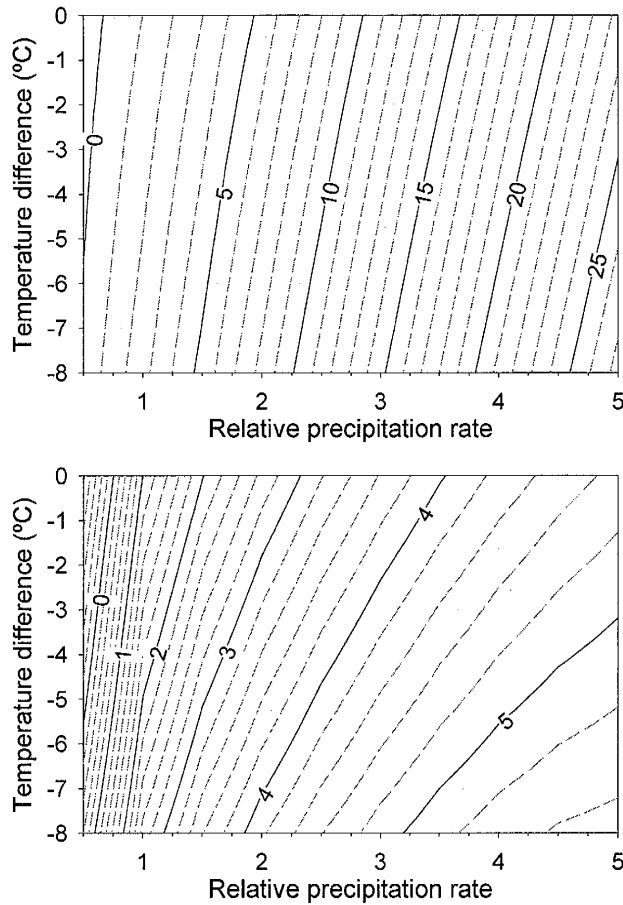


Figure 3-16. Modeled runoff response of the Owens Valley to changes in temperature and precipitation in contours of (top) relative runoff (normalized to present-day value) and (bottom) relative runoff coefficient

changes in relative basin runoff, modeled evapotranspiration (Figure 3-16) is sensitive to changes in both precipitation and temperature with greater apparent sensitivity to precipitation. Large increases in relative runoff occur even under modest increases in precipitation; a 50% increase in precipitation for example yields a trebling in runoff with no change in temperature and more than 500% increase when accompanied by a temperature depression of 8°C. This is similar to the relationship between temperature, precipitation and runoff observed by Langbein [1958, 1962] (Figure 3-3). The large amplification in the response to precipitation is a result of relatively large

changes in the runoff coefficient for the basin (Figure 3-16B) and is in keeping with the predicted sensitivity for arid basins described by Wigley and Jones [1985]. The basin runoff coefficient displays greatest sensitivity to precipitation where precipitation is lowest and becomes increasingly more

sensitive to temperature as conditions get colder and wetter.

#### *EXTENSION TO LAKE SURFACE AREA*

The runoff response described by the water balance model can be used to predict the response of lake surface area in the Owens Valley by incorporating the modeled runoff into the water balance equation for the lakes. As described previously, we model the response of the lakes themselves with a simple water balance model for the lake system that considers, for each lake in the chain, basin geometry, base evaporation and sensitivity of evaporation to temperature calculated using the mean temperature of each basin and the slope of the saturated vapor pressure curve at that temperature. Combining the runoff response of the basin with the response of the lake suggests that lake surface area in the basin would respond as described in Figure 3-17. This relatively simple analysis suggests that fairly small temperature depression and modest increases in precipitation would be sufficient to cause very large changes in lake surface area in the Owens Valley. For example, the combined area of the lakes when Searles Lake is at or near its sill is approximately  $17 \times 10^8 \text{ m}^2$ . According to our analysis, even under only slightly cooler temperatures ( $-2^\circ\text{C}$ ) the lakes would expand to that level given a 75% increase in precipitation. With a larger, but still reasonable, temperature depression of  $-8^\circ\text{C}$ , a 20% increase in precipitation would suffice.

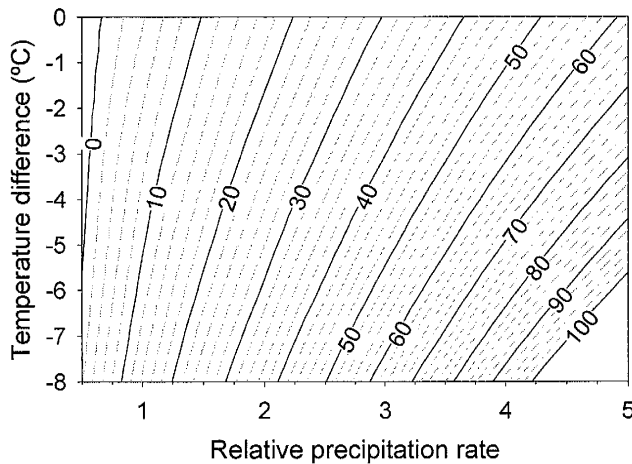


Figure 3-17. Lake surface area ( $10^8 \text{ m}^2$ ) as a function of temperature and precipitation changes in the Owens Valley and the resultant runoff as calculated using a Thornthwaite water balance model.

The large amplification observed in the response of the basin water balance model to changes in precipitation and temperature suggests that the water balance model yields a relationship between those parameters that is similar to that noted by Langbein [1949, 1962].

To compare these relationships, we produced a modified form of the Langbein curves by interpolating data

points from the plots presented by Mifflin and Wheat [1979], fitting a surface to them via multiple non-linear regression, and producing a modified form of the plot in terms of contours of runoff coefficient (Figure 3-18A). We then used the modern mean basin precipitation rate ( $\sim 33 \text{ cm}$ ) and mean annual temperature ( $\sim 6.5^\circ\text{C}$ ) for the Owens Valley to plot the runoff response of the Thornthwaite water balance model in terms of climatic means for the basin and runoff coefficient (Figure 3-18B). Comparison of those relationships (Figure 3-18) reveals a similar form, particularly at high precipitation rates. The contours diverge at lower precipitation rates, where the Langbein curves generally predict lower annual runoff. The Thornthwaite water balance model of the Owens Valley also exhibits much larger changes in sensitivity to both temperature and precipitation, with greatest precipitation sensitivity at low precipitation rates.

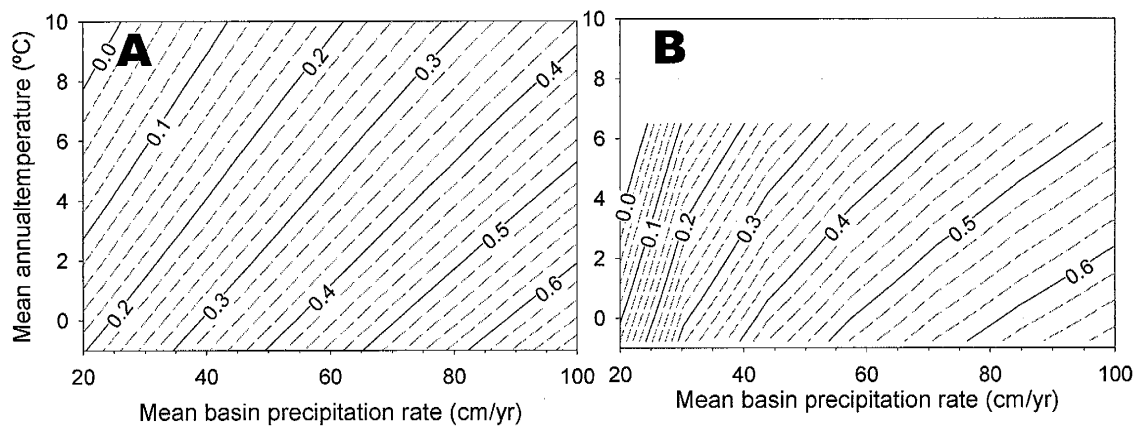


Figure 3-18. Contours of constant runoff coefficient, as a function of mean annual precipitation and temperature, from (A) the Langbein [1949, 1962] summary of runoff in the U.S. and (B) application of the Thornthwaite water balance model of the Owens Valley for a wide range of climatic conditions. Figure A was derived by multiple non-linear regression of data interpolated from the Mifflin and Wheat plot of the original Langbein [1949] curves.

#### ***SPATIALLY DISTRIBUTED APPLICATION OF THE LANGBEIN RELATIONSHIP***

The similarity of the water balance model results to the Langbein relationship suggested an alternative approach to predicting the changes in runoff that might accompany changes in temperature and precipitation. Assuming that the runoff response to climate change would mirror the precipitation-temperature-runoff (P-T- $\alpha$ ) relationship observed under modern climate, application of the Langbein relationship to the Owens Valley should provide a reasonable means of estimating its response to changes in temperature and precipitation. The Langbein relationship was derived from discharge data from basins across the U.S. In arid regions, usable records were concentrated in the headwaters of the larger streams because streamflow in the larger basins is typically altered by irrigation diversions [Langbein, 1949]. To the extent possible, runoff was also calculated for partial basin areas to “define areal variations in runoff more closely” [Langbein, 1949]. Accordingly we applied the Langbein relationship in a spatially distributed manner, treating each cell in the grid described in the previous section as a separate small drainage basin. We calculated runoff for each cell directly from its mean annual temperature and mean annual precipitation using a polynomial representation of the Langbein relationship. As with the Thornthwaite model, we found

that the model could not adequately describe the evapotranspiration in the riparian area of water that originated in the high mountains. We therefore used the riparian area evapotranspiration data from the Thornthwaite model results to incorporate this 'displaced evapotranspiration' in our spatially

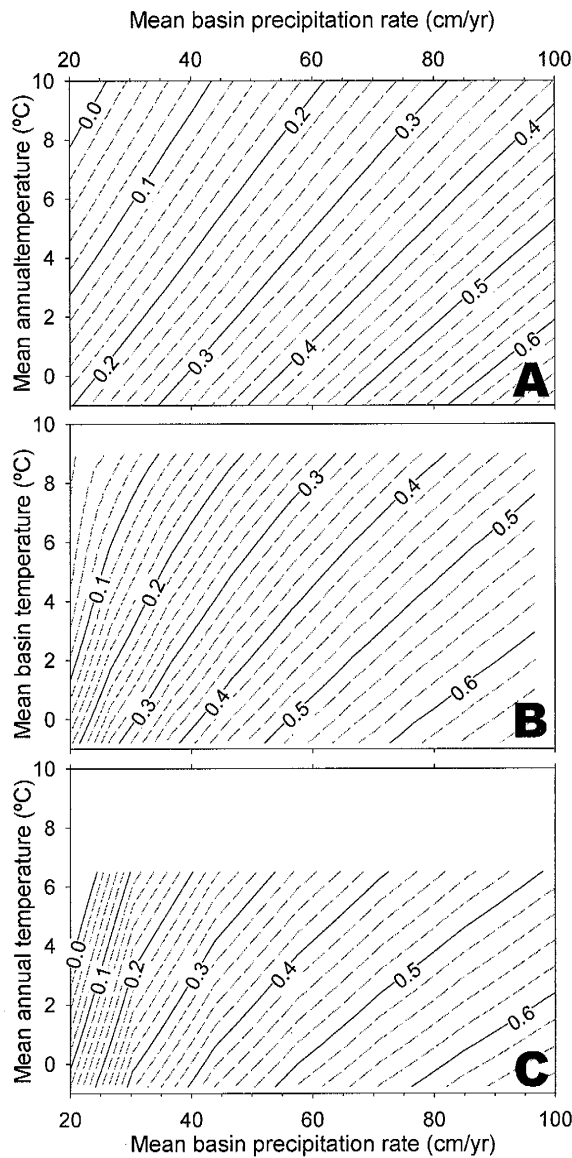


Figure 3-19. Comparison of the runoff coefficient contours generated from (A) the Langbein summary of runoff in the U.S., (B) results of a spatially distributed application of the Langbein precipitation-temperature-runoff relationship, and (C) the Thornthwaite water balance model of the Owens Valley.

distributed Langbein model. Direct calculation of the riparian area response in the Thornthwaite model requires integration of the spatially and temporally (monthly) distributed temperature data in the potential evapotranspiration calculation. We found that use of the mean annual average basin temperature produces the same result if that temperature is adjusted upward by two degrees, and used this simplified approach for the riparian area ET calculations.

Using the additional riparian area runoff and direct application of the Langbein relationships to the grid, we calculated basin-wide runoff for the Owens Valley for a range of climatic conditions to compare the climatic sensitivity using this approach to that using basin averages and also to that determined using the Thornthwaite water balance model (Figure 3-19). The spatially distributed application of

the Langbein P-T- $\alpha$  relationship, with inclusion of trunk stream riparian ET losses, produces a response surface (Figure 3-19B) with significantly more range in the relative sensitivity to temperature versus precipitation than the original Langbein curves (Figure 3-19A). In particular, the sensitivity of runoff to precipitation increases considerably with decreasing amount of precipitation. The difference between the two plots appears to be due to the non-linearity in the relationship between climate and runoff. As Langbein [1962] recognized, “a basin where half the area has 20 inches of precipitation and half, 5 inches, will produce more runoff than a basin where the precipitation is everywhere 12.5 inches.” He therefore recommended that allowances be made for this non-linearity when computing basin averages of temperature and precipitation for runoff estimation. Our distributed application of the Langbein relationship, in accordance with Langbein’s recommendation, simply reflects the non-linearity of the system better than the straight application of basin-wide averages.

The response surface calculated from the spatially distributed application of the Langbein relationship is remarkably similar to that of the Thornthwaite water balance approach (Figure 3-19C), which is calculated on the same grid, using the same precipitation and temperature functions, but is based on a simple physical, rather than empirical, model of the basin water balance. Part of the similarity can, of course, be attributed to the fact that the same trunk-stream riparian ET function was included in each model. Nonetheless, that does not affect the supply of water to the riparian area and the close match in the climatic sensitivity of the two models, with only that common feature, suggests that the P-T- $\alpha$  relationship summarized in the oft-referenced Langbein curves reflects a relatively simple relationship between potential evapotranspiration and climate.

#### ***SUMMARY***

Prediction of the changes in the water balance in response to changes in climate is at best highly

uncertain. A distressingly large number of factors potentially play a large role in the adaptation of a given basin to climatic change and incorporation of all such factors would be a daunting task. Rather than try to include all such factors here, we have instead assumed a relatively simple relationship between the two primary controls on the overall water balance – the supply of moisture from the atmosphere and the availability of energy with which to return that moisture to the atmosphere. We describe that relationship using a distributed-parameter Thornthwaite-type water balance model of the Owens Valley. The model is based primarily on estimates of soil moisture storage and potential evapotranspiration and is independent of stream distribution, vegetation type, and distribution and other effects on basin water balance. In that sense, it implies, for example, that vegetation communities are completely opportunistic and can adapt, by shifting distribution, vegetation type, or simply altering water uptake, to make the best possible use of the available moisture and energy. Flaschka *et al.* [1987] considered that their Thornthwaite water balance approach was more reliable for moderate climate change scenarios than those for more extreme climate change. In contrast, based on comparisons with the precipitation-temperature-runoff relationship observed among modern basins, we argue that the Thornthwaite model provides a very reasonable means of estimating runoff response to extreme climate change.



---

## CHAPTER 4 - GLACIAL CHRONOLOGY

---

As a record of changes in the extent of the glaciers in the Owens Valley we use a chronology of advances that we developed for Bishop Creek. Located at the north end of the Owens Valley, Bishop Creek is one of the largest tributaries draining the eastern side of the Sierra Nevada (Figure 4-1). The area of the Bishop Creek watershed above Coyote Creek is approximately 190 km<sup>2</sup>, and elevations in the basin range from ~1700 m, at the confluence with Coyote Creek, to ~4000 m, at locations along the crest. The main tributaries of the creek are its North, South and Middle Forks. Glaciers flowing out of each of these valleys joined together during glacial times to produce a glacier that extended as much as 28 km from the modern cirque glaciers in Middle Fork. We also developed glacial chronologies for two nearby, but considerably smaller, drainages - Horton Creek and McGee Creek - in order to compare the climatic response of glaciers of varying size. Glacial advances during the last glacial maximum (LGM) extended about 8 km and 6 km, respectively, from the modern cirque glaciers in those drainages.

### COSMOGENIC CHRONOLOGY

To refine the existing chronology of glacial advances in the eastern Sierra Nevada we determined exposure ages of a variety of glacial features via the in-situ accumulation of cosmogenic <sup>36</sup>Cl. Extensive Tioga- and Tahoe-age moraine complexes exist in Bishop Creek, Horton Creek and McGee Creek [Phillips *et al.*, 1996]. The larger examples of these moraines are easily seen in aerial photographs (Figure 4-2 through Figure 4-4) while the more diminutive moraines may only be readily identified in the field. In this paper we focus on the behavior of the lakes and glaciers in the Owens Valley during the last deglaciation. We therefore primarily consider moraines developed during the several stages (I-IV) of the Tioga period [Phillips *et al.*, 1996] and the Recess Peak advance at approximately 13 ka [Clark and Gillespie, 1997]. Snowline lowering throughout the Sierra Nevada

during the Tioga maximum has previously been estimated as approximately 800 m [Burbank, 1991], while Clark and Gillespie [1997] recently presented evidence indicating that the Recess Peak advance resulted from a regional snowline depression of approximately 200 m.

#### ***SAMPLING***

To obtain rock samples for  $^{36}\text{Cl}$  exposure age determinations, we chiseled one- to five-cm thick fragments from the upper side of large, stable moraine boulders; glacial erratics; and polished bedrock surfaces. We sampled and analyzed 56 surfaces from Tioga II and later advances in the Bishop Creek drainage (Figure 4-5), 65 from McGee Creek and 24 from Horton Creek (Figure 4-6). Working from a relatively well-established chronology of the earlier stage Tioga advances, we generally sought to date later advances of the Tioga glaciation, the rate of retreat following the last Tioga advance and the timing and position of apparent Recess Peak deposits in those basins.

#### ***PROCESSING AND ANALYSIS***

We processed the rock samples using the method described in Appendix B. The procedure includes substantial modifications to those that have become standard practice for preparation of samples for  $^{36}\text{Cl}$  analysis by accelerator mass spectrometry (AMS). In general, the process involves dissolving approximately 50 – 100 grams of rock in a concentrated solution of hydrofluoric and nitric acid. After the dissolution stage is complete, barium nitrate is added to precipitate barium sulfate from the solution. Sulfur is an isobar of chlorine-36 and interferes with its measurement so we incorporate a number of steps to reduce sulfur levels. After allowing time for the precipitation of barium sulfate, the supernatant is separated from the residual solid material and silver nitrate is added to precipitate the rock chloride as silver chloride. The silver chloride precipitate is then purified via a sequence of dissolution and resolution steps in which barium is again added to the samples to precipitate sulfur as barium sulfate. Measurement of the  $^{36}\text{Cl}:\text{Cl}$  ratio is made via AMS and samples

for this study were analyzed at the Purdue Radioisotope Measurement (PRIME) laboratory at Purdue University, Purdue, Indiana.

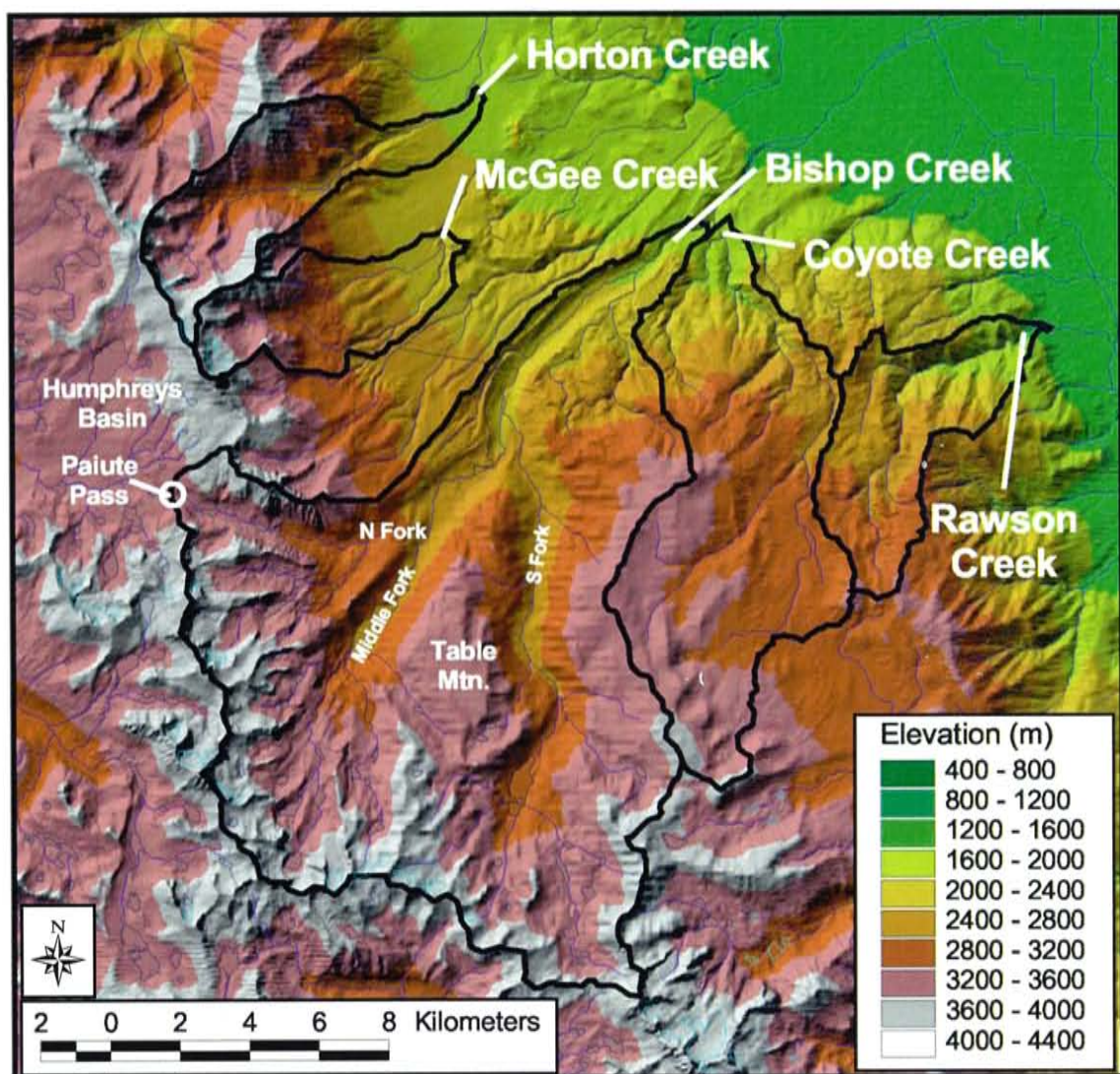


Figure 4-1. Map of Bishop Creek and the surrounding area showing locations of other creeks and drainage basins referenced in the text. Digital elevation data is from USGS 7.5-min STDs DEMs. The striping apparent in portions of the surface is an artifact of errors in the USGS digitization that have since been corrected.





*Figure 4-2. Oblique aerial photo of Bishop Creek terminal moraine complex showing several Tahoe and Tioga lateral and terminal moraines.*





Figure 4-3. Oblique aerial photo of Horton Creek showing several Tahoe- and Tioga-stade moraines.

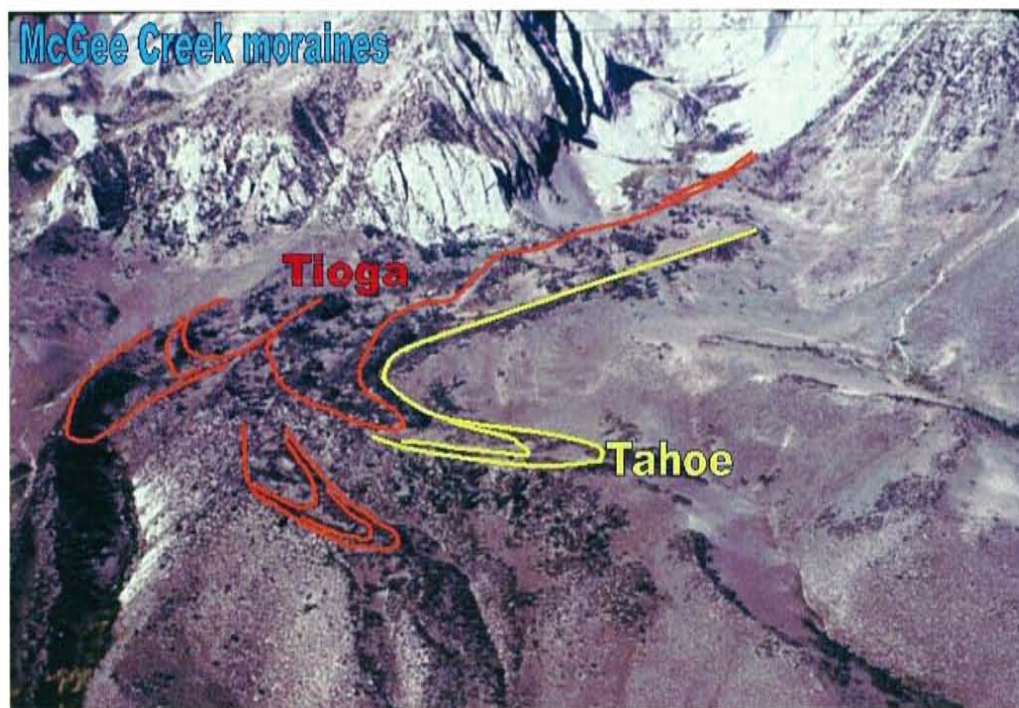


Figure 4-4 Oblique aerial photo of the moraines below McGee Creek with Tioga and Tahoe moraines indicated.

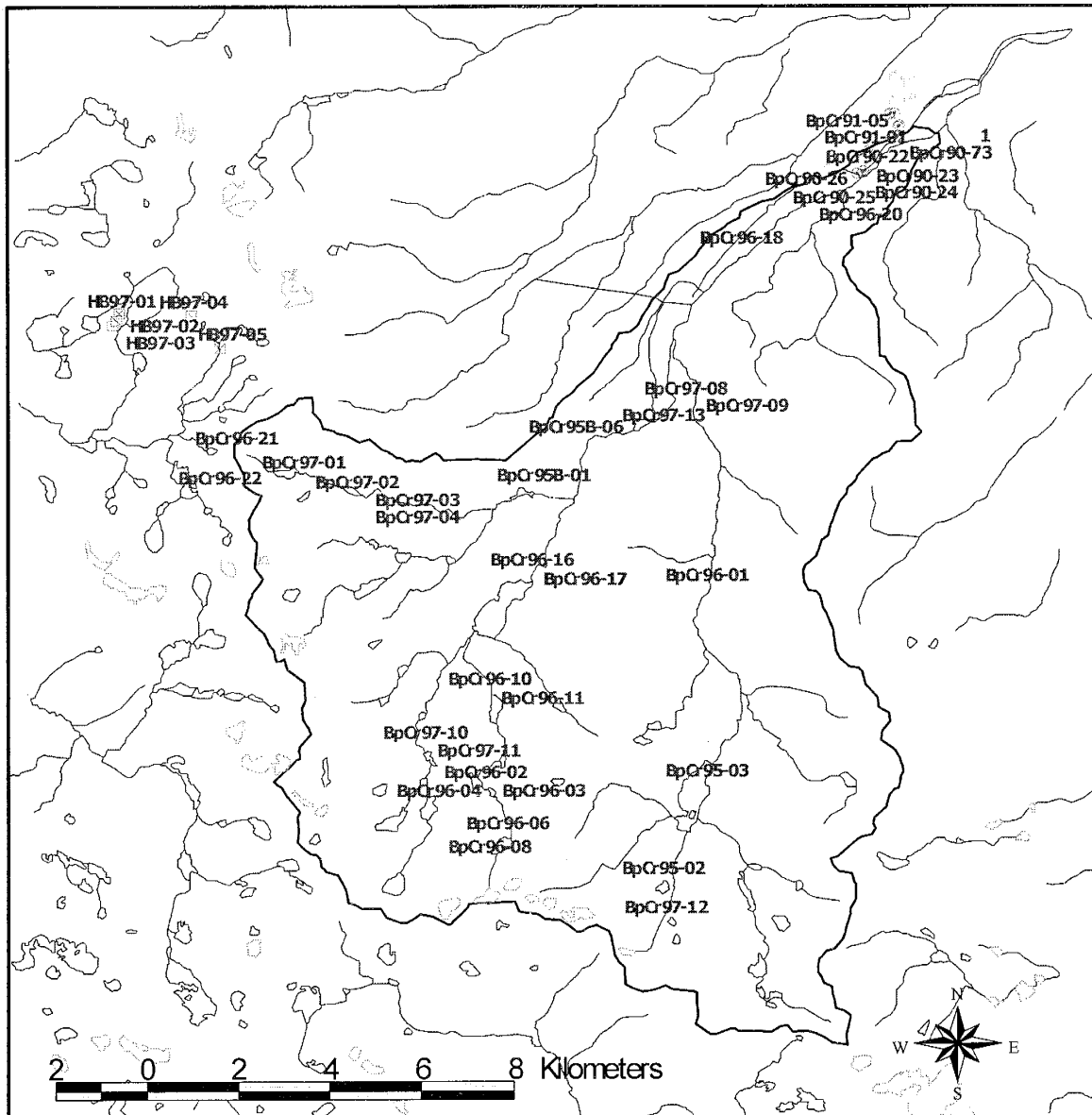


Figure 4-5. Locations of moraine boulders, polished or striated bedrock, and erratics sampled and analyzed in the Bishop Creek basin and in Humphreys Basin.

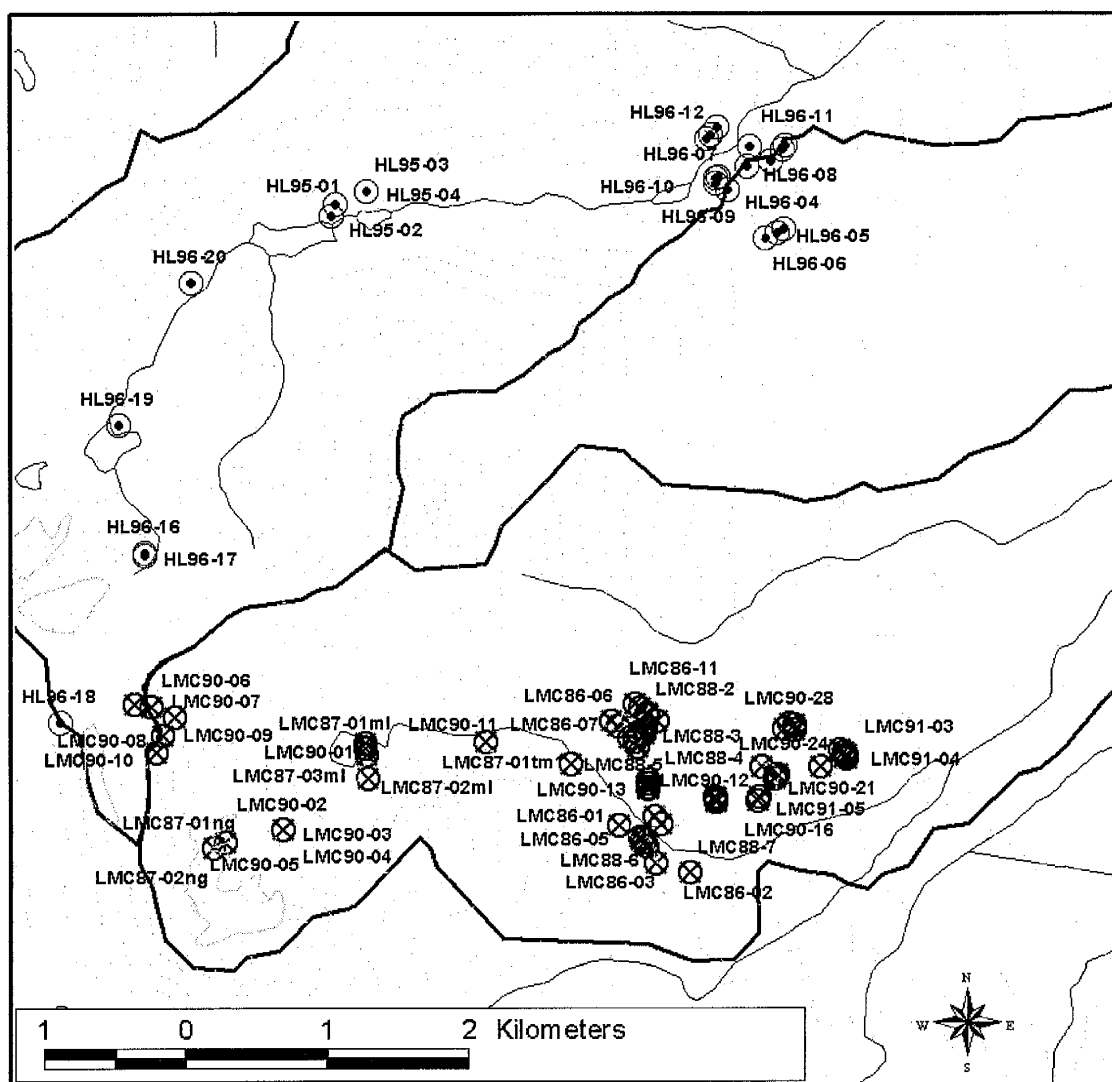


Figure 4-6. Locations of moraine boulders, polished or striated bedrock, and erratics sampled and analyzed in the Horton Creek (HL-series, circles) and McGee Creek (LMC-series, crossed circles) basins. Contour interval is 100 meters.

One of the difficulties in obtaining precise cosmogenic ages via chlorine-36 analysis of rock samples is accurate determination of the rock-chloride concentration. Until recently we measured chloride concentrations in rock samples by dissolving a small amount of rock in hydrofluoric and nitric acid in a specially designed teflon diffusion cell and measuring the chloride concentration in the

cell with an ion selective electrode. The primary drawback of that method is low precision at low chloride concentration. To increase precision of our chloride concentration measurements for this study, we used isotope dilution mass spectrometry (IDMS). This involves adding an aliquot of virtually pure  $^{35}\text{Cl}$  to each sample during the rock dissolution step. The ratio of  $^{35}\text{Cl}$  to  $^{37}\text{Cl}$  is relatively constant in natural samples and this ratio is routinely calculated during the accelerator mass spectrometry measurement of the  $^{36}\text{Cl}$ : $^{35}\text{Cl}$  ratio. The added  $^{35}\text{Cl}$  alters the natural  $^{35}\text{Cl}$ : $^{37}\text{Cl}$  ratio by an amount indicative of the amount of chlorine in the sample. The IDMS approach thus provides a means of measuring Cl concentration as well as  $^{36}\text{Cl}$ :Cl ratio. The accuracy of the Cl determination is primarily limited by the uncertainties associated with the measurement of the  $^{35}\text{Cl}$ : $^{37}\text{Cl}$  ratio and its natural variability.

Accurate calculation of chlorine-36 cosmogenic exposure ages requires that a large number of parameters be measured or otherwise accounted for during sampling, sample preparation, and analysis. These include the chemical composition of the rock, including major, minor, and trace elements, which controls absorption and diffusion of thermal neutrons; latitude and longitude, which affect the influx of cosmic rays; and a host of geometric, topographic and meteorological details of the sample and sample site, which affect shielding of the sample from cosmic ray exposure. In addition, chlorine-36 is produced by thermal neutron absorption as well as neutron spallation reactions, and production is strongly influenced by the erosion rate of the overlying material, which is generally unknown. Calculation of exposure age thus involves solution of a non-linear equation for any assumed erosion rate. To simplify the entry of sample data, facilitate calculation of exposure ages and save the relevant data in a convenient and accessible format, we developed the Microsoft Excel spreadsheet-based program CHLOE [Phillips and Plummer, 1996] using a combination of built-in mathematical functions and custom functions programmed in Microsoft's Visual Basic for Applications. The program includes a number of routines designed to facilitate calculations for a



variety of geomorphic problems, including automatic calculation of exposure ages for a prescribed range of erosion rates, predicted  $^{36}\text{Cl}$  ratio as a function of age, combined analysis of  $^{36}\text{Cl}$  and a separate spallogenic cosmogenic nuclide, and calculation of depth-profiles of  $^{36}\text{Cl}$  production and estimation of erosion parameters via curve-fitting to measured profile concentrations. Derivation of the equations employed in CHLOE is described in Gosse and Phillips [2001]. The program is freely available from the authors, is readily adapted to include additional features, and is relatively widely used in the terrestrial cosmogenic nuclide dating community.

## ***RESULTS***

Chlorine-36 exposure ages determined during this study, and during our previous work in the Bishop Creek area, are summarized here in separate figures for Bishop Creek, Horton Creek, and McGee Creek. Tabulated data and more detailed analysis and discussion of the  $^{36}\text{Cl}$  data and field mapping will be included in a separate, companion study devoted to the glacial chronology itself. The information is summarized here primarily to lay the groundwork for the combined analysis of the glacial and lacustrine chronologies of the Owens Valley that is the focus of this study.

The ages reported here, which are best estimates of calendar age, should be considered ' $^{36}\text{Cl}$  exposure ages,' in that they involve production parameters and assumptions specific to in-situ  $^{36}\text{Cl}$  production that evolve over time, as new data become available. The calculation of chlorine-36 exposure ages involves a large number of parameters and, therefore, a large number of uncertainties. In summarizing the calculated ages here, we show only the standard deviation in the AMS measurement of the chlorine-36 ratio. We estimate that systematic errors in the primary  $^{36}\text{Cl}$  production rates (via thermal neutron activation of  $^{35}\text{Cl}$ , and spallation of K and Ca) lead to a 10% uncertainty in calculated ages. Random errors in the measurements of chemical composition, in the determination of shielding factors, and in the equations describing the production mechanisms are

believed to be relatively small compared to the uncertainties associated with the exposure histories of the samples. We attempt to account for the latter by sampling surfaces that appear to have been stable for a long time and by obtaining numerous samples from each morphostratigraphic unit to be dated. In estimating ages from several samples, we place more weight on the older ages, as erosion tends to produce a young-skewed distribution of ages [Zreda *et al.*, 1995].

One source of uncertainty in the determination of exposure ages is the amount of  $^{36}\text{Cl}$  that may have accumulated in a sample via exposure prior to the glacial period that led to its reestablishment as a glacial deposit. Subsequent accumulation of  $^{36}\text{Cl}$  is simply added to this ‘inherited’  $^{36}\text{Cl}$ , thereby yielding erroneously old ages when the prior exposure is significant. To provide a rough indication of the potential inheritance that may exist in the boulders we sampled for this study, we analyzed a sample from a large angular boulder near the terminus of a small rock glacier above Sunset Lake in the Sabrina basin below Mount Thompson. The calculated age for that sample is  $\sim 4,000$  years. If we assume that that boulder was actually plucked from the bedrock and deposited during the last century, then the inheritance might be assumed to contribute on the order of 4000 years or more to a moraine boulder. Given the boulder’s present position, well below the existing glacier, this is unlikely. On the other hand, it is possible that the rock was deposited at its present location  $\sim 4,000$  years ago and that its inheritance is effectively nil. The latter hypothesis is supported by work of Konrad and Clark [1998], who argued that the neoglacial period in the Sierra Nevada began  $\sim 3,000$  to 4,000 years ago. While the truth is likely somewhere between these two extremes, we believe that the inheritance problem is minor for the glacial advances considered in this study for two reasons. First, erosion and plucking rates were likely much greater during the periods when the glaciers extended to several kilometers beyond their present limits. This would tend to minimize inheritance, particularly for the more severe climate of the most extensive glacial advances. Second, one would expect that the degree of inheritance is highly variable, depending on whether the rock is removed by glacial plucking, frost

action on cliffs above the glaciers or some other means. Thus, if inheritance ranges from nearly nil to as much as several thousand years, we would expect that boulders from the moraines we sampled would display a minimum age range of at least a couple of thousand years. Variability in calculated moraine ages has continually declined, however, as sample processing and analytical methods have improved. The standard deviation of ages for the most recently dated features in Bishop Creek and Horton Creek (Figure 4-7) is, for all practical purposes, the same as the average uncertainty of the AMS measurements from which they are derived [Plummer and Phillips, 1999]. We conclude that inheritance is a minor problem in the development of a chronology of glacial advances in the eastern Sierra.

While we believe that inheritance in glacial moraine boulders is insignificant for the samples considered in this study, the question of inheritance is an interesting one, warranting further study. Sampling of boulders from active moraines below a variety of modern glaciers would provide a means of more carefully assessing the inheritance issue and of learning more about the erosive power of glaciers of different sizes and types.

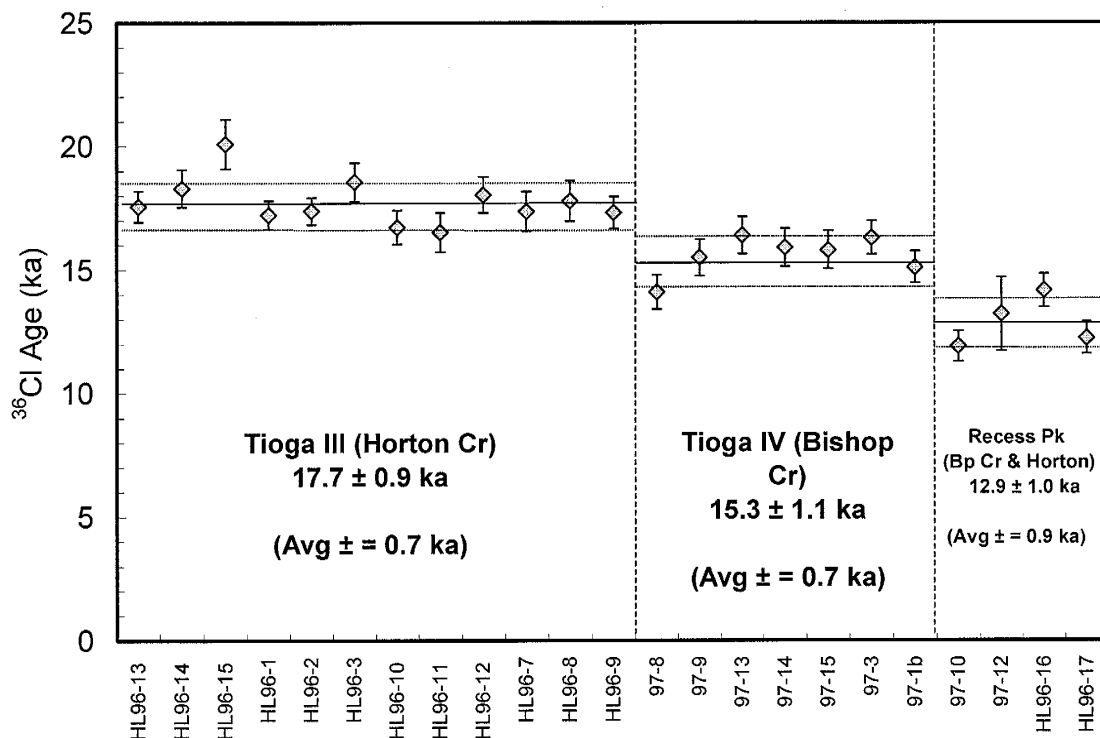


Figure 4-7. Ages from the most recently dated features in Bishop Creek and Horton Creek. Uncertainties shown are the standard deviation of the AMS analysis.

#### BISHOP CREEK

Figure 4-8 summarizes the ages of the sampled surfaces from Bishop Creek. There are three distinct sets of moraines among the four Tioga-age advances mapped by Phillips *et al.* [1996]. The oldest of these, at an elevation of  $\sim 1860$  m are the uppermost terminal loops in the Sand Canyon drainage, the glacier having taken the same path laid down by the numerous older advances of Tahoe, and pre-Tahoe, age. These moraines, designated Tioga I, have exposure ages ranging from about 16 to 28 ka, with an apparent upper limit of about 28 ka. Using the average of the four oldest ages from these samples, we assign an age of about 27 ka to these moraines. There appears to have been a period of intermittent glacial expansion and retreat before the next recorded advance because the next younger moraines are right and left lateral moraines pasted along the sides of Bishop Creek, which cuts directly through the right lateral of the Sand Canyon moraines, and a poorly developed set of

terminal loops near the confluence with Coyote Creek. These are the Tioga II moraines that represent the last glacial maximum. This change in the path of Bishop Creek is a dramatic one; the elevation of the glacier snout in the new location near the confluence of Coyote and Bishop Creeks would have been approximately 1700 meters. Under its previous path and gradient in Sand Canyon, the snout would have been at least 100 meters higher. Evidence of the Tioga III glaciation is primarily morainal debris pasted along the lower banks of Bishop Creek below the Tioga II crests. From their position relative to the Tioga II moraine ridges, we deduce that the terminal position during Tioga stage III would have been at an elevation of approximately 1830 m. From the average of all but two anomalously young samples in this group, we assign an age of  $\sim 18$  ka to the Tioga III moraines. Upstream of the confluence of Bishop and Coyote Creeks, and below the confluence of the Middle and South Forks, there are several small terminal moraines that cut across the valley floor. A sample from a boulder about 1 km upstream of the Bishop Creek powerhouse (BpCr96-20) and another from a very large boulder just below Dutch Johns meadow (BpCr96-18) yielded ages of  $\sim 19$  ka and  $\sim 16$  ka, respectively. The youngest moraines in the Tioga sequence are the large and prominent moraines at the confluence of the Middle and South Forks. Evidence of a terminus there is preserved in descending left and right lateral moraines below the confluence. Of five samples collected from these moraines, four yield exposure ages between 15 and 16 ka and the other is only slightly younger, at  $\sim 13.5$  ka. We therefore assign an age of 15-16 ka to the Tioga IV moraines in Bishop Creek. Apparent correlative moraines in the South Fork are not as clearly defined as those below the confluence, and it appears that the South Fork glacier terminus was at least 1 to 2 km upstream of the confluence at that time.

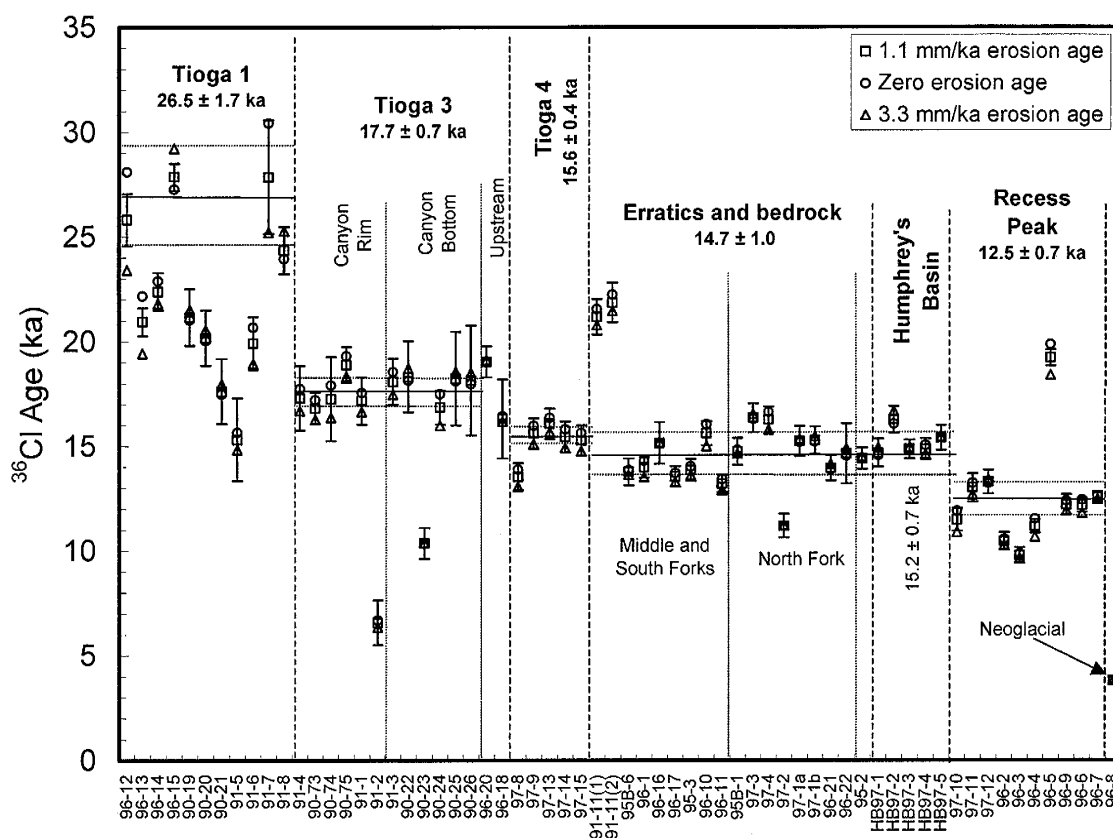
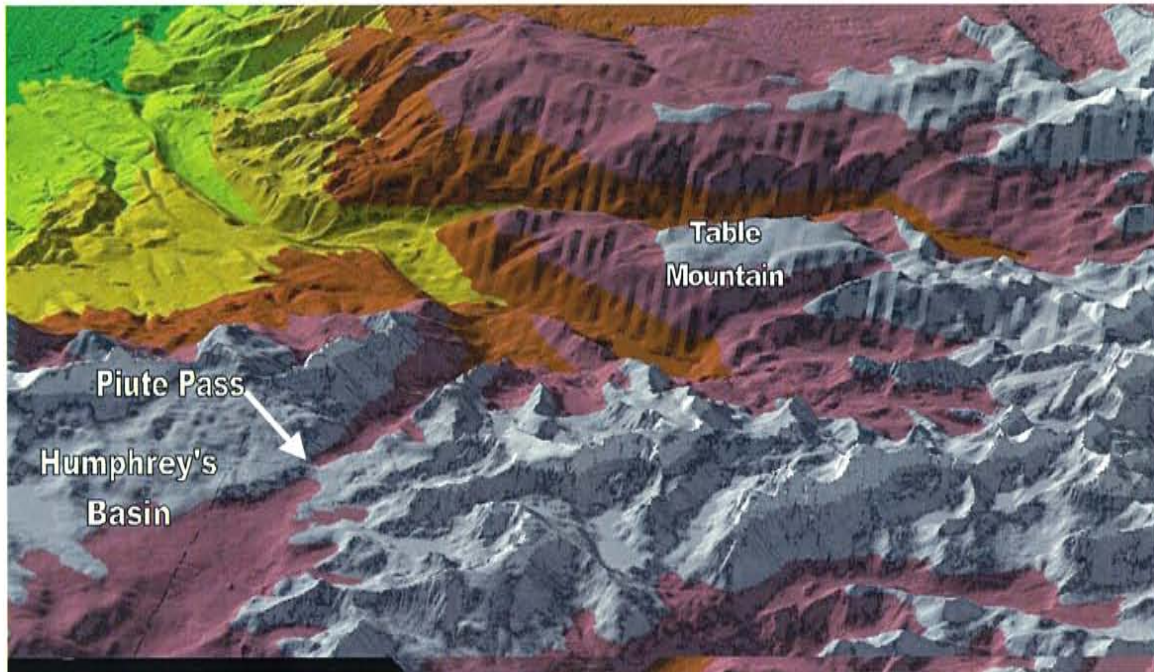


Figure 4-8. Summary of  $^{36}\text{Cl}$  ages of samples from the Bishop Creek basin. Different symbols represent ages assuming different erosion rates. Groupings indicate locations of the sampled moraines and deposit types. Age ranges are our estimates of uncertainty based on the range and spread of ages associated with each deposit. Error bars give the one sigma standard deviation in age given by the uncertainty in the AMS measurement.

The next younger terminal positions in Bishop Creek that can be readily identified from either field or aerial-photo mapping are Recess Peak moraines such as those that Clark and Gillespie [1997] dated at Baboon Lakes in the Middle Fork. We collected 10 samples to date the apparent Recess Peak moraines at Baboon Lakes and Topsy Turvy Lake, in the upper reaches of the S. Fork and from the Treasure Lakes above South Lake. Three of these were samples of polished bedrock or erratics just above or below the moraines. The remaining samples were obtained from boulders on the moraines themselves. One of the samples, BpCr96-5, had an anomalously old exposure age. The remaining nine exposure ages ranged from ~10 to 13 ka, with a mean of about 12 ka. This agrees well with the minimum limiting age of ~13 ka determined by Clark and Gillespie [1997] from

radiocarbon dates on basal sediments retrieved from cores from lakes dammed by Recess Peak moraines. Clark and Gillespie's regional mapping of Recess Peak and Matthes deposits indicates that there was no regional glacier advance more extensive than the Matthes in the Sierra Nevada after the Recess Peak advance. The Matthes moraines in Bishop Creek evidence glaciation only slightly more extensive than that which exists today. Clark indicates that the Matthes advance represents a regional lowering of equilibrium line altitude of approximately 100 m, while the Recess Peak advance represents a lowering of approximately 200 m.

There is virtually no evidence of a significant glacial advance between the Tioga IV moraines and the Recess Peak moraines several kilometers upstream. In fact, it appears that very little till of any kind was deposited between those two advances. The bedrock basins above Sabrina and South Lakes are, for example, surprisingly barren of glacial deposits, with only a light scattering of erratics to remind the viewer of the hand that carved and smoothed the exposed bedrock surfaces. This lack of glacial debris suggests that the glaciers retreated quite rapidly from their Tioga IV position at the confluence of the South and Middle Forks. To better gauge that rate of retreat, we collected approximately 18 samples from erratics and polished or striated bedrock located between those two deposits in all three forks of Bishop Creek. With only three exceptions, these samples yielded exposure ages between approximately 13 and 16 ka. The mean age of those samples is about 15 ka and the similarity of these ages to those of the Tioga IV moraines again suggests that the glaciers retreated rapidly following this last Tioga advance.



*Figure 4-9. Three-dimensional view looking eastward across Humphreys basin through Piute Pass into North Fork, Bishop Creek.*

The head of the North Fork of Bishop Creek displays morphology quite distinct from that of the upper Middle and South Fork. The bedrock at and above Piute Pass, which sits on the crest of the range between the N. Fork of Bishop Creek and Humphreys Basin, is distinctly rounded and P-forms are clearly evident both at the pass itself and above and below it. Clearly, glaciers have overridden the pass at some time in the past and the direction of that flow is preserved in crescentic fractures on both sides of the pass. Those fractures clearly demonstrate that the glacier at one time flowed from lower elevations in Humphreys basin up and over the pass into Bishop Creek. This area therefore represents a potential source of error in the estimation of snow accumulation area here. To determine the approximate contribution of this 'extra-basin' ice, we delineated the flow pattern of the glaciers when they flowed across the divide (Figure 4-9) by mapping the glacial striae, crescentic fractures and P-forms in the area. We also dated a glacial erratic and polished bedrock from Piute Pass to estimate how long the pass has been ice-free. These ages indicate that glaciers have not flowed across the crest since about 14 ka. A map of the paleo-ice-flow indicators in the area around



Piute Pass (Figure 4-10) clearly indicates a line of divergent flow roughly parallel to the crest and extending through Summit Lake on the west side of Piute Pass.

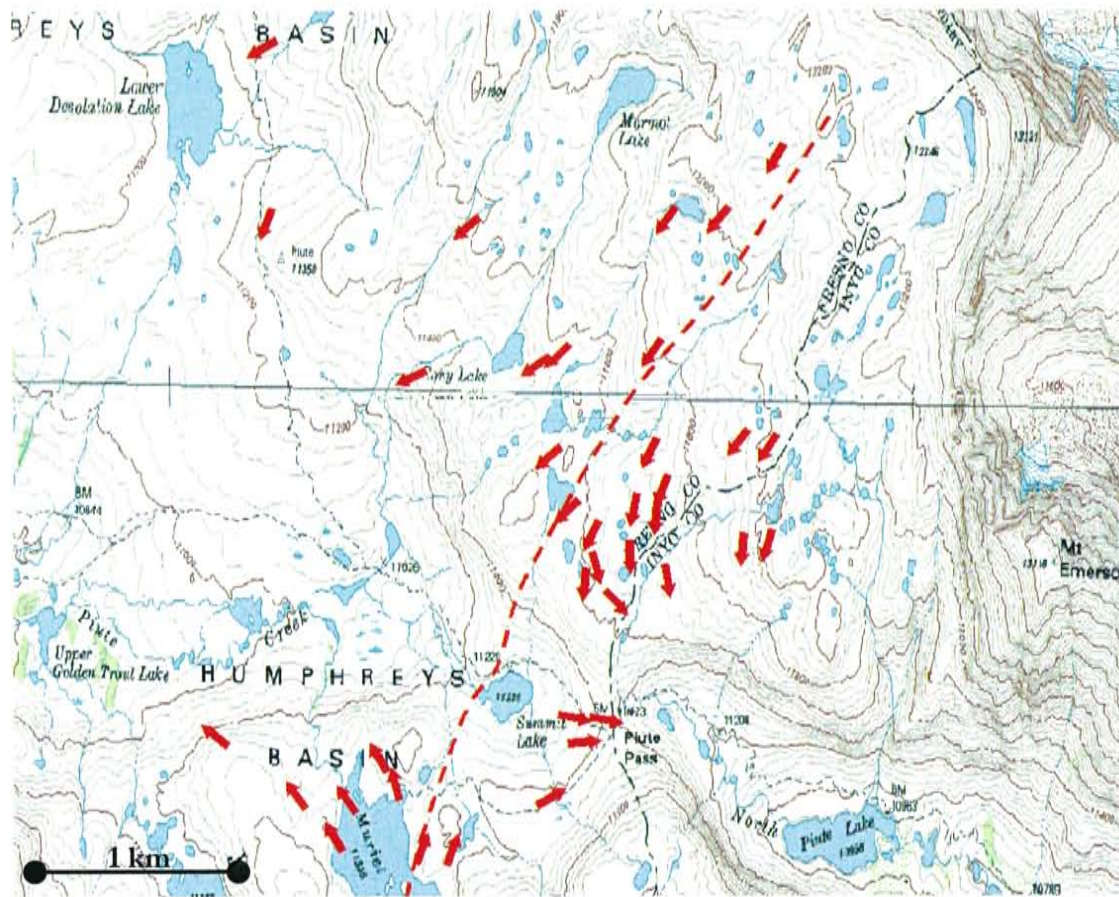


Figure 4-10. Map of paleo iceflow indicators above Piute Pass at the head of the north fork of Bishop Creek. Dashed line shows inferred location of the ice divide during the last glacial maximum.

As recession of the glaciers from the North Fork included retreat across Piute Pass into upper Humphreys Basin, our sampling of glacial deposits there included erratics and bedrock surfaces from Piute Pass and Humphreys Basin. These included three samples of a moraine located just west of the outlet of Desolation Lake and two erratics from locations closer to the crest. Examining these samples separately, we see that the exposure ages display a tight grouping between about 15 and 16 ka with a mean of approximately 15 ka. Again, this supports the argument that the glaciers receded rapidly following some tempering of the climate after 15 ka.

## HORTON CREEK

A complicated history of glacial advances is preserved in a virtual mountain of morainal deposited at the mouth of Horton Creek. Many of these appear to record Tahoe or earlier advances and, as at Bishop Creek, the glacier snout at the front of the mountain range appears to have dramatically altered its position several times. Most recently the glaciers seem to have followed the modern path of Horton Creek, though the lowest terminus position is not readily apparent within the canyon. From suggestions of descending lateral positions on the northern canyon wall we surmise that the Tioga maximum glaciation, stage II, might have advanced to a low elevation of ~2200 meters. We have not, however, obtained exposure ages to confirm or refute this conclusion.

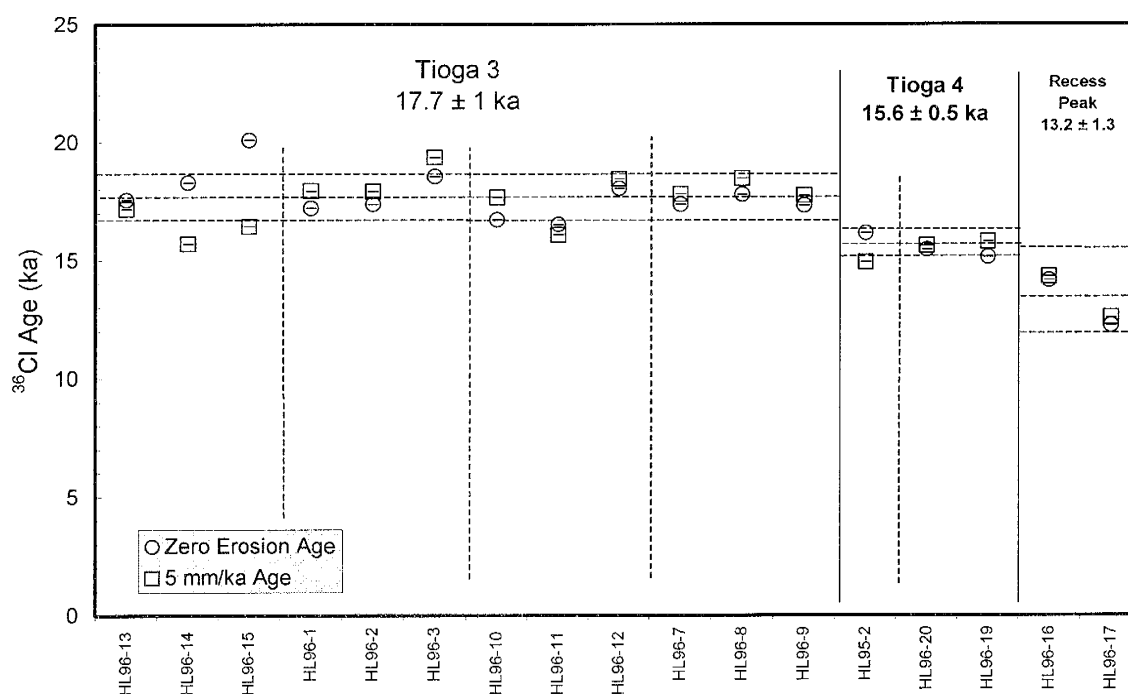


Figure 4-11 Summary of  $^{36}\text{Cl}$  ages of samples from the Horton Creek basin. Different symbols represent ages assuming different erosion rates. Groupings indicate locations of the sampled moraines and deposit types. Age ranges are our estimates of uncertainty based on the range and spread of ages associated with each deposit. Error bars show 1-sigma standard deviation in age due only to the uncertainty in the AMS measurements.

As at Bishop Creek, a sequence of terminal moraines appears to have been deposited in Horton

Creek during Tioga stage III. In Horton Creek these moraines have filled a significant portion of the canyon at the mountain front so that there is now a sharp steepening of the stream gradient below it. On the southern side of the canyon an apparent left and right lateral moraine pair evidences an advance that took a path that diverges dramatically from the modern stream path. Three samples on these moraines gave ages of 47, 73, and 86 ka, indicating that they represent a pre-Tioga advance. A number of apparent Tioga-age moraines are located just below the Horton Creek meadow, between about 2600 and 2700 m elevation. Our 15 exposure ages from samples on these moraines display a remarkably tight grouping in the range of 17 to 18 ka, with an average of about 18 ka. This is also consistent with the ages obtained from Tioga III moraines in Bishop Creek which also averaged ~18 ka. The moraine of Tioga-stage scale and appearance that is furthest upstream is located at the outlet of Horton Lake. Four samples obtained from that moraine indicate that it was deposited by the Tioga IV advance, at ~15 ka. Likely sites for Recess Peak age moraines in upper Horton Creek drainage were obscured by large amounts of talus. The only indication of a possible Recess Peak advance was a low and unobtrusive moraine above the upper of the Upper Horton Lakes. We collected only two samples from that deposit. The ages, ~13 and ~14 ka, suggest that it very likely represents the Recess Peak advance in Horton Creek. Dates from one bedrock sample above Horton Lake and another from just below lower Upper Horton Lake were both ~15 ka. As in Bishop Creek, we conclude that retreat following the Tioga IV advance was relatively rapid.

#### *MCGEE CREEK*

The stratigraphy and  $^{36}\text{Cl}$  dates on the moraines in that basin are summarized in Phillips *et al.* [1996]. We include a summary plot of the  $^{36}\text{Cl}$  ages only for ease of comparison with the new data from Bishop and Horton Creeks. Most of the exposure ages were obtained using less sophisticated processing techniques than we currently use and the ages consequently display more scatter than our more recent dates from the other basins.

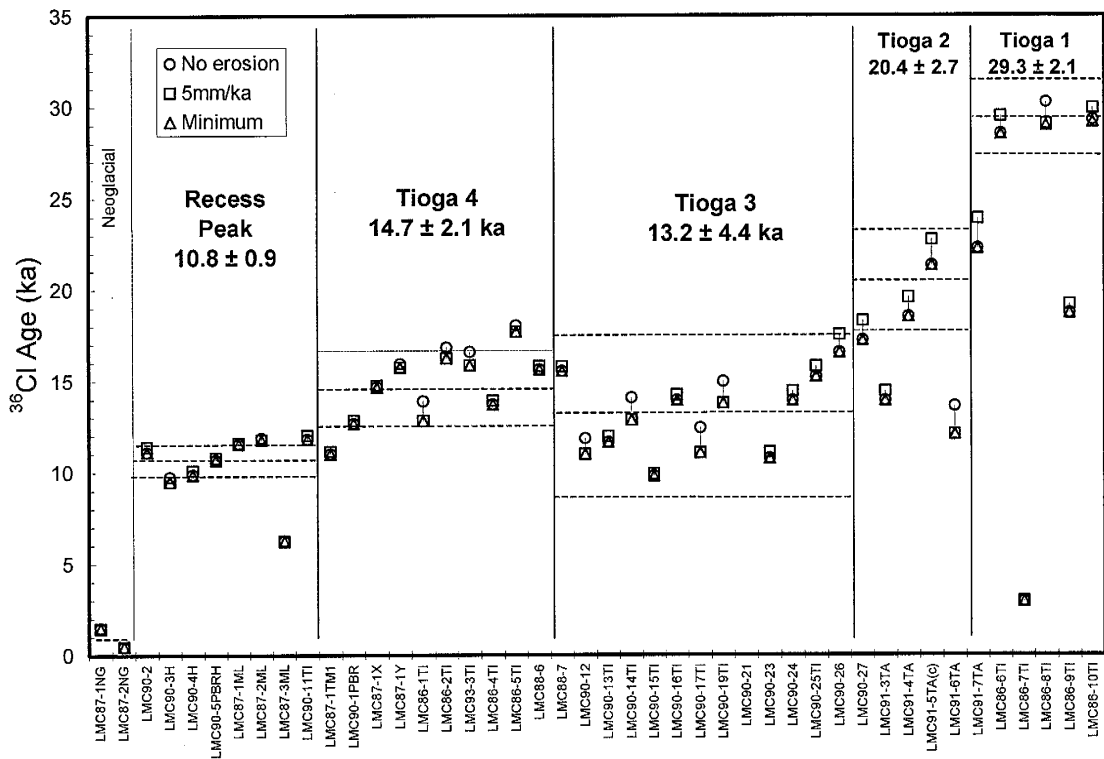


Figure 4-12. Summary of  $^{36}\text{Cl}$  ages of samples from the McGee Creek. Different symbols represent ages assuming different erosion rates. Groupings indicate locations of the sampled moraines and deposit types. Age ranges are our estimates of uncertainty based on the range and spread of ages associated with each deposit. Error bars give the one sigma standard deviation in age given by the uncertainty in the AMS measurement.

The record of glaciation in McGee Creek is displayed in a complex set of interconnected terminal loops, lateral moraines, and apparent ramps that demonstrates, even more than in the other basins, a complicated history of dramatic shifts in the path of the advancing glaciers. Pre-Tioga advances in McGee Creek actually flowed out, and to the northeast, of the modern McGee Creek drainage. Moraines developed during glacial retreat from that passage apparently blocked that path from further use and the Tioga maximum advances took a different course, about halfway between the modern McGee Creek and that of the Pre-Tioga advances. Morphostratigraphic evidence suggests that the Tioga III advance then returned to the path of the pre-Tioga advances and only the Tioga IV moraines appear to have been confined to the path of the modern McGee Creek. The most consistent set of dates from a moraine in McGee Creek are those considered to represent the Recess

Peak advance. These samples, from moraines located near Longley Lake, yield exposure ages of approximately 11 ka.

#### *BIG PINE CREEK*

Sampling of a large blocky moraine field in Big Pine Creek just above Third Lake provided three ages between 13 and 15 ka. This suggests that these deposits, which appear to have been developed either by slow retreat of a small glacier or as an ice-cored rock glacier, represent Recess Peak deposition in Big Pine Creek.

#### *TERMINUS POSITION CHRONOLOGY*

Glacial chronologies are typically summarized in terms of changes in ELAs, as estimated using an assumed accumulation area ratio<sup>6</sup> (AAR) of ~0.65 and an assumed glacier shape. The actual evidence defines, at best, the glacier's terminal position. To minimize interpretation in presentation of the raw chronological data, we have arbitrarily chosen to use terminus position elevation as an index of glacial extent. Changes in terminus position elevation for the Tioga-II, -III, -IV and Recess Peak advances in Bishop, Horton and McGee Creeks are compared to estimated modern terminus positions in Table 4-1 and Figure 4-13. In Figure 4-13, these terminal positions are plotted against distance along an arbitrary flowline adjacent to the terminal positions and beginning at the elevation of termini of the modern cirque glaciers. The mostly linear relationship between terminus elevation and glacier length indicates that they are effectively equivalent measures of glacial extent.

---

<sup>6</sup> The 'accumulation area ratio,' or AAR, of a glacier is the fraction of the area of the glacier over which there is net annual accumulation.

	<b>Bishop Creek</b>	<b>Horton Creek</b>	<b>McGee Creek</b>
<b>Tioga I</b>	1860 $\pm$ 15	-	2804 $\pm$ 25
<b>Tioga II</b>	1700 $\pm$ 30	2200 $\pm$ 100	2620 $\pm$ 30
<b>Tioga III</b>	1830 $\pm$ 60	2560 $\pm$ 50	2830 $\pm$ 30
<b>Tioga IV</b>	2200 $\pm$ 30	2850 $\pm$ 140	2895 $\pm$ 30
<b>Recess Peak</b>	3290 $\pm$ 30	3410 $\pm$ 90	3260 $\pm$ 20
<b>Modern</b>	3630 $\pm$ 15	3600 $\pm$ 15	3690 $\pm$ 20

*Table 4-1. Terminal position elevations (meters above mean sea level) of glaciers in the Bishop Creek area.*

In summary, the terminus positions of the Tioga I - III glaciers, dating between ~18 and 25 ka, were approximately 1800 meters lower than that of the modern glaciers in Bishop Creek. In the smaller basins to the north, the difference is less well defined but appears to be between 1000 and 1400 meters. Moraines of the Tioga IV advance, dating between ~15 and 16 ka, are well defined in each basin. In Bishop Creek the terminus position appears have been at an elevation of 2200 meters at that time (~1400 meters lower than modern). The correlative moraines in Horton and McGee Creeks lie at an elevation of 2900 meters, ~800 meters below their modern counterparts. Finally, terminal moraines of the Recess Peak advance, which appear to have been deposited about 13,000 years ago, lie at an elevation of ~3300 meters in Bishop Creek, just 330 meters below modern glacier termini in the basin, and between 3410 m and 3260 m in Horton and McGee Creeks, respectively.

The ages and terminus positions summarized here describe a chronology of the glacial advances in the Bishop Creek area that reflects large-scale climate changes in the Owens Valley region. Interpreting these changes in terms of changes in specific climatic parameters is, however, not a simple matter. Paleoclimatic reconstructions based on evidence of past glacial extent typically rely on comparison of the equilibrium line altitudes (ELA) of modern glaciers with those of the paleoglaciers. That approach is fraught with uncertainty due to the assumptions that must be made to estimate not only past ELAs but, in areas where modern glaciers are sparse or non-existent, even the modern ELA. Meierding [1982] compared several different methods of estimating ELA depression

and associated temperature depression in the Colorado Front Range and concluded

*"Pleistocene ELA depression should only be computed if present and past glaciers can be approximately standardized for size, shape, and surrounding topography, and if the same ELA determination method can be used for both time periods. ... Conversion of ELA depression to temperature involves high error and is premature pending a clearer understanding of ELA temperature relationships."*

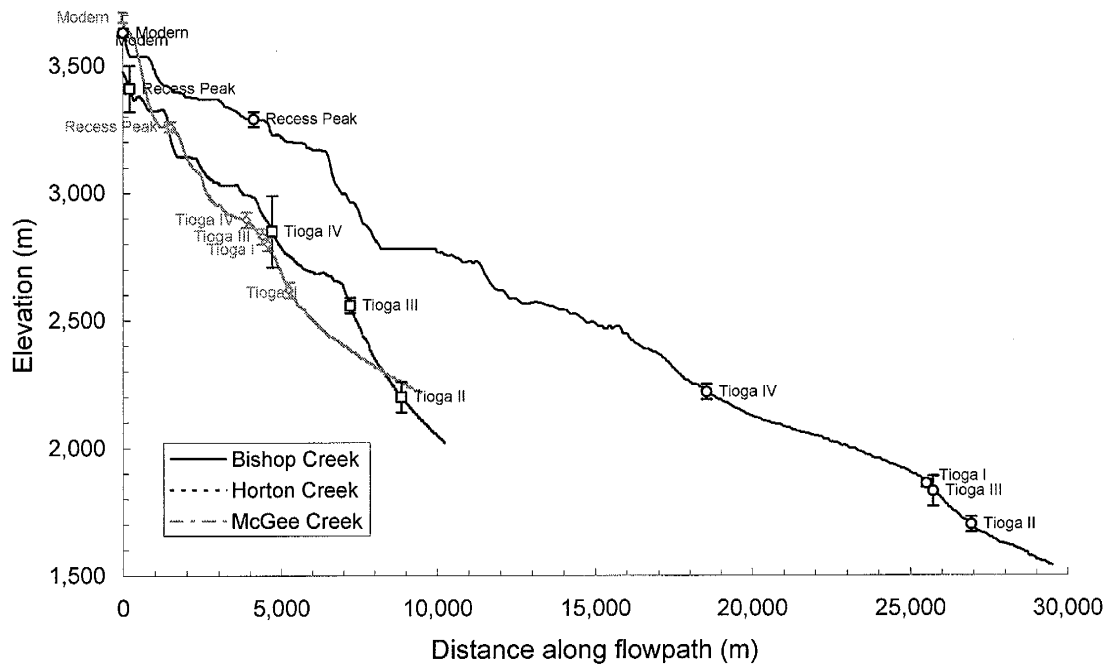


Figure 4-13. Terminal position elevations of glaciers in the Bishop Creek area. Lines are creek profiles within each basin.

For these reasons, ELA depression estimates and paleoclimatic reconstructions based on glacial deposits are often made using data from many drainages along a single mountain range [Clark and Gillespie, 1997] or even across several mountain ranges [Dohrenwend, 1984; Brakenridge, 1978]. These estimates attempt to minimize topographic and scaling effects by averaging results from several basins that are selected to have similar orientation and aspect characteristics. Such approaches are of little use if we desire to know the paleoclimatic conditions associated with a feature observed in only a few locations. Moreover, they cannot take advantage of the increasingly detailed glacial

chronologies that are becoming available via in-situ cosmogenic nuclide accumulation dating and other recent advances in Quaternary dating methods. To provide an improved means of interpreting the paleoclimate represented by indicators of past glacial extent, we developed a physically based numerical modeling approach that simulates the glaciers that would develop under a given climate. This approach includes a spatially distributed surface energy and mass balance model to determine net annual snow accumulation rates, and a glacier flow model to determine the shape of the glacier in equilibrium with the surface energy balance. These models are described in Section Five.



---

## CHAPTER 5 - GLACIER MODELING

---

One of the primary goals of this study was to develop a means by which a detailed glacial chronology from a single drainage basin could be converted to paleoclimatic information. We therefore sought to address directly the effects of basin size, shape, topography as well as a multitude of climatic variables on glacier distribution and extent at the drainage basin scale. To accomplish this, we developed two 2-D, in-the-horizontal-plane, numerical models. The first model simulates the net annual accumulation/ablation of ice based on monthly calculations of surface energy balance and precipitation. The output from this model feeds into a second, vertically integrated, glacier flow model that describes the accumulation and flow of ice in response to the prescribed pattern of accumulation and ablation. Together, the models allow us to build, 'from scratch,' the glacier that would theoretically develop under a wide variety of climatic conditions and examine its response to changes in the net annual accumulation of snow.

### SNOW/ICE ENERGY AND MASS BALANCE

The snow/ice energy and mass balance model is designed to predict the distribution of the net accumulation/ablation of snow or ice across an irregular surface, typically a drainage basin or portion thereof. The objective of this model is slightly different than those of other snow/energy balance models. Many studies that have modeled the energy balance of a glacier or snow surface were aimed at predicting, typically, monthly or weekly snowmelt from meteorological data [e.g., Marks and Dozier, 1992] or examining the climatic changes that caused relatively recent variations in modern glaciers [e.g., Oerlemans and Hoogendorn, 1989]. This study aims to determine the different climatic conditions that could produce glaciers of widely varying extent. The climatic conditions tested might range from slightly colder and much wetter to a vastly colder but significantly drier climate. Certain assumptions that might be appropriate in the former studies might therefore be inappropriate here.

Under modern conditions, for example, one might reasonably assume a rather constant length for the accumulation and melt seasons. If the temperature is much colder however, that assumption would not likely hold true for higher, colder parts of the accumulation area. Similarly, the latent heat exchange term is often neglected in glacier energy balance studies because several studies have shown that over alpine glaciers it is roughly an order of magnitude less than the sensible heat exchange term [Kuhn, 1979]. If, however, both temperature and precipitation rate were reduced drastically, sublimation losses would almost certainly become much more important (the latent and sensible heat exchange terms are, for example, of comparable magnitude over subpolar glaciers [Kuhn, 1979]). For this reason, we have attempted to include in the model most of the processes that might substantially alter the surface energy balance under widely varying climatic conditions.

The precipitation and energy balance model requires monthly averages of precipitation, temperature, humidity, cloudiness, and wind speed as primary input. Melting, evaporation and sublimation of ice from the surface are determined from monthly energy balance calculations for each point on a grid of elevations. The source for the elevation grid is typically digital elevation model (DEM) data from the U.S. Geological Survey.

#### ***ESTIMATION OF MONTHLY METEOROLOGICAL VARIABLES***

##### ***TEMPERATURE***

Accurate estimation of temperatures across the study area is critical to successful use of the model because many calculated parameters in the model depend on air temperature. These include sensible heat flux, longwave emission from the atmosphere and surrounding terrain, and the fraction of precipitation that falls as snow. In the Sierra Nevada, where roughly 90% of total precipitation falls in the winter, the latter parameter may not be as important as in a region where a larger portion of the total precipitation occurs in the spring. On the other hand, the mild climate of the Sierra and

the fact that warm Pacific storms are the source of most of the precipitation tend to increase the temperature sensitivity of the rain-snow apportioning.

Energy balance studies of glaciers commonly assume linear relationships between the primary climatic variables and elevation. While that may be reasonable over relatively narrow elevation ranges, it likely leads to increasingly large error as the elevation range increases. We calculate temperature and precipitation over a wide range in elevation in this study. Rather than assume linearity, we attempted to capture the elevation dependence of these parameters as realistically as possible, using long-term climatic data from as wide a range of elevations as possible.

Available temperature records in the area include long-term climatic means from National Weather stations in the Owens Valley and short-term, 1- to 2-year records from South Lake, Big Pine Creek and, further to the southwest, from Emerald Lake. These data indicate that temporal variations in temperature are similar over the region. Temperature generally varies with elevation in a manner predicted by local pseudo-adiabatic lapse rates. We produced polynomial expressions for temperature vs. elevation by regressing mean monthly temperatures from Death Valley, Trona, Bishop, Lodgepole, and the White Mountain Research station. The resultant expressions produced lapse rates that increased with altitude, in agreement with findings of Dohrenwend [1984] for mountain ranges in the Great Basin, and produced reasonable matches to the available data from South Lake and Emerald Lake. The temperature relationships developed for each month are illustrated in Appendix C.

#### *PRECIPITATION*

Precipitation estimation can be difficult in mountainous areas because precipitation rates vary significantly with elevation and even from basin to basin because of the strong topographic controls on storm tracks. In addition, precipitation measuring stations are concentrated at lower elevations,

where access and maintenance is relatively easy. The importance of the southern Sierra Nevada in supplying water to Los Angeles, however, means that long-term monitoring has been conducted at a moderately large number of stations in the Owens Valley. Additional information regarding snowfall and water balance of the high Sierra derives from the Emerald Lake Watershed Study [Tonnesen, 1991] in Sequoia National Park. The availability of information for estimating both the annual amount and monthly distribution of precipitation for the Bishop Creek area is therefore comparatively good.

The southern Sierra Nevada has a Mediterranean-type climate, with most of the precipitation falling in winter. The distribution is approximately 18% in September-November, 50% in December-February, 30% in March-May, and 2% in June-August [Tonnesen, 1991]. Average annual precipitation at the crest of the range generally exceeds 40 in. (~100 cm) whereas on the valley floor the average annual precipitation is approximately 5 to 6 in. (~14 cm) and the White and Inyo Mountains and Coso Range receive approximately 7 to 14 in./yr (18 - 36 cm/yr) [Hollett *et al.*, 1991]. Available meteorological station records include mean monthly precipitation data from Bishop, Bishop Creek - Intake 2, Lake Sabrina, South Lake, and many stations outside of the Bishop Creek drainage (Figure 5-1). To estimate precipitation at the crest, where local precipitation data are largely unavailable, we used monthly precipitation maps produced by the PRISM project [Daly *et al.*, 1994]. Those maps incorporate data from snow and precipitation stations throughout the Sierra Nevada, and calculate the distribution of precipitation using an algorithm that specifically addresses the difficulty of interpolation in mountainous terrain. Although the resolution of the PRISM maps (cellsize = ~4 km) is too coarse to use as the sole basis for precipitation estimation in this study, their precipitation values for the crest should provide a reasonable estimate of the precipitation rate at the highest elevations in Bishop Creek.

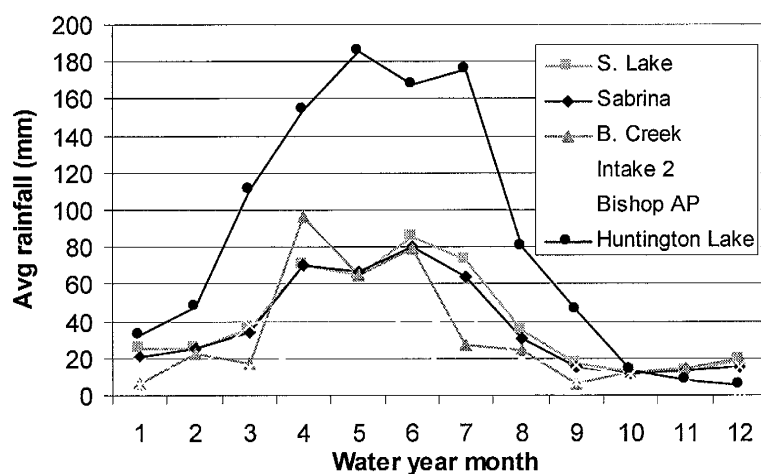


Figure 5-1. Precipitation data used to estimate monthly precipitation as a function of elevation for the Bishop Creek area. Sites included in the regression were South Lake, Lake Sabrina, Bishop Creek and Bishop Airport.

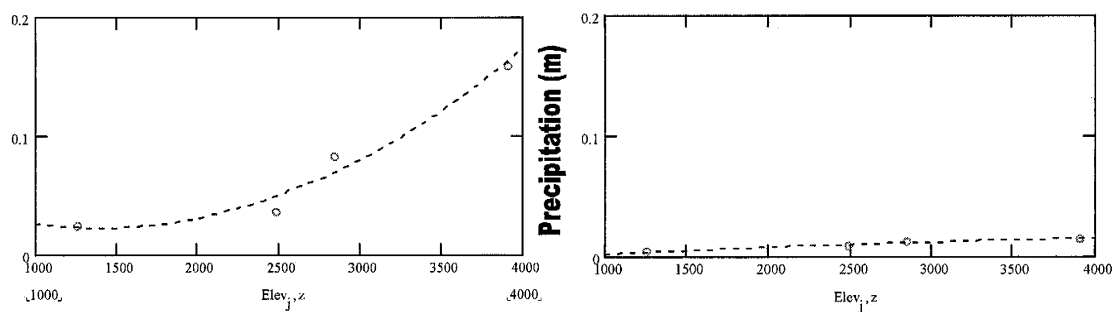


Figure 5-2. Precipitation as a function of elevation in February (left) and July (right).

Using the mean monthly precipitation estimates at four different elevations within the basin, we produced a series of polynomial coefficients for each month to estimate precipitation as a function of elevation (Figure 5-2, Appendix C). The resultant mean annual precipitation as a function of elevation is shown as Figure 5-3.

The polynomial expressions for monthly temperature versus elevation were developed specifically for Bishop Creek. Given their proximity to Bishop Creek the two smaller basins immediately to the north should have an essentially similar precipitation pattern. The influence of high-mountain relief, however, can be substantial, funneling descending air masses and attendant

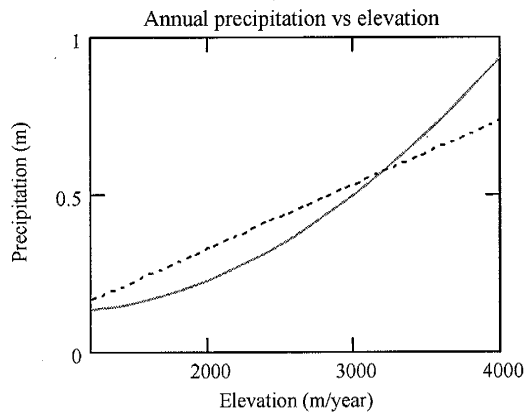


Figure 5-3. Mean annual precipitation versus elevation regression used in this study (solid red line) and Danskin's [1998] linear regression for the west side of the Owens Valley.

precipitation through some passes while leaving others relatively dry. Precipitation in the eastern Sierra Nevada is a critical part of the water supply for Los Angeles. The USGS and the Los Angeles Department of Water and Power (LADWP) therefore carefully monitor the annual snowpack. That monitoring has included regular measurements at approximately 20 precipitation and snow survey stations for 50 years or more [Danskin, 1998]. The USGS's map of average annual precipitation in the Owens Valley, derived from that data, suggests that highest precipitation rates at the crest in the Bishop Creek basin are on the order of 15% greater than those at the crest in the Horton and McGee basins to the north. Discussions with the LADWP [Tillemans, personal communication, 2001] also suggested that precipitation in the smaller basins is considerably less. If precipitation rates near the crest in the Horton and McGee basins are indeed lower it may well be related to the topography of the crest itself, which is formidable around Mount Humphreys, the ~14,000-foot peak that stands at the head of those basins. By comparison, relief is more subdued along much of the crest in the much larger Bishop Creek basin.

To estimate the differences in precipitation between Bishop Creek and the smaller basins nearby (Figure 4-1) we analyzed the relationship between measured discharge from each of the basins

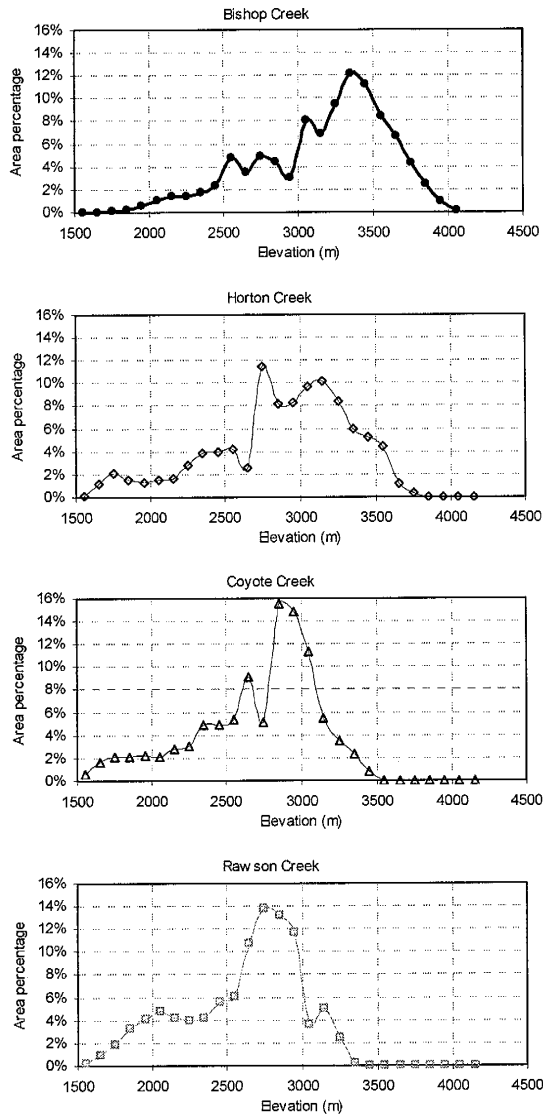


Figure 5-4. Hypsometry of Bishop Creek and several nearby basins

We first calibrated the Langbein runoff model to the Bishop Creek area using measured discharge data from Bishop Creek, for which our precipitation function is assumed to apply without correction. We also assumed that the mean annual temperature function developed for Bishop Creek applied to the entire area. Discharge calculated with the Langbein model matched the measured

[Hollett *et al.*, 1991], hypsometry, and estimated temperature and precipitation, using the spatially distributed Langbein precipitation – temperature – runoff (P-T- $\alpha$ ) model described in Section 3 (without the riparian area adjustment). We assume that a basin's runoff coefficient is largely controlled by basin hypsometry (see Figure 5-4 and Figure 5-5), and we estimate that relationship using the Langbein P-T- $\alpha$  model. Differences in Langbein-calculated runoff coefficients from those calculated using measured discharges and our estimate of annual precipitation in Bishop Creek are assumed to reflect differences in precipitation. Because of the non-linearity of the Langbein P-T- $\alpha$  relationship, we used an iterative process to calculate precipitation correction factors for each basin.

discharge in Bishop Creek when a correction factor of 1.35 was applied to the Langbein runoff coefficients. We applied that correction factor to the Langbein model calculation of runoff for all subsequent calculations. We then estimated the precipitation correction factors for each basin that would be needed to match the runoff coefficients calculated with Langbein model to those calculated using the resultant total annual precipitation and measured annual discharge. Using those factors, we recalculated basin runoff coefficients and total annual precipitation until the runoff coefficients calculated with the different approaches matched to within one percent. Results are summarized in Table 5-1.

The hypsometry of Horton Creek is similar to that of Bishop Creek and its runoff coefficient, from measured discharge and our estimate of the precipitation-elevation function, is only slightly lower. Our analysis using the Langbein P-T- $\alpha$  relationship to take advantage of the hypsometric data suggests that precipitation in Horton Creek is about 12% lower than that in Bishop Creek. Review of the USGS precipitation map for the Owens Valley [Danskin, 1998] suggests that this is probably a

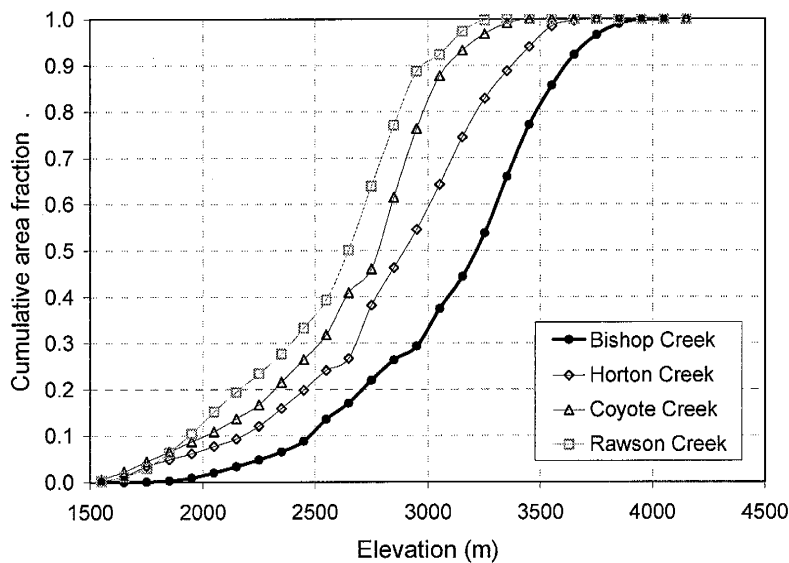


Figure 5-5. Hypsometric integral curves for Bishop Creek and nearby basins

conservative estimate of the difference. Coyote Creek is the drainage that abuts Bishop Creek to the southeast. Both Coyote Creek and Rawson Creek comprise generally lower elevations and our model suggests that the relationship developed for



Bishop Creek would overestimate precipitation in these basins by 250% and 190%, respectively.

<b>A</b>	<b>B</b>	<b>C</b>	<b>D</b>	<b>E</b>	<b>F</b>	<b>G</b>	<b>H</b>	<b>I</b>	<b>J</b>
<b>Basin</b>	<b>Mean annual discharge (m<sup>3</sup>/yr)</b>	<b>Area (km<sup>2</sup>)</b>	<b>Langbein <math>\alpha</math> adjustment (-)</b>	<b>P adjustment (-)</b>	<b>Mean annual P (cm)</b>	<b>Mean annual T (°C)</b>	<b>Mean annual runoff depth (cm)</b>	<b>Langbein- based runoff coefficient (-)</b>	<b>Discharge &amp; Pavg - based runoff coefficient (-)</b>
Bishop Creek	71587980	191	1.35	<b>1.00</b>	59.2	-0.8	37.6	0.63	0.63
Horton Creek	7568154	23	1.35	<b>0.88</b>	53.3	-0.8	32.5	0.61	0.61
Coyote Creek	5092290	66	1.35	<b>0.40</b>	19.7	0.6	7.8	0.40	0.39
Rawson Creek	1660851	25	1.35	<b>0.52</b>	18.9	2.9	6.6	0.35	0.35

<b>Column</b>	<b>Explanation</b>
<b>A</b>	Basin name
<b>B</b>	Mean annual discharge, based on USGS data [Hollet <i>et al.</i> , 1991]
<b>C</b>	Area
<b>D</b>	Adjustment applied to the spatially distributed Langbein model runoff coefficient to calibrate it to the Bishop Creek area
<b>E</b>	Precipitation correction factor
<b>F</b>	Mean annual precipitation, incorporating the precipitation correction factor (E)
<b>G</b>	Mean annual temperature
<b>H</b>	Mean annual discharge as volume of water per unit area
<b>I</b>	Runoff coefficient calculated from the spatially distributed Langbein relationship, with Bishop Creek calibration factor, and precipitation correction factor
<b>J</b>	Runoff coefficient calculated from the measured annual discharge and the mean annual, correction-adjusted, precipitation

Table 5-1. Summary of basin precipitation (P), temperature (T) and runoff coefficients ( $\alpha$ ) used or calculated in the estimation of precipitation differences among basins in the Bishop area.

### Snowfall

In addition to reproducing the temporal and spatial distribution of precipitation, we need to accurately estimate the partitioning of each month's precipitation between snow and rain. Snow increases snowpack thickness whereas rainfall does not and rain has the added effect of adding heat energy to the snowpack. When the temperature of the snowpack is below the freezing point, conversion of precipitation on the glacier to ice releases the latent heat of fusion and the ice pack warms. In many regions, this is an important factor in removing the winter cold wave from the snowpack. While the temporal distribution of precipitation within a month may be essentially independent of temperature, the fraction of precipitation that falls as snow is not. Many studies report that in the higher elevations of the Sierra, 90% or more of the precipitation that falls in winter falls as snow. The relative amounts of precipitation that occur as rain or snow, however, are

infrequently recorded, making it difficult to accurately determine the relationship between snowfall fraction and temperature. Excellent meteorological records are maintained at the Central Sierra Snow Lab (CSSL) near Donner Pass, where researchers measure both snowfall and rainfall throughout the year. Unfortunately, long-term means are not yet available from the CSSL. While it is clear that snowfall dominates winter precipitation in the Sierra Nevada, Osterhuber [1997] suggests that rain-on-snow events may play an underestimated role in the annual water balance:

*“Much of the snowfall at 2000 m elevation precipitates within a few degrees of 0°C. Hence it is not unusual for rain to fall during any month of the Sierra winter. When conditions are ideal, large low-pressure air masses brimming with great amounts of warm, tropical moisture clash with unstable air from the Gulf of Alaska. This combination can produce warm, wet, and especially violent storms throughout California and the Sierra Nevada. The largest storms – the mid-winter rain storms – are notoriously potent: above-freezing temperatures, high precipitation intensities, and destructive winds are quite common.... Of the twenty largest precipitation events recorded since 1946 at the Central Sierra Snow Laboratory (elevation 1098 m) near Soda Springs, California, eleven have not been associated with record snowfall. ... The largest precipitation events in the central Sierra Nevada are rain-on-snow events.”*

While this suggests that large rain-on-snow events may comprise a significant portion of the winter precipitation, it does not provide a means of accurately estimating that fraction.

We chose to partition precipitation into snow and rain on a statistical basis using a critical temperature of 2°C [Orndorf & Craig, 1994]. We assume that within each month precipitation is uniformly distributed and temperature is normally distributed. The number of days in a month with a mean temperature

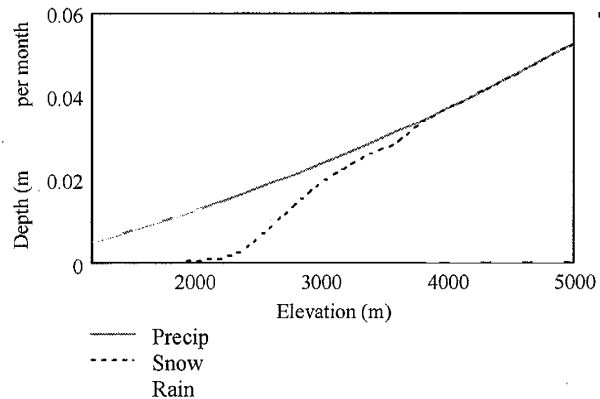


Figure 5-6. Total precipitation, snowfall and rainfall as a function of elevation in Bishop Creek under modern climatic conditions.

below the critical temperature is calculated from the normal probability distribution, using the month's mean temperature and standard deviation of temperature within that month. While the standard deviation of the mean monthly temperature may also be a function of elevation, we do not have data on which to base such a function and have assumed that the standard deviations for the Bishop Airport apply uniformly throughout the basin. The fraction of the month falling below the critical temperature is then used directly to determine the fraction of the monthly precipitation that falls as snow. The remainder is assumed to fall as rain at the temperature of the ambient air. Figure 5-6 illustrates the model's partitioning of precipitation into snow and rain as a function of elevation in the Bishop Creek basin while Figure 5-7 illustrates the modeled temporal distribution of precipitation by type and amount.

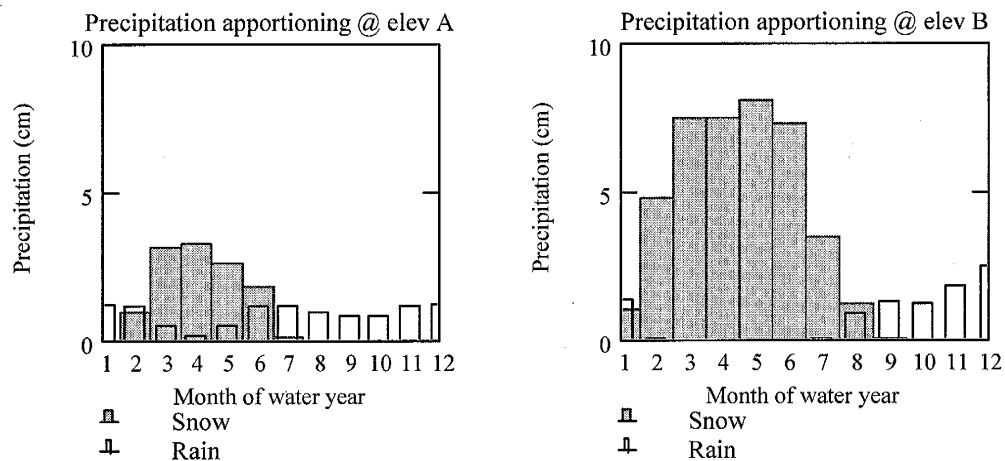


Figure 5-7. Calculated monthly precipitation for Bishop Creek partitioned into snow and rain for an elevation of (left) 2000 m and (right) 3000 m.

#### *Snow accumulation below steep slopes*

To approximate the effect of snow redistribution due to sloughing, avalanches and wind currents around steep slopes, we incorporated a maximum slope function that assumes that all snow falling on grid cells above a critical slope (55°) is immediately redistributed to down-gradient nodes. The accumulation that results at the base of steep slopes in the model is roughly consistent with our

observations of snow distribution below steep slopes in the basin and with observations made in Emerald Lake Watershed studies [Elder, 1991]:

*Many of the snow patches that persist for the longest period into the melt season in the Emerald Lake watershed are avalanche deposits or snowbanks found at the foot of steep cliffs fed by sloughing from above... Depths of drifts and avalanche deposits during the 1986 season sometimes exceeded 10 m, and sloughing from steep rock faces produced many depths exceeding 8 m.*

#### CLOUDINESS

Western U.S. Climate Historical Summaries - Local Climatological Data Summaries provide mean monthly fraction of sky cover for Bishop, CA (sunrise to sunset) and several other stations in CA. The Bishop cloudiness data, described as a monthly average of the fraction of the sky, in tenths, obscured by clouds is used for those calculations that require cloudiness.

#### WIND SPEED

Wind speed data for the area are very limited, including only the long-term record at the National Weather Station at the Bishop airport (Figure 5-8), measurements of Duell [1990] for the years 1984-

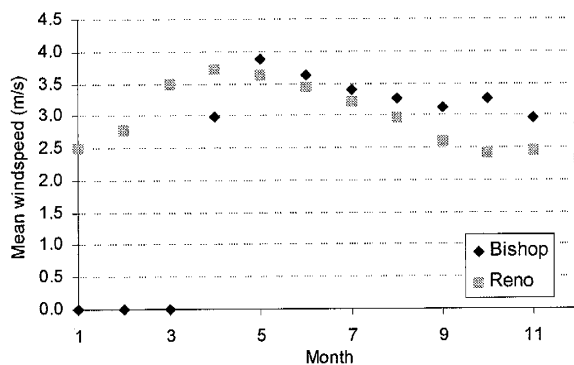


Figure 5-8. Average wind speed at Bishop, CA and – for comparison – Reno, NV. Values of zero represent gaps in the data.

1985 at several sites in the Owens Valley, and meteorological data from the Emerald Lake Watershed Study from the other side of the crest of the Sierra Nevada. The turbulent exchange of latent and sensible heat is approximately linearly related to wind speed. We used a simple expression to estimate average wind speed for the basin, a linear function of elevation designed to

provide ~6 m/sec at 4000 m when the base wind speed is 3 m/sec in Bishop. This range is quite similar to a range of values of 2-m (above surface) wind speeds over melting glaciers summarized in Kuhn [1979]. Recent studies of snow evaporation in the Sierra Nevada [Leydecker and Melack, 1999], including wind speed measurements in several basins, suggest that the Marks and Dozier wind speed data, from which our estimate is derived, are anomalously high and that the mean is closer to 2 m/sec. Given that long-term means in the Owens Valley are greater than 2 m/sec, a lower wind speed for the neighboring mountains seems counterintuitive. Clearly more measurements of wind speed and turbulent energy transfer characteristics are needed in alpine terrain.

#### *RELATIVE HUMIDITY*

As with wind speed, relative humidity data are available only from the Bishop Weather Station records and from the 1988-1989 Emerald Lake Watershed study [Marks and Dozier, 1992]. Relative humidity data included in the Bishop Climate data summary of the NCDC are given for certain times of the day, without corresponding air temperatures. We converted the reported humidity averages to absolute humidity by estimating temperatures for the different measurement hours using the long-term temperature data. For high elevation relative humidity data we used data from the Emerald Lake Watershed study [Marks and Dozier, 1992].

#### *ENERGY BALANCE CALCULATIONS*

The change in thermal energy of a snow body is given by the sum of the net transfers of energy via radiation, turbulent transfer of sensible and latent heat, advection, and conduction, minus the energy that goes into melting;

$$\Delta Q = R_{net} + H - L + A + G - \lambda_f \cdot M, \quad \text{Eq. 5-1}$$

where  $\Delta Q$  = net rate of change in stored heat energy,  
 $R_{net}$  = short- and long-wave radiation balance,  
 $H$  = sensible heat exchange,

- $L$  = latent heat exchange,
- $A$  = energy advected into the snow via precipitation,
- $G$  = conductive heat exchange with ground,
- $\lambda_f$  = heat of fusion of water (333.5 kJ kg<sup>-1</sup>), and
- $M$  = rate of melting of snow or ice.

Latent heat transfer occurs via evaporation/condensation or sublimation,

$$L = (E + S) \cdot (\lambda_v + \lambda_f), \quad \text{Eq. 5-2}$$

- where  $\lambda_v$  = heat of vaporization of water (2257 kJ kg<sup>-1</sup>), and
- $E$  = rate of evaporation from surface (negative for condensation).
- $S$  = rate of sublimation from surface.

The advective term includes the energy available due to the difference in temperature between the precipitation and the surface, and the internal latent heat released if the temperature of the snow is cold enough to freeze the precipitation. The advective term is thus

$$P \cdot (T_p \cdot c_w + \lambda_f), \quad \text{Eq. 5-3}$$

- where  $P$  = rate of precipitation as rain,
- $T_p$  = temperature difference between precipitation and snow, and
- $c_w$  = specific heat of water.

The net rate of change of heat storage in the ice or snowpack, in expanded form, is therefore

$$\Delta Q = R_{net} + H + G + [P \cdot (T_p \cdot c_w + \lambda_f)] - [(E + S) \cdot (\lambda_v + \lambda_f)] - \lambda_f \cdot M. \quad \text{Eq. 5-4}$$

Rewriting the equation to solve for the rate of melting of ice or snow yields

$$M = \{ R_{net} + H + G + [P \cdot (T_p \cdot c_w + \lambda_f)] - [(E + S) \cdot (\lambda_v + \lambda_f)] - \Delta Q \} / \lambda_f. \quad \text{Eq. 5-5}$$

If the snow temperature does not drop below the freezing point during the period when the energy balance produces melting, equation 5-5 can be simplified to

$$M = \{ R_{net} + H + G + (P \cdot T_p \cdot c_w) - [(E + S) \cdot (\lambda_v + \lambda_f)] \} / \lambda_f. \quad \text{Eq. 5-6}$$

The snow and energy balance model developed for this project implements equation 5-6 to determine the mass of snow melted during each month. When the air temperature is below freezing, only the latent heat term is calculated, using the air temperature as the surface temperature, to determine the amount of sublimation.

The magnitudes of the various components of the energy balance vary from place to place but the conductive and advective terms are generally negligible in comparison to the others. Actual measurements of the various components are invaluable in assessing the relative importance of each of the components as well as in developing empirical equations to describe them as a function of climate parameters. The most detailed such studies that have been conducted in the Sierra Nevada are those conducted in the Emerald Lake watershed, approximately 75 km south of Bishop Creek and 20 km west of the crest of the range. Detailed energy balance measurements of the seasonal snowpack at Emerald Lake were summarized by Marks *et al.* [1992] and Marks and Dozier [1992] for the period 1986 - 1987. Monthly averages of temperature, snowmelt, evaporation/sublimation losses and the individual energy balance components at the lake site in that basin are summarized in Figure 5-9. The data demonstrate that the shortwave energy is the largest component of the energy balance and that the next largest components - the sensible and latent heat fluxes - are of similar magnitude but opposite sign. The latent heat term indicates significant sublimation during the winter. The relative magnitude of the snow loss via that mechanism, as compared to the loss via snowmelt, can be estimated by considering that the energy used in evaporation is approximately eight times that used in melting. Longwave energy transfer is clearly a significant energy loss throughout the year but the remaining fluxes, the advection and conduction terms, are negligible during the melt season.

The snow/ice energy and mass balance model calculates monthly snow accumulation and loss for each point on a grid to track the snow balance throughout the year and produces a final grid of net annual snow accumulation, individual values of which may be positive or negative. Because we do not know beforehand the glacier's final shape, we assume that the entire underlying surface is ice. Positive values in the net accumulation grid represent snow accumulation areas and negative values represent ablation. This approach has the minor disadvantage of ignoring heat transfer between the glacier and bare ground, which would have different sensible and radiative characteristics.

Calculation of the surface energy balance of snow is relatively straightforward when the surface temperature is known or can be measured directly. Otherwise the calculation is complicated by changes in the thermal energy of the snowpack, and coupled thermal and energy balance equations must be solved. Fortunately, the energy balance is only needed when melting occurs, and during the melt season the temperature of the snowpack is almost always at the melting point. As is commonly done in energy balance measurements of glaciers [Oerlemans, 1992; Greuell and Oerlemans, 1986], we use the melting point in most of the energy balance calculations requiring the snow surface temperature.

The monthly energy balance record of Marks and Dozier [1992](Figure 5-9) demonstrates that significant melting occurs only after the monthly average air temperature rises above 0°C and that this corresponds well with the time at which the surface temperature reaches the melting point. Our snow/ice energy and mass balance model thus calculates snowmelt only when the air temperature rises above zero. Temperatures, the addition of rain or snow, and several other functions are the primary independent variables that are calculated each month. When the air temperature in any cell is above zero, its surface energy balance is calculated to determine the amount of melting, sublimation and/or evaporation for that month. For areas where the average temperature is below zero, only the latent heat term is calculated – to determine the sublimation loss. Because of the discontinuity in the energy balance calculations at 0°C, and the relatively coarse time-step used (one month), we incorporate a fractional month and adjusted temperature when the monthly temperature is close to zero. The length and temperature of the fractional month are calculated by interpolation of the preceding and following month's temperatures.



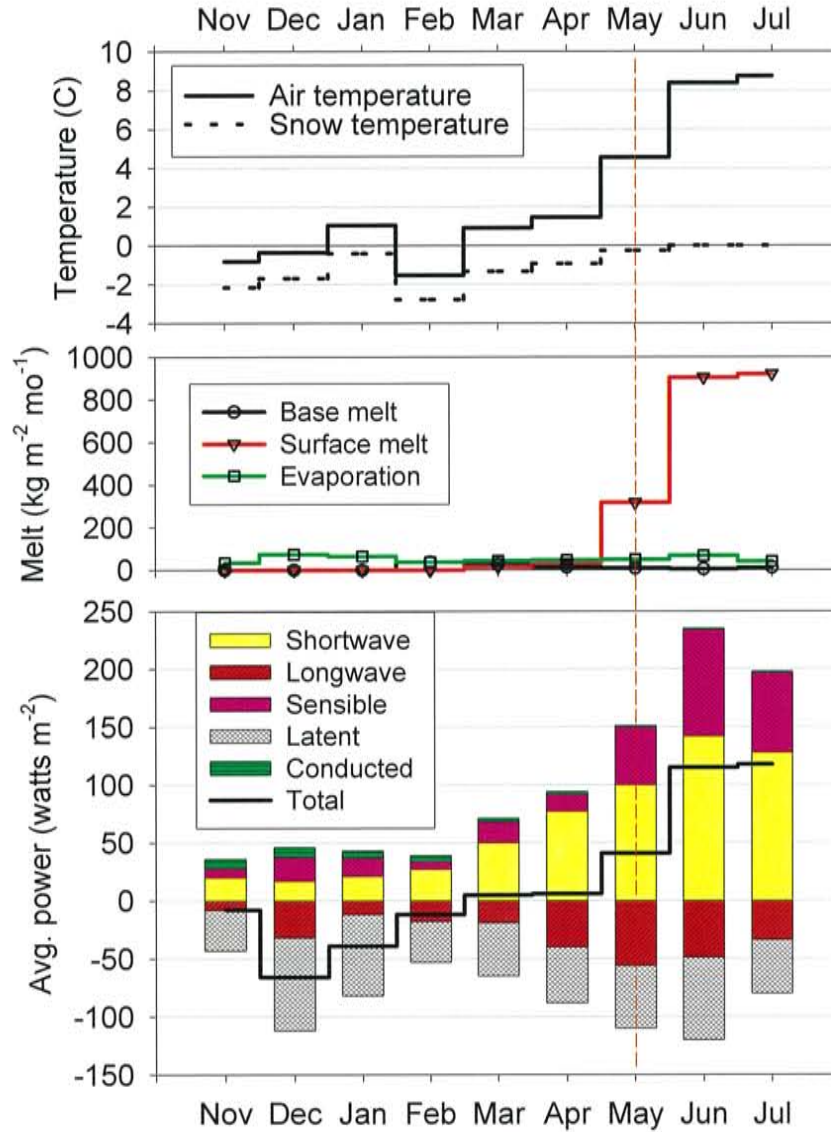


Figure 5-9. Summary of mean monthly meteorological, energy-balance and snow-balance measurements of Marks *et al.* [1992] and Marks and Dozier [1992] at the 'Lake site' in the Emerald Basin during 1988 and 1989. The vertical dashed line indicates the first month for which there is significant melting. This corresponds to the first month for which the average temperature is considerably above zero.

Details of the equations and methods by which each of the components of the energy balance is implemented are discussed below. Meteorological means for each month are used to calculate the mean monthly energy flux for each term (unless the temperature is everywhere below zero) and the sum determines the energy available for melting. Accumulation of snow during each

month is then balanced against the melting and evaporation losses to determine the monthly net loss or gain of snow. The cumulative effects of the monthly energy balance thus determine the net annual accumulation rate of snow by summing the effects over a year. The mean shortwave radiation for each month is estimated from the midmonth total daily irradiance, calculated by integrating instantaneous irradiance at regular intervals (~8 were used for simulations presented here) over the length of the day.

#### *SHORTWAVE RADIATION*

The largest component of the surface energy balance is the influx of shortwave radiation. Calculation of this component is based on a combination of physical principles and empirically derived approximations to some of the factors affecting their magnitude. The shortwave radiation is determined from solar angle calculations computed in a Mathcad worksheet and application of those angles to the topography via an Arcview script. The overall calculation scheme is described briefly here; details are included in attached Mathcad worksheets (Appendices D and E).

The general scheme is to calculate elevation-, albedo-, and climate-dependent parts of the insolation calculations first and pass these to a subroutine that determines atmospheric transmission coefficients from temperature, cloudiness and relative humidity data. The insolation subroutine then computes the direct, diffuse and backscattered radiation components and returns these to the main program. Aspects of the insolation calculation that may vary with changes in primary and secondary climatic variables include surface albedo, atmospheric transmission coefficients affected by cloudiness and precipitable water content. These values are calculated within the main subroutine for each annual cycle. A central part of the calculation of the shortwave radiation component is the integration of the instantaneous irradiance on the irregular terrain. The direct shortwave component is proportional to the cosine of the incidence angle and is zero when surrounding topography shades

the surface. These effects are incorporated via the hillshade function in the Arcview Spatial Analyst Extension. The angle of incidence and shading effects vary with solar azimuth and zenith angle and are therefore integrated by numerical quadrature; irradiance for a sequence of solar angles is summed and weighted by the duration of time representing the time between sun positions. The timestep for the model calculations is one month. Rather than attempt to integrate the direct irradiance for an entire month we consider that the integrated value for a single day in the middle of any month provides a representative value. The sequence of angles for integration of radiation over the day begins after the local sunrise and ends at sunset. The length of the daylight period is evenly divided to determine both the sun position angles and the timestep length for the quadrature. These sun position angles, time-step length and other solar parameters are described in greater detail in Appendix D.

Because the model is designed to include topographic effects on solar insolation, a fundamental part of the shortwave radiation calculations is a routine that uses solar azimuth and zenith angles to determine the shading and shadowing of any point on the surface of interest. These angles, as well as the mean Earth-Sun distance, are affected by cyclical variations in the lunar and planetary orbits on the scale of tens of thousands of years. Those cycles are believed to have a strong influence on the long-term climatic variations of the Earth through as-yet poorly understood amplifying feedbacks. Though the effect on the shortwave radiation at any particular location is relatively minor, the radiation calculations in the model include the ability to consider the effects of these Milankovitch cycles directly. Further details are included in Appendix D - the solar angle and Earth-Sun distance calculations.

The final output of the Mathcad worksheet describing the orbital and annual variations in sun position are:

- 12 (monthly) values of the Earth-Sun distance correction
- Number of steps for the daily integration (spaced for an open quadrature method such as the midpoint trapezoidal rule), time interval between measurements
- 12 sets of solar azimuth and altitudes for times specified by the sampling interval

These data are then used by the snow/ice energy and mass balance model to compute the direct, diffuse and backscattered radiation incident on the surface during each interval, and the resultant grids are integrated via the trapezoidal rule. The calculations of diffuse, direct and backscattered radiation are based largely on the equations described in Dingman [1993]. An additional term to estimate the elevation-dependence of the incident radiation is based on the data of Klein [1948]. Shading from surrounding topography and the effect of the slope of the surface on the angle of incidence is calculated using the hillshade function of Arcview.

#### *Direct component*

The incoming direct shortwave radiation,  $k_{\text{dir}}$ , on a horizontal plane normal to the solar beam is described as  $k_{\text{dir}} = \tau \cdot k_{\text{ET}}$ , where  $\tau$  is the total atmospheric transmissivity and  $k_{\text{ET}}$  is the incident radiation at the top of the atmosphere. The direct irradiance is first modified by the atmospheric transmissivity. Atmospheric transmissivity is generally calculated as described in Dingman [1993], except that we determine it for instantaneous, rather than average daily, radiation. The transmissivity

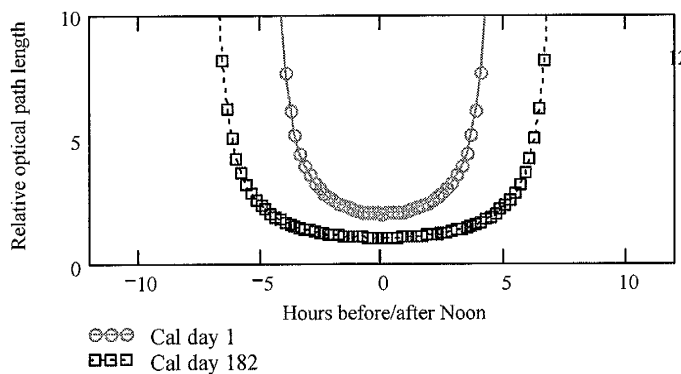


Figure 5-10. Relative optical path length for the first day of the year (circles) and the middle day of the year (squares).

calculation thus involves the instantaneous relative optical path length (relative to the zenith direction). The Arcview script currently calculates that with the secant approximation. That approximation is poor at oblique solar angles but radiation is

relatively weak at low angles and the error introduced is small. It would, however, be relatively straightforward, and inexpensive computationally, to calculate or input optical path lengths from Kastens formula [Iqbal, 1983] or another better approximation [Kondratyev, 1969].

Relative optical path lengths as a function of hour of day are shown in Figure 5-10. Precipitable water in the atmosphere is calculated from surface dewpoint temperature using the approximation described by Bolsenga [1964]. Because the calculation requires elevation-dependent relative humidity and temperature values, a precipitable-moisture grid is calculated in the main part of the program and passed to the insolation calculations. Under constant relative humidity, increasing elevation leads to a decrease in dewpoint. This results in a slight increase in transmissivity with elevation.

Many of the published expressions for determining atmospheric transmissivity were derived for single locations at or near sea-level. Atmospheric transmissivity however is elevation dependent, and

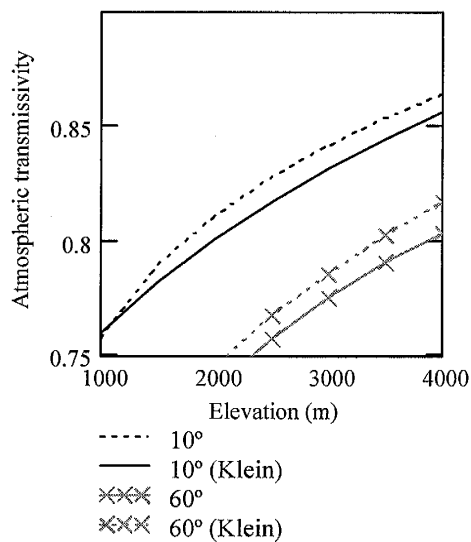


Figure 5-11. Atmospheric transmissivity coefficient dependence on temperature at different zenith angles as calculated in this model (solid lines) and using the polynomial expression of Klein [1948].

in high-relief terrain this effect on the largest component of the energy balance may be significant. Dozier [1980] reports that under typical conditions the incoming solar radiation at 1200 m (elevation at Bishop is 1265 m) is 25% less than at 4400 m. Though the approximations described above include a dependence on elevation through the calculation of precipitable water content, that effect modifies the direct shortwave irradiance only slightly. Klein [1948] examined the dependence of transmissivity on elevation and developed a polynomial approximation for total

atmospheric transmissivity as a function of elevation. The function is highly inaccurate at high zenith angles and low elevations, so we incorporated that information using an elevation-dependent

exponential correction factor that effectively alters the exponential scaling height of the atmosphere to ~9000 m. Figure 5-11 compares the transmissivities calculated by the model to those of Klein [1948] for different zenith angles.

#### *Diffuse component*

About one-half the energy scattered from the solar beam reaches the surface as diffuse radiation, and its magnitude is generally about 20% of the total shortwave irradiance. Diffuse radiation in the model is calculated as described in Dingman [1993], incorporating, again, a relative optical path-length-dependent transmission coefficient. The intensity of diffuse radiation is slightly anisotropic over the dome of sky. Because of the relatively low intensity of skylight however, the isotropic approximation is sufficient for practical purposes [Temps and Coulson, 1977]. The amount of diffuse radiation is calculated from the extraterrestrial irradiance on a flat surface, which is proportional to the cosine of the angle between a normal to a horizontal plane and the solar zenith angle. Instantaneous values calculated in that manner are integrated over the range of zenith angles for any particular day to determine the daily energy flux from diffuse radiation. Transmission coefficients incorporate elevation dependence from the precipitable moisture grid and the optical path length calculation.

Because the model is primarily designed for high-relief terrain, the diffuse irradiance is reduced by the degree to which the sky is obscured by surrounding terrain [Dozier 1980; Temps and Coulson 1977]. To obtain the portion of the total sky dome visible from each point on the surface, a viewfactor grid is calculated by integrating a sequence of solar zenith angles around the compass. A hillshade calculation at each sun position is used to determine the region of the surface in shadow. The viewfactor for that solid angle of the sky is zero; all other values indicate visible sky. The resultant viewfactor for each cell of the surface grid ranges from 0 to 1 but is generally greater than

0.7. As the viewfactor does not change unless the surface topography changes, the integration is only performed once for each surface.

#### *Backscattered component*

Of the direct and diffuse radiation striking the surface, a fraction given by the albedo is reflected back to the atmosphere. A portion of that radiation returns to the surface and is again partially reflected and so on. In general, about one-half of the direct and diffuse radiation reflected is absorbed again. In calculating the backscattered radiation component, we arbitrarily assumed that its local value is influenced by the reflected radiation from an approximately 1-km<sup>2</sup> area.

#### *Effect of cloudiness on atmospheric transmissivity*

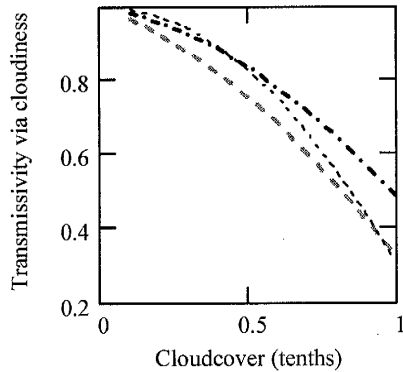


Figure 5-12. Oerlemans approximation for the effect of cloud-cover on the atmospheric shortwave radiation transmission coefficient at 1500 m (dashed red line) and at 4000 m (dotted blue line). The approximation of Barashkova [Kondratyev, 1969] (thin black dotted line) is shown for comparison.

We used the approximation of Oerlemans [1992] to calculate the reduction in atmospheric transmissivity due to cloudcover. This equation produces values similar to those of simpler approximations, such as that of Barashkova (Figure 5-12), but includes a correction for elevation, which must be considered in mountainous terrain. The expression, written in terms of cloud amount,  $n$ , in tenths, is

$$\tau_c = 1 - (0.41 - 0.000065h)n - 0.37n^2, \quad \text{Eq. 5-7}$$

where  $h$  is elevation, in meters, and  $\tau_c$  is the atmospheric transmissivity correction that is applied to the clear-sky shortwave radiation value.

#### *Albedo*

Albedo is one of the most important factors in the energy balance of a snow or ice surface because it directly modifies shortwave irradiation. Unfortunately, it is also highly variable (Figure

5-13) and strongly dependent on the amount of debris contained in the ice and the amount of melting that has occurred. It is therefore difficult to estimate the albedo for a glacier that has effectively disappeared. In this study, our initial goal is to calculate the energy balance without prior knowledge of the shape or the length of the glacier. For that reason, we did not attempt a parameterization, like that of Oerlemans [1993], that incorporates distance from the ELA, thickness of ice melted relative to total ice thickness, or other glacier-dependent factors. Inclusion of these effects on albedo might improve the model, but would require a stronger coupling between the surface energy balance and the glacier flow model than we have attempted in this study.

The difficulty in estimating albedo is simplified somewhat because we only need estimates for the melt season; the calculation of evaporation during the winter is based only on temperature. At present we use only two albedos in the model, one for melting snow and one for melting ice. Oerlemans and Knap [1998] analyzed a one-year record of global radiation and albedo in the ablation zone of Morteratschgletscher, Switzerland. The measured variations in albedo reflect a full cycle of snow accumulation and ablation and generally reflect a bimodal distribution with a rapid change between those modes during the spring snowmelt period. During early spring, the albedo is typically between 0.6 and 0.8, but during April it drops rapidly and is close to 0.4 throughout the summer. Based on that record, we incorporated an albedo of 0.4 for regions where all of the current winter's snowpack had melted and a value of 0.7 for areas where some fraction of the snowpack still remained.



Surface	Range	Mean
Dry snow	80-97	84
Melting snow	66-88	74
Firn	43-69	53
Clean ice	34-51	40
Slightly dirty ice	26-33	29
Dirty ice	15-25	21
Debris-covered ice	10-15	12

Figure 5-13. Shortwave radiation albedos for a range of snow and ice conditions. From Paterson, 1994.

Albedo is also a function of cloud cover, which tends to increase it. To simulate the mean influence of cloud cover on albedo, we incorporate the expression suggested by Petzold [Male and Granger, 1981],

$$\% \text{ Change From Clear Sky Albedo} = 0.449 + 0.0097 n^3 \quad \text{Eq. 5-8}$$

where cloud amount,  $n$ , is expressed in tenths.

As a simple check on the cloudiness dependence of the albedo in our model, we calculated 365 average daily shortwave radiation values for a horizontal surface at 37° latitude and 1300 meters elevation, with a randomly generated cloudiness function based on mean monthly cloudiness data from Bishop. The results compare very well with Duell's [1990] measurements for a site in the northern Owens Valley.

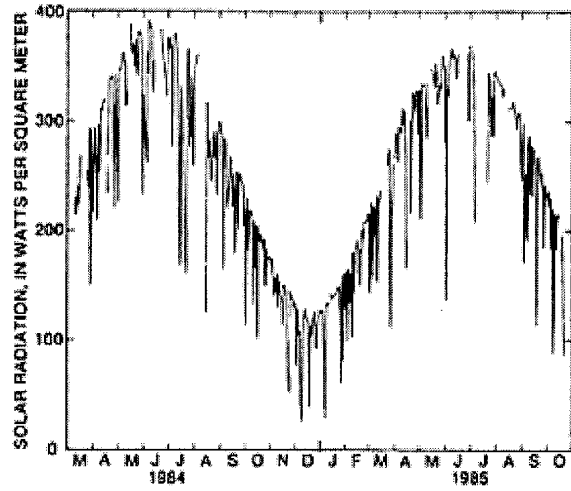
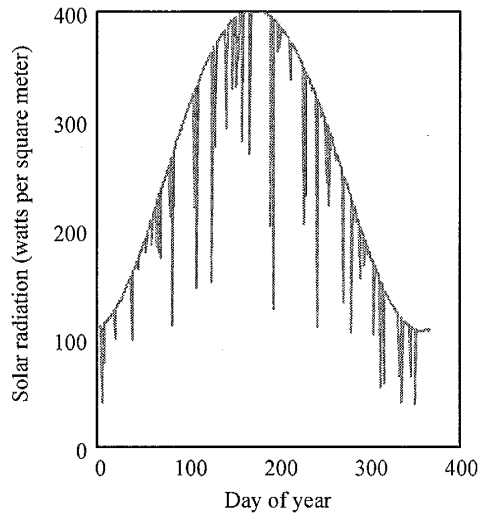


**Figure 9.** Daily average solar radiation at site C, March 1984–October 1985.

*Figure 5-14. Simulated daily average solar radiation on a horizontal plane at an elevation 1300 m with random cloudiness (left) compared with daily average solar radiation measurements made during 1984 and 1985 at a site in the northern Owens Valley [Duell, 1990].*

#### LONGWAVE RADIATION

##### *Outgoing longwave radiation*

Outgoing longwave radiation is that emitted by the snow surface. The total rate of energy emission  $I_o$  per unit area is given by

$$I_o = \varepsilon_{\text{snow}} \sigma T_s^4, \quad \text{Eq. 5-9}$$

where  $\sigma$  is Stefan's constant,  $T_s$  is the surface temperature in Kelvin.  $\varepsilon_{\text{snow}}$ , the emissivity of the snow surface is assigned a value of 0.99 because a snow or ice surface radiates as a blackbody in the infrared. During the ablation season, the temperature of the snow is easily determined because the snow reaches the melting point but cannot rise above it. During the accumulation season, however, the temperature of the snow, particularly near the surface, may drop considerably below zero. Thus, to accurately estimate winter emission, the temperature of the snow must be known. Similarly, calculation of the sensible heat flux, which tends to balance the loss due to radiation, also requires knowing the temperature of the snow. Fortunately, changing the temperature of the snowpack

requires much less energy than does melting. The energy required to warm the snowpack back to the melting point is therefore rapidly supplied in the early spring and we ignore that heat transfer in our energy balance calculation. For the temperature of the snow during the melt season we used the approach taken by Oerlemans (1992) and others, and assumed that the temperature of the snow surface stays close to the melting point.

#### *Incoming longwave radiation*

Longwave radiation emitted by the atmosphere under clear skies is given by

$$I_i = \varepsilon_a \sigma T^4, \quad \text{Eq. 5-10}$$

where  $\varepsilon_a$  is the atmospheric emissivity. Calculation of clear-sky atmospheric emissivity in the model is performed using the expression of Idso and Jackson [Male and Granger, 1981],

$$\varepsilon_a = 1 - 0.261 \cdot \exp\{-7.77 \cdot 10^{-4} \cdot (273 - T^2)\}, \quad \text{Eq. 5-11}$$

as it involves only air temperature (Kelvin) as a variable. Numerous empirically derived expressions have been developed to model longwave radiation from the atmosphere and most of these produce results that are quite similar<sup>7</sup>.

Cloudcover tends to increase the longwave emission received by the snow, as clouds are a relatively powerful source of thermal radiation [Kondratyev, 1973]. We model the increase in thermal emission from the atmosphere due to the presence of clouds using the expression suggested by Mura [Arnold, 1996] to relate effective emissivity,  $\varepsilon^*$ , cloudiness fraction,  $n$ , and clear-sky emissivity,  $\varepsilon_a$ :

$$\varepsilon^* = (1 + 0.26 \cdot n) \varepsilon_a. \quad \text{Eq. 5-12}$$

---

<sup>7</sup> Male and Granger [1981] report that studies have shown that the Idso-Jackson and Swinbank formulae tend to underestimate longwave atmospheric emission by as much as 8% during parts of the diurnal cycle. This should be considered if the model is adapted to calculate energy balance at that temporal scale.

### *Longwave emitted by surrounding surfaces*

In areas of high relief, the longwave radiation emitted by surrounding terrain makes a significant contribution to the total longwave flux at a point. Male and Granger [1981] explain how the contribution may be accounted for:

*"In order to calculate this contribution the point in question is considered to be at the center of an imaginary hemisphere. The unobscured fraction of this hemisphere, termed the thermal view factor,  $V_f$ , is determined by a comparison with the elevations of surrounding terrain. It is expressed as a number between 0 and 1, calculated from the equation*

$$V_f = \cos^2(H).$$

*H is the average horizon angle. Details concerning the calculation of horizon angles are given by Dozier and Outcalt [1979]. Total incoming radiation at a point is computed from*

$$L = (\epsilon_a \sigma T_a^4) V_f + (\epsilon_s \sigma T_s^4) (1 - V_f)$$

*where  $\epsilon_s$  is the emissivity of the surrounding surface and  $T_s$  the surface temperature. Marks and Dozier [1979] point out that the view factor is usually greater than 0.9 and therefore reasonable approximations are adequate for  $T_s$  and  $\epsilon_s$ ."*

Longwave emission from the surrounding terrain is calculated using a value of 0.4 for the surface emissivity and the viewfactor grid discussed previously, rather than the  $\cos^2(H)$  expression suggested by Male and Granger.

In order to determine the longwave energy flux to the surface, we must integrate the incoming

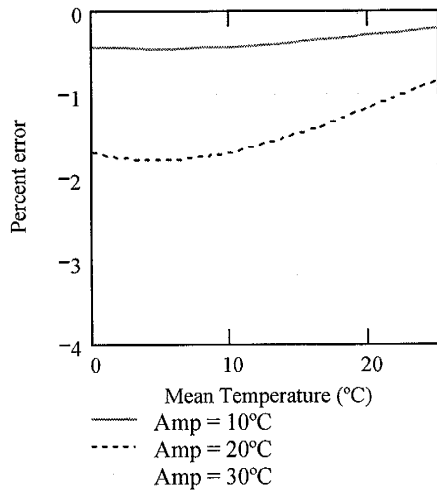


Figure 5-15. Error caused by calculating atmospheric longwave radiation from a mean temperature instead of integrating over the diurnal temperature cycle.

and outgoing longwave functions over the 24-hour period we choose as representative of the monthly value.

Often, however, the only information available is the month's average temperature so the model currently uses only average temperature in the calculation of the longwave emitted by the atmosphere. (This is not a significant issue with snow surface radiation, as the temperature is assumed to remain fixed.)

Figure 5-15 illustrates the error resulting from using the mean daily temperature rather than integrating over the diurnal temperature cycle. The relatively small difference in the

integrated value is due to the fact that although longwave emission is a highly non-linear function of temperature, the temperature is in Kelvin. The differences in the temperature are thus very small compared to the mean value of the temperature itself. As the plots illustrate, the error is less than 5% even when the diurnal temperature range is as much as 30°C (54°F) and most of the error is actually due to non-linearity in the emissivity function. Interestingly, based on data from the National Weather Service, [www.weatherpages.com](http://www.weatherpages.com) lists Bishop CA as the U.S. city with the greatest diurnal temperature range ([www.weatherpages.com/variety/diurnal.html](http://www.weatherpages.com/variety/diurnal.html)). Although that term is not well defined, the listed range for Bishop, 108.9°F, appears to be a maximum range. Based on the National Climatic Data Center summary data for Bishop (Appendix C), the mean monthly diurnal temperature ranges from about 32°F in January to 41°F (~23°C) in July. Although the model currently uses only the mean temperature for calculation of the longwave energy flux, mean monthly maximum and minimum temperatures are commonly available. It would be relatively straightforward to add that data to the model input and incorporate an analytical expression that would integrate the longwave

equations over that range.

#### *Summary of effects of cloudiness*

Cloudiness has a number of effects on the surface energy balance. It tends to decrease the largest part of the energy balance - the direct shortwave component - while increasing the much smaller diffuse component and increasing the longwave radiation received by the snow surface from the atmosphere. In this model, cloudiness is incorporated through the following calculations:

- Reduction in atmospheric transmissivity for shortwave radiation
- Increase in snow surface albedo for shortwave radiation
- Increase in longwave emission from the atmosphere

#### *TURBULENT ENERGY EXCHANGE*

We calculate the turbulent transfers of sensible and latent heat using a simple bulk transfer scheme [Paterson, 1994], in which a single dimensionless transfer coefficient summarizes the primary characteristics of the turbulent air exchange, such as surface roughness, vertical profiles of temperature and wind speed, and atmospheric stability. In this approach, the sensible heat flux,  $H$ , is a linear function of the bulk transfer coefficient,  $k$ , wind speed,  $\bar{u}$ , and the difference in temperature between the snow,  $T_s$ , and the ambient air,  $T$ :

$$H = \rho c_p k \bar{u} (T - T_s), \quad \text{Eq. 5-13}$$

where  $\rho$  is the density and  $c_p$  the specific heat capacity of the ambient air. The latent heat flux, similarly, is proportional to wind speed and the difference in vapor density between the surface of the snow,  $q_s$  and the ambient air,  $q$ :

$$L = \rho k u (\lambda_v + \lambda_f) (q - q_s), \quad \text{Eq. 5-14}$$

where  $\lambda_v$  and  $\lambda_f$  are the specific heats of vaporization and condensation, respectively.

Because the heat transfer coefficient is a function of local processes, it is difficult to evaluate for ice bodies, like the Tioga-age glaciers of the Sierra Nevada, that no longer exist. Assuming that turbulent heat exchange processes are similar within the region, we used the detailed energy balance

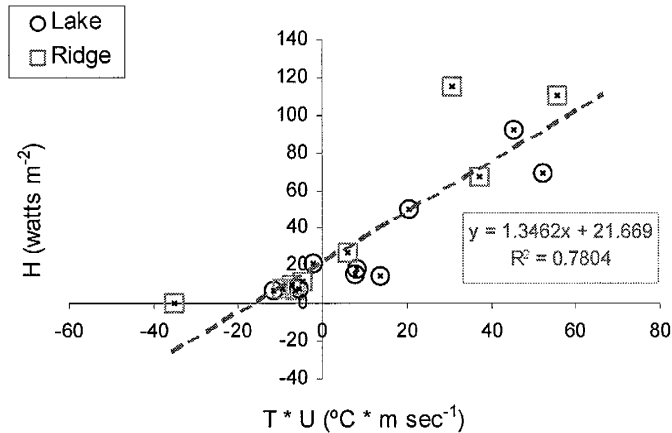


Figure 5-16. Monthly sensible heat ( $H$ ) values from the Emerald Basin [Marks and Dozier, 1992] plotted against the product of mean temperature and wind speed. Box shows the equation and  $R^2$  value for a linear regression (dotted line) of the data.

measurements of Marks *et al.* [1992] and Marks and Dozier [1992] to estimate its value. We calculated the transfer coefficient by regression of their sensible heat flux data because they appeared to have a much higher signal to noise ratio than did the latent heat data. Figure 5-16 shows the reported monthly average sensible heat fluxes for 1988 - 1989, plotted against

the product of wind speed and temperature from two sites in the Emerald Basin. Linear regression of those data, constrained to intercept the origin, has an  $R^2$  of  $\sim 0.5$ . This regression yields a dimensionless transfer coefficient of 0.0019. A better fit ( $R^2 = \sim 0.8$ ) to the Marks and Dozier data is a line of lower slope that does not pass through the origin. That regression yields a heat transfer coefficient of about 0.0015, with an offset in the monthly average temperature of  $+2.6^\circ\text{C}$ . The energy balance model employed for this study uses the lower transfer coefficient and, for the sensible heat flux, a temperature offset of  $2.1^\circ\text{C}$ . The temperature offset is not applied to the latent heat flux calculation. In retrospect, it would be better to use the simpler linear regression with the zero-y-intercept for both calculations; sensible heat values for periods at or near  $0^\circ\text{C}$  are nearly negligible, so the difference likely adds complexity without a corresponding increase in accuracy.

Some formulations of the sensible heat term lump wind speed into the bulk transfer coefficient.

Comparison with those values requires an assumed wind speed. Paterson [1994] lists dimensionless transfer coefficients found in a number of studies. Table 5-2 lists those values and additional data from Oerlemans [1992] and Kuhn [1979]. The values of 0.0015 and 0.0019 calculated from alternative regressions of the Marks and Dozier [1992] data compare well with published values and the range of values in Table 5-2 suggests that the magnitude of the uncertainty associated with this parameter is on the order of a factor of two.

Surface	Transfer coefficient x 1000	Reference
Snow	1.66	Holmgren, 1971, Part D [see Paterson, 1994]
Snow/ice	2.0	Hogg and others, 1982 [see Paterson, 1994]
Snow	1.3	Ambach and Kirchlechner, 1986 [see Paterson, 1994]
Ice	1.9	Ambach and Kirchlechner, 1986 [see Paterson, 1994]
Ice	3.9	Hay and Fitzharris, 1988
Ice	4.5	Kuhn, 1979
Snow/ice	1.1	Oerlemans, 1992
Snow	1.5 - 1.9	Regression of Marks & Dozier [1992] data

*Table 5-2. Sensible heat transfer coefficients from the literature. The value for Oerlemans is calculated from the published bulk transfer coefficient and an assumed average wind speed of 6 m/sec.*

Based on values reported in the literature, Paterson suggests that the transfer coefficient for ice may be approximately 30% greater than that for snow. Accordingly we incorporated an adjustment to the turbulent transfer equations that increases the sensible and latent heat exchange terms by that amount when all of the winter's snowpack has melted.

#### ADVECTIVE HEAT TRANSFER

This is the energy gained by the ice from precipitation because the rain is warmer than the melting point. It is calculated using the mean air temperature for the month and the amount of precipitation falling as rain (also a function of temperature). Note that this term does not include the effect of the phase change when rain freezes into the snowpack. Because the snow is assumed to be



at the melting point already, that phase change would also release the heat needed to melt that amount of snow.

#### *CONDUCTIVE HEAT TRANSFER*

The heat conducted into a glacier is generally a small part of the energy balance. Based on the energy balance measurements of Marks and Dozier [1992], we used a constant value of  $\sim 1$  watt/m<sup>2</sup> for the Bishop Creek area during the ablation season. Though conductive heat fluxes are slightly higher in the winter, the model currently does not attempt to account for the potential basal melting that could occur before the entire thickness of the glacier reaches the melting point.

#### *INTERMEDIATE GRID EXAMPLES*

The snow/ice energy and mass balance model computes monthly grids for each of the meteorological and energy balance components. These grids are intermediate to the final net accumulation map produced for the prescribed surface. Examples of some of the intermediate grids for the Bishop Creek watershed are shown in Figure 5-17.

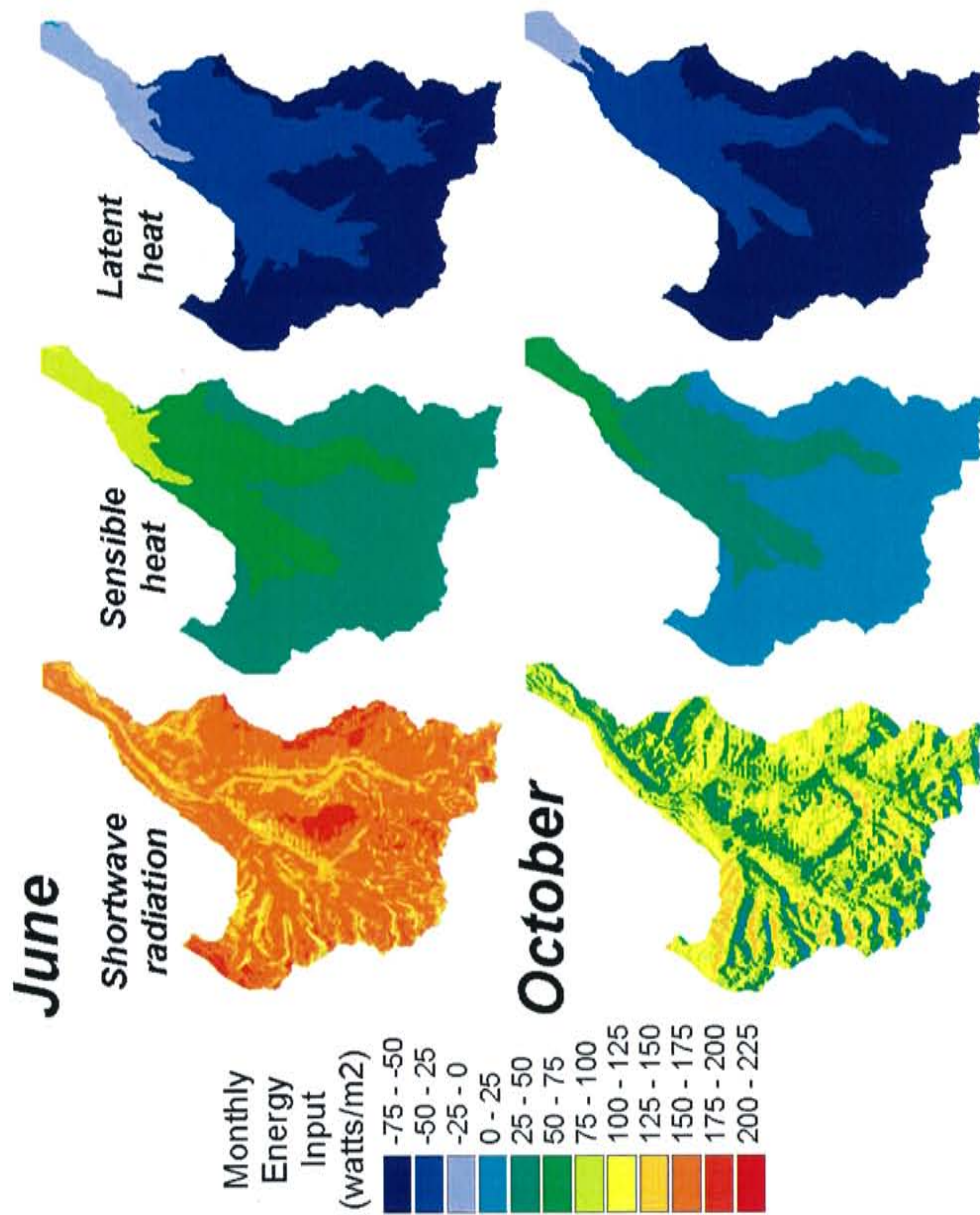


Figure 5-17. Examples of calculated monthly energy flux via shortwave radiation (1<sup>st</sup> column), sensible heat transfer (2<sup>nd</sup> column) and latent heat transfer (3<sup>rd</sup> column) from the mass and energy balance model applied to the Bishop Creek drainage. Upper row are grids for July, lower row is October. Energy fluxes are mean monthly values (watts m<sup>-2</sup>).

## GLACIER FLOW MODEL

The energy and mass balance calculations described in the previous section are used to determine a net annual snow accumulation rate on a snow/ice surface for a given set of climatic parameters. The region where that rate is positive effectively defines the accumulation area for the glacier corresponding to those climatic conditions.<sup>8</sup> There, annually accumulated snow builds up until increasing stress causes the mass to flow outwards. As the accumulation area tends to be at higher altitude, the outward flow generally transports the ice mass downhill, into areas where the net accumulation rate is negative. This becomes the ablation area for the glacier. If climatic conditions remain relatively stable for a sufficiently long period, this area will eventually grow to a steady-state condition where net annual ablation from the glacier equals the net annual accumulation. To predict the glacier that would exist under given climatic conditions, we use a 2-D, in the horizontal plane, glacier flow model to determine the ablation area. The flow model calculates the time-dependent flux of ice into or out of each cell in a grid from a set of finite difference equations relating flow to ice thickness, surface-slope and bed-slope. This section describes the physical basis for those equations.

For ice, the constitutive equation relating the shear strain rate to the applied shear stress is Glen's law,

$$\dot{\epsilon}_{zx} = A \tau_{zx}^n, \quad \text{Eq. 5-15}$$

where  $\epsilon_{zx}$  = shear strain rate along the x-y plane in the x direction,  
 $A$  = flow parameter, and  
 $\tau_{zx}$  = shear stress along the x-y plane.

Widely different values of  $n$  and  $A$  have been obtained by different experimenters but  $n=3$  is generally adopted for glacier studies (Paterson, 1994). The value of the fitting parameter,  $A$ , is dependent on temperature, pressure, crystal size and orientation, the presence of liquid water, the

---

<sup>8</sup> This assumption may be invalid in cases where ice flowed in or out of the defined basin boundary.

presence of impurities and other factors. The shear stress is the driving stress for ice flow and it is a function of the thickness and geometry of the glacier. Paterson [1994] states, "... basal shear stresses in alpine valley glaciers usually lie between 50 and 150 kPa." For the simple case of an ice mass of constant thickness flowing on an inclined surface (Figure 5-18) in the  $x$  direction, the driving stress,  $\tau_{zx}$ , is the vector component of the normal force along the plane of the incline,

$$\tau_{zx} = \rho \cdot g \cdot H \sin(\alpha), \quad \text{Eq. 5-16}$$

where  $\rho$  = ice density,  
 $g$  = acceleration of gravity,  
 $H$  = ice thickness, and  
 $\alpha$  = slope of ice surface (from horizontal reference).

For the ice slab to be stationary, the driving force must be balanced by an equal and opposite basal shear stress,  $\tau_{zx}$ . As surface slopes in real glaciers tend to mirror average bed slope, we can use the relationship

$$H = \frac{\tau_{zx}}{\rho \cdot g \cdot \sin(\alpha)} \quad \text{Eq. 5-17}$$

to estimate glacier thickness as a function of bed slope. The average density of ice is  $\sim 900 \text{ kg/m}^3$ , and slopes along Bishop Creek below the confluence of the Middle and South Forks are typically about  $3^\circ$ . Assuming a basal shear stress of  $\sim 100 \text{ kPa}$ , this relationship suggests that glacier thicknesses in Bishop Creek might be on the order of 200 meters. A correction factor of 0.5 to 0.9 is usually applied to the denominator in equation 5-17 for valley glaciers [Paterson, 1994], indicating that actual thicknesses might be more on the order of 300 meters.

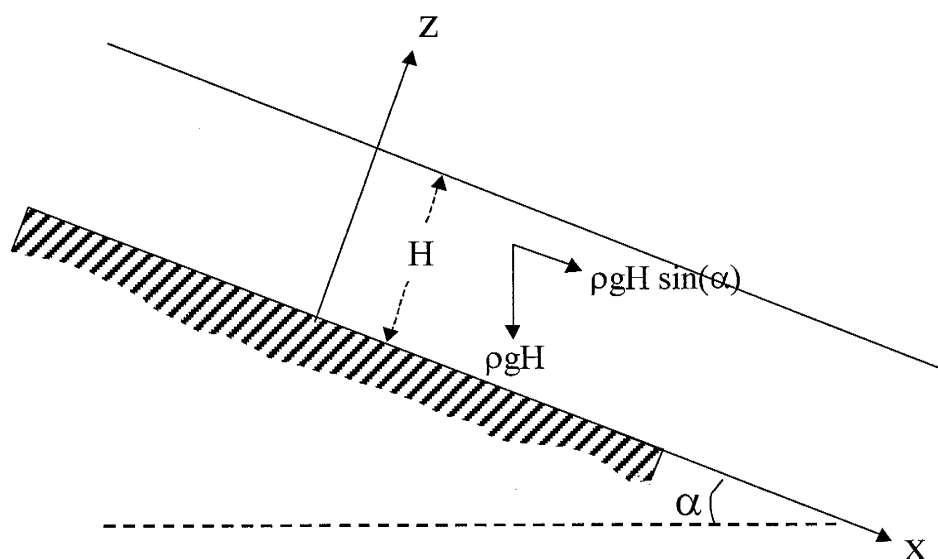


Figure 5-18. Hypothetical glacier cross-section (longitudinal slice) illustrating the driving stress for a parallel-sided (top and bottom sides, that is) slab of ice on an inclined plane.

While differences between the slope of the surface and the slope of the bed introduce some differential stress, it can be shown [Paterson, 1994] that when the slopes are small, the basal shear stress is the same as in the case of a slab of ice of constant thickness.

To relate ice flow to shear stress, we incorporate the constitutive equation relating shear strain rate to the driving shear stress. By the flow law for ice, the strain rate,  $\dot{\epsilon}_x$ , is related to the shear stress by  $\dot{\epsilon}_x = A \tau_{zx}^n$ ; for simple shear in a parallel-sided slab model of a glacier, the velocity at a point,  $u$ , is related to the shear strain rate [Paterson, 1994] by

$$\dot{\epsilon}_x = \frac{1}{2} \frac{du}{dz}. \quad \text{Eq. 5-18}$$

The velocity is therefore related to the shear stress by

$$\frac{1}{2} \frac{du}{dz} = A \tau_{zx}^n. \quad \text{Eq. 5-19}$$

Shear stress, and therefore strain rate and velocity, varies with depth in the ice slab by the relation

[Paterson, 1994]

$$\tau_{zx} = \rho g (H - z) \sin(\alpha). \quad \text{Eq. 5-20}$$

Substituting equation 5-20 into equation 5-19, and integrating, gives the velocities as a function of depth:

$$u_s - u = \frac{2A}{n+1} (\rho g \sin \alpha)^n (H - z)^{n+1} \quad \text{Eq. 5-21}$$

$$u_s - u_b = \frac{2A}{n+2} (\rho g \sin \alpha)^n H^{n+1}. \quad \text{Eq. 5-22}$$

Here,  $u_s$  and  $u_b$  are the surface and basal velocities, respectively, and  $u$  is the velocity at depth ( $H - z$ ).

Integrating equation 5-21 and dividing by thickness gives the average horizontal ice velocity for laminar flow due to deformation,  $\bar{u}_d$ :

$$\bar{u}_d - u_b = \frac{2A}{n+2} (\rho g \sin \alpha)^n H^{n+1}. \quad \text{Eq. 5-23}$$

If  $n$  is taken as 3 [Paterson, 1994] this can be written as the following function of the basal shear stress:

$$\bar{u}_d - u_b = \frac{2A}{5} H \tau_{zx}^3. \quad \text{Eq. 5-24}$$

The velocity due to sliding at the base is more difficult to analyze because it depends on the liquid pressure in the glacier; we use a simple form similar to that described by Fastook and Chapman [1989] and Pfeffer *et al.* [1997],

$$u_b = \left( \frac{\tau_{zx}}{B'} \right)^2, \quad \text{Eq. 5-25}$$

where  $B'$  is an adjustable, glacier-specific, parameter that depends on the mechanical and thermal properties of the ice, characteristics of the bed, and basal water pressure. The depth-integrated ice velocity,  $\bar{u}$ , is the sum of the velocity due to deformation,  $\bar{u}_d$ , and the velocity due to sliding,  $u_b$ .

Dropping the subscripts from the basal shear stress term,  $\tau$ , to simplify notation for other coordinate systems, the depth-integrated velocity equation is

$$\bar{u} = \bar{u}_d + u_b = \left( \frac{\tau_{zx}}{B'} \right)^2 + \frac{2A}{5} H \tau_{zx}^3. \quad \text{Eq. 5-26}$$

This is similar to the expression commonly used in many 1-D, centerline flow modeling studies [Oerlemans, 1988; Schlosser, 1997],

$$\bar{u} = u_b + \bar{u}_d = \frac{k_2 \tau^3}{N} + k_1 H \tau^3, \quad \text{Eq. 5-27}$$

where  $k_1$  = constant of proportionality relating velocity due to deformation to ice thickness,  
 $k_2$  = constant of proportionality relating velocity due to sliding to ice thickness,  
 $H$  = ice thickness,  
 $N$  = normal load on bed ( $\rho g H$ ).

Because of the larger basal shear stress exponent in the sliding velocity term of equation 5-7, and the normal stress in the denominator of that equation, the equations differ by factor of  $\sin(\alpha)$ . The flow constants for velocity due to sliding and deformation are expressed in different ways by different authors. In keeping with Pfeffer *et al.* [1997], we now write equation 5-27 in terms of coefficients,  $A'$  and  $B'$ , where  $A'$  follows the form  $\dot{\epsilon}_x = (\tau_{zx}/A')^3$ . Including a proportionality factor,  $f$ , that represents the proportion of flow due to sliding; and dropping the subscripts from the basal shear stress  $\tau$ ; equation 5-27 becomes

$$\bar{u} = f \left( \frac{\tau}{B'} \right)^2 + (1-f) H \frac{2}{5} \left( \frac{\tau}{A'} \right)^3. \quad \text{Eq. 5-28}$$

The flux per unit width of the glacier,  $q$ , is the depth-averaged velocity multiplied by the thickness of ice,  $H$ :

$$q = \bar{u} H = H \left[ f \left( \frac{\tau}{B'} \right)^2 + (1-f) H \frac{2}{5} \left( \frac{\tau}{A'} \right)^3 \right]. \quad \text{Eq. 5-29}$$

For a horizontal reference plane, instead of the sloped reference plane described in Figure 5-18, the basal shear stress,  $\tau$ , in the  $x$  direction would be

$$\tau = -\rho g H \frac{\partial h}{\partial x}, \quad \text{Eq. 5-30}$$

where  $H$ , as before, is ice thickness and  $h$  is snow-surface elevation above datum. Substituting equation 5-30 into equation 5-29, the ice flux in the  $x$  direction,  $q_x$ , is given by

$$q_x = -H \left[ f \left( \frac{\rho g H}{B'} \frac{\partial h}{\partial x} \right)^2 + (1-f) H \frac{2}{5} \left( \frac{\rho g H}{A'} \frac{\partial h}{\partial x} \right)^3 \right]. \quad \text{Eq. 5-31}$$

#### GENERAL CONTINUITY EQUATION

To describe the two-dimensional distribution of glacier ice as a function of climate — as reflected in the spatially distributed map of net annual ice balance at the glacier surface — we developed our flow model for 2-D flow in the horizontal plane. The corresponding mass continuity equation, still assuming flow occurs only via plane strain, is

$$\frac{\partial h}{\partial t} = M - \frac{\partial q_x}{\partial x} - \frac{\partial q_y}{\partial y}, \quad \text{Eq. 5-32}$$

where  $h$  = ice surface elevation above datum,  
 $M$  = annual snow balance,  
 $q$  = ice flux per unit width of ice, and  
 $x$  and  $y$  are subscripts indicating the direction of flux.

The expressions for flux,  $q$ , in equation 5-32 are highly non-linear. For solution via finite differences, we rewrite equation 5-32 as a non-linear diffusion equation with the non-linear elements of the flux terms lumped into a conductance term,  $k$ ;

$$\frac{\partial h}{\partial t} = M - \frac{\partial}{\partial x} \left[ -k_x(h) \frac{\partial h}{\partial x} \right] - \frac{\partial}{\partial y} \left[ -k_y(h) \frac{\partial h}{\partial y} \right]. \quad \text{Eq. 5-33}$$

The coefficients,  $k_x$  and  $k_y$ , are determined by expanding the flux equation (5-31),



$$q_x = - \left[ f \left( \frac{\rho g}{B'} \right)^2 H^3 \left( \frac{\partial h}{\partial x} \right)^2 + (1-f) \frac{2}{5} \left( \frac{\rho g}{A'} \right)^3 H^5 \left( \frac{\partial h}{\partial x} \right)^3 \right], \quad \text{Eq. 5-34}$$

and dividing through by the gradient of the surface elevation to give

$$k_x = - \left[ f \left( \frac{\rho g}{B'} \right)^2 H^3 \left| \frac{\partial h}{\partial x} \right| + (1-f) \frac{2}{5} \left( \frac{\rho g}{A'} \right)^3 H^5 \left| \frac{\partial h}{\partial x} \right|^2 \right]. \quad \text{Eq. 5-35}$$

Taking the density of ice as constant and lumping appropriate constants into the coefficients of sliding due to sliding,  $c_B$ , and deformation,  $c_A$ , the conductance term can be simplified to

$$k_x = - \left[ f c_B H^3 \left| \frac{\partial h}{\partial x} \right| + (1-f) c_A H^5 \left| \frac{\partial h}{\partial x} \right|^2 \right], \quad \text{Eq. 5-36}$$

where  $c_A$  = coefficient for deformational velocity and  
 $c_B$  = coefficient for sliding velocity.

#### **FINITE DIFFERENCE FORM AND SOLUTION**

The above equations properly describe only 1-D flow in an ice sheet, without longitudinal or compressive stresses. In a valley glacier, where there is both longitudinal compression and extension in three dimensions, this simple plane-strain model is only approximate. Our primary goal in this application, however, is not a precise model of ice thickness, shape and flow patterns of the former glacier but only the position of the terminus at steady state. At steady state, the shape of the glacier is primarily a function of the plasticity of the ice and the annual mass balance at the surface. The former determines how the ice interacts with the topography; extremely stiff ice can be considered to be only weakly influenced by topography, as it may not flow until its thickness is much greater than the topographic relief. Ice of lower viscosity, by comparison, is generally thinner and, thereby, more sensitive to subtle variations in topography. In applying the plane-strain equations to a valley glacier, we assume that (1) ice thickness is the primary control on how the glacier interacts with the topography and (2) thicknesses calculated using the plane-strain flow model are, at least to a first-

order, reasonably accurate and that inaccuracies in thickness due to the inadequacies of the flow model are effectively second order. By using flow parameters that produce a glacier thickness that matches the geological evidence reasonably well, we can therefore capture the essential characteristics that control the position of its terminus.

We use a fully explicit, centered in space, finite difference form of the mass continuity expression, equation 5-33. For flow in two dimensions, with a source term,  $M$ , this is

$$\frac{h_{i,j}^{n+1} - h_{i,j}^n}{\Delta t} = M_{i,j}^n - \left[ \frac{[q_{i+\frac{1}{2}} - q_{i-\frac{1}{2}}]}{\Delta x} + \frac{[q_{j+\frac{1}{2}} - q_{j-\frac{1}{2}}]}{\Delta y} \right]^n. \quad \text{Eq. 5-37}$$

Expanding the flux terms in terms of the finite difference surface gradient and conductance term,  $k$ , yields

$$\frac{h_{i,j}^{n+1} - h_{i,j}^n}{\Delta t} = M_{i,j}^n - \frac{1}{\Delta x} \left\{ \left[ -k_{i+\frac{1}{2},j}^n \left( \frac{h_{i+1,j}^n - h_{i,j}^n}{\Delta x} \right) \right] - \left[ -k_{i-\frac{1}{2},j}^n \left( \frac{h_{i,j}^n - h_{i-1,j}^n}{\Delta x} \right)^2 \right] \right\} - \frac{1}{\Delta y} \{ \dots \}, \quad \text{Eq. 5-38}$$

$$\text{where } k_{i+\frac{1}{2},j}^n = \left[ f c_B (H_{i+\frac{1}{2},j}^n)^3 \left| \frac{h_{i+1,j}^n - h_{i,j}^n}{\Delta x} \right| + (1-f) c_A (H_{i+\frac{1}{2},j}^n)^5 \left| \frac{h_{i+1,j}^n - h_{i,j}^n}{\Delta x} \right|^2 \right], \quad \text{Eq. 5-39}$$

$$\text{and } H_{i+\frac{1}{2},j} = \frac{H_{i+1,j} + H_{i,j}}{2}. \quad \text{Eq. 5-40}$$

Here  $i$  = cell number in the x direction,  
 $j$  = cell number in the y direction, and  
 $n$  = time-step level.

Using the current values of ice-surface elevation, ice thickness, and the source term, these equations are solved at each time step for a new ice-surface elevation. To remain stable, the Courant number, which is proportional to both timestep and diffusivity (here represented by the conductance

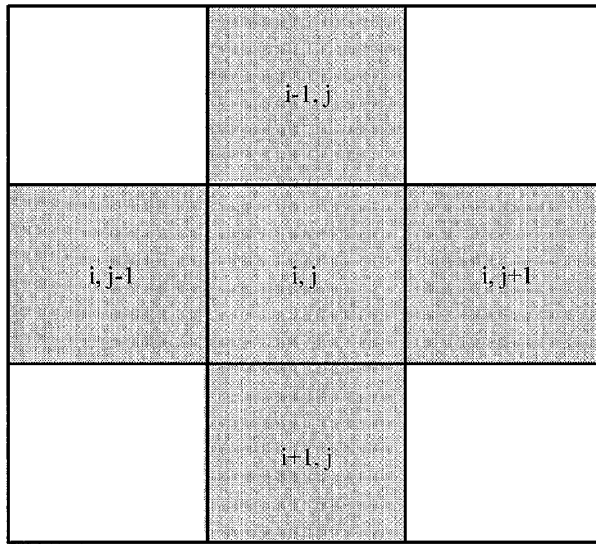


Figure 5-19. Five-point finite difference star used to calculate ice-flow velocities.

term) must be less than unity. To ensure stability, the model continually calculates and uses the maximum allowable timestep according to that criterion. The timestep thus decreases rapidly as ice thickness and ice-surface slope increase.

The solution method is, in general, a standard fully explicit, 5-point, finite difference approximation (Figure 5-19). The unknown location of the boundary of the

ice, however, introduces several difficulties that must be addressed for successful application of the finite difference method. The primary dependent variable in the model calculations is ice-surface elevation, the behavior of which is not constant across the grid. Ice-surface elevation can increase or decrease in ice-covered portions of the grid but can only increase or remain constant in ice-free areas. The finite difference formulation of the continuity equation does not inherently recognize this difference and conditions that lead to a decrease in ice thickness can thus lead to errors. In our model, these errors are corrected after each application of the finite difference equations. The conditions that require subsequent corrections include (1) ablation in cells where the ice thickness is zero, and (2) a positive divergence that exceeds the mass of ice in a cell. These difficulties reflect the fact that this is actually a moving-boundary, or Stefan, problem. The approaches we used to deal with some of the resultant difficulties are summarized below.

1. The net annual snow accumulation term may be positive or negative. The source term consequently acts to continually reduce elevation in ice-free areas. Where the resultant ice-thickness is less than zero, the ice-surface elevation is simply corrected back to match ground-surface elevation.

2. In steep terrain, or where there are large contrasts in the accumulation rate, the gradient and conductance may lead to a flux out of a cell that is greater than the mass of ice contained in it. This creates inappropriate mass and must be prevented or significant mass balance problems will develop. As the possibility of such an occurrence during a time-step is not known a priori, results of each thickness adjustment are compared to the divergence to determine whether or not this error has occurred. 'Delinquent' cells - where the new ice surface elevation is lower than the ground surface elevation - are first reset to zero ice thickness (ice surface elevation equals ground surface elevation). The ratio of the mass of ice removed to the total mass that exited the cell is then used to correct mass in the adjacent cells that received flow from the delinquent cell.
3. Ice can flow from ice-covered cells to ice-free cells, but not vice versa. To prevent that occurrence, the surface-gradient-dependent conductivity between two cells is set to zero if the ground elevation of the ice-free cell is greater than the adjacent ice-surface elevation.

The solution method was programmed in FORTRAN90, using allocatable arrays to allow changes in grid dimension without changes to the code. The "5-point star" finite difference expression is written as a series of FORTRAN90 matrix (rather than 1-D array) calculations, using pointers to reference the appropriate subsections of the full grid. The FORTRAN code is included in Appendix F. The program begins by reading in a NAMELIST-type parameter file for locations of files and control parameters for flow, timestepping and other issues. It then reads a rectangular grid of surface elevation data and determines from it the grid structure for other input grids and subsequent matrix calculations. Subsequent input grids include the net accumulation map calculated by the energy/snow balance model and ice thickness, which may be output from an earlier simulation. Ice thickness can also be entered as a single-valued constant, using the appropriate statement in the parameters file. The net accumulation grid represents a source term in the model. It is input in units of millimeters of water per year<sup>9</sup> and is then converted to meters of ice by multiplying by (1000 gms water/900 gms ice) / 1000 mm m<sup>-1</sup>.

Boundary conditions for the simulation are determined from the shape and values of the input grids. The primary boundary is the edge of the drainage basin. This is a no-flow boundary and may

---

<sup>9</sup> Output of the energy/mass balance model is in units of mm/year so that it may be stored in integer, rather than floating-point, form, thereby reducing file size.

be chosen to restrict flow of the ice to areas where the topography that once constrained the glacier has been altered. The model determines the location of this boundary by examining the source term grid. Cells outside the basin have a null-data value (-9999) while active cells describe the net accumulation rate of glacier ice in millimeters per year. To simplify description of the boundary, two 'connection' arrays are generated with value 1 between active nodes and value 0 where one of the adjacent nodes is inactive. The separate arrays represent connections between cells in the x direction and y direction.

Calculations begin with determination of the inter-node conductances, which represent both the depth-integrated ice velocity and the thickness available to accommodate flow. No-flow boundary conditions are applied by multiplying the static connection matrices by the time-dependent conductance terms. The conductance is non-linear function of the average thickness between two cells and the absolute value of the ice-surface gradient between the two cells. Due to the non-linear nature of the equations, it is difficult to determine the correct thickness to use in the conductance term. Lacking evidence to suggest a more complicated form, we used the average thickness between neighboring cells as the appropriate height.

After determining the time-dependent conductances, the continuity equation is applied to determine the change in ice-surface elevation at each cell. Corrections are then made, as necessary, to account for changes in the glacier boundary, and the ice thickness is then recalculated. A variety of descriptors of the glacier mass balance and extent are then printed to screen and file, depending on the specified output frequency. The code then returns to the calculation of conductances and repeats the above-described process. Execution is halted when the specified maximum number of timesteps or a specified maximum time is reached. Primary output is a grid of ice thickness values. This is printed at the end of the simulation and at intervals during the simulation as specified by the user. This allows the user to track various indicators of the glacier's movement and stop the simulation

when the desired final condition is reached.

### FLOW PARAMETERS

In studies of modern glaciers, the coefficients for the deformation and sliding velocities ( $k_1$  and  $k_2$ ) are commonly used as fitting parameters to match glacier thickness along a flow line, typically using a one-dimensional flow-line model of the glacier. The range of reported values for these constants (Table 5-3) provides some indication of the range of values that might provide reasonable simulations for alpine glaciers, although, as discussed previously, most of those studies use an a sliding velocity term that is more sensitive to the surface slope of the glacier. Figure 5-20 illustrates the relationship between ice flux ( $\text{m}^3/\text{yr}$  per unit width), ice thickness and ice surface gradient given by application of the constants used in our model.

	Reference	$k_1$ ( $\text{yr}^{-1} \text{ kPa}^{-3}$ )	$k_2$ ( $\text{m yr}^{-1} \text{ kPa}^{-2}$ )
A	Paterson, 1994	$2.1 \times 10^{-7}$	-
B	Schmeits & Oerlemans, 1997	$3.0 \times 10^{-8}$	$7.9 \times 10^{-3}$
C	Oerlemans, 1988	$2.2 \times 10^{-8}$	$3.2 \times 10^{-3}$
D	Oerlemans, 1989	$3.0 \times 10^{-6}$	$2.8 \times 10^{-1}$
E	Stroeven, Van De Wal & Oerlemans, 1989	$1.9 \times 10^{-8}$	$3.0 \times 10^{-3}$
F	Huybrechts, Nooze & Decleir, 1989	$8.0 \times 10^{-8}$	-
G	Average of above values	$5.6 \times 10^{-7}$	$7.5 \times 10^{-3}$
H	Maximum:minimum ratio	137	187
I	Pfeffer <i>et al.</i> , 1997	$3.6 \times 10^{-8}$	1.0
J	Values used in this study	$1.0 \times 10^{-7}$	$1.5 \times 10^{-3}$

Table 5-3. Empirically determined coefficients for glacier ice flow due to deformation ( $k_1$ ) and sliding ( $k_2$ ). Row G shows the average of many values reported in the literature, and row H provides the ratio of the largest of the values to the smallest. Row I shows the values used by Pfeffer *et al.* [1997] that assumes a slightly different form of the sliding velocity term than those studies listed in rows A through F. Values used in this study are shown in row J.

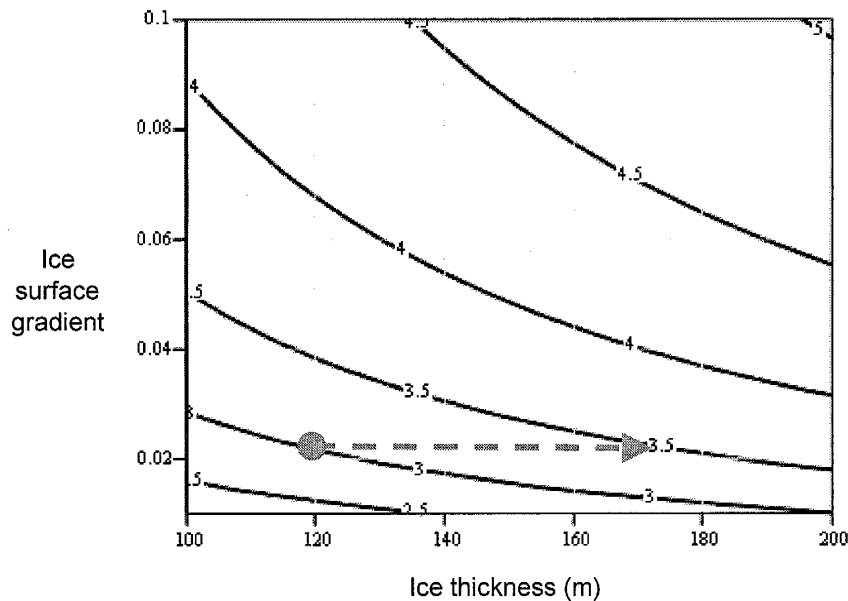


Figure 5-20. Log ice flux ( $m^3/yr$  per unit width) contours as a function of ice thickness (m) and ice-surface gradient. Flow parameter,  $f$ , equals 0.5 (i.e. equal weights are assigned to the sliding and deformation terms of the ice flow equation). Arrow indicates that at a surface slope of  $\sim 2\%$ , and initial ice thickness of 120 m, a tripling in ice flux from  $\sim 900 m^3/yr$  to  $\sim 2700 m^3/yr$  (per unit width) requires an increase in thickness of  $\sim 55$  m.

In this application, we know the position of the surface of the ice only approximately. Though we can still tune the model by varying the ice-flow parameters, it is unrealistic to attempt to refine the fit by varying the relative proportions of flow due to sliding and deformation. Assuming that such tuning would cause only minor adjustments in ice thickness, we used constants for the deformation and velocity terms that effectively attributed most of the flow to deformation (Table 5-3). We conducted initial simulations with the flow model using the deformation coefficient,  $k_1$ , presented by Paterson [1994]. The resultant ice thickness for the Tioga maximum glacier was generally a good match to estimates based on trim-line altitudes and moraine heights but appeared slightly thin in the ablation area where the left lateral moraines provide a good guide to the actual glacier thickness. Based on the necessary change in thickness and the average gradient along the center flow line, we calculated (as demonstrated in Figure 5-20) that reducing the ice-flow parameters by a factor of  $\sim 5$  would increase the surface elevation by the appropriate amount. These values, shown in the last row of Table 5-3, were used for all subsequent simulations.

---

## CHAPTER 6 - PALEOCLIMATIC INTERPRETATION OF CHANGES IN GLACIAL EXTENT USING 2-D MODELS OF SNOW/ENERGY BALANCE AND ICE FLOW

---

The snow/ice energy and mass balance model and glacier flow model developed for this project can be used in a number of ways to improve our understanding of the relationship between climate, topography and glacial extent. In this study we focus on using the models to aid in the interpretation of glacial landforms that describe the past extent of alpine glaciers. Traditional approaches to interpreting such features are commonly based on empirical relationships between glacier shape, equilibrium line altitude (ELA), and temperature. Those methods generally neglect spatial variations in snow accumulation that result from topographic controls on energy balance. They also require fairly detailed reconstructions of paleo-glacier shape, which are typically derived from limited field evidence. In this section we demonstrate how 2-D models of energy balance and ice flow improve on those methods by, among other things, explicitly addressing one of the primary controls on both energy balance and ice redistribution in alpine glaciers – the topography itself. Unlike the landforms in the basin, the topography requires little interpretation, is little changed since the last glacial period, and a wealth of data is available to describe it at a variety of resolutions.

Though these models could be applied to virtually any surface, we demonstrate them using data from Bishop Creek, California and, to a lesser extent, two smaller basins – Horton Creek and McGee Creek – within a few kilometers of that basin.

### ACCUMULATION AREA RATIO (AAR) METHOD AND LAPSE-RATE ESTIMATES OF TEMPERATURE DEPRESSION

An alpine glacier consists of an area of net annual accumulation, in the upper colder part of the basin, and an area of lower elevation where there is net annual ablation of ice. The glacier achieves a steady-state mass balance by transporting the ice accumulated in the higher elevations to the lower elevations, where the ice is removed via evaporation and melting. The line separating the



accumulation area from the ablation area is the equilibrium line and, as it generally follows an elevation contour, its elevation is known as the equilibrium line altitude (ELA). At or near steady state, increased glacial extent is associated with an increase in accumulation area and, consequently, a decrease in ELA. A relatively simple method of estimating the climatic difference represented by differences in glacial extent is to apply a simple lapse rate calculation to determine the difference in temperature represented by the difference in ELA of the glaciers. This of course requires the average ELA of the glaciers. That may be readily determined for modern glaciers but it is considerably more difficult to estimate for prehistoric glaciers. Fortunately, many measurements of modern glaciers demonstrate that the accumulation area of an alpine glacier is typically about 65% of the total glacier area (Meirding, 1982; Porter *et al*, 1983). Thus, if the general outline of the glacier can be constructed from glacial moraines, trim lines and other such evidence, its ELA may be estimated by assuming an accumulation area ratio (AAR) of  $\sim 0.65$ . An abundance of geologic evidence in the Bishop Creek basin indicates that the outline of the Tioga II glacier in Bishop Creek was approximately as shown in Figure 6-1A. A polygon defining the entire accumulation and ablation area of that glacier would thus appear as shown in Figure 6-1B. From similar evidence, we estimated the shape of the Tioga II glacier within the Middle Fork and North Fork drainage basins (little evidence of terminal position remains for the South Fork portion of the glacier). That glacier extended to just below the confluence of the South and Middle Forks. From the hypsometry of the basin within those areas (Figure 6-2), AAR-based estimates of ELA for the Tioga II and Tioga IV glaciers are 3200 and 3300 meters, respectively. ELAs of the small cirque glaciers that presently exist in the basin are about 3800 m; so the ELA depression associated with the larger glaciers is approximately 500 to 600 meters. Assuming an environmental lapse rate of  $\sim 7^{\circ}\text{C}/1000\text{ m}$ , the temperature decreases associated with the Tioga and Confluence glaciers are on the order of  $3.5^{\circ}\text{C}$  and  $4^{\circ}\text{C}$ , respectively.

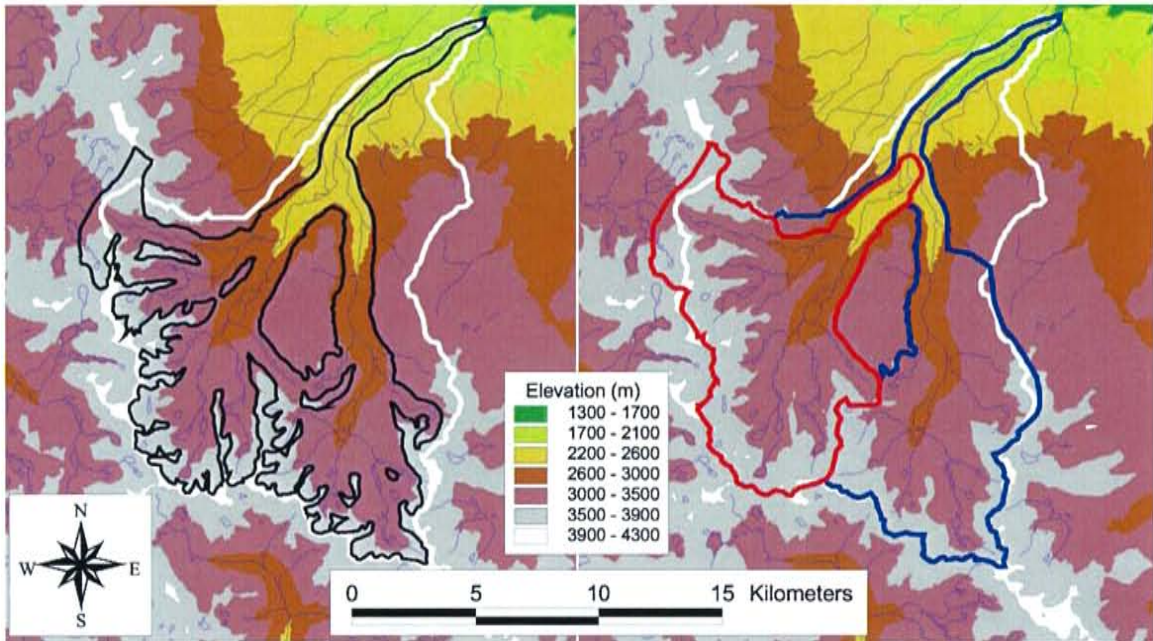


Figure 6-1. USGS Digital elevation model (DEM) for the area of the Bishop Creek drainage basin with stream and stream diversions from the USGS hydrography digital line graph map. Drainage basin for Bishop Creek above Coyote Creek is shown in white. Black outline (A) is the Tioga maximum ice extent as inferred from field mapping of glacial features. Right-hand figure shows the areas used for calculating integrated surface balance for the Tioga maximum glacier (blue outline) and the Tioga IV glacier (red outline) in Bishop Creek.

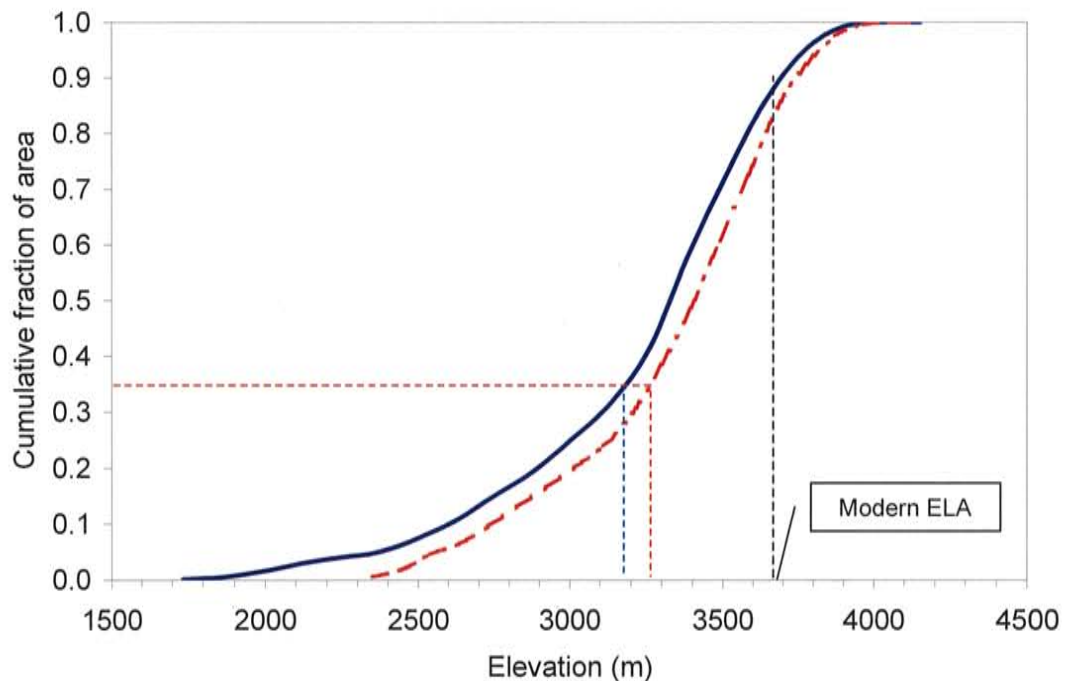


Figure 6-2. Hypsometric curves for the areas defined in the polygons shown in Figure 6-1. Solid line is hypsometric curve for the Tioga I glacier area, dashed line is for the Tioga IV glacier. Dashed vertical lines indicate elevations that would describe an accumulation area ratio of 0.65. The ELA of the modern glaciers, approximately 3700 meters, is shown for comparison.

Simple lapse rate estimates are prone to error because they commonly neglect other climatic controls on snowline and ELA, not the least of which is the relationship between precipitation and elevation. Though this can be accounted for by considering the modern elevation-distribution of seasonal snowpack thickness, a more difficult problem lies in determination of the actual ELA depression, which requires comparison of the modern glacial ELA with that of the paleoglaciers. The modern cirque glaciers exist only because of the dramatically decreased radiation incident in the extremely protected cirques that exist in the rugged topography near the crest. The ELA on those glaciers is thus much lower than if the gentler relief of the lower mountain slopes extended up to and beyond those elevations.

Differences in ELA therefore reflect more factors than can be accommodated with a simple lapse rate model, and conversion between changes in temperature or other climate parameters, and changes in snow distribution, must account at least for the most influential of these factors. The energy and mass balance model developed for this study is designed to perform that function.

#### **APPLICATION OF THE 2-D SNOW AND ENERGY BALANCE MODEL TO THE RELATIONSHIP BETWEEN GLACIERS AND CLIMATE**

The energy and mass balance model calculates the monthly accumulation and loss of snow under climatic conditions prescribed as a change from the existing climate. In addition to temperature and precipitation, prescribed changes may include virtually any of the climatic inputs or constants incorporated in the model, including, for example, wind speed, surface albedo, snow surface temperature, cloudiness, and turbulent heat transfer coefficients. Model output includes tabulated monthly and average annual meteorological and energy balance values for selected locations on the grid and a final grid of net annual snow (water equivalent) accumulation. Figure 6-3 displays the net annual accumulation map for a simulation of modern climatic conditions. The model predicts that great depths of snow could be removed from virtually all but the most rugged parts of the crest. Near

the mouth of Bishop Creek, for example, the net accumulation map indicates that melting and sublimation/evaporation could remove >10 meters of snow water equivalent annually. A shaded relief image (Figure 6-4) of the higher elevation parts of the drainage illustrates the importance of aspect on the distribution of modern snowfields and glaciers. Areas of significant accumulation are almost entirely restricted to the north sides of steep ridges and peaks, where shade occurs during much of the day.

Figure 6-5 shows average annual values of the main energy balance components for South Lake, in the South Fork of Bishop Creek for simulations of the modern climate and climate that is 4°C colder. Colder temperatures are reflected primarily in a decrease in sensible heat transfer to the snow and an increase in the energy removed via longwave radiation and sublimation and evaporation.

#### ***CLIMATIC SENSITIVITY OF ELA***

Snow accumulation predicted by the energy and mass balance model displays a high degree of variability within the basin, resulting primarily from topographic control on the net shortwave radiation balance. Equilibrium line altitude in the basin is thus a very local effect that depends not only on climate but also on topography. Under modern conditions for example, the ELAs of various snowfields and glaciers within the Bishop Creek drainage vary by at least 100 meters. In order to use a single parameter to compare the snow accumulation distribution under such conditions to those in which most of these independent glaciers would coalesce to form one large glacier, we define here the local ELA as the average ELA of all the permanent snowfields and glaciers within the basin.

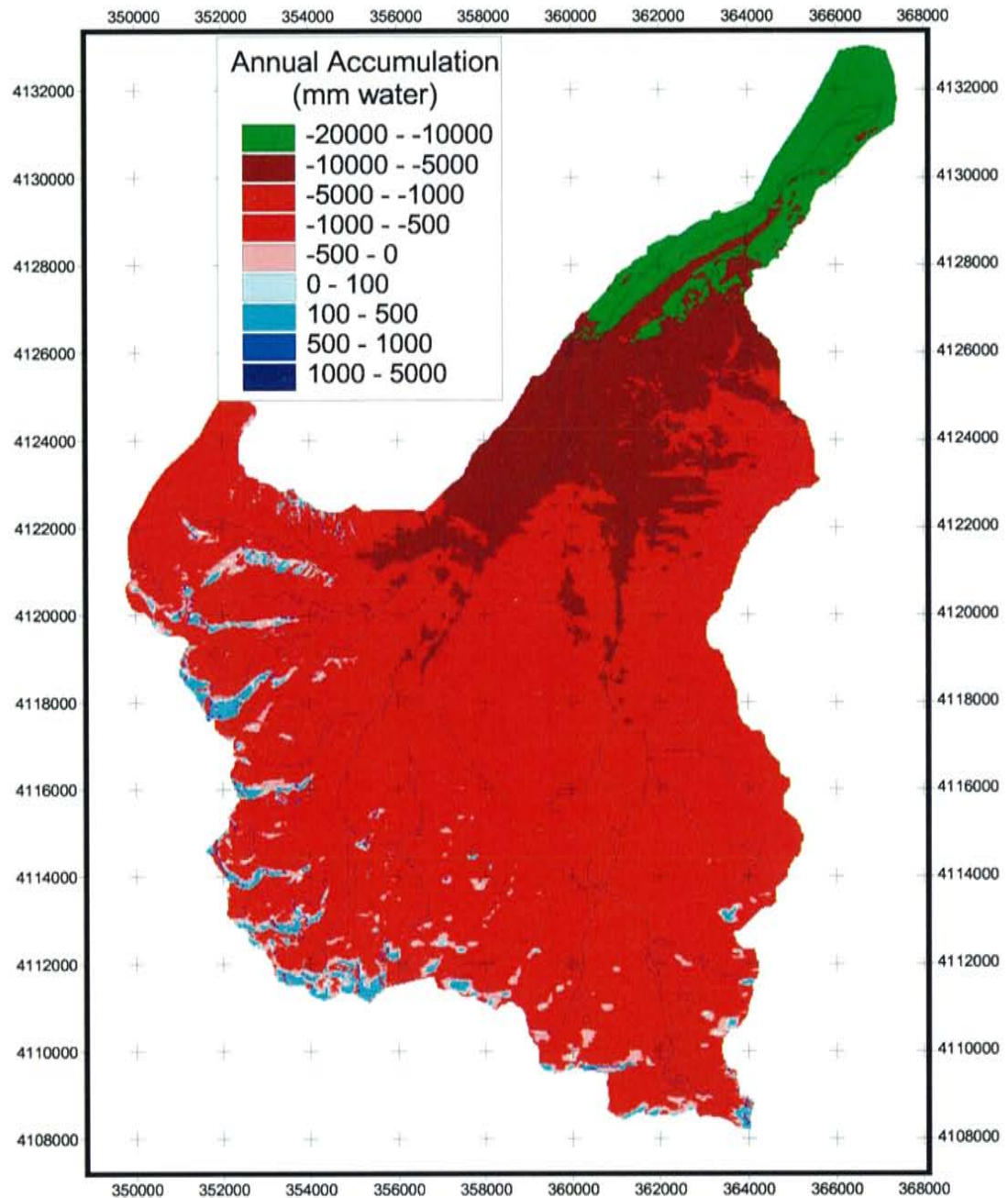


Figure 6-3. Modeled net annual accumulation of snow (mm of snow water equivalent) in the Bishop Creek basin for modern climatic conditions. Blue indicates areas of positive net accumulation. Red indicates areas of negative net accumulation (ablation). Grid is universal transverse mercator projection showing northing and easting in meters.



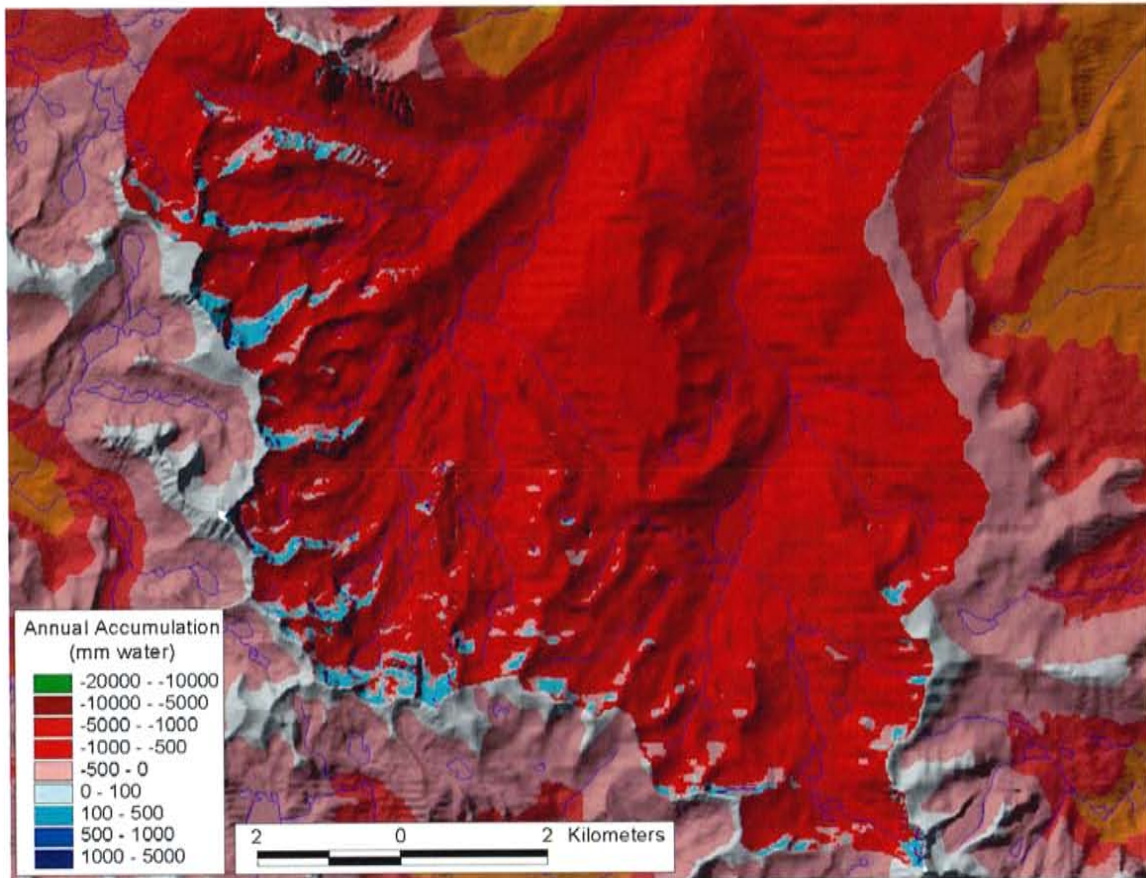


Figure 6-4. Enlarged view of a portion of Figure 6-3 shown as shaded relief. Color-coding for net annual accumulation of snow (mm of snow water equivalent) is only approximate due to relief shading. Areas outside the Bishop Creek drainage basin are color-coded by elevation, not snow accumulation.

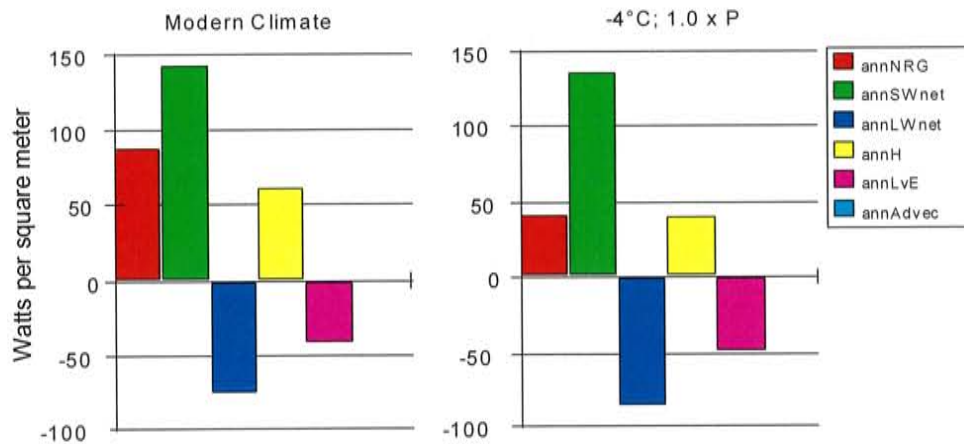


Figure 6-5. Comparison of annual average energy fluxes at South Lake in the South Fork of Bishop Creek for (left) modern climatic conditions and (right) a temperature decrease of 4°C and no change in precipitation. Bars are, left-to-right, the average annual energy used for melting, and average annual shortwave, longwave, sensible, and latent energy fluxes.

To examine the climatic sensitivity of this local ELA, we used the energy and mass balance model to simulate a wide variety of colder and/or wetter climates in Bishop Creek (Figure 6-6). We then calculated the local ELA for each net accumulation map from the mean of all grid cell elevations with positive<sup>10</sup> accumulation rates below 10 cm yr<sup>-1</sup>, and plotted the ELAs as a response

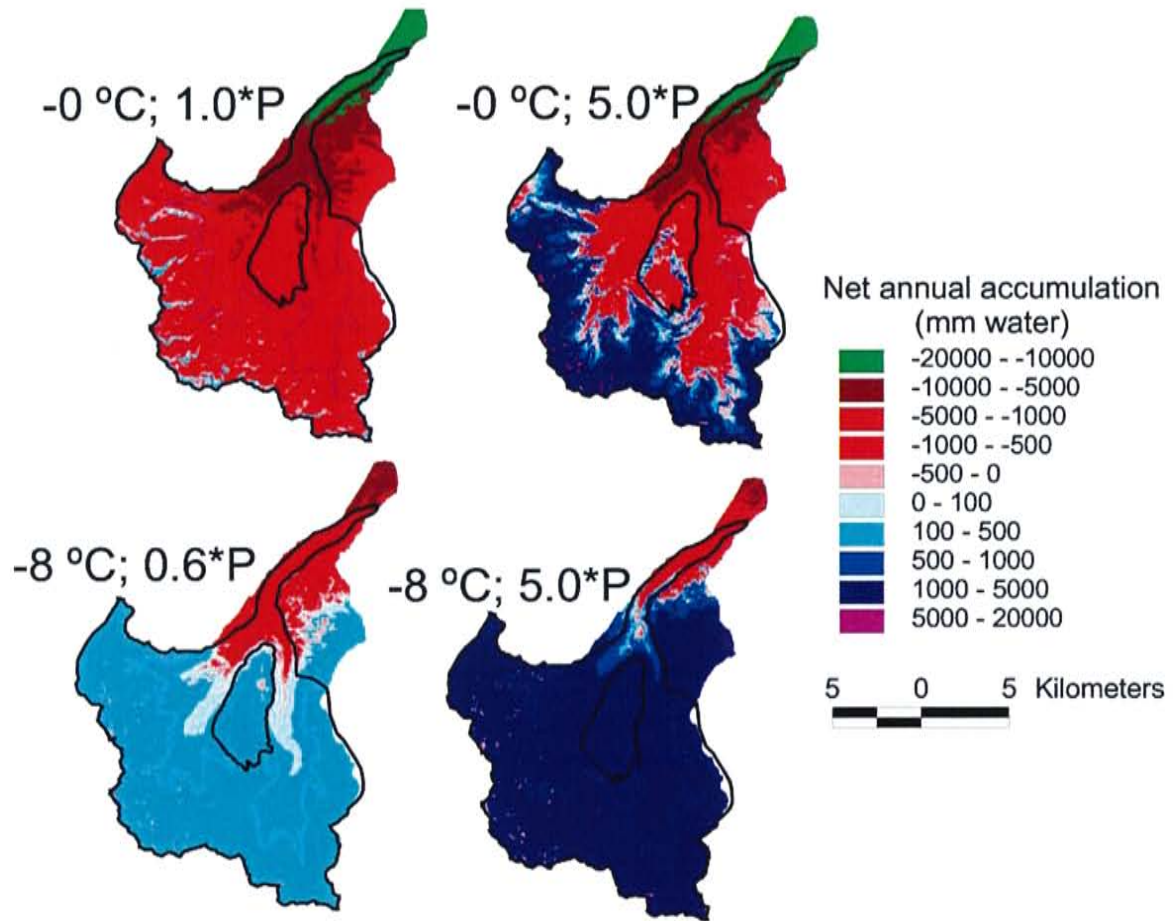


Figure 6-6. Simulated net annual snow (water equivalent) accumulation in Bishop Creek for four different climatic conditions. Climatic changes are indicated by the difference in temperature from modern ( $^{\circ}\text{C}$ ) and the rate of precipitation relative to modern conditions (i.e.  $5.0*P$  = five times the modern precipitation rate). The region between the two black polygons illustrates the area that, based on geological evidence, we considered the likely contributing area for the Bishop Creek glacier during the last glacial maximum. Thin blue line is the 3300-m elevation contour.

<sup>10</sup> Only positive near-zero values were used because near-zero negative values commonly occurred on steep slopes due to the snow sloughing function built into the model. Including those values artificially raises the ELA. In retrospect, it would be relatively easy to repeat the slope calculation to exclude those cells and the average should, in the future, include both positive and negative values near zero.

surface relative to changes in temperature and precipitation (Figure 6-7)<sup>11</sup>. Throughout a wide range of temperature and precipitation changes, local ELA appears to maintain an essentially constant relative sensitivity to temperature versus precipitation. [Seltzer, 1994] noted that ELAs of modern glaciers typically reflect a mutual dependence of temperature and snow accumulation between  $2.5 \times 10^{-3}^{\circ}\text{C}/\text{mm}$  and  $3.3 \times 10^{-3}^{\circ}\text{C}/\text{mm}$ . Calculated ELAs for Bishop and Horton Creeks, reflect a similar relationship, about  $2.3 \times 10^{-3}^{\circ}\text{C}/\text{mm}$  precipitation<sup>12</sup>.

Though climatic sensitivity of ELA is generally similar throughout most of the range we examined, it is least under modern climatic conditions, and appears to decrease in extremely cold and wet conditions. We performed only a few simulations in those more extreme conditions, however, and the latter conclusion may be an artifact of insufficient data. The lower sensitivity under modern conditions can be explained by the hypsometry of the basin. The ELA shifts upward or downward in response to changes in the energy balance and snow accumulation rate. In this basin, further upward movement of the ELA is limited by the lack of area at elevations greater than about 3800 meters, and by the extreme relief at the headwall of the basin, which provides numerous shady recesses where permanent snowfields may persist under otherwise very unfavorable conditions. The local ELA is thus very effectively buffered against upward movement by the hypsometry of the basin. The patchy distribution of permanent snow and glaciers in the basin demonstrates that the current ELA is largely a result of this buffering effect. The ELA cannot descend much below the shaded cirques and other recesses until temperature is sufficiently reduced, or precipitation increased, to balance the large radiation incident on the surrounding unshaded areas.

---

<sup>11</sup> The ELAs calculated in this manner do not realistically represent those of glaciers that would develop in the basin because they are based on the existing topography, not the topography that includes the glacial ice. Nonetheless, an analysis of the climatic sensitivity of these ELAs, as described below, should be broadly similar to those that would be calculated on simulated glacier surfaces, and are, at least, illustrative of the analytical value of this approach.

<sup>12</sup> Seltzer [1994] considered that relationship in terms of estimated snow accumulation rates that were directly proportional to precipitation.



Simple lapse rate estimates of temperature depression from ELA depression assume that ELA sensitivity to temperature is relatively constant and predictable. The ELA response surface of Figure 6-7 shows that the sensitivity of ELA to temperature and precipitation increases by a factor of about two in going from the modern climate to a climate about 7°C colder. This demonstrates the degree of error that may be involved in assuming a constant relationship between temperature and ELA, aside from those involved in simply determining the slope of the assumed linear relationship. In this basin, our simple lapse rate interpretation of our AAR-derived ELA for the Tioga II glacier suggested a temperature depression of about 4°C. In contrast, using our 2-D energy and mass balance model to interpret the same ELA depression suggests a temperature depression that, assuming no difference in precipitation, is closer to 6°C - a considerable difference.

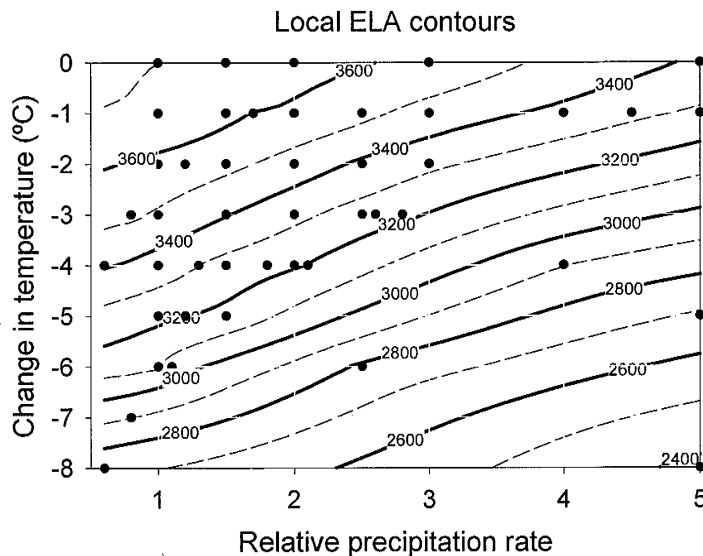


Figure 6-7. Contours of equilibrium line altitude (ELA) derived from application of the spatially distributed snow and energy balance model. The local ELA includes shading and shadowing effects of the terrain. Circles indicate simulations on which the contours were kriged.

Though the climatic sensitivity of local ELA appears to be only slightly non-linear, it is not readily apparent to what degree that sensitivity is influenced by topography. Indeed we cannot say even whether the sensitivity to climate would be of greater or lesser magnitude or more or less uniform if the topographic

effects were removed. In order to consider the effects of climate on ELA independent of topographic effects, we define a hypothetical 'regional ELA' as the ELA that would exist if all surfaces were horizontal and unaffected by surrounding terrain. To examine the climatic sensitivity of this regional ELA, we again simulated the net annual snow accumulation distribution that would exist

under a wide range of climatic conditions, this time for a hypothetical basin of horizontal surfaces with an unlimited range of elevation, a flat hypsometric curve (i.e. equal area at each elevation), and a climate identical to that of Bishop Creek. For efficiency, we made these calculations using the Mathcad worksheet included in Appendix E. It is essentially a 1-D implementation of the energy and mass balance program coded in the Arcview scripting language, with the exception of the shortwave radiation component, which neglects topographic effects. The resultant response surface (Figure 6-8) illustrates the sensitivity of the regional ELA to temperature and precipitation.

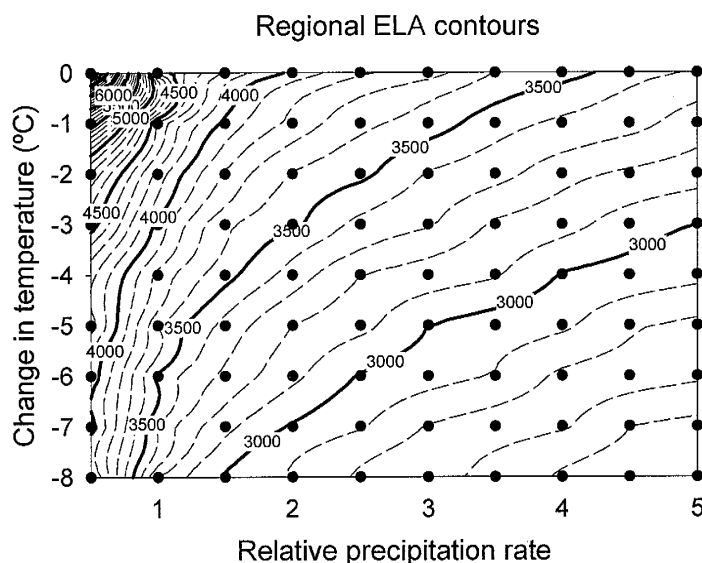


Figure 6-8. Regional ELA as a function of changes in temperature and precipitation from the modern climate. Circles indicate simulations for which ELA was calculated. Calculations are as shown in Appendix E.

The response is remarkably different than that of the local ELA. Here overall sensitivity and relative sensitivity to precipitation increase dramatically as conditions become drier. The greater sensitivity to precipitation reflects, in this case, the lack of the protected cirque areas and limiting hypsometry that serve to buffer the maximum local ELA. Direct

comparison of the calculated local and regional ELAs (Figure 6-9) emphasizes their different dependence on temperature and precipitation. As one might anticipate, the regional ELA under modern conditions is higher than the local ELA, by ~600 m according to the models. As precipitation and temperature decrease, the contrast between the response surfaces becomes more pronounced. At the opposite extreme - very wet conditions but under the modern temperature regime - the surfaces converge. The difference in response can be explained by considering, in addition to hypsometric effects, how the energy and mass balance is affected by changes in

precipitation, temperature and topography. Changes in precipitation affect not only the amount of precipitation at each location, but also the slope of the relationship between precipitation and elevation. The slope of the temperature vs. elevation relationship, on the other hand, is constant. In our model, precipitation is roughly linear in elevation, and the proportionality constant for that relationship thus decreases linearly with precipitation. As precipitation decreases, the regional ELA moves upward into colder and colder temperatures, where shortwave radiation increasingly dominates the energy balance and more snow is removed by evaporation and sublimation than by melting. Shortwave radiation is only a weak function of elevation, however, so as precipitation decreases, a greater change in the ELA is required to reduce the input energy enough to compensate for the decreased snowfall. This effect is virtually non-existent in the local ELA however, because the increasing relief with increasing elevation makes the shortwave radiation component very sensitive to elevation.

At the other extreme in precipitation, the opposite occurs. The ELA descends as precipitation increases, because warmer conditions are required to melt the greater annual snowfall. The sensible heat component thus increasingly dominates the energy balance at the ELA. Since temperature is largely independent of topographic relief, the local ELA becomes less and less sensitive to topography as precipitation increases and eventually becomes identical with the regional ELA. The relative constancy in the relationship between local ELA, temperature and precipitation is interesting, as it indicates that a simple lapse-rate interpretation of climatically induced changes in local ELA yields a reasonable approximation of the actual temperature change because of the strong control exerted by the topography, not despite it. The shape of the local ELA response surface indicates that topographic effects have effectively shifted the energy and mass balance of the system into a region where sensible heat exchange is far more important than it would be without those effects.

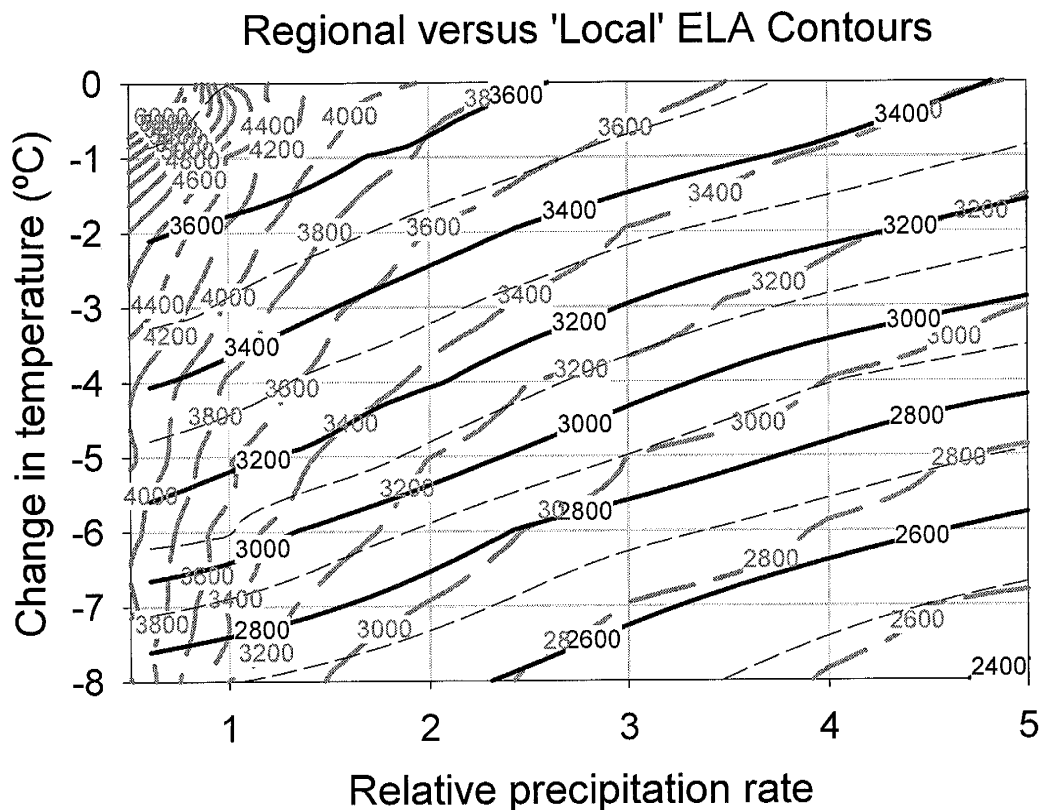


Figure 6-9. Comparison of regional ELA contours (dashed red curves) and 'local ELA' contours (blue curves).

#### ***SURFACE-INTEGRATED WATER BALANCE***

We can take several approaches to using the net annual ice accumulation maps produced by the mass and energy balance model to determine what climatic conditions could produce a particular glacial advance. The simplest approach is to use field evidence to reconstruct the shape of the glacier that existed and construct from that a surface that includes the entire accumulation area available to the glacier and describes, in the ablation area, the actual limits of the glacier (Figure 6-1). Integration of the net accumulation rate over that area provides an indication of the net balance of the hypothetical glacier surface. For the hypothetical glacier shape to be at steady state requires that this surface integrated water balance equal zero (ie. no accumulation or ablation excess). Examples of net annual snow accumulation maps meeting this criterion for the Tioga II and Tioga IV glaciers in Bishop Creek are shown in Figure 6-10. The ELA for the net annual snow accumulation map in

Figure 6-10 appears to be about 2800 meters. Our grid-based calculation of the ELA for that map (temperature depression = 6°C; modern precipitation rate), however, is about 3100 meters. This emphasizes the high degree of variability in the topographically influenced ELA and the difficulty in using it as an index of glacial extent.

To find the range of climatic conditions that could produce the Tioga II and Tioga IV glaciers using the modeled snow accumulation distributions, we contoured the surface integrated water balance for the assumed Tioga II and Tioga IV shapes. Figure 6-11 shows just the contour for each area that corresponded to an integrated water balance of zero. Those contours reflect the climatic conditions that could produce the steady-state glaciers with the presumed shape. The curves indicate that the Tioga II glacier could be produced by a temperature depression of about 6°C, with no change in precipitation; or by a precipitation increase of a factor of about six, and no change in temperature. Interpreted as a difference in temperature, the climatic conditions associated with the Tioga IV advance appear to have been about 1°C warmer than during Tioga stage IV. The curves also indicate that the relative sensitivity of the glaciers to temperature versus precipitation increases slightly with precipitation

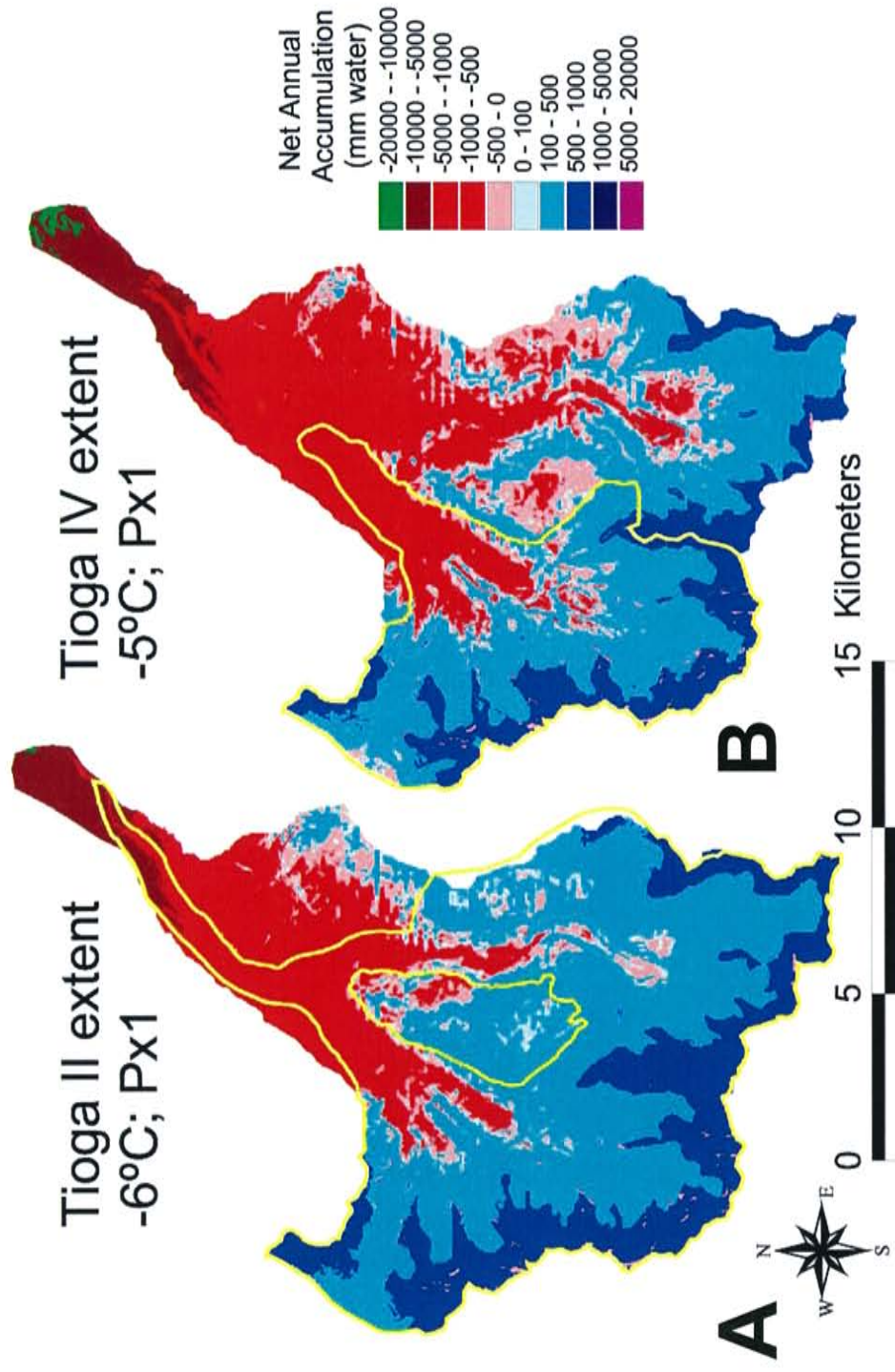


Figure 6-10. Simulated net annual accumulation distribution in Bishop Creek assuming a temperature depression of (A) 6°C and (B) 5°C. The net accumulation patterns produce near-zero surface integrated water balances for the Tioga maximum glacier (A) and the Confluence glacier (Tioga IV) (B). Yellow polygons indicate the areas over which the water balance was integrated (excluding area within inner polygon in A). Thin blue lines are the 3000-m and 3100-m contours, respectively, corresponding to an AAR of 0.65. Px1 indicates precipitation rate is 100% of modern.

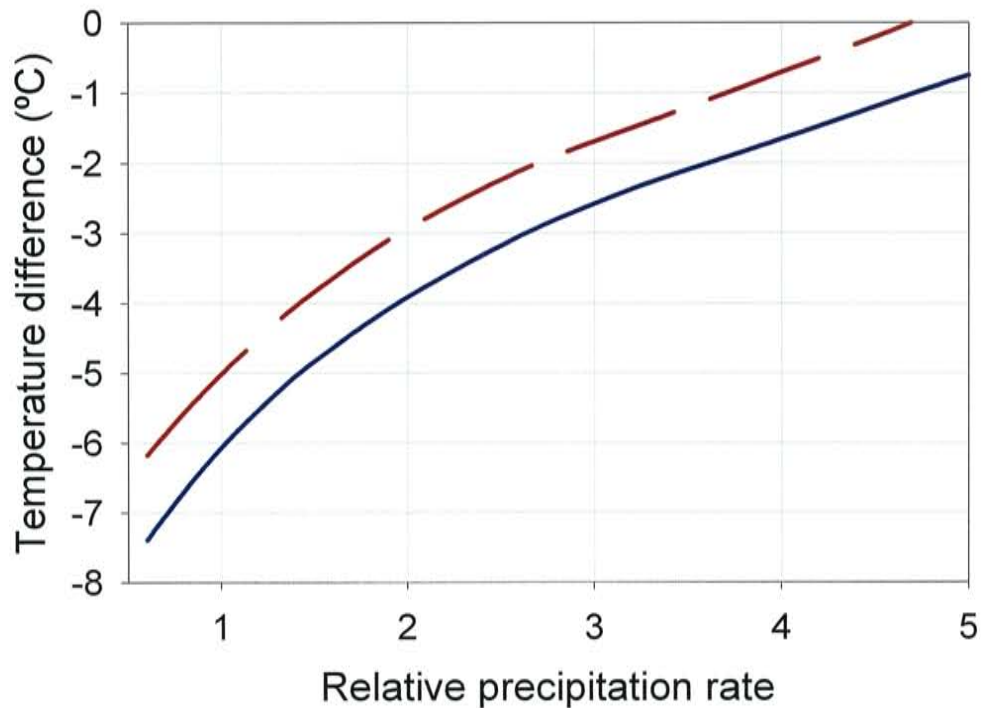


Figure 6-11. Curves representing zero integrated net accumulation for the Tioga II (solid line) and Tioga IV glacier (dashed line) in Bishop Creek. Integrated balance is over the polygon areas shown in Figure 6-1.

#### CLIMATIC SENSITIVITY OF AAR.

The glacier sensitivity indicated by these curves is quite different than that inferred if one assumes a constant relationship between ELA and glacier area (Figure 6-7). The local ELA contours suggest that if temperature remains constant an order of magnitude increase in precipitation would be required to depress ELA enough to produce the Tioga II glacier with an AAR of 0.65. Though large, the surface integrated water balance approach indicates that the required increase would be on the order of half that. Since the two approaches are based on the same assumed glacier shapes and net annual snow accumulation distributions, the contours developed by integrating water balance over surface area clearly do not reflect a constant accumulation area ratio. The variability in the AAR can be seen in a plot of AAR as a function of average water balance (Figure 6-12) within the area assumed for the Tioga II and Tioga IV glaciers. The average water balance is zero for simulations

that would yield a steady state glacier. Most of the conditions that satisfy that criterion intersect the zero net balance line at an AAR of  $0.7 \pm 0.05$ . The higher values reflect colder, drier climates, where accumulation occurs over a large fraction of the basin but at a low rate so that a relatively small ablation area is needed to dispose of the accumulating ice.

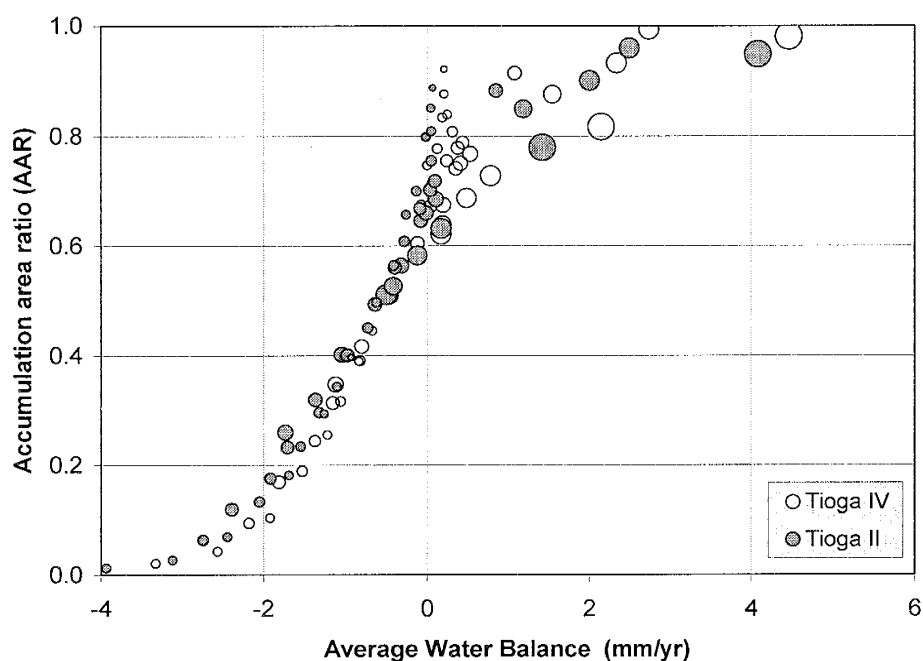


Figure 6-12. Accumulation area ratio versus average annual snow accumulation in the polygons shown in Figure 6-10 for the Tioga II (gray circles) and Tioga IV (open circles) glaciers. The average water balance is zero for distributions that produce a steady-state glacier. Area of symbols is proportional to precipitation rate.

The contours shown in Figure 6-11 suggest that the temperature difference between the Tioga IV and Tioga II glaciations is about  $1^{\circ}\text{C}$  and that a temperature depression of  $6^{\circ}\text{C}$ , with no change in precipitation, would produce the Tioga II advance. This agrees well with other estimates of temperature depression in the Great Basin [Dohrenwend, 1984].

This approach provides a relatively rapid and simple means of using the detailed net accumulation maps of the snow/ice energy and mass balance model to interpret glacial evidence. No assumptions about the value of the AAR or its relationship to ELA are necessary and it allows a



detailed accounting of topographic effects on energy balance. An additional refinement can be incorporated by using the reconstructed surface of the glacier as the surface for the snow/ice energy and mass balance calculations. Our preliminary tests using that approach yielded results similar to those discussed here, with slightly greater climate changes required to produce the same glaciers. Growth of the glacier brings the surface up to regions more exposed to shortwave radiation than the underlying canyons, although this effect is somewhat offset by the colder temperature and increased precipitation due to the increased elevation. The main difficulty in applying this approach is the need to know, a priori, the shape of the glacier. Although that may be straightforward in the ablation area, it is considerably more difficult in the accumulation area (see, for example, Figure 6-6 and Figure 6-10). The approach is therefore more effective for larger glaciers, where the exact shape of the glacier is generally better known, and the areas where the shape is not well known are likely to be relatively small compared to the whole glacier and therefore an insignificant part of the net mass balance.

#### **THE 2-D SNOW/ICE ENERGY AND MASS BALANCE MODEL COUPLED TO A 2-D FLOW MODEL**

The difficulty in applying the assumed shape – integrated surface balance approach increases when smaller glacial advances are considered. Moraines and other depositional features for smaller advances are generally much less distinct and trim-lines are generally only apparent for the largest advances. Moreover, the method has no predictive capability, as it requires prior knowledge of glacier shape and extent. To develop a method without those limitations, we created the 2-D, map-plane, finite difference glacier flow model described in the previous chapter to simulate the growth to steady-state of the glaciers that would develop from the net annual accumulation rates predicted by the mass and energy balance model. The flow model calculates the time-dependent ice distribution using the net annual accumulation map produced by the energy and mass balance model as the source term. Output of the model is ice thickness and/or surface elevation.

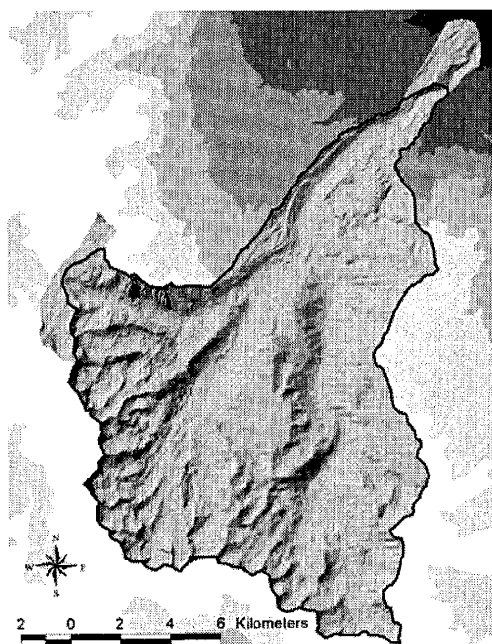


Figure 6-13. Shaded relief image of the area of used for modeling glacier snow/ice energy and mass balance and glacier flow in Bishop Creek. Black line is the watershed boundary.

#### MODEL DOMAIN AND EXAMPLE SIMULATIONS

We apply the model on an elevation surface derived from USGS 30-m DEMs, assembled and trimmed to the shape of the basin of interest. For Bishop Creek, this includes (Figure 6-13) the drainage basin above Coyote Creek, an extension below Coyote Creek to allow the glacier to flow beyond the estimated maximum position, and the estimated area of contribution from across the crest in Humphreys Basin. A single smaller area was used for Horton and McGee Creeks, which share a common boundary that extends eastward from the crest.

Figure 6-14 and Figure 6-15 illustrate examples of simulated glaciers in Bishop Creek for modern conditions and for three climatic conditions with no change in precipitation but with temperature depressions ranging from  $1^{\circ}$  to  $3^{\circ}\text{C}$ . The intricacies in the shapes of the glaciers that make it difficult to reconstruct their shape only from glaciomorphologic evidence are clear, and the patterns of development and extension appear reasonable but not obvious. Increases in the overall extent of the glaciers are relatively minor for temperature depressions of up to  $2^{\circ}\text{C}$ , but additional cooling, to  $-3^{\circ}\text{C}$ , produces a marked size increase. Ice thickness in the Middle Fork for the  $-3^{\circ}\text{C}$  simulation is nearly double that at  $-2^{\circ}\text{C}$  and the North Fork contains a 7 kilometer long glacier with a maximum thickness greater than 100 meters.

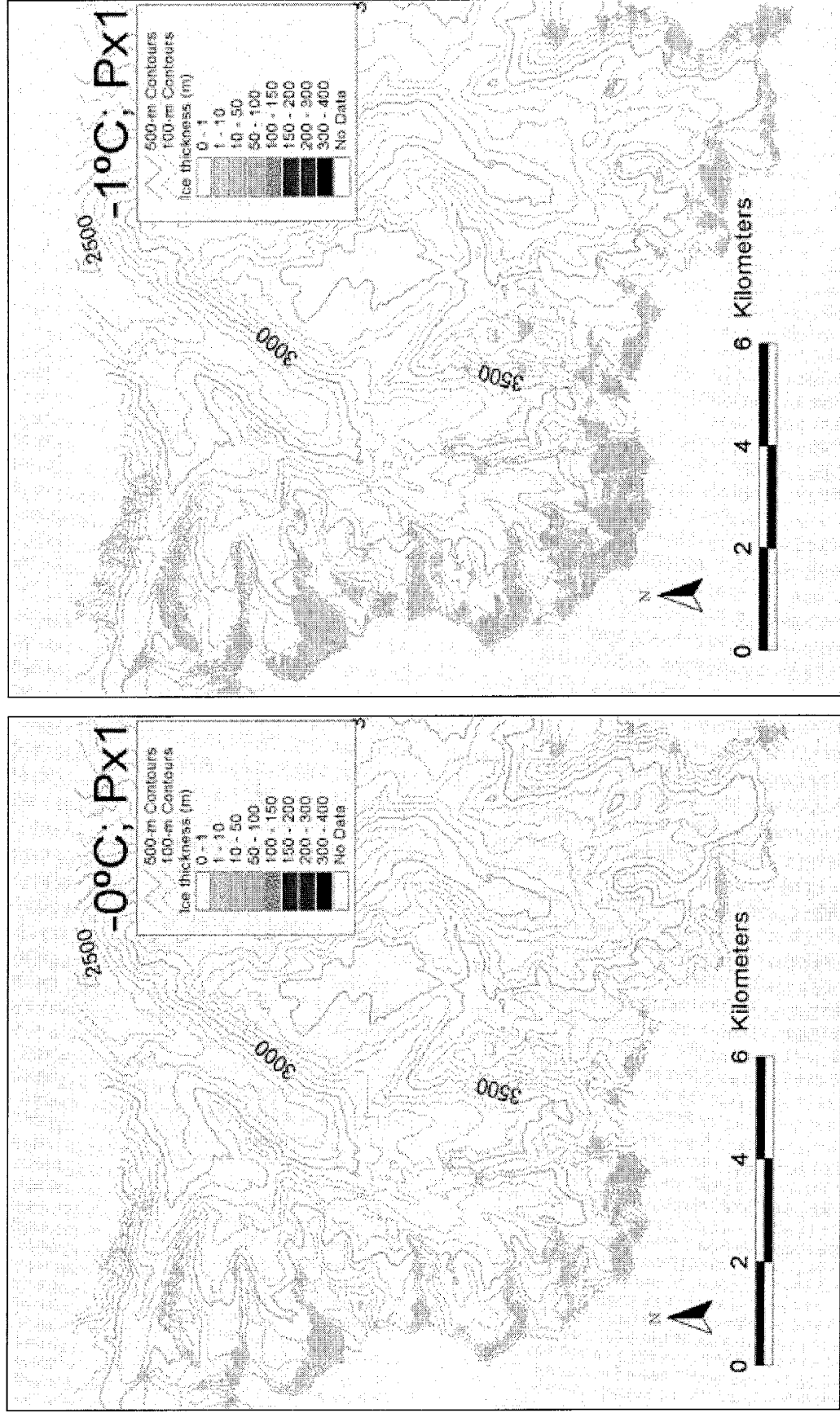


Figure 6-14. Simulated glacier output for the Bishop Creek basin for (left) modern precipitation rate and temperature and (right) a decrease in temperature of 1°C and no change in precipitation.

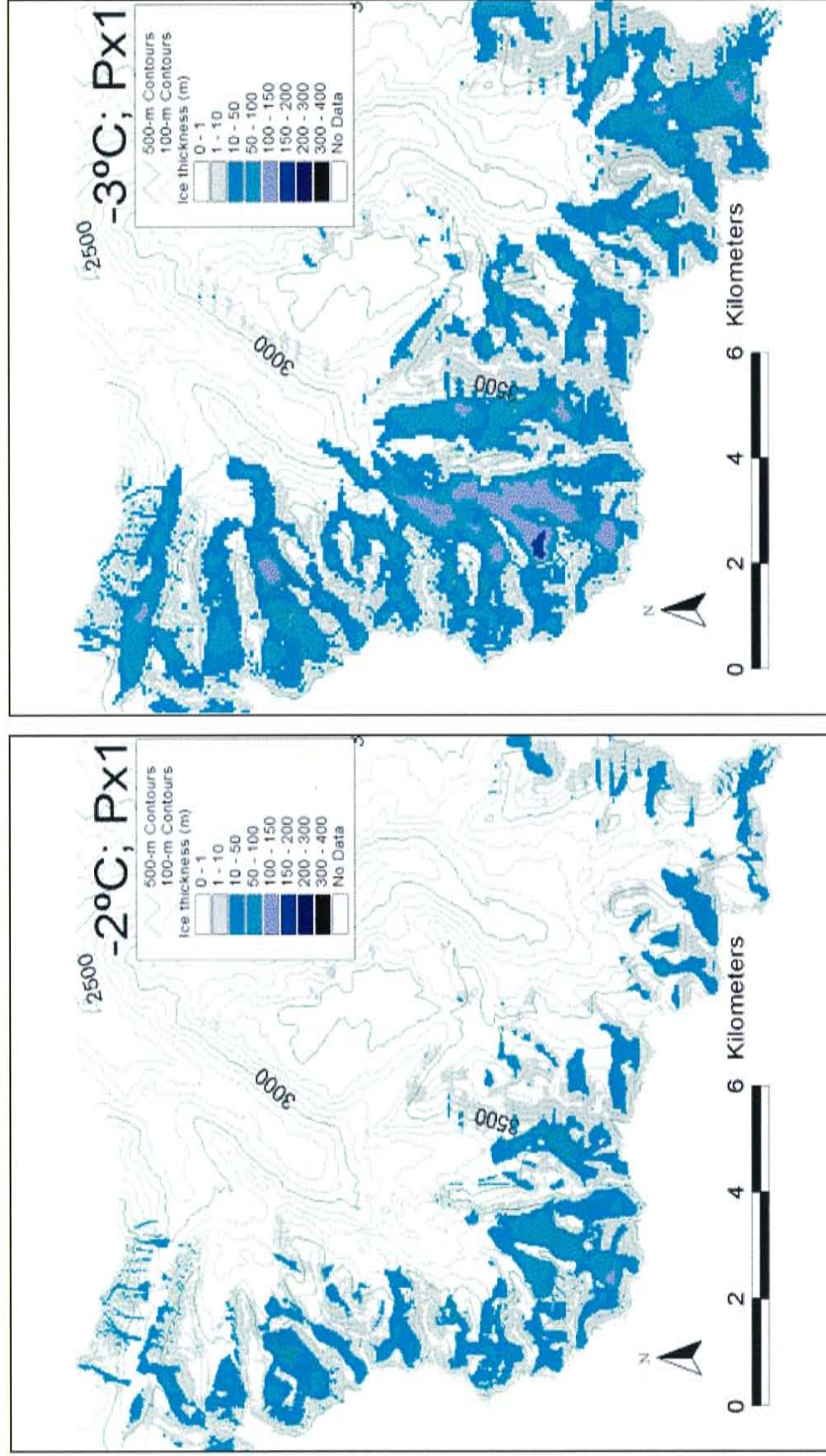


Figure 6-15. Simulated glacier output for the Bishop Creek basin assuming no change in precipitation and a decrease in temperature of (left) 2°C, (right) 3°C.

#### ***SIMULATED GLACIER DISTRIBUTION UNDER MODERN CLIMATE***

The snow/ice energy and mass balance model used to produce the net accumulation maps for the ice flow model was based on our best estimates of the energy balance parameters and monthly meteorological norms for the Bishop Creek watershed, and we made no attempt to calibrate the model after completion. Despite this, the coupled snow accumulation and glacier flow models produce very reasonable net annual accumulation rates and ice thickness maps for simulated modern glaciers. The distribution of glaciers and permanent snowfields, in particular, shows remarkably good agreement with the distribution shown in the USGS topographic maps of the area (Figure 6-16 through Figure 6-19). Calibration of the model would probably require more accurate maps of the glaciers and ‘permanent’ snowfields in the basin than are currently available. Accurate mapping of the glaciers and snowfields is complicated by the rockfall that obscures significant portions of many of the modern glaciers, or in other cases, forms rock glaciers. Standard digital elevation models also do not differentiate permanent snow from earth, and extant glaciers are thus part of the land surface over which our simulated glaciers flow. The simulated glaciers thus must have a slightly different form and flow along at least a slightly different path than their real counterparts.

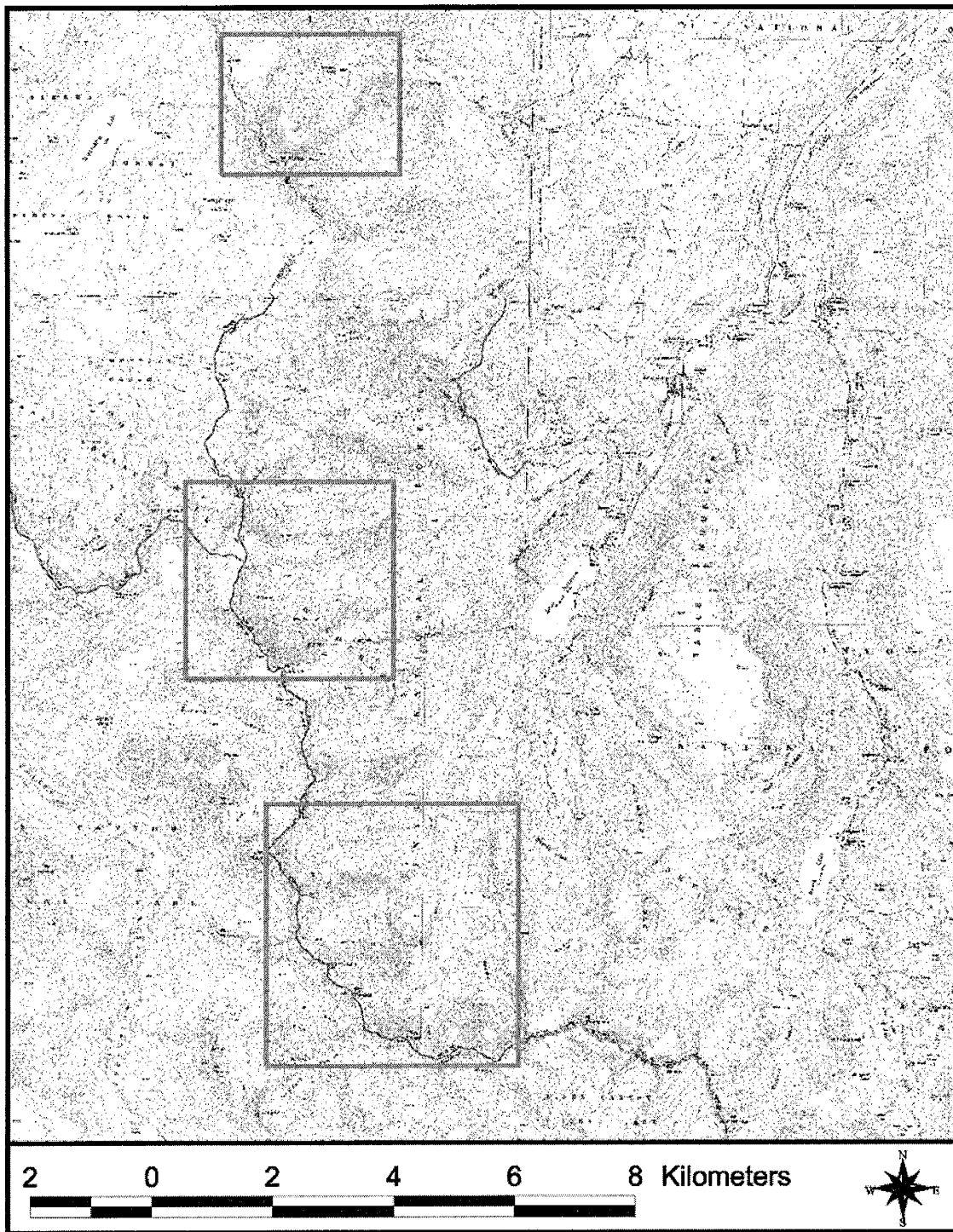


Figure 6-16. Simulated glacier distribution in the Bishop Creek area under modern climate. Boxes show locations of glaciers in following plate. Simulated glaciers (grey and blue shaded areas) are overlain by the USGS topographic maps of the area.



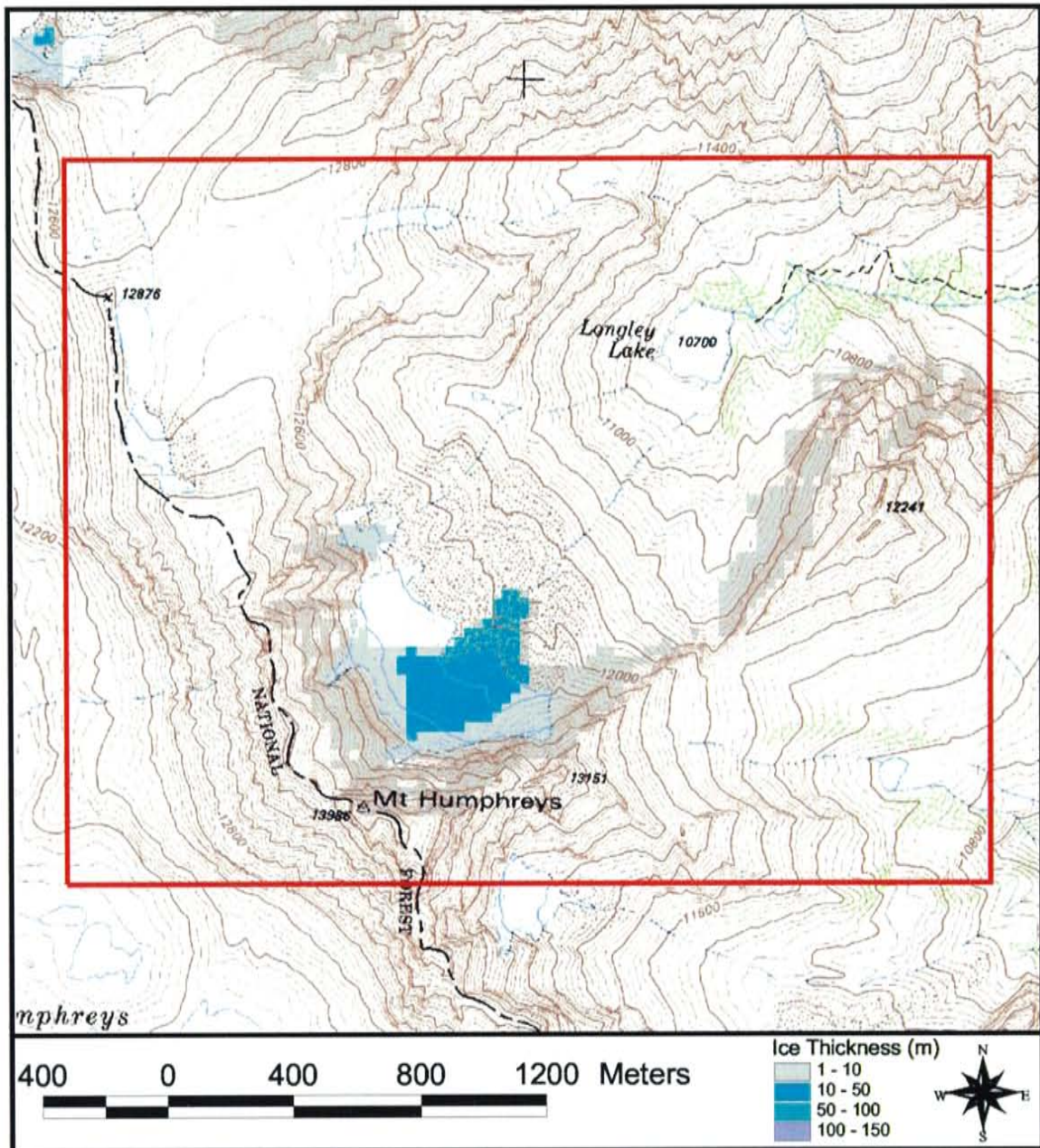


Figure 6-17. Comparison of simulated glacier distribution under modern climate with the USGS-mapped glaciers and permanent snowfields for the area below Mt. Humphreys at the head of McGee Creek. Simulated glaciers (grey and blue shaded areas) are overlain by the USGS topographic maps of the area. Existing glaciers are mapped in white with blue contour lines.



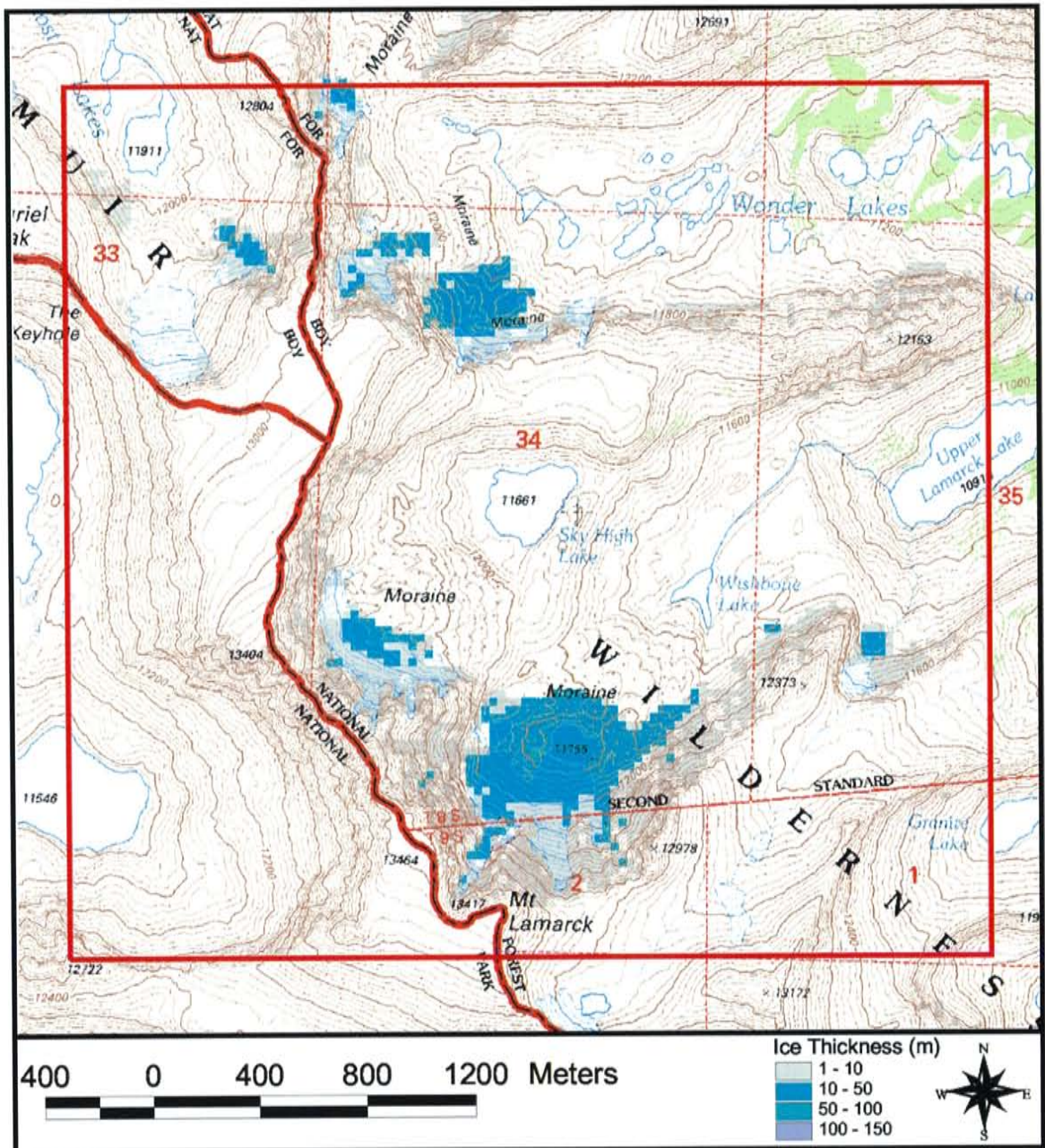


Figure 6-18. Comparison of simulated glacier distribution under modern climate with the USGS-mapped glaciers and permanent snowfields for the area above Upper Lamarck Lake in the north fork of Bishop Creek. Simulated glaciers (grey and blue shaded areas) are overlain by the USGS topographic maps of the area. Existing glaciers are mapped in white with blue contour lines.



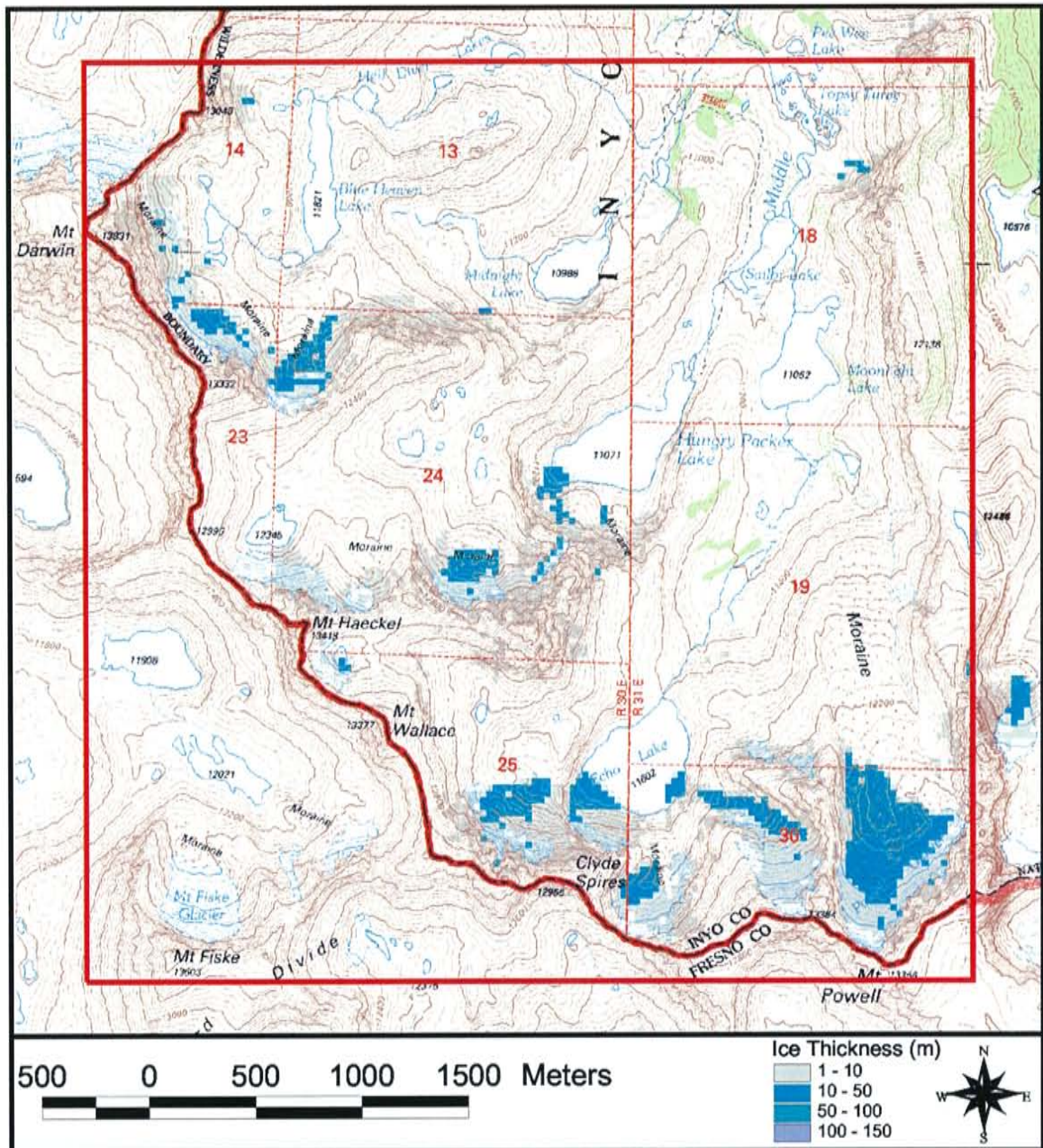


Figure 6-19. Comparison of simulated glacier distribution under modern climate with the USGS-mapped glaciers and permanent snowfields for the area near the Powell Glacier in the middle fork of Bishop Creek. Simulated glaciers (grey and blue shaded areas) are overlain by the USGS topographic maps of the area. Existing glaciers are mapped in white with blue contour lines.

#### **SIMULATED LARGE GLACIERS – FAITHFULNESS TO FIELD EVIDENCE**

The glacier flow model includes only two adjustable parameters, the coefficients related to sliding velocity and ice deformation. The thickness of the glacier for any given velocity and bed slope is

determined by the magnitude of these coefficients. We initially used the coefficient for ice deformation recommended by Paterson [1994] with a corresponding sliding velocity determined by the average of that relationship as described in several 1-D (along a flowline) modeling studies. We calibrated the flow model by adjusting those constants so that the thickness of the simulated Tioga II glaciers in Bishop Creek matched the geological evidence along Bishop Creek. The same constants were then applied to all subsequent simulations, which included a wide variety of climatic conditions.

Because we tuned the flow parameters to make the simulated glacier thickness match the geological evidence along Bishop Creek, thickness of the glacier in the main canyon cannot be used to estimate how well the glacier model simulates the large glaciers that once occupied the basin. That only small adjustments to the flow constants were necessary to provide that match suggests, however, that the simulated glaciers are at least reasonable facsimiles of real glaciers. Several other lines of evidence make that case stronger. First, we tuned glacier thickness only to the lower part of Bishop Creek and can therefore use the glacier thickness and shape in the upper basin as an indicator of how well the model mimics the shape of the Tioga maximum glaciers. Comparison of our field mapping of the extent of the Tioga-maximum glaciers with a simulated Tioga-maximum glacier shows (Figure 6-20) that the model reproduces the shape and thickness of those glaciers quite well. Second, model-calculated velocities (Figure 6-21) are similar to those of modern glaciers of comparable size and surface slope. Finally, the simulated ice flow directions appear reasonable given the constraining topography. Where evidence of the Tioga-maximum ice flow directions is preserved, in fact, the velocity vectors of a simulated Tioga-maximum glacier match the field evidence as well as can be expected given the scale of the model basemap.

Based on the above observations and other comparisons with field evidence in Bishop, Horton, McGee and Coyote Creek, we conclude that our simulated glaciers mimic the shape and thickness of actual glaciers remarkably well. Because the simulated glacier distributions and shapes are highly

dependent on the mass and energy balance model as well as the glacier flow model, the coupled models should provide an excellent means of examining glacial sensitivity to large-scale changes in climate. We acknowledge, however, that the flow model is based on assumptions that are violated in this application. A more rigorous derivation of appropriate flow laws and/or calibration studies with extant glaciers (in terms of both snow/ice energy balance and ice flow) would be a logical next step in further development of this approach.

#### ***SIMULATED GLACIER DISTRIBUTION UNDER ALTERED CLIMATE***

After choosing flow constants by fitting simulated glaciers to geological evidence, we ran simulations for a wide range of temperature and precipitation combinations to observe the climatic sensitivity of the glaciers and determine which combinations could produce the Tioga and Recess Peak glaciers. Examples of simulated glaciers that reasonably matched certain glacial advances are displayed in Figure 6-23. The upper part of Figure 6-23 illustrates two very different climatic conditions that could produce the Tioga II glacier. The first is only 3°C colder but precipitation is ~260% of the modern rate. The second simulates a climate 6°C colder and precipitation identical to the modern rate. Though both produce essentially the same glacial extent, the glacier is thicker in the wetter climate because the ice flux is higher. The pattern of snow accumulation is also quite different. The model predicts, for example, that Table Mountain – the mesa-like surface between the South and Middle Forks – would be virtually ice free under the warmer, wetter conditions but completely ice covered under the much colder climate.



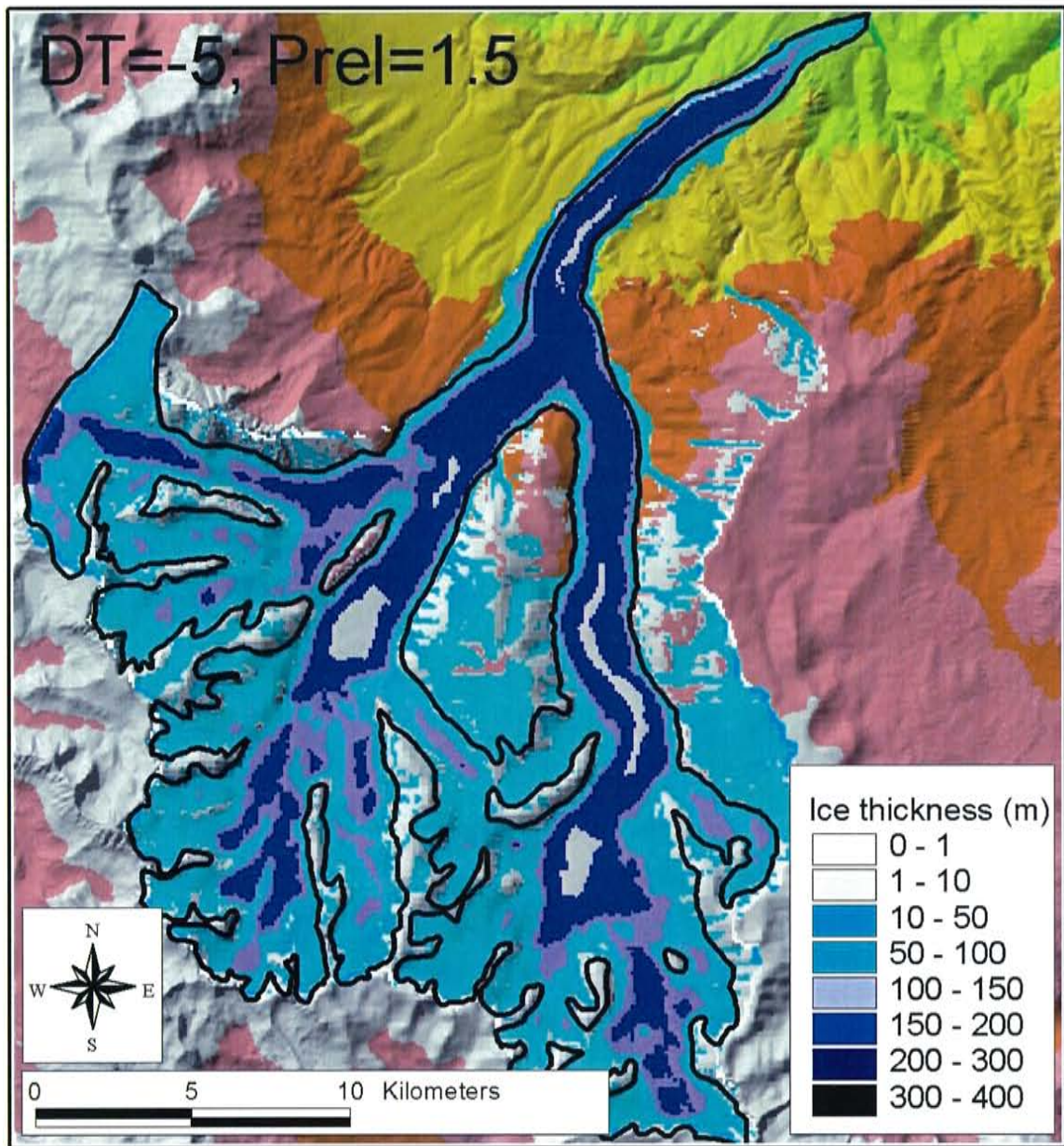
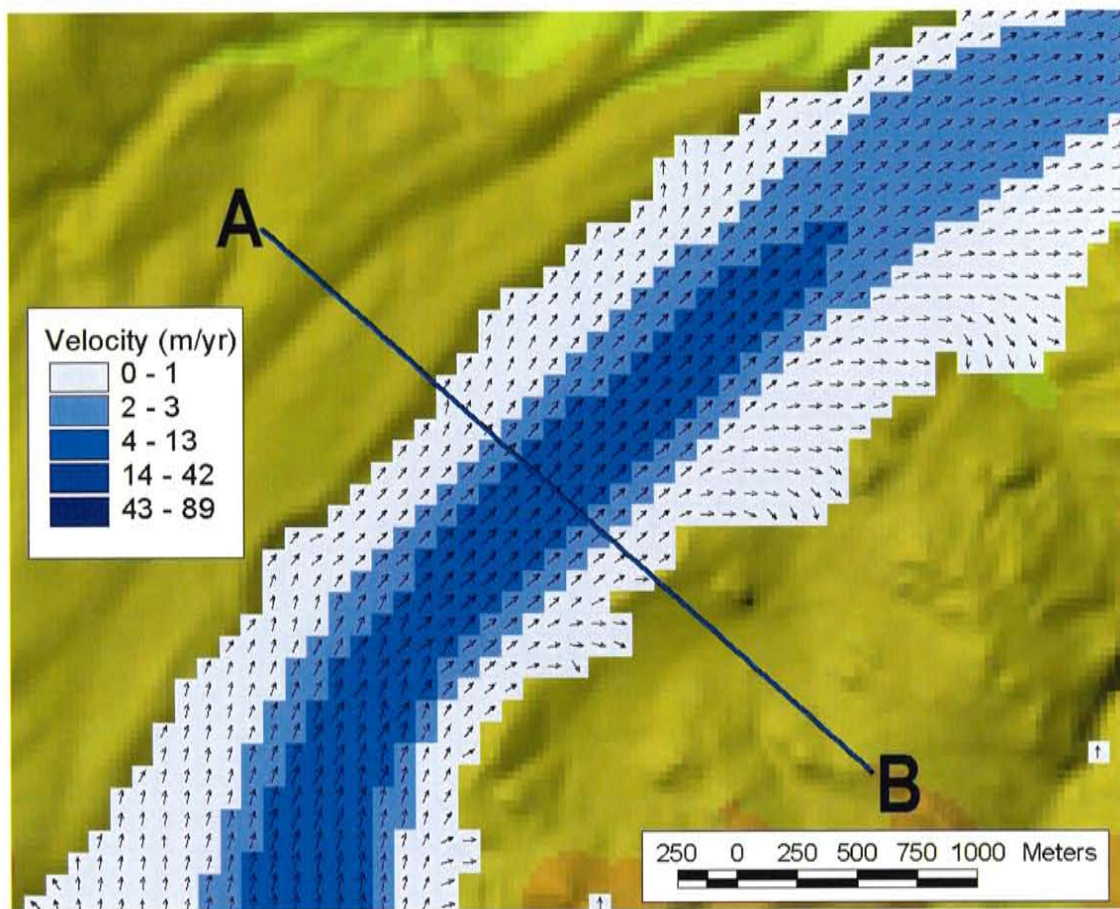


Figure 6-20. Comparison of a simulated Tioga maximum glacier (produced by a 5°C temperature depression and a 50% increase in precipitation) with our estimate of the glacier's shape (black line) based on field mapping of glacial trimlines and other glaciomorphologic features.



### Glacier Cross-section A-B

Vertical exaggeration 2.5 X

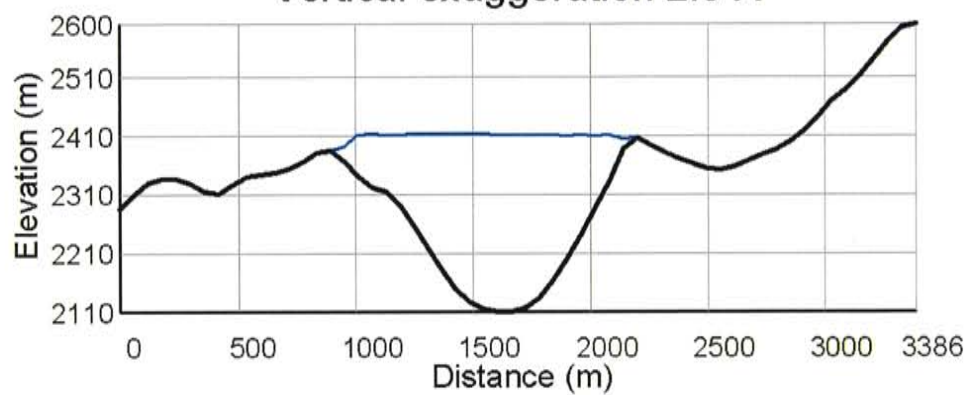


Figure 6-21. Ice velocity vector map for a simulated Tioga maximum glacier in Bishop Creek, overlain on a digital relief image of the terrain. Area shown is just below the confluence of the South and Middle Forks. The plot shows a cross-section of the terrain and glacier at A-B.



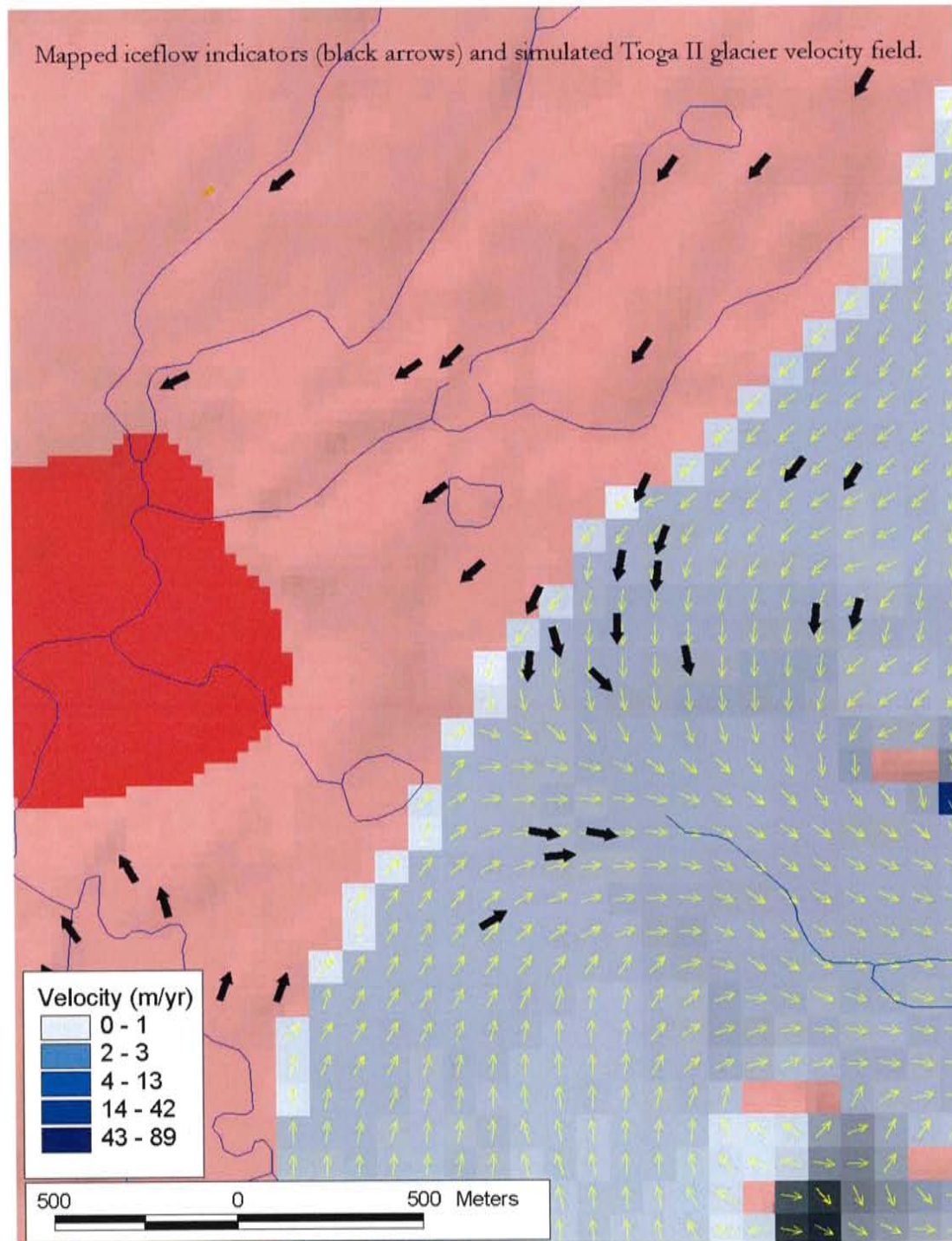


Figure 6-22. Comparison of simulated-glacier velocity vectors (yellow arrows) for a Tioga maximum glacier in Bishop Creek with mapped flow indicators (bold black arrows). Area shown includes Piute Pass and part of Humphrey's Basin above the North Fork of Bishop Creek and the mapped flow indicators are those shown in Figure 4-10. Red-shaded area shows relief; gray and blue colors indicate ice-flow velocity.

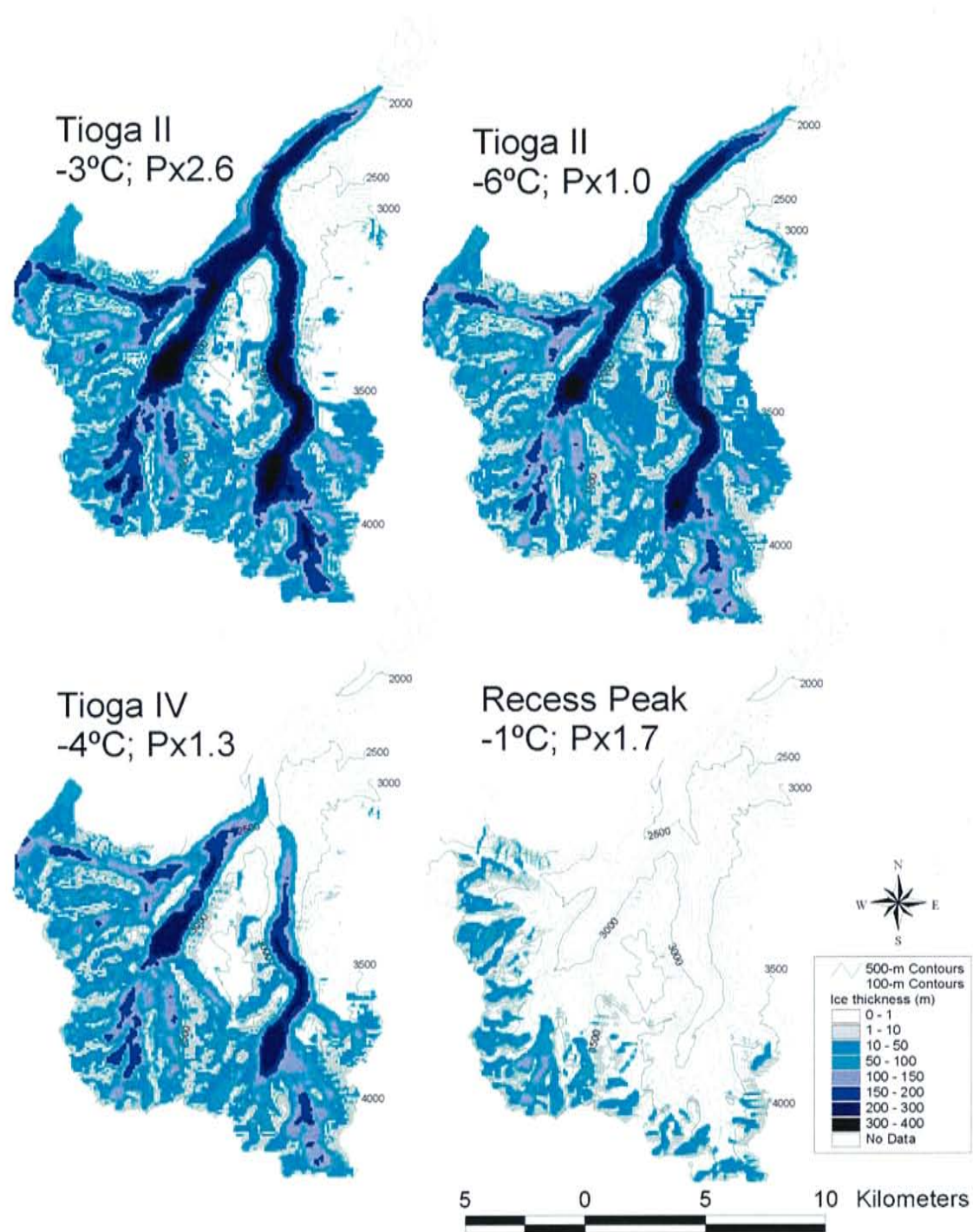


Figure 6-23. Simulated glaciers in Bishop Creek under four different combinations of temperature and precipitation. Upper simulations both match glaciomorphologic evidence of ~Tioga II glaciers. Upper left represents temperature 3°C colder and precipitation 260% greater than modern; upper right represents a change due only to temperature depression (-6°C). Lower left simulation matches the Tioga IV glacial advance and lower right the Recess Peak advance.

We summarized the response of the glaciers to climate change by finding the lowest point on the glacier along a reference flowpath chosen to intersect as many dated terminal positions as possible. In

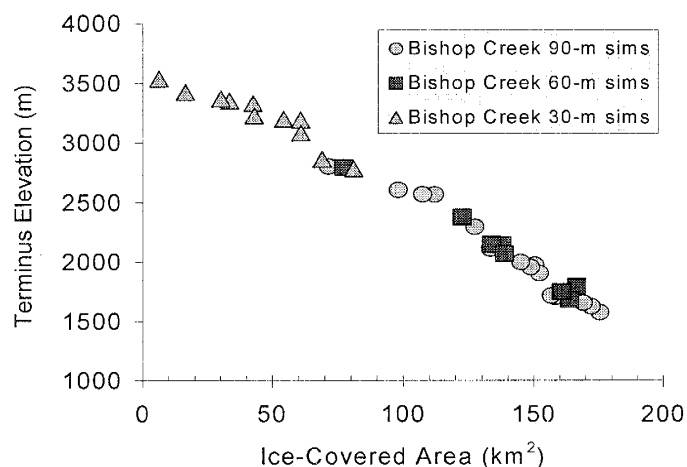


Figure 6-24. Terminus elevation along an arbitrary reference flowpath versus total ice-covered area at the end of each simulation. Different symbols correspond to different grid resolutions.

that this terminus-elevation index of glacial extent is generally linearly proportional to ice-covered area (Figure 6-24).

As in previous tests of basin response, we considered precipitation changes ranging from about 75% to 500% of normal and temperature depressions of up to 8°C. Maximum glacier dimension was limited by the dimensions of the surface we used to represent the basin, which was chosen to minimize computational requirements but allow glacier growth up to and slightly beyond the Tioga maximum along the present path of Bishop Creek. As a result, simulation of the full range of conditions considered in similar analyses of ELA response was not possible. Due to the excessive computations required for simulations of large glaciers on fine grids, we used grids of lower resolution for simulations of larger glaciers. Simulations in Bishop Creek were done with a 30-m, 60-m or 90-m grid. A 30-m grid was sufficiently small for all simulations in the smaller domain used for Horton and McGee Creek.

Bishop Creek, the reference flowpath begins in a glacier that lies below and just east of the Clyde Spires, on the Crest at the head of the Middle Fork drainage (Figure 6-19). The reference flowpaths in Horton and McGee Creeks begin in the glaciers that lie southwest of Horton and Longley lakes, respectively. Results of numerous simulations demonstrate



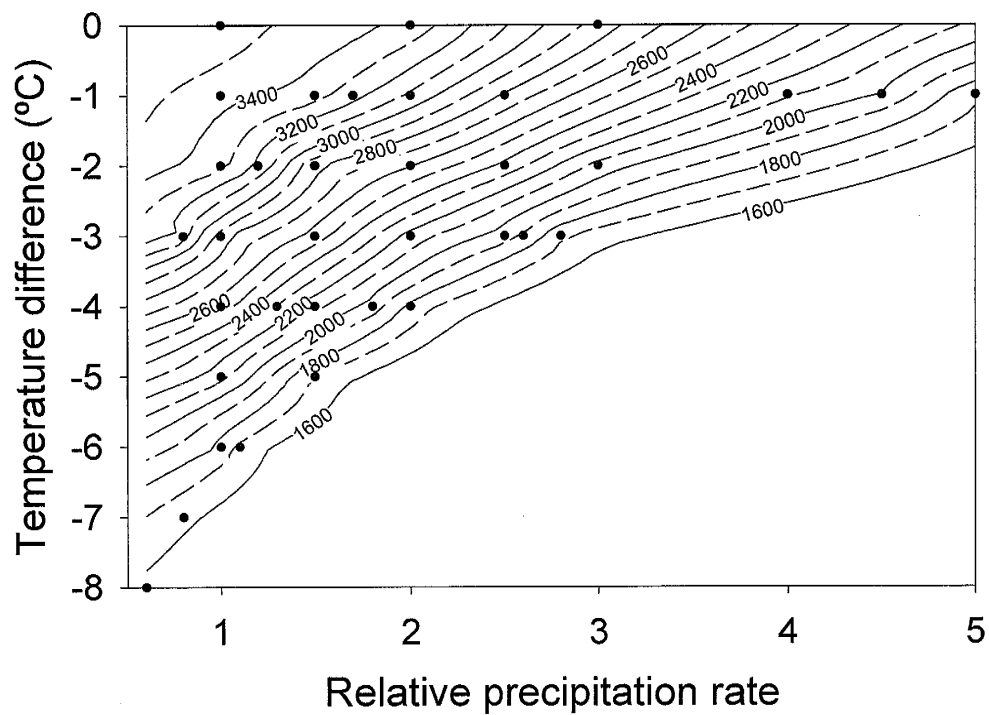


Figure 6-25. Contours of glacier terminus position, as meters elevation, for simulated Bishop Creek glaciers under different climatic conditions. Contours were developed by kriging the results of the simulations indicated by the symbols.

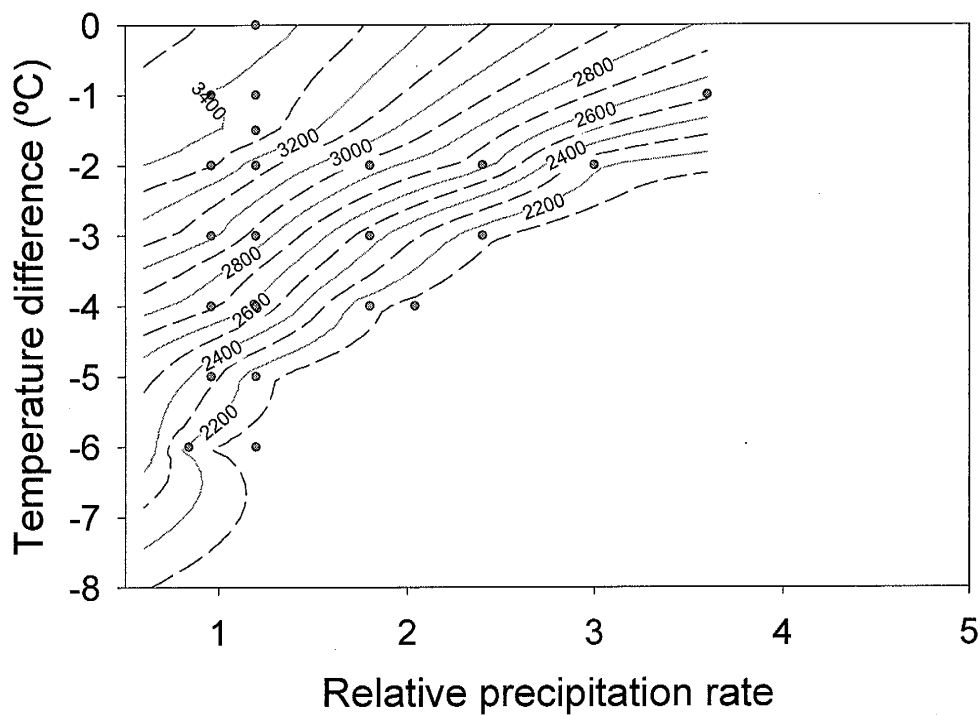


Figure 6-26. Contours of glacier terminus position, as meters elevation, for simulated Horton Creek glaciers under different climatic conditions. Contours were developed by kriging the results of the simulations indicated by the symbols.

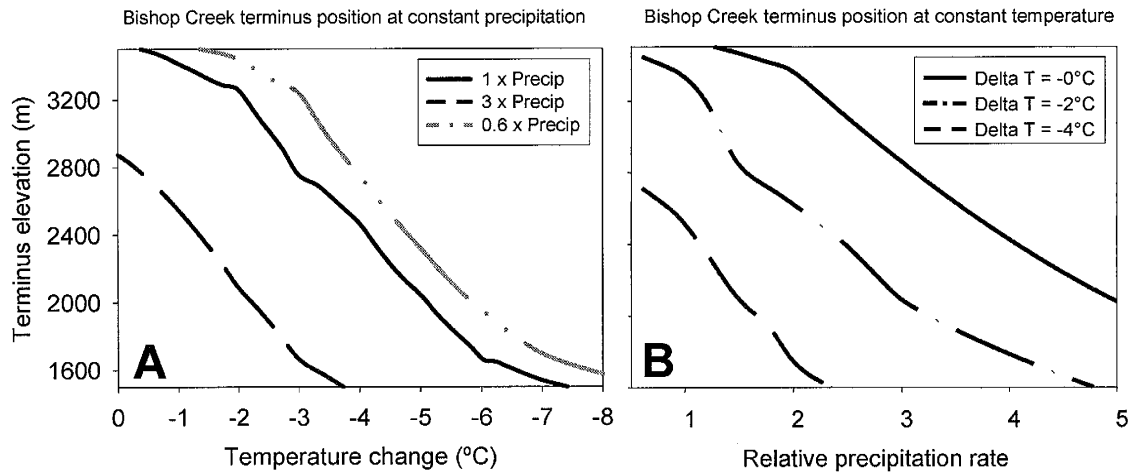


Figure 6-27. Changes in terminus position (m elevation) of glaciers in Bishop Creek glacier as a function of (A) temperature and (B) precipitation.

The climatic sensitivity of glacial extent, as measured using simulated glacier terminus position, is similar in Bishop and Horton Creeks (Figure 6-25 and Figure 6-26). The response is similar to that of local ELA (Figure 6-7), with least sensitivity for climatic conditions similar to modern climate. Again, we attribute this to the steep gradient in incident shortwave radiation with elevation that occurs in the vicinity of the modern glaciers. Sensitivity to climate change appears essentially linear throughout a wide range of conditions, with a slope of  $\sim 400$  m/°C and  $\sim 700$  m per unit increase in relative precipitation. Parameter-specific plots of terminus position as a function of temperature or precipitation (Figure 6-27) suggest that the glacier's sensitivity is slightly lower as the terminus descends below  $\sim 1800$  m, approaching the Tioga maximum position. Though somewhat questionable due to the lack of simulations under such conditions, this decreased sensitivity is an expected result of the basin's hypsometry. The basin narrows with distance downstream (Figure 6-1) so each step down in ELA is accompanied by a smaller increase in accumulation area. Another factor that would lead to decreased sensitivity with increasing glacial extent is the slight non-linearity in the dependence of temperature and precipitation on elevation. Temperature dependence is greater at lower elevation while precipitation dependence is slightly weaker and the greater sensitivity is to the

former.

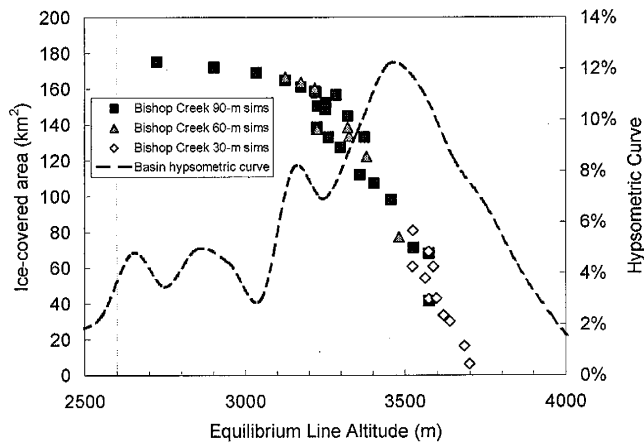


Figure 6-28. Total ice-covered area of simulated glaciers (symbols) versus ELA compared to hypsometric curve (dashed curve) – the fraction of total basin area below each elevation.

comparison of the changes in glacial extent as a function of ELA and the basin's hypsometric curve (Figure 6-28). Even the largest change in the curve, reflecting the change in hypsometry at the distal end of the basin is significantly offset from the inflection point in the sensitivity data. The relationship between basin hypsometry and climatic sensitivity, as well as the interrelationships between these factors and the magnitude of climate change have yet to be fully explored however, and that would appear to be an interesting and worthwhile application of the tools developed in this study.

The Tioga II glacier in Bishop Creek is represented by the ~1700-m terminus elevation contour in Figure 6-25. The Tioga IV glacier terminated at an elevation of ~2220 meters. The climatic conditions for which the model produces that glacier correspond very closely to those determined via the integrated surface balance approach (Figure 6-11) except for the increased sensitivity to precipitation that the latter displays at low precipitation rates. The Tioga II results are also similar, although the curve defined by the simpler approach lies along the 1800- and 1900-m contours of the response surface using the flow model. The discrepancy in the results of the two methods, which is

Somewhat surprisingly, variations in the basin's hypsometric curve generally appear to have little influence on the sensitivity of the glaciers. Total glacier area should be most sensitive to ELA at peaks in the hypsometric curve, reflecting large changes in the accumulation area relative to the ablation area. This is not readily apparent in a

nearly negligible for the larger glacier, is due to the differences in glacier shape over which the surface energy balance is calculated. In the 2-D flow modeling approach, the shape of the glacier is part of the solution, and it depends on both climate and topography. In the simpler approach, the shape of the glacier is determined once, primarily from field evidence in the ablation area. The shape remains constant for all climatic conditions considered and therefore cannot account for the changes in the glacier's accumulation area, or ablation area, that may accompany changes in climate.

Figure 6-29 shows glaciers simulated with the 2-D flow model for climatic conditions that provide balanced surfaces for the polygons used to approximate the Tioga II and Tioga IV glaciers. Although the match is reasonably good in both cases, there are areas, in each, in which the shape of the simulated glacier is significantly different from the a priori estimate of glacier shape. In reconstructing the Tioga II glacier from field evidence, we decided that Table Mountain, the inner polygon in Figure 6-29A, probably did not contribute a significant amount of ice to the glacier. The ice-flow model result suggests that, at least in this example, it would have. (Interestingly, simulated ice accumulation and flow on Table Mountain varies considerably with climate, and reconstructing its glacial history may yet yield additional paleoclimatic clues). In constructing a Tioga IV glacier shape from field evidence, we excluded South Fork from the integrated surface balance analysis area because of the lack of apparent Tioga IV – age moraines in that drainage. The flow model result (Figure 6-29B) demonstrates that the two drainages cannot be considered independently when convergent flow of two lobes is a possibility. A flow simulation that better matches the Tioga IV terminus position (Figure 6-30) suggests that the South Fork glacier had actually retreated ~1 km upstream from the confluence at that time. This is more consistent with the observed arrangement of terminal moraines at the confluence, and the implied greater climatic sensitivity of the South Fork tributary provides a plausible explanation for the comparative lack of terminal or lateral moraines in that canyon. We suggest that the flow modeling approach may thus provide insight into the processes that control deposition of glacial features that will aid in their geomorphic, as well as

paleoclimatic, interpretation.

#### ***ACCUMULATION AREA RATIOS OF SIMULATED GLACIERS***

As existing glaciers typically have accumulation area ratios of about 0.65, we expect that the model should reproduce this characteristic. AARs of the simulated glaciers (Figure 6-31) are indeed generally close to that value, with all but the largest glaciers having values between 0.55 and 0.75. The relationship between AAR and ELA noted in Figure 6-12 appears to be evident in the AARs of the largest glaciers simulated in Bishop Creek, but there also appears to be an overall increase in AAR with increasing glacial extent. This may be related to a combination of factors, including topographic effects on flow and energy balance as well as basin hypsometry. The detailed output that the model provides indicates that this 2-D modeling approach should be very useful in elucidating the controls on AAR. Though often noted, few explanations have been offered for its relative invariance.

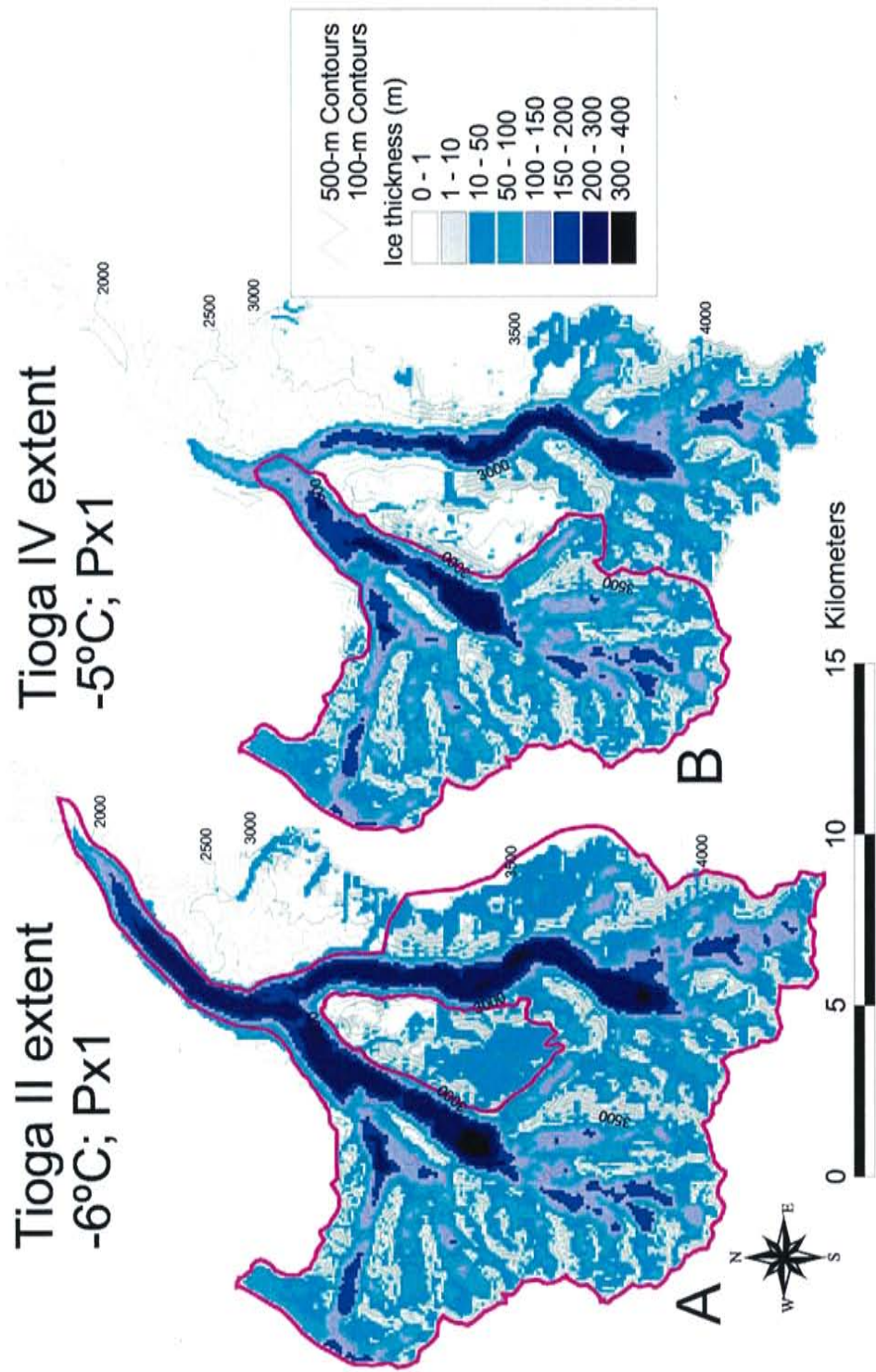


Figure 6-29. Simulated glaciers for climatic conditions that provide near-zero surface integrated water balance within the presumed polygonal areas that describe (A) the Tioga II glacier's extent and (B) the Tioga IV glacier's extent. Both examples illustrate the difficulties in reconstructing the shape of even relatively large glaciers solely from field evidence. The extent of the Tioga IV glacier, for example, depends significantly on the degree of contribution from South Fork, where little evidence of that advance remains.

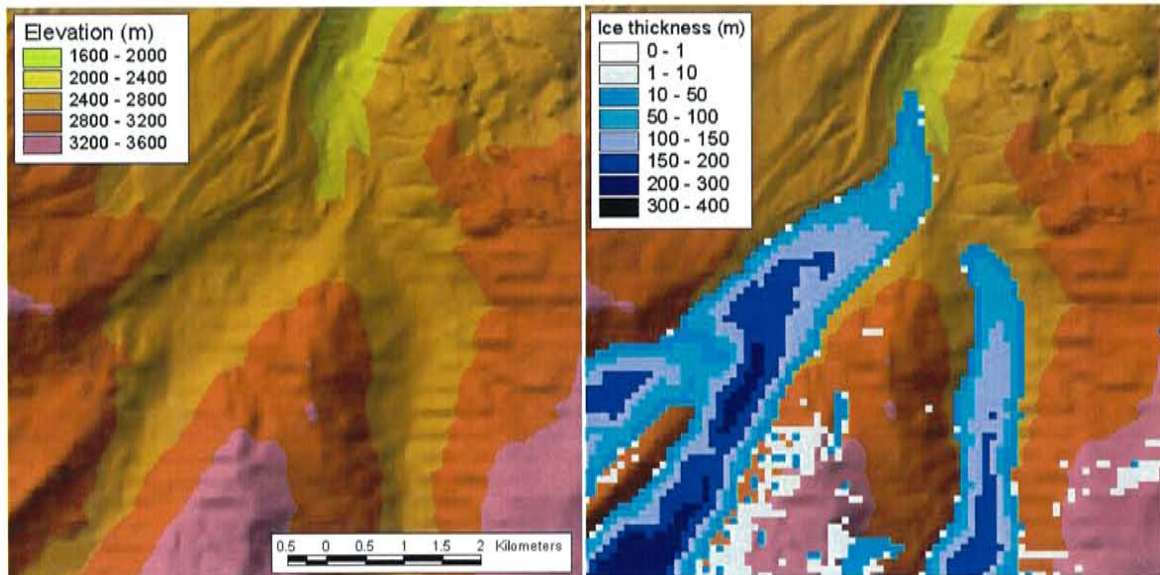


Figure 6-30. Shaded relief image of the confluence area showing (left) the descending left and right lateral moraines extending from the Middle Fork of Bishop Creek. The simulated glacier for a temperature depression of 4°C and 30% precipitation increase (right) provides an excellent match to the morainal evidence.

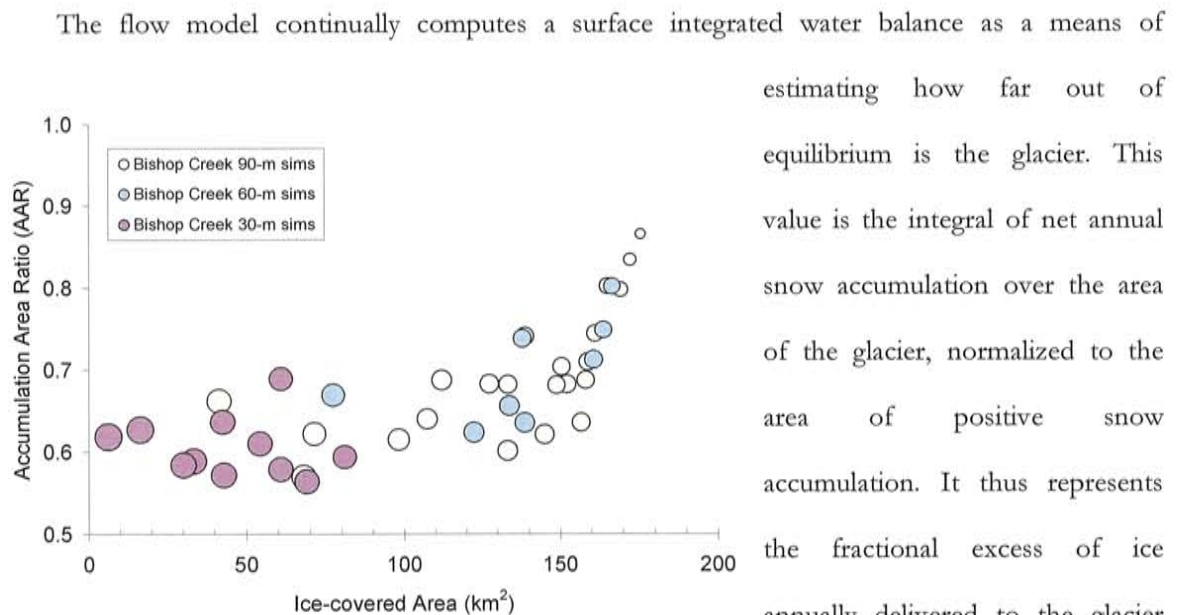


Figure 6-31. Accumulation area ratios of simulated glaciers as a function of total glacier surface area. Symbol size is proportional to equilibrium line altitude. Different symbols correspond to different grid resolutions.

estimating how far out of equilibrium is the glacier. This value is the integral of net annual snow accumulation over the area of the glacier, normalized to the area of positive snow accumulation. It thus represents the fractional excess of ice annually delivered to the glacier that is not removed by ablation. As such, positive values imply an

advancing glacier and negative values indicate a retreating glacier. If the simulated glacier has reached

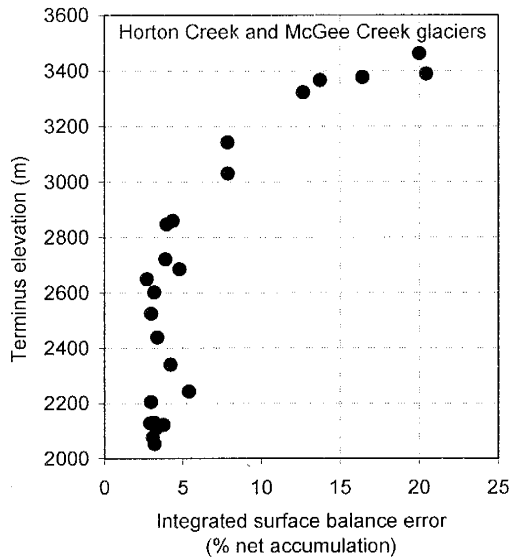


Figure 6-32. Terminus elevations of simulated glaciers plotted against the glacier's integrated surface balance error at steady state.

steady state however, the value represents the water balance error for the glacier. Our simulated glaciers typically reached steady state with integrated surface balance errors of up to 10%. The error is caused by the finite difference approximations and the substantial non-linearity of this model. The best data with which to analyze the errors are from modeling of the Horton and McGee Creek glaciers, where all simulations were performed using the same cell size.

A plot of terminus elevation versus integrated surface balance error for those drainages (Figure

6-32) indicates that the mass balance error increases as the glaciers decrease in size. This is because each active cell represents a larger fraction of a small glacier, increasing the error associated with boundary effects.

#### TRANSIENT RESPONSE OF THE FLOW MODEL

Most of the simulations conducted for this study were started from a condition of bare ground and run until the glacier appeared to have achieved steady state in both integrated surface balance and maximum ice thickness. Periodic output from the model includes

- Time since start and size, number of time-steps passed and length of last time-step
- Integrated surface balance normalized to the surface integrated accumulation rate
- Total ice volume
- Maximum ice thickness
- Elevation of lowest cell containing ice
- Integrated mass balance error at that time step

The integrated surface balance output is normalized to the total net accumulation on the grid.



The integrated balance error thus starts at 100% and decreases as ice flows into the ablation area (Figure 6-33A). It approaches zero net balance asymptotically and most simulations reach steady state at an integrated surface balance of less than 5%. The error increases with the ratio of the grid cell-size to the area of the steady-state glacier but does not exceed 10% (Figure 6-32). Though due to a combination of factors, a significant part of the error can be attributed to the fact that ice in any grid cell is either on or off and the glacier's moving boundary can only adjust by whole cell values. Unfortunately, the final adjustment to steady state occurs at the terminus, where ablation is greatest and the mass balance most strongly influenced by addition or removal of a single cell.

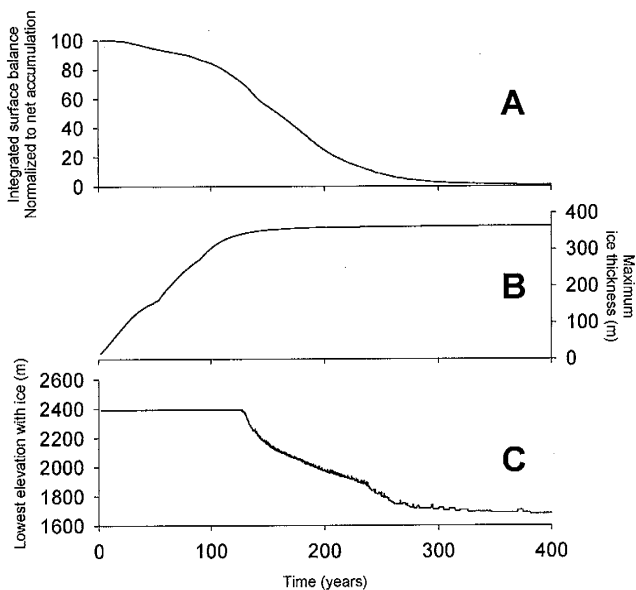


Figure 6-33. Simulated glacier growth in the Bishop Creek basin. Initial ice thickness is zero; final steady state simulates Tioga-maximum conditions. Parameters shown are (A) integrated surface balance, (B) maximum ice thickness and (C) lowest elevation with ice.

Maximum ice thickness is another parameter we use to monitor the approach to steady state. It commonly reflects the surface slope at the location of the terminus; increasing slowly when the terminus is on relatively steep terrain and rapidly when the terminus is on flatter ground. The sudden increase in maximum ice thickness that occurs at approximately 60 years in the example shown in Figure 6-33B is where the terminus in the Middle Fork reached Lake Sabrina, where the slope is 0°.

The elevation of the lowest cell with ice is intended to monitor the position of the terminus. Unfortunately, the growth of a glacier from scratch occurs as a multitude of small advancing tongues of ice from the many cirques and high elevation basins. The lowest accumulation area tends to

dominate this measure, even if its accumulation rate is relatively small, until a lobe of advancing ice descends to a lower elevation. This occurs after about 125 years for the simulation profiled in Figure 6-33C. Under conditions where only small glaciers develop, it may not occur at all. Future changes to the model should include a means of profiling, over time, the position of the glacier along a specified flowline. This would provide interesting details of the growth history of the flow. The current output does not provide a means of identifying the surface location associated with any of the measures profiled.

The transient output of the model provides a direct means of evaluating the response time of the glacier. Most of the simulations performed for this study were started from a condition of zero ice thickness, effectively growing the glaciers from scratch. Though this is a relatively unrealistic scenario, it is interesting to compare the times needed to reach steady state in these simulations. Figure 6-34 shows estimates of those times for the simulations in Bishop Creek. These are rough estimates from a cursory review of the output data; simulations were generally run until all of the output measures appeared to be relatively constant. The time to reach steady state ranges from

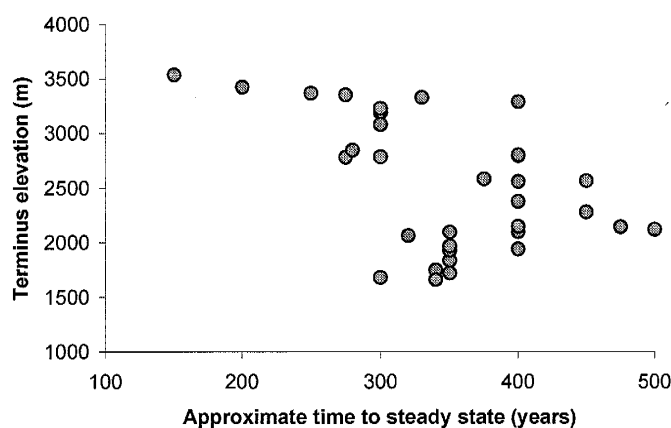


Figure 6-34. Estimated time to reach steady state versus terminus elevation. Vertical collections of points reflect the fact that many simulations were run to a rough estimate of the minimum time required.

approximately 150 to 500 years, increasing significantly with glacial extent. Although the goals of this study did not include development of a glacier flow model for transient flow simulations, it would be an extremely useful tool if the model proved thus capable. At first brush, based on the behavior of the glacier during growth, the model shows promise of

performing that task more than adequately. The apparent response times for glaciers of varying size to reach steady state from scratch, or following a perturbation to a previous condition, is consistent with observations of alpine glaciers and with the theoretical 100-yr to 1000-yr perturbation response times that Johannesen *et al.* [1989] calculated for alpine glaciers.

#### ***TERRAIN ALTERATION TO MATCH SIMULATED GLACIERS TO FIELD EVIDENCE***

Glaciers alter the landscape by erosion and, in the ablation zone, deposition. By altering the terrain over which they flow, they change the constraints on the flow system. Lateral moraines tend to constrain flow to previous paths of advance, while terminal moraines and recessional moraines effectively block the glacier from that path. This effect is most prominent at the glacier's terminus, where deposition rates are high and the natural topographic relief low. The extensive terminal moraine complexes common in the eastern Sierra often reflect many shifts in terminus position due to this effect. The flow paths of our simulated glaciers reflect the alterations incurred during the last recession. In Bishop Creek, only small recessional moraines developed during the last retreat, and simulated glaciers in that drainage readily follow the same path of the last major advance to the terminal moraine complex. In Horton Creek however, simulations of larger advances consistently follow a path that predates the Tioga-II-age lateral moraines along lower Horton Creek. Reaching an area of low-angle slopes near the mountain-front, the glaciers thicken and flow, via several lobes, away from and to the southeast of Horton Creek (Figure 6-35A). Preliminary chlorine-36 dates on the moraines that constrain those lobes, however, demonstrate that they were formed approximately 40,000 years ago, and our field mapping indicates that the Tioga II advance actually followed the present-day path of Horton Creek. The deposits that seem to cause this diversion of the glacier's flowpath are a succession of Tioga III terminal loops near the top of the large terminal moraine complex that has accumulated at the mountain front in Horton Creek. To allow the glacier to follow the path that we believe represents that of the Tioga glaciers, we numerically excavated a channel through that

moraine complex into lower Horton Creek, altering the DEM (compare contours in Figure 6-35A and Figure 6-35B) to provide a new surface for the ice flow simulations. Glacier simulations on that surface (Figure 6-35B) differ significantly from those on the original DEM. The glacier flows much further downstream on the modified terrain, probably because of reduced incident radiation in the shady confines of lower Horton Creek. The simulations summarized in Figure 6-26 and discussed below reflect flow on this modified surface.

#### ***INTERBASIN COMPARISON – BISHOP CREEK AND HORTON CREEK***

The climatic sensitivity of simulated glaciers in the smaller basins to the north of Bishop Creek – Horton and McGee Creeks – is similar to, but significantly greater than, those in Bishop Creek. Comparison of Figure 6-25 with Figure 6-26 shows that termini of simulated glaciers in Horton Creek, for example, descend approximately 200 meters lower than in Bishop Creek under a wide range of more colder and wetter climates. The precipitation and temperature functions applied for the simulations in the smaller basins were the same as those used in Bishop Creek. As discussed in Section 5, however, precipitation is probably considerably less in the smaller basins. Using the spatially distributed application of the Langbein precipitation-temperature-runoff model described in Section 3, we estimated that precipitation in Horton Creek is approximately 14% less than in Bishop Creek (Table 5-1). To compare basin climatic response curves under that assumption, we replotted the contours of Figure 6-26 to reflect that difference. Figure 6-36 shows these contours overlain on those for Bishop Creek. This reduces the difference between the glaciers of the two basins considerably. Except for conditions similar to modern climate, the glaciers in the two basins reach similar elevations throughout most of the range of simulated climates. This is counter, however, to the record described by the moraines in Horton and McGee Creek, which suggest (Table 4-1) much lower climatic sensitivity in the smaller basins. The Tioga IV terminal moraines in Horton and McGee Creek, for example, are 600 to 700 meters higher than their Bishop Creek counterparts, and

other Tioga-stage glaciers show similarly large differences. The large disparity in the apparent sensitivity of the glaciers between the smaller basins and Bishop Creek suggests that something other than the spatial variability of precipitation is at work. Though several explanations may be advanced, we anticipate that only a significant difference in the net radiation term could explain the magnitude of the discrepancy. We suggest that surface albedo, one of the least well-constrained parameters in the model – and a primary control on net shortwave radiation, is the most likely explanation. A higher ratio of debris to ice would produce a significantly dirtier glacier, with correspondingly lower albedo. Relative to the size of the basin, the morainal deposits at the mouth of Horton Creek seem inordinately large. It is not unreasonable to suppose then, that the mineralogy of the bedrock, or other factors peculiar to the smaller basins, led to significantly dirtier glaciers than those that developed in Bishop Creek. Their lower albedo would have significantly restricted their ability to expand in response to climate change, offering a plausible reason for the discrepancy between the sensitivity of the simulated glaciers and the sensitivity evidenced by the moraine chronology. Though one might counter that dirtier ice would actually have an insulatory effect, leading to increased climatic sensitivity, that phenomenon is only commonly observed in rock glaciers, where the ice flux is low enough that the debris may remain on top of the ice, rather than be subsumed upstream and melted out at lower elevation.

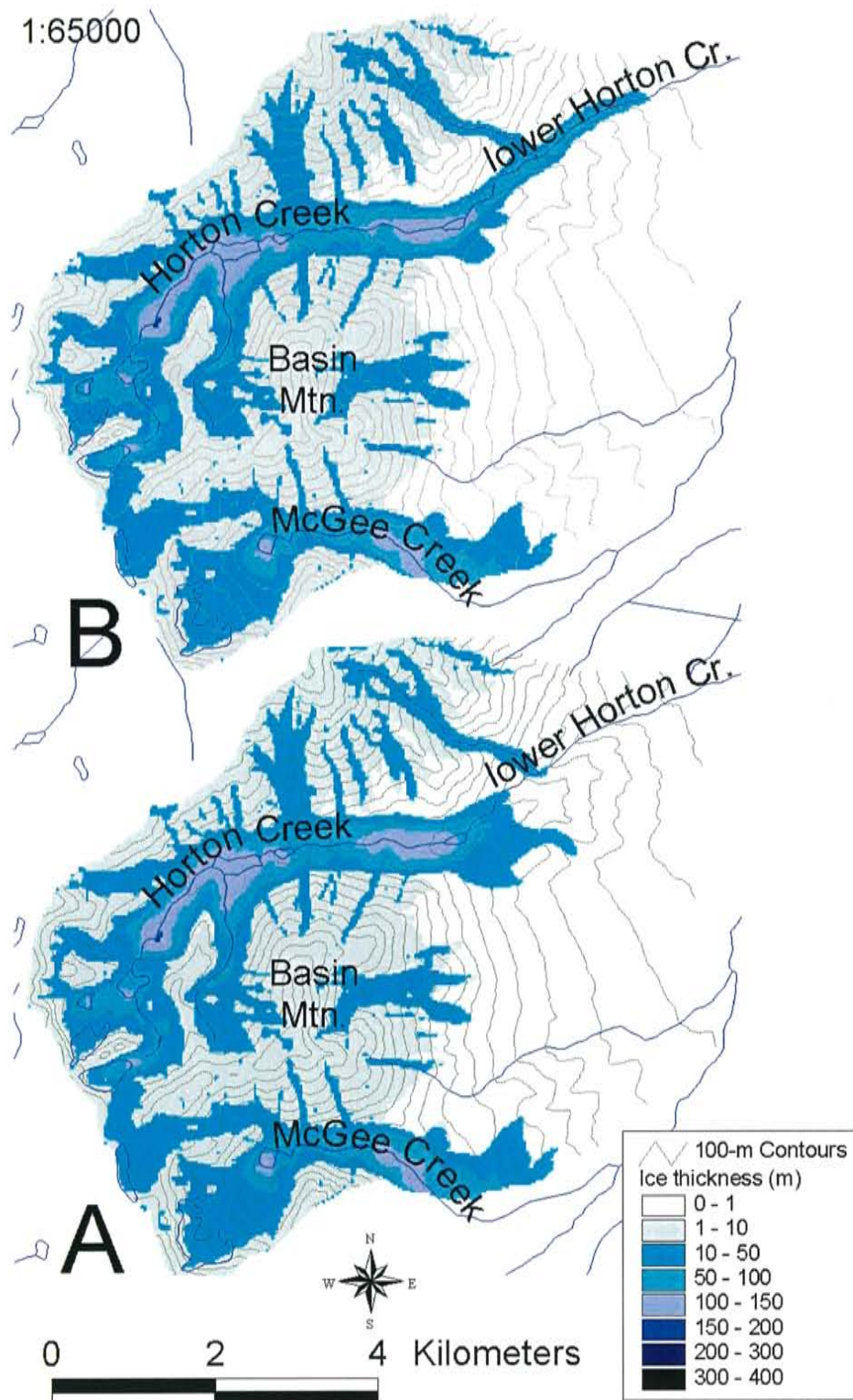


Figure 6-35. Examples of simulated glaciers in Horton and McGee Creeks under a 5°C temperature depression. (A) The Horton Creek glacier, flowing on the existing topography leaves Horton Creek at the terminal moraine complex and two lobes of ice flow to the southeast. (B) Simulated glaciers on a modified surface, excavated to allow the ice to flow along Horton Creek. Contour interval is 100 meters.

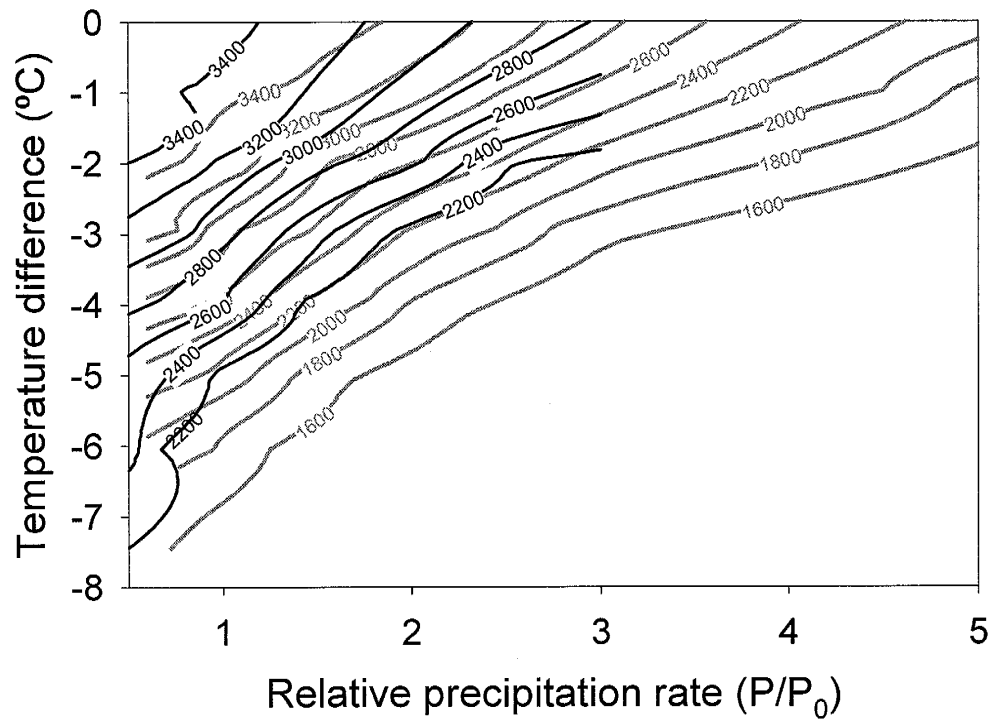


Figure 6-36. Terminus elevation (m) contours of glaciers in Bishop Creek (heavy gray lines) and Horton Creek (black lines) assuming that mean annual precipitation in Horton Creek is ~14% less than in Bishop Creek. Temperature difference and  $P_0$  refer to modern climatic conditions.

#### **SENSITIVITY TO MODELING ASSUMPTIONS AND UNCERTAIN PARAMETERS**

Sources of error and uncertainty in the modeling process include the assumptions of the model itself and in the parameters used to fit the model to the study area. These effects add uncertainty to the predictions of the model. In using the model to reconstruct the temperature and precipitation of past climates, we must also consider that second-order climatic variables may have been significantly different than their present values, adding uncertainty to conclusions based on the response of the glacier model. To estimate the overall impact of these effects, we conducted a number of simulations in which we varied aspects of the model likely to contribute the greater part of the error, or uncertainty, in its response to climate change.

Assuming that the snow/ice energy and mass balance model captures the critical physical processes, the uncertainties in its parameterization are probably largest in the turbulent energy

transfer calculations and in the albedo term for the glacier surface. Shortwave, longwave, advected, and conducted energy transfers are, by comparison, more physically based and generally involve better-constrained parameters. In the preliminary uncertainty analysis discussed here, we thus consider uncertainty in the turbulent heat transfer coefficient but neglect it in the other terms. Uncertain parameters in the model also include the functions that we use to relate temperature and precipitation to elevation. Of these, we consider only the latter a significant source of uncertainty, primarily because precipitation data from high elevations, where precipitation rates are highest, is largely lacking. The effect of this uncertainty on model predictions of glacial extent, however, should decrease with increasing glacier size, as larger glaciers integrate precipitation over a much wider area, and precipitation at moderate elevations in the eastern Sierra Nevada is closely monitored and relatively well known.

Meteorological parameters that might have been significantly different in the past include wind speed and atmospheric stability, cloudiness, surface albedo, as well as the primary climatic variables. In addition to changes in mean value, these parameters may have had a significantly different seasonal and/or spatial distribution. We consider only a small set of the possible variations in this analysis, focusing on examples - cloudiness, wind speed and surface albedo - that directly alter the dominant components of the surface energy balance.

Assuming that our 2-D flow modeling predicts at least the steady state shape of alpine glaciers with reasonable accuracy, the largest source of uncertainty in that approach are the flow constants in the relationship between shear stress and mean ice velocity. We use those constants as fitting parameters and we demonstrate the sensitivity in that process with several simulations. The base case for those, and the other sensitivity tests described below, is the simulated annual snow accumulation distribution and glacier in Bishop Creek under a 5°C temperature depression and 50% precipitation increase. The resultant Tioga maximum size glacier should produce, if anything, a more conservative



estimate of the model's sensitivity than would changes in glacial extent under modern conditions.

#### *SENSITIVITY TO FLOW CONSTANTS*

Adjustable parameters in the flow model include coefficients for ice velocity via deformation of the ice and via sliding. In studies of the mass balance of modern glaciers, these constants are fitting parameters in the calibration of the model. In modeling paleo-glaciers, the best information we have for establishing these values is the shape of the glacier defined by trim-lines and moraine crests. To illustrate the effect of changes in these parameters on glacier shape and length, we ran simulations using flow constants one order of magnitude above and below our preferred values. Profiles of the glaciers along a stream path (modern, not glacier) from above Echo Lake to Coyote Creek are shown as Figure 6-37 and ice thickness maps are displayed in Figure 6-38. With the higher conductance, the ice distribution is much more constrained by the topography and the glacier, ranging from ~100-m to 200-m thick, is too thin to match actual moraine heights in the basin. It is difficult to estimate the resulting increase in glacier length because the ice flowed to the edge of the grid and spread along the boundary to achieve steady state. With an order of magnitude decrease in conductance below our base-case values, the ice thickness is excessive, ranging from ~300 meters to a maximum of 600 meters at Lake Sabrina. An ~10% (3-km) decrease in length also results from the order-of-magnitude decrease in flow parameters but this is minor compared to the change in thickness. An interesting feature of the response of the simulated glaciers to changes in the flow constants is the high sensitivity that exists at steep slopes that lie upstream of areas of very low slope. When the ice is highly fluid, the glacier is very thin at those points, reflecting only the dominant local control of the underlying surface. When the ice is more viscous, however, the increasing ice thickness downstream effectively backs up to the steep slopes and the ice thickness increases rapidly. This is exemplified in these simulations (Figure 6-37) by the steep terrain above Lake Sabrina, which lies about 10 km from the crest. The sensitivity of ice thickness to changes in flow parameters at such points should provide

a good means of tuning the ice flow parameters, if the corresponding field evidence preserves indications of paleo-ice thickness.

From the results of these tests, and because thickness can generally be constrained at several points, we estimate that the uncertainty in the terminus position due to uncertainty in the flow constants is on the order of 1 kilometer. Assuming an uncertainty in the flow constant of a factor of less than 5, we estimate that the corresponding uncertainty in terminus elevation would be on the order of  $\pm 100$  meters or  $\pm 1$  kilometer. As the base case glacier represents a descent in the terminus position of  $\sim 1960$  meters, the uncertainty associated with estimation of the flow constants is about 5%.

#### *CHANGES IN NET ACCUMULATION DUE TO GLACIER-INDUCED CHANGES IN TOPOGRAPHY*

The initial energy balance from which the net annual accumulation maps are produced is calculated based on the modern ground surface topography, assuming an underlying surface of glacier ice. Growth of a glacier on that terrain modifies the topography in a manner that significantly alters the energy balance. In this discussion, we address the feedback between glaciation and surface energy balance only in a rudimentary manner, in order to estimate the uncertainty in terminus position that results from neglecting this effect. In the future, we hope to couple the snow/ice energy and mass balance model with the glacier flow model in an iterative fashion, forcing recalculation of the snow/ice energy balance whenever the topography is significantly altered by the growth of glaciers.

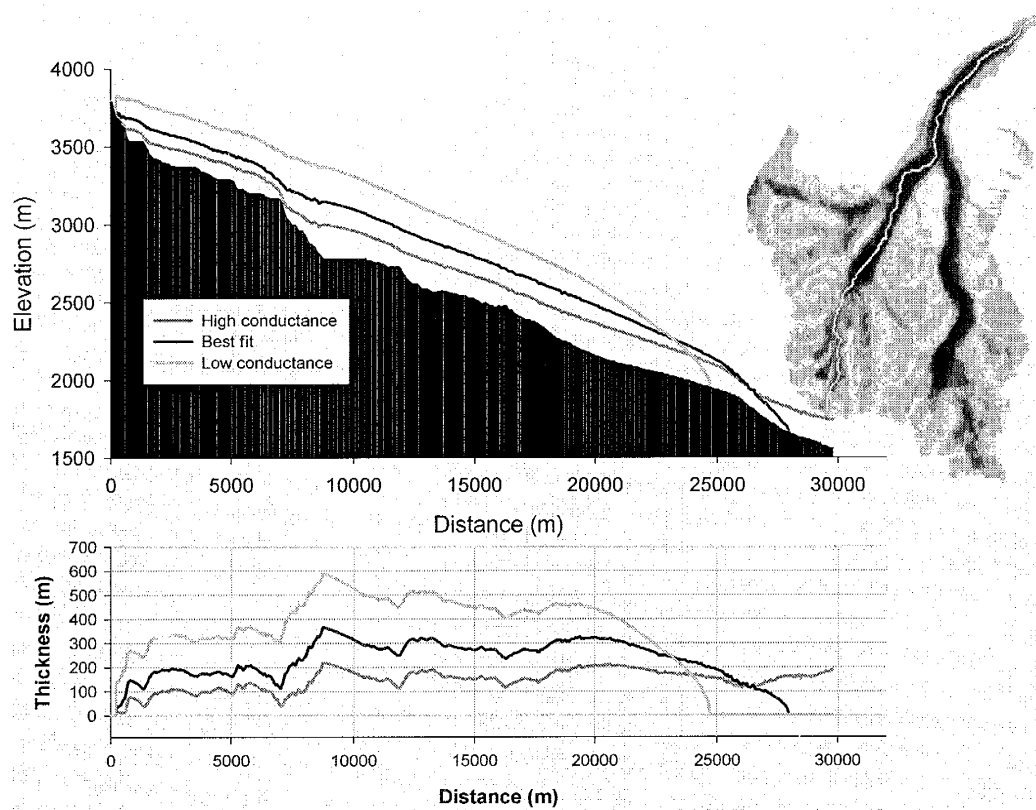


Figure 6-37. Profiles of three simulated glaciers along a streamline of the existing topography (black region). Accompanying glacier thickness map shows reference path with the glacier produced using the “best-fit” conductance values of this study.

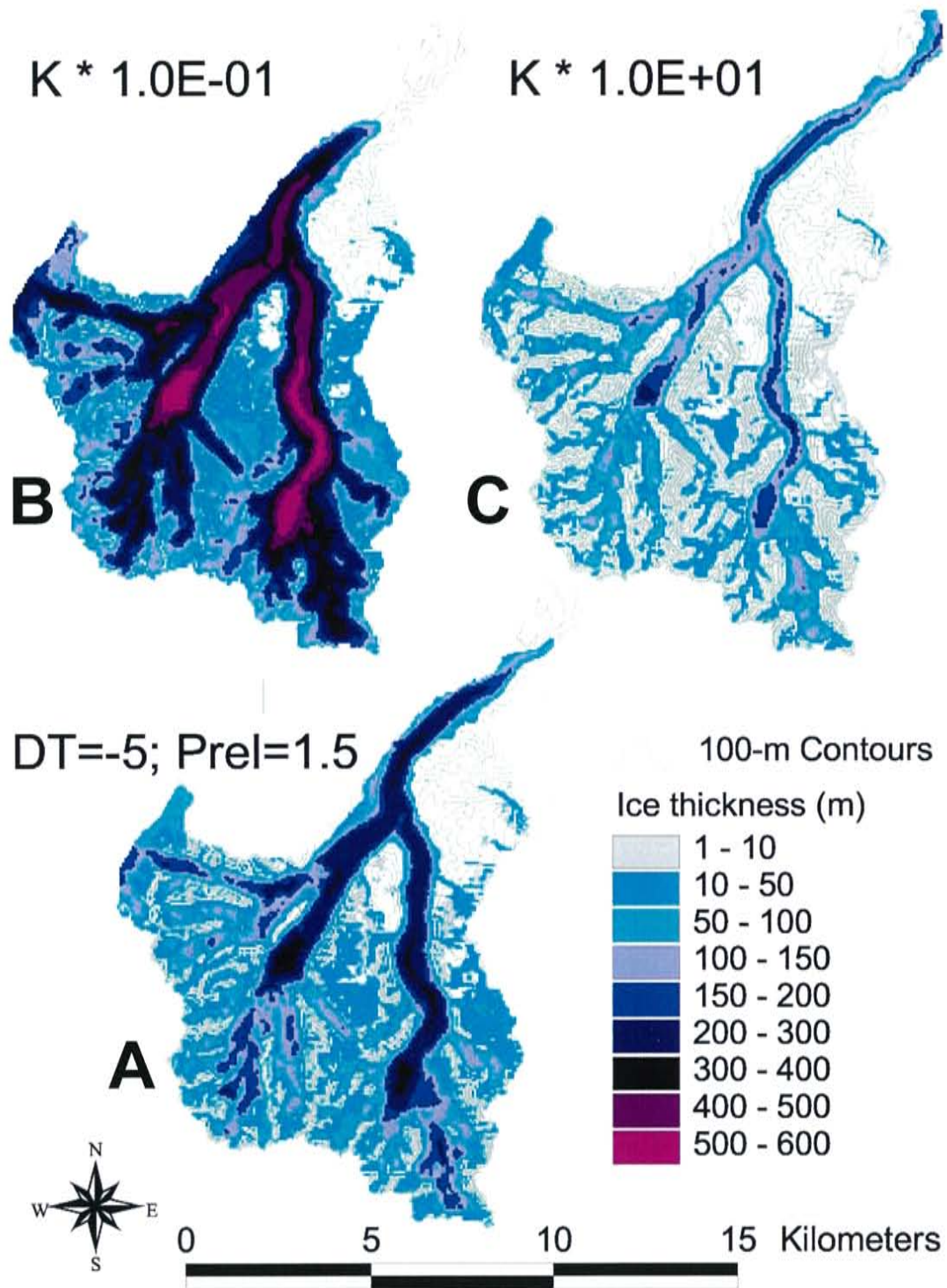


Figure 6-38. Differences in a simulated steady-state Tioga-maximum glacier in Bishop Creek as the sliding and deformation coefficients are varied from those of the (A) base-case simulation by (B) a decrease of one order of magnitude, and (C) an increase of an order of magnitude. Climatic adjustment is a 5°C decrease in temperature and a 150% increase in precipitation.

To examine the effect of the ice surface topography on the mass balance of the glacier, and the resultant glacier adjustments, we first simulated glacier development from the ground-surface-based estimate of the net ice accumulation map for a climate 5 degrees colder and 50% wetter than the modern climate. In an iterative approach to coupling the models, this would be the end of the first iteration. We then calculated the snow/ice energy and mass balance for a terrain model that included that glacier. The increased altitude of the ice surface over the ground surface topography has two primary effects on the energy balance. First, the greater elevation, which may be as much as several hundred meters, causes a slight decrease in temperature and increase in precipitation. Second, growth of the glacier out of the valley bottoms and shaded declivities of the cliffs significantly increases its exposure to direct radiation. The net effect of the altered surface thus depends on the topography and the thickness of the glacier. Areas where the base topography is quite flat, for example, already have considerable exposure to shortwave radiation. The primary effect of increased elevation in those areas tends to be a slight increase in the net accumulation rate. Figure 6-40 illustrates the change in the net annual accumulation induced by the change in topography. Areas where the base topography is relatively horizontal, such as valley bottoms, lakes and high-elevation plateaus display an increase in snow accumulation. Other areas, previously protected from direct radiation by shadowing, display a large increase in ablation. This effect is particularly noticeable along the edges of the tongue of the glacier where the canyon is relatively deep but the surrounding mountains much less rugged. The net effect of the glacier-altered topography is a significant decrease in annual snow accumulation over the surface of the glacier.

Using the net accumulation distribution calculated for the surface of the first iteration glacier, we ran the flow model again to allow the glacier to adjust to the new energy balance. We then repeated that process to produce a glacier representing three iterations of the coupled processes of energy balance and ice flow. The terminus position of the third iteration glacier is ~14% (260-m) higher in

elevation and ~2.9-km shorter in length than the first iteration, base case, glacier.

#### *SENSITIVITY TO INITIAL CONDITIONS*

Early simulations with the snow/ice energy and mass balance model indicated that it was relatively insensitive to initial conditions. The only parameter that carries over from one year to the next is the surface albedo and the surface energy balance calculations begin in October. This limits sensitivity to albedo because winter snowfall almost immediately resets all of the pertinent albedo values. We therefore developed the annual snow accumulation maps in this study by computing the snow/ice energy and mass balance over only one annual cycle. Subsequent changes to the model increased this sensitivity and introduced unnecessary error in the results. Figure 6-41b illustrates the change in the net accumulation map from the base case after running the calculations for a second cycle. Simulation of ice flow using the 2-cycle net accumulation map indicated that by neglecting initial conditions we systematically overestimate terminus position descent by about 5%<sup>13</sup> (100 meters in elevation; 0.9 km distance).

#### *SENSITIVITY TO ESTIMATED ALBEDOS*

The energy balance model is currently parameterized to include only two albedos, one for snow and one for ice. The actual albedo is likely to be highly variable and time-dependent, particularly in the ablation area. To estimate the sensitivity to this uncertain parameter, we considered the possibility that much of the ablation area might consist of much dirtier ice than the glacier from which the original parameterization was based. Accordingly we altered the albedo of ice to 0.25, recalculated the surface energy balance, and simulated glacier flow using the resultant net accumulation map. The effect is, predictably, a significant increase in ablation in the lower portions of the basin. In response

---

<sup>13</sup> The initial albedo in these calculations was set to the mean of the two possible values incorporated. Given that the error is essentially only in the ablation area, the need for calculations through multiple cycles could almost certainly be avoided by setting the initial albedo to that of melting ice.

to this change in surface accumulation, the base case glacier retreats upward by 18% (~260 m higher, 2.9 km shorter).

#### *SENSITIVITY TO WIND SPEED*

The latent and sensible heat fluxes are both proportional to wind speed in the mass transfer approach to turbulent heat transfer. An increase in wind speed thus removes additional heat from the snowpack via increased sublimation and evaporation and adds thermal energy by an increase in sensible heat flux. The net effect depends on the ambient air temperature, relative humidity, length of the ablation season and the magnitude of the other components of the energy balance. Figure 6-42 illustrates the effect of a doubling in wind speed. The result is increased ablation over most of the surface, with the greatest increases coincident with highest mean annual temperature. However, in high-elevation areas where protection from surrounding terrain is minimal, a larger proportion of the energy available for melting is via shortwave radiation. Associated turbulent transfers tend to be negative and the wind speed therefore increases net snow accumulation in these areas, in many cases even changing ablation areas to accumulation areas. This is a particularly noteworthy result in that it clearly demonstrates that the model is capable of reproducing the detailed interplay between the various components of surface energy balance in a way that simpler models cannot hope to emulate. For the base case Tioga maximum glacier considered here, a doubling in wind speed makes the terminus retreat by about 18% (350 m increase in elevation, 4.2 to 5 km decrease in length).

The sensitivity of the model to wind speed also reflects its sensitivity to the turbulent energy transfer coefficients, because they are simply proportionality factors in the turbulent heat transfer calculations. We believe, however, that the bulk transfer coefficients are fairly well constrained for modern conditions and less likely than wind speed to vary with climate. For the purpose of estimating uncertainty in the turbulent heat transfer term in Bishop Creek, we assume that a change

in wind speed of a factor of  $\sim 2$ , up or down, might have been associated with the last glacial maximum climate, and that a decrease in wind speed would have an equal and opposite effect on the position of the terminus.

#### *SENSITIVITY TO CLOUDINESS*

Cloudiness affects several of the energy balance components of the model. Increased cloudiness decreases the atmospheric transmissivity of shortwave radiation; increases the emissivity of the atmosphere and, thereby, the longwave radiation incident on the ice; and increases the surface albedo of the ice surface. The net effect of increased cloudiness thus depends on the temporal distribution of cloudcover and the ambient air temperature and radiation balance of the surface. Figure 6-42 illustrates the results of (A) a doubling in cloudcover (up to a maximum of 100%) and (B) a shift in the seasonal distribution of cloudcover by six months. Monthly values of the relevant energy fluxes calculated at South Lake are shown in Figure 6-39. Again the reference simulation is the  $\Delta T = -5$ ,  $P = 150\%$  net accumulation for the existing topography.

The dominant effect is clearly the decrease in shortwave radiation and across much of the grid ablation is reduced by several centimeters. There is virtually no effect in the highest accumulation areas where the global radiation is already low. Increases in ablation are apparent in a few small areas scattered across the surface. These are typically close to the local ELA and presumably have substantial radiant cooling. The increase in incoming longwave radiation in those areas appears to override the corresponding decrease in shortwave radiation. Again, this demonstrates the power of this approach in illustrating the complex relationship between the various components of the energy balance in high-relief terrain. The net effect of these increased cloudiness simulations, accomplished either by shifting timing or simply doubling it, was essentially the same, resulting in a  $\sim 5\%$  increase (100 m decrease in elevation, 1.5 km increase in length) in glacial extent relative to the base case



glacier.

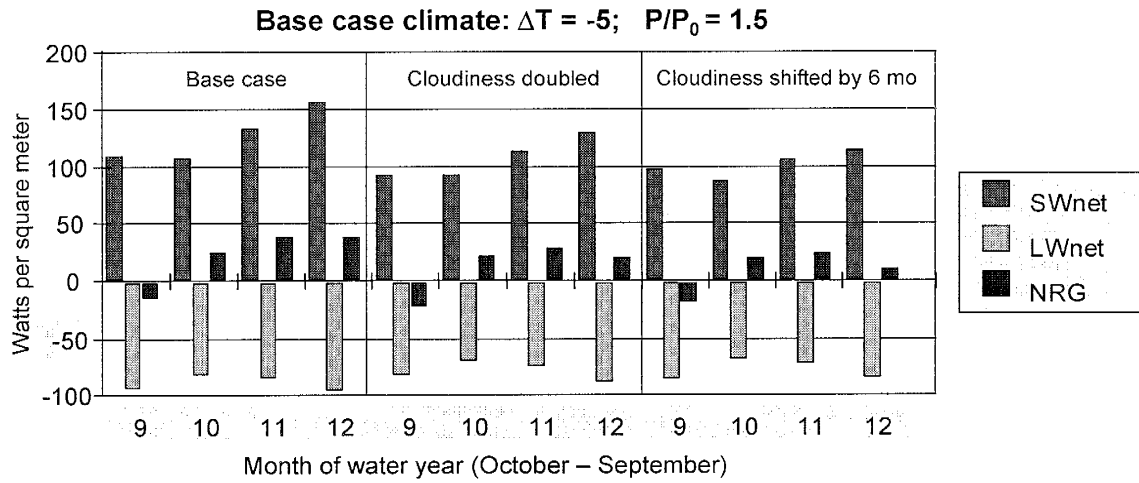


Figure 6-39. Mean monthly shortwave, longwave and net energy fluxes to the glacier surface at South Lake in the South Fork of Bishop Creek under climatic conditions of  $-5^{\circ}\text{C}$  and 1.5 times precipitation assuming (left) modern cloudiness conditions, (center) a doubling in cloudiness and (right) cloudiness distribution shifted by 6 months. Only months where temperature is above zero are shown; first month in each series is June.

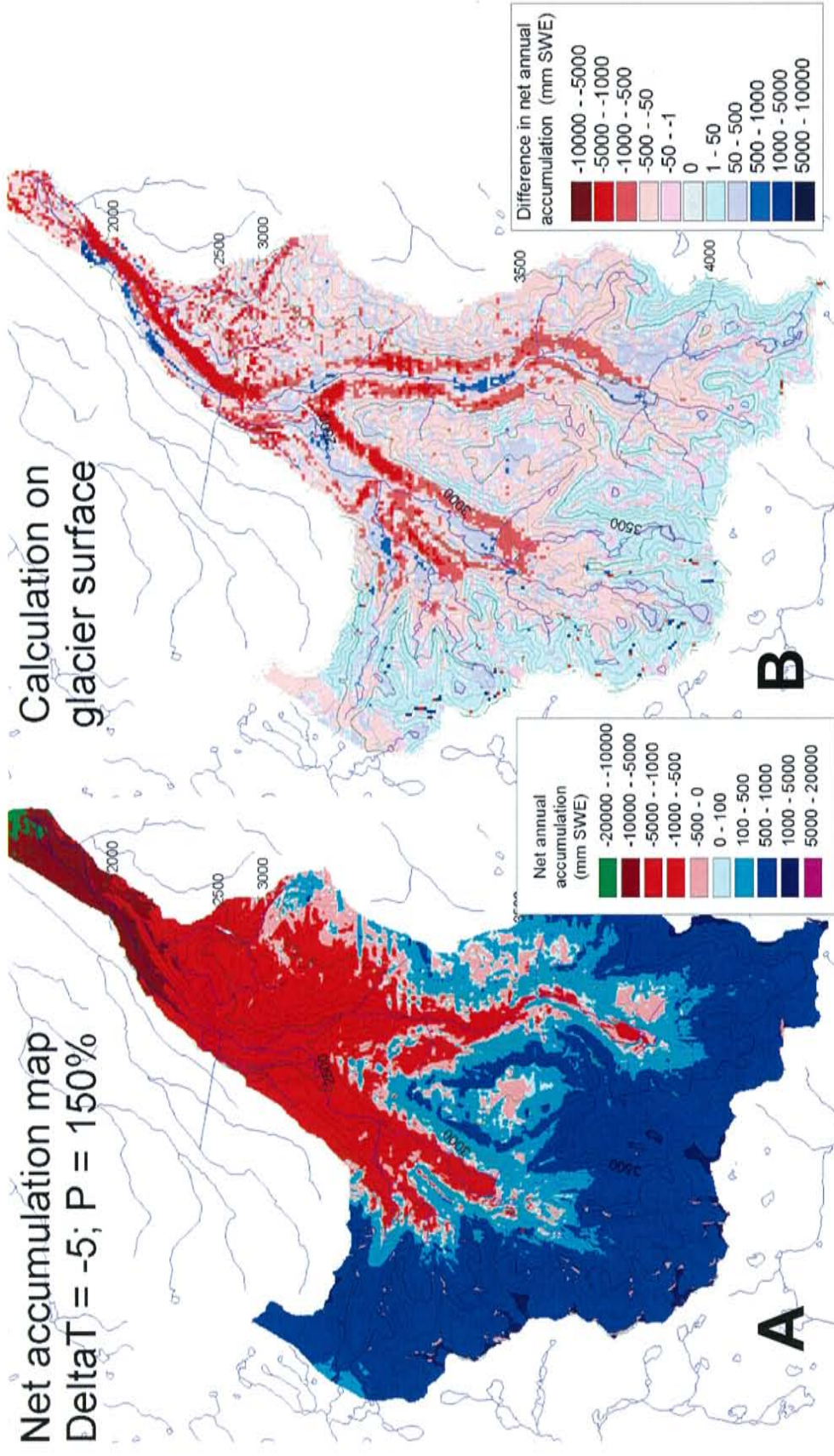


Figure 6-40. (A) Net accumulation map for a 5°C temperature depression and 50% precipitation increase and (B) the change in net accumulation induced by calculating the snow/ice energy and mass balance on the surface of the Tioga maximum glacier rather than the modern ground surface.

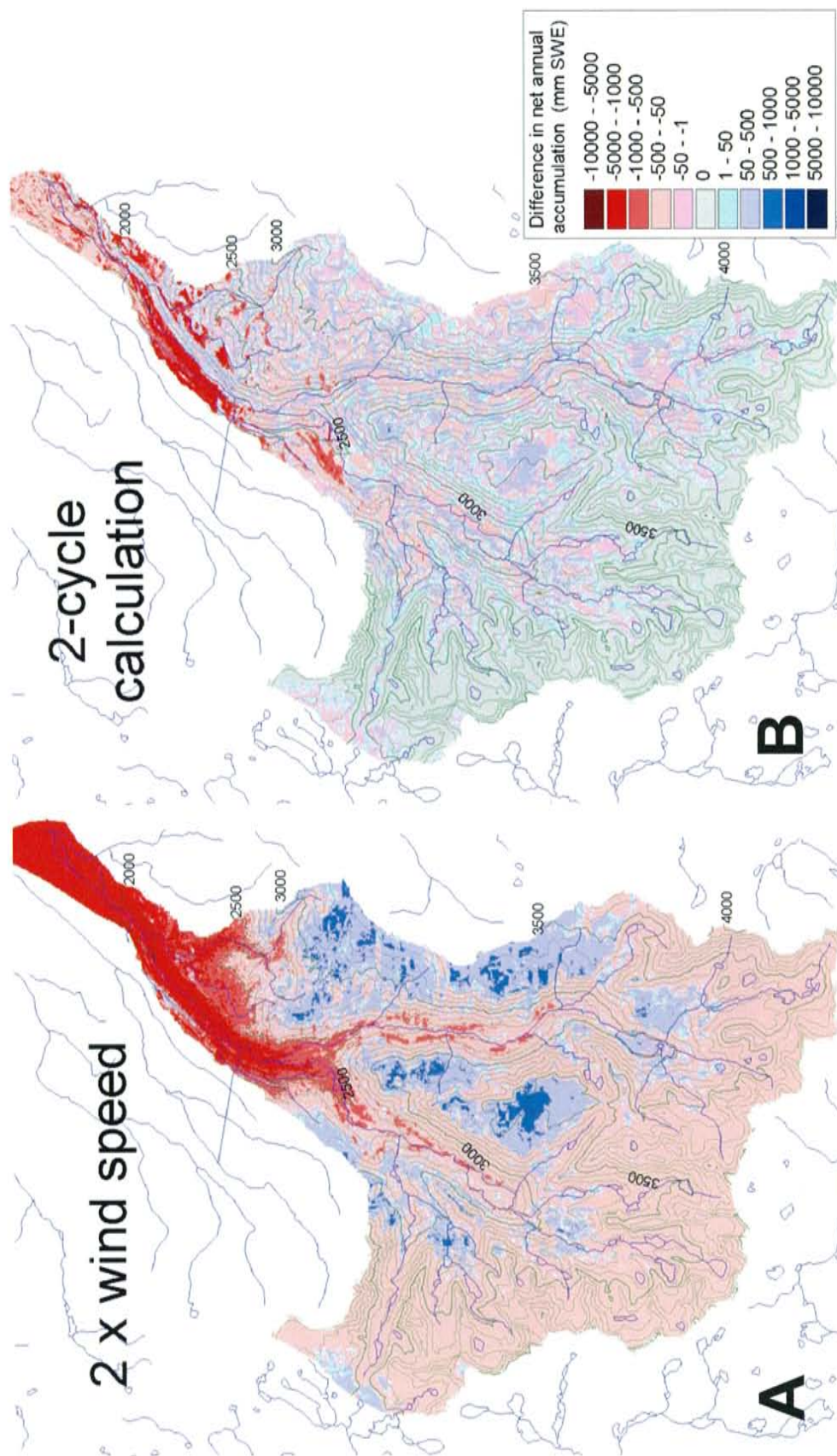


Figure 6-41. Change in net accumulation induced by (A) a doubling in wind speed and (B) calculating the snow/ice energy and mass balance over two, rather than one, annual cycle.



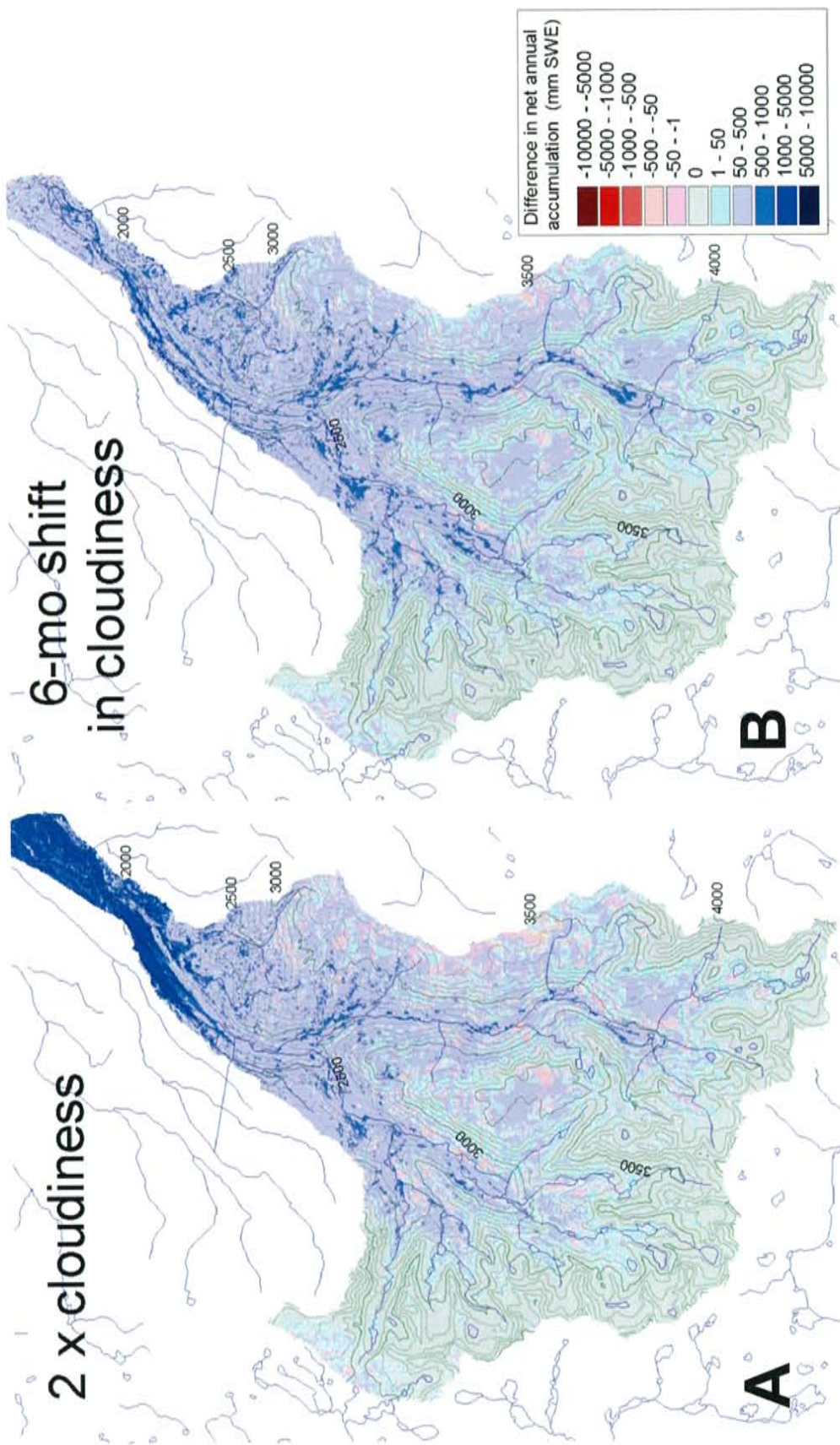


Figure 6-42. Change in net accumulation induced by (A) a doubling in cloudiness and (B) a shift in monthly cloudiness by six months (winter to summer).

## SUMMARY

The sensitivity tests we conducted are summarized in Table 6-1. They demonstrate significant sensitivity to certain assumptions and parameters of the model, some of which result in systematic, and therefore correctable, errors in model predictions and some of which simply add uncertainty to those predictions. Thus far we have described model sensitivity in terms of glacial extent. In using these models to infer paleoclimatic conditions however, we need to describe those changes in terms of paleoclimatic parameters. As a direct comparison of the effect of a simple temperature change on the glacier with these effects, Table 6-1 also shows the difference in glacial extent between the base case glacier and that produced from conditions 1°C warmer (Table 6-1 H). The sensitivity to temperature is about 420 m/°C. Given the decrease in extent that occurs when the energy and flow models are coupled through three iterations, we anticipated that a temperature depression of ~5.65 °C, with the same 150% relative precipitation rate, would actually be needed to sustain the base case glacier. To test that, we conducted three colder climate simulations using the base case glacier surface for topography and incorporating multiple-cycle energy balance calculations to the effect of initial condition. Those simulations (Table 6-1: I-K) indicate that the combined effect of neglecting initial conditions and glacier topography in the energy balance calculations is an ~0.75°C underestimation of the needed temperature depression, or equivalent precipitation increase. Although this implies that a systematic correction should be applied to the contours of Figure 6-25, that correction should be proportional to glacial extent, as the changes in topography resulting from growth of small glaciers are relatively minor. It is also possible that the energy balance calculated with the glacier topography as the ice surface might in some areas yield more accumulation than that calculated using the underlying topography as the ice surface. The extent to which the two models should be coupled in order to provide the necessary detail should be determined on a case-by-case basis.

Source of error/uncertainty		$\Delta Z$ (m)	$\Delta Z_{\text{frac}}$ (%)	$\Delta X$ (km)	$\Delta X_{\text{frac}}$ (%)
A	Flow constants for deformation and sliding (actual from k/10)	-270	-13	-2.9	-11
B	Glacier growth feedback on energy balance, iteration 2	-297	-15	-3.4	-12
C	Glacier growth feedback on energy balance, iteration 3	-265	-14	-2.9	-11
D	Low Albedo = 0.25	-345	-18	-4.2	-15
E	2 x Cloudiness	+95	+5	+1.5	+5
F	2 x Wind Speed	-315	-16	-3.5	-13
G	Neglecting initial conditions	-95	-5	-0.9	-3
H	-4.0°C, 150% P – calculated on existing topography	-417	-21	-5.8	-21
I	-5.5°C, 150% P – calculated on surface of base case glacier	-84	-4	-0.9	-3
J	-5.8°C, 150% P – calculated on surface of base case glacier	+50	+3	+0.7	+3
K	-6.0°C, 150% P – calculated on surface of base case glacier	+90	+5	+1.5	+5

Table 6-1. Changes in terminus position as a result of various sensitivity tests described in the text.  $\Delta Z$  and  $\Delta X$  are, respectively, the vertical and horizontal changes in terminus position.  $\Delta Z_{\text{frac}}$  and  $\Delta X_{\text{frac}}$  are the fractional changes in the decrease in elevation (1950 m) represented by the base case, and the total length (27.5 km) of the base-case glacier. Note that item C also corrects for the effect of initial conditions described by simulation G.

To interpret the sensitivity to uncertain model parameters and possible changes in second-order climate parameters in terms of temperature and precipitation, we used the climatic sensitivity of the base case glacier as illustrated by Figure 6-25, ~420 m/°C and ~800 m per unit change in relative precipitation. Table 6-2 summarizes the resultant uncertainty for changes we consider useful in estimating the impact on paleoclimatic inferences made with the model.

Source of error/uncertainty		$\Delta T$ (°C)	$\Delta P/P_0$ (%)
A	Glacier growth feedback on energy balance	+0.75	+38
B	Neglecting initial conditions	+0.20	+12
C	Flow constants for deformation and sliding	$\pm 0.25$	$\pm 13$
D	Albedo	$\pm 0.80$	$\pm 43$
E	Cloudiness	$\pm 0.20$	$\pm 12$
F	Wind Speed	$\pm 0.75$	$\pm 40$
G	Turbulent transfer coefficients	$\pm 0.75$	$\pm 40$
H	Precipitation regression	$\pm 0.40$	$\pm 20$

Table 6-2. Estimated paleoclimatic uncertainties associated with various errors and uncertainties in the modeling process. Effects of the uncertainties are described in terms of the difference in temperature depression ( $\Delta T$ ), and the difference in the relative precipitation rate ( $\Delta P/P_0$ ) that would be required to produce the Tioga maximum glacier *relative* to the base case simulation. Items A and B are considered systematic errors. Estimated uncertainties are based on (C) a factor of 5 uncertainty in both flow constants, (D) an ~40% error in the albedo of ice, (E) a factor of 2 difference in cloudiness, (F) a factor of 2 difference in windiness, (G) a factor of 2 difference in turbulent transfer coefficients, and (H) a 20% difference in precipitation.

To illustrate how these uncertainties are likely to affect paleoclimatic interpretations based on the glacier flow model, we conducted a preliminary uncertainty analysis using a logic tree approach

[Mishra, 2002]. We subjectively estimated Bayesian probabilities associated with certain deviations from the parameters used in our model of the Bishop Creek glaciers. Because the glaciers are relatively more sensitive to temperature than precipitation, we used the difference in temperature between that required for the base case glacier and that needed under the new conditions (based on the data summarized in Table 6-1 and Table 6-2) as an index of the effect on the model's output. Probabilities and temperature effects associated with the various conditions are summarized in Table 6-3.

Effect & magnitude	Difference in temperature estimate (°C)	Probability of occurrence
<i>Flow Constants</i>		
x 5	0.25	0.17
x 1/5	-0.25	0.17
As Is	0	0.67
<i>Ice Albedo</i>		
x 0.4	-0.8	0.33
x 1.4	0.8	0.17
As Is	0	0.50
<i>Precipitation</i>		
x 0.9	-0.2	0.33
As Is	0	0.67
<i>Mean Wind Speed</i>		
x 2	-0.75	0.33
As Is	0	0.67
<i>Cloudiness</i>		
x 2	0.2	0.33
As Is	0	0.67
<i>Bulk Transfer Coefficient</i>		
x 2	-0.75	0.17
x 0.5	2	0.17
As Is	0	0.67

*Table 6-3. Parameter changes included in the logic tree uncertainty analysis, estimated probabilities, and the difference in temperature from the temperature predicted using the base-case model.*

Due to computational limitations<sup>14</sup>, we considered only a limited range of effects connected with parameter uncertainty in this analysis (systematic errors are treated separately). We considered only increases in wind speed and cloudiness, for example, because it seems unlikely that they would have been reduced during the glacial period. If our precipitation model is in error, it is probably biased toward too much precipitation in the higher elevations. We based the high-elevation estimate on data from the PRISM project [Daly *et al.*, 1994], but the 4-km grid cells along the crest in that data set are probably skewed toward the much higher precipitation rates that exist on the west side of the crest. We therefore included a 33% probability that precipitation is ~10% less than that used in the model. The albedo of

<sup>14</sup> Improved programming, particularly in terms of the coupling of the two models, should effectively eliminate those restrictions.

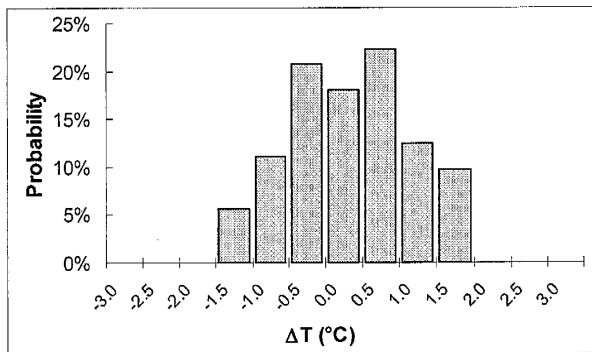


Figure 6-43. Histogram of increases- over the base-case model estimates - in temperature depression needed to sustain a given glacier at steady state.

melting ice on the Sierra Nevada glaciers of the late Pleistocene is difficult to estimate but, if anything, is probably lower than the 40% value we used. We used higher and lower values in our logic tree but assigned higher probability to the latter. We applied a factor of two increase and decrease in the turbulent heat transfer coefficient and a

factor of five increase and decrease in the ice flow constant, with equal weights on either side.

Effects and probabilities associated with the various parameter changes are summarized in a histogram in Figure 6-43. The outcomes describe how much warmer, relative to the base-case model, conditions would need to be to sustain a given steady-state glacier. Results suggest that a one-standard-error estimate of the uncertainty in the temperature depression predicted by the glacier model is approximately  $\pm 1^\circ\text{C}$ . The histogram is slightly skewed (mode and mean) toward positive temperature differences, indicating the greater proportion of alternative scenarios would require slightly greater temperature depression for a particular glacial extent.

Although the glacier modeling approach described here is central to the goals of this project, the larger purpose of this study is to examine how combined analysis of glacial and lacustrine records may be used to better constrain estimates of paleoclimatic conditions. We have not, therefore, attempted a detailed analysis of the glacier model's sensitivity to various parameters. The preliminary analysis described is primarily intended to illustrate the sensitivity of model to the most influential of numerous uncertain parameters, and, perhaps more importantly, the highly detailed information that can be obtained during such tests. Further sensitivity analyses should lead to improvements in the model but may also refine our understanding of the interaction between the energy balance and flow



of glaciers, and their climatic and topographic controls. In contrast, assumptions commonly included in simpler approaches to reconstructing paleoclimate from glacial landforms largely preclude such analyses.

#### ***POTENTIAL APPLICATIONS OF THE 2-D GLACIER MODEL***

As hinted at in the sensitivity discussions, our glacier modeling approach shows particular promise as a means of interpreting complicated distributions of ice cover and differences in past glacial extent in different basins. It should, for example, prove particularly valuable in differentiating between latest-glacial and Holocene glacial features. Some Recess Peak deposits in the Sierra Nevada, for example, have been mapped as Matthes deposits and vice versa [Burbank, 1991]. Distinguishing between those features can be difficult because the ELA depressions represented are similar and the advances are small enough that topographic controls make changes in one basin radically different than those in another basin of differing slope and aspect. Researchers have long recognized the importance of topographic controls on such advances, citing differences in radiation, wind, snow-drift, and precipitation as potentially important effects [Clark and Gillespie, 1997]. Our model provides a means of specifically addressing the question of what are the dominant topographic controls on small glaciers, and a means of predicting, correlating and mapping such features in basins of vastly different orientation, aspect, and overall geometry. In its current form, the model reproduces remarkably well the modern glaciers in the Bishop Creek area. Comparison of modeled Recess Peak glacial extent with preliminary mapping of Holocene deposits in Bishop Creek [Clark, personal communication, 1999] indicates excellent agreement in some areas and considerable differences in others. Given the preliminary nature of the field mapping, it is impossible to say whether the glacier model or the field mapping more accurately describes the distribution of small glaciers in Bishop Creek during the Recess Peak advance. Even if the model proves to yield only a poor fit to the field evidence however, it provides a tool that can be used to explore the possible

causes for the discrepancies and thereby lead to an improved version of the model and a better understanding of the controls on glacier extent.

Other questions that the model could be used to explore include:

- Why are AARs of glaciers typically close to 0.65. Is AAR primarily controlled by surface energy balance or the flow characteristics of ice?
- How do the feedbacks between the surface energy balance and the surface topography affect glaciers of varying size, shape and orientation?
- What are the effects of the feedback between glaciation and surface energy balance due to glacial erosion? Through a series of glacial cycles, glaciers tend to increase relief as they carve the valleys deeper but leave the windblown mountain peaks relatively untouched. How does this process affect the extent of glaciation during the next glacial cycle?
- How do ice flux and velocity, as controlled by surface energy balance; transient state; and topography affect debris deposition? Moraine development is largely a result of stability, as the glacier annually advances toward and away from the same margins. How sensitive are the locations of these margins to perturbations in mass balance as a function of topography and mass balance? Can the glacier flow model be used to predict where and when significant moraines would develop under different conditions?

The latter two questions suggest that with the addition of an erosion function and debris-transfer scheme to the model, transient simulations of glacier growth and recession would be a valuable means of addressing several interesting geomorphological questions.

Another potential application of the model becomes evident when we carefully examine results of simulations that produce similar glacial extents with dissimilar climatic conditions. Figure 6-44 illustrates two different combinations of temperature and precipitation that could produce the Tioga maximum advance in Bishop Creek. The first represents a condition 6° C colder and 10% wetter

than modern. The second is a much wetter and warmer climate, only 2° colder but with ~3 times the modern precipitation rate. Figure 6-45 displays the simulated steady-state glaciers that would result from those net accumulation patterns. While the glacier terminus in each of these simulations is essentially the same, there are several interesting differences in the overall pattern of ice distribution. Both accumulation rates and ablation rates are higher in the wetter simulation and the flux through the glacier, reflected in the ice thickness, is thus considerably greater. The accumulation area in the wetter simulation, however, is significantly smaller because the steeper mass balance gradient concentrates the accumulation at the high elevations. The colder climate simulation displays a much gentler mass balance gradient and the accumulation area extends to lower elevations. As a result several small glaciers develop at low elevations in the basin, many of which are too small to coalesce with the main glacier. In contrast, as almost all of the snow in the wetter climate falls at high elevation, virtually all of it is within the contribution area of the main Bishop Creek glacier.

As discussed previously (Figure 6-23), conditions on Table Mountain, the flat-topped mountain between the Middle and South Forks, are also quite dissimilar under different climate scenarios. Under the colder climate most of it is capped by a thin glacier that flows outward from the center of the mountain. Under the wetter climate, small glaciers form on its flanks but most of the upper surface remains ice-free. The climatic sensitivity of areas like Table Mountain, and the small, subordinate glaciers that can develop at low elevations, suggests that geomorphic evidence from such areas may be diagnostic of the relative importance of temperature versus precipitation changes in producing a particular glacier, at least for extreme differences in the relative importance of temperature and precipitation.

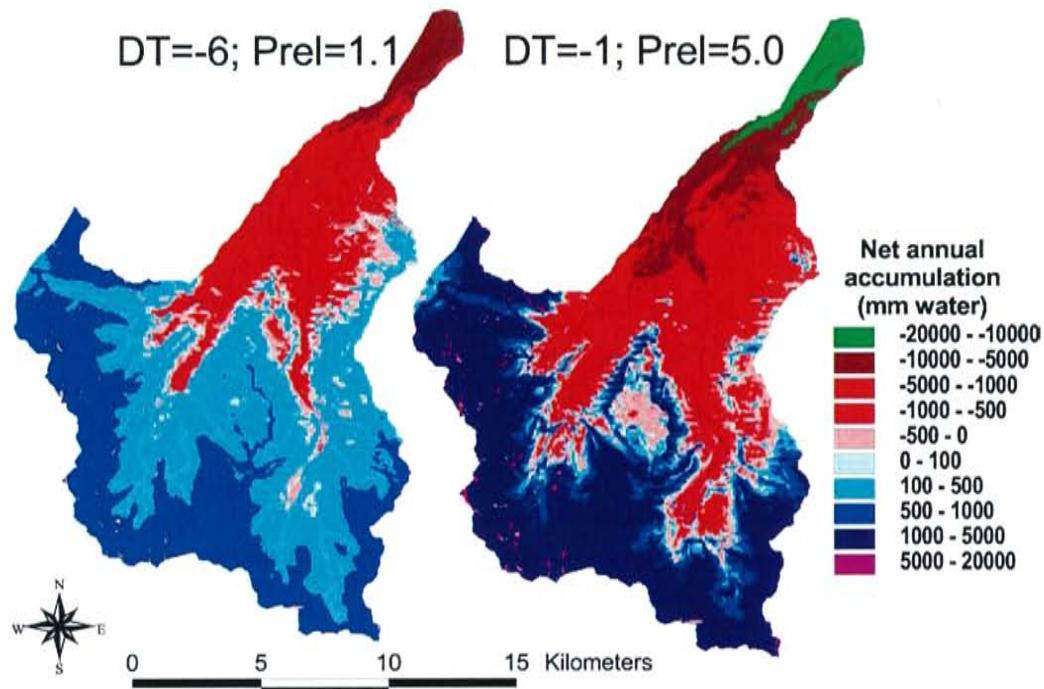


Figure 6-44. End-member net accumulation maps for the Tioga II glacier in Bishop Creek. DT = temperature difference from modern climate. Prel = precipitation rate normalized to that of the modern climate.

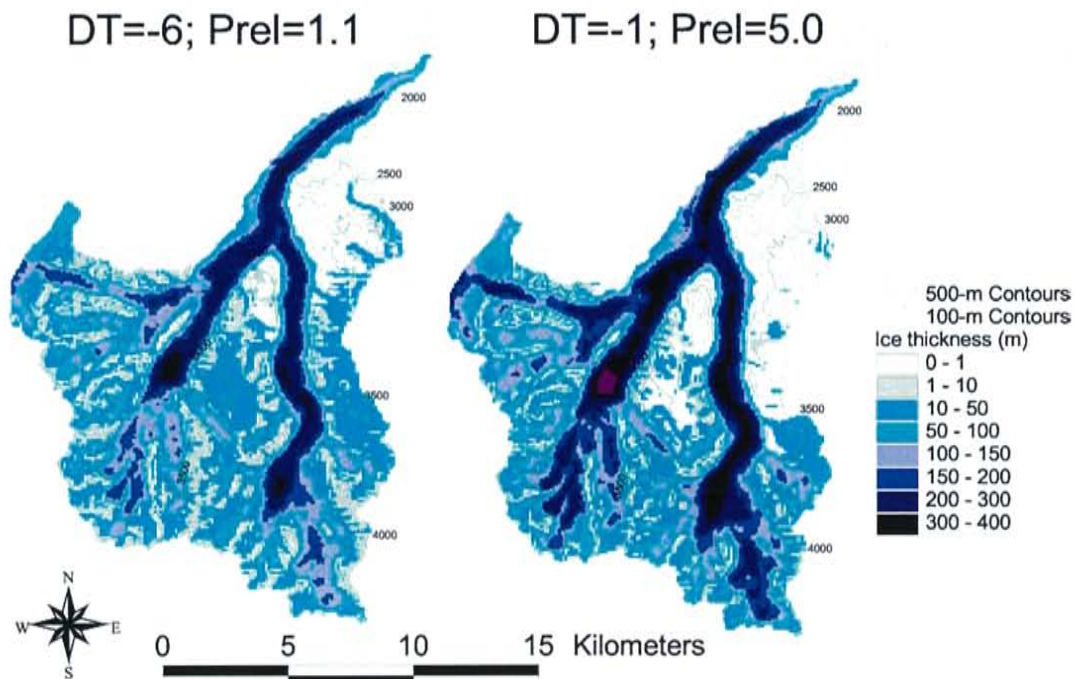


Figure 6-45. Simulated glaciers developed from the net accumulation maps in Figure 6-44. DT = temperature difference from modern climate. Prel = precipitation rate normalized to that of the modern climate.

---

## CHAPTER 7 - COMBINED ANALYSIS OF GLACIAL AND LACUSTRINE RECORDS

---

The Thornthwaite water balance model described in Section Chapter 3 -, combined with a simple saturation vapor-pressure based estimate of lake evaporation sensitivity, provides us with a response surface that describes the changes in cumulative lake surface area that would likely accompany changes in precipitation and temperature in the basin (Figure 3-17). Similarly, the glacier model described in Section 5 provides a means of estimating glacier response to a wide range of changes in temperature, precipitation and other parameters such as wind speed, relative humidity, and cloudiness. Comparison of the response surfaces of the Bishop Creek glacier and the Owens Valley terminal lake system (Figure 7-1) illustrates several important points relevant to their use as a means of reconstructing paleoclimatic conditions. First, as evidenced by the contour intersection angles, the glaciers and terminal lake systems have dramatically different relative sensitivities to the primary climatic variables. The glacier displays much greater relative sensitivity to temperature while the lakes are much more responsive to changes in precipitation. Thus, to the degree to which these models adequately capture the physics of the two systems, they should provide a valuable means of more firmly constraining the climatic conditions implied by a given combination of lake and glacier extents. Second, the sensitivity of both systems to changes in temperature and precipitation is essentially linear throughout the range of climatic changes tested. As most of the energy balance equations are, at best, weakly non-linear functions of the primary climatic variables, this is not surprising. Third, while changes in the terminal lake system are essentially linear, the lake system is extremely sensitive to precipitation, reflecting from the amplified response of runoff to precipitation. The effect of evaporation depression on the lakes themselves is minor in comparison. Amplification in the runoff response to precipitation is consistent both with analysis of historical records of streamflow response and with theoretical considerations of how runoff in arid basins responds to climate change. Moreover, the magnitude of the modeled runoff response is consistent with

observed relationships between temperature, precipitation and streamflow in the U.S. [Langbein, 1949].

We now consider how these combined response surfaces can be used to interpret a chronology

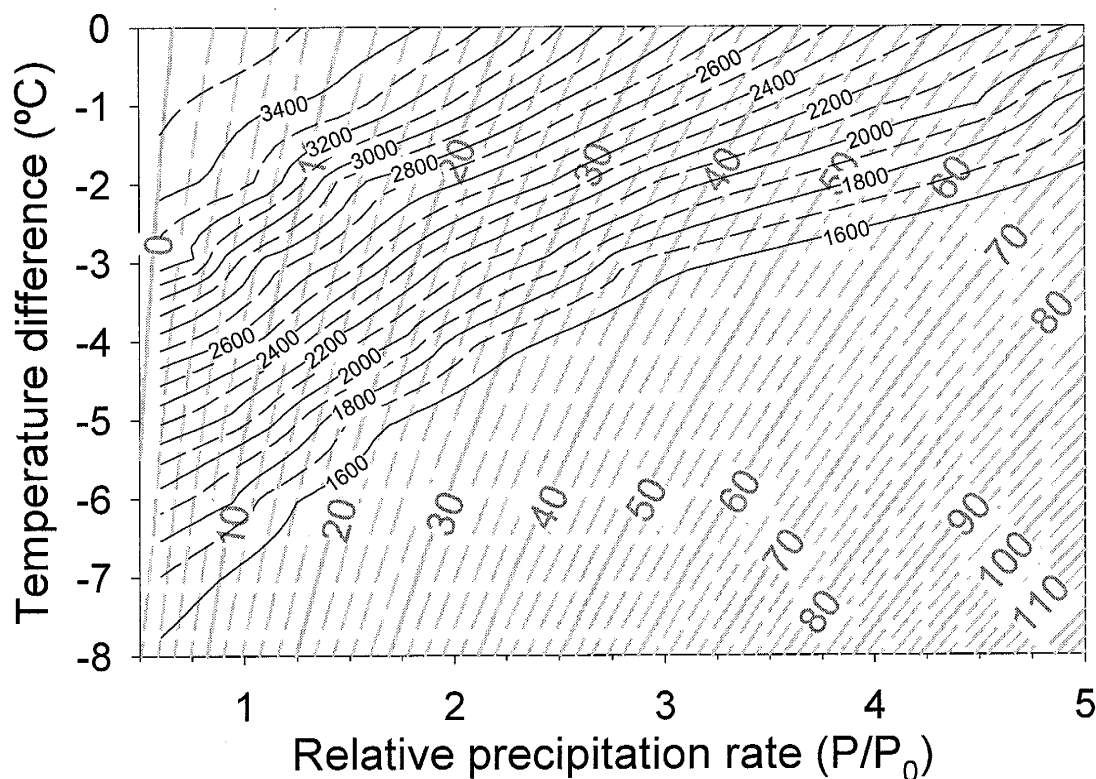


Figure 7-1. Overlay of the Bishop Creek glacier response surface (thin black, subhorizontal, contours of equal terminus elevation (m)) and the Owens Valley lake system response surface (thick gray contours of cumulative lake surface area ( $10^3 \text{ m}^2$ )). Temperature and precipitation reference ( $P_0$ ) conditions refer to modern climate.

of changes in both the glacial and lacustrine systems. The amplified response to precipitation demonstrates that only a small subset of the climatic conditions displayed in Figure 7-1 is necessary for analysis of the possible lake surface area in the Owens Valley. Even without a change in temperature, the sensitivity of the lake system to precipitation means that a 5-fold increase in precipitation could produce a cumulative lake surface area of  $>6,000 \text{ km}^2$ , a value well beyond what might be considered reasonable for the combined basins (even with Panamint Lake full, the

combined surface area of the system would be less than 2500 km<sup>2</sup>) Interestingly, however, the corresponding glacier response is entirely within the range of changes observed in the geologic record, with the same conditions producing a glacier not even as extensive as the Tioga maximum glaciers.

Based on data from Owens Lake, Searles Lake, and the glacial deposits in Bishop Creek and Horton Creek, we have developed chronologies for both systems (Figure 2-3, Table 4-1). The timing of major events in these chronologies is quite consistent and suggests the following broad chronology for the entire hydrologic system for the period dating from the last glacial maximum (Figure 7-2). The oldest glacial deposits that represent the last glacial maximum in Bishop Creek date to approximately 26 ka. Evidence of the position of the lakes at that time is sparse but isotopic data from Owens Lake suggests that this was only a moderately wet period for Searles Lake. The next event, designated Tioga stage III and occurring between about 20 ka and 17.7 ka, is relatively well constrained in both time and spatial extent for both systems. The glacier in Bishop Creek extended down to an elevation of ~1675 m, to near the mouth of Coyote Creek, and lake sediments deposited at Poison Canyon indicate that Searles Lake was very likely at its sill and overflowing. A long hiatus (~3 kyr) in the Owens Lake record occurs between the Tioga III advance and the last major Tioga pulse - the Tioga IV advance - that terminated at the confluence of the South and Middle Forks in Bishop Creek. Climatic conditions between the Tioga III and Tioga IV advances are, as a result, poorly constrained. The unconformity in the sediments of Owens Lake strongly indicates an interval of much drier conditions, but the duration of that period is unknown. The lack of glacial deposits with ages between the Tioga III and Tioga IV events is consistent with the occurrence of a warm, dry period during that interval but data from Searles Lake suggests a return to alternating wet and dry episodes in Searles Basin by ~17 ka.

Our dates on Tioga IV moraines are consistently around 15 ka and this coincides with the age of

tufa deposits at Searles Lake, indicating that the lake again reached its sill during the Tioga IV glaciation. The end of Tioga stage IV, as evidenced by dates from the glaciers and Searles lakebed deposits, seems to correspond with the established date for onset of the Bolling/Allerod warm period, 14.76 ka. The lake records, however, indicate that very wet conditions persisted until about 13 ka. From this, and George Smith's chronology [1987] of the pluvial period in Owens Lake, we conclude that Searles lake was probably relatively large but below its sill during the Bolling/Allerod (~14.7 – 12.9 ka). The end of this wet period is concurrent with the construction of the Recess Peak moraines, which typically yield ages close to 13 ka.

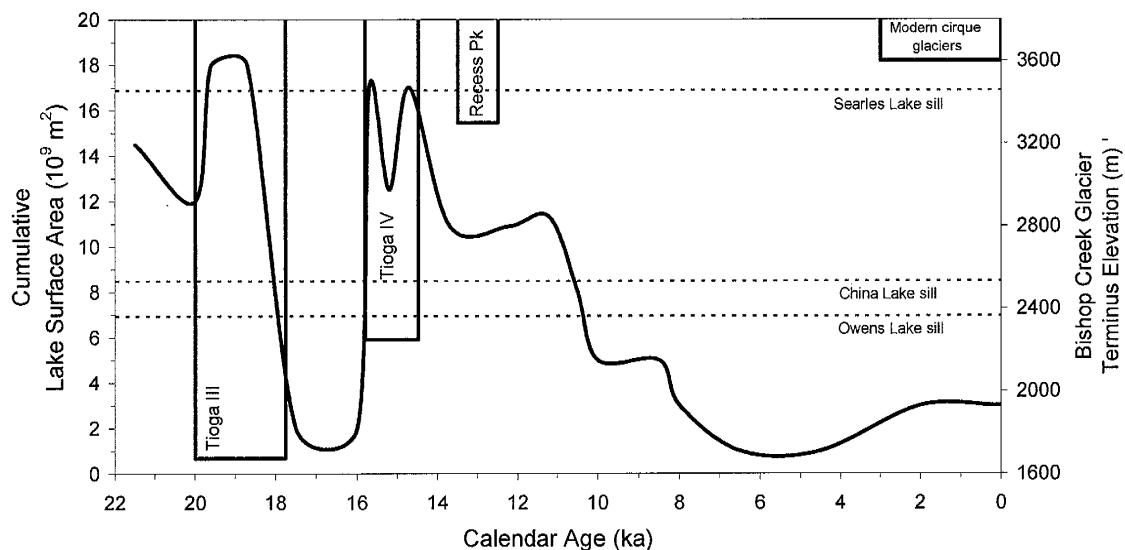


Figure 7-2. Estimated history of changes in the glacial and terminal lake system in the Owens Valley for the past ~20 kyr. Curved line (left ordinate) is cumulative surface area for the Owens Valley lake system. Dotted lines indicate lake surface area at lake sills. Bars (right ordinate) represent elevations of glacial termini during advances or relatively stable glacial periods in Bishop Creek.

Our interpretation of the chronology of changes in the hydrologic systems in the Owens Valley during the past ~25 ka yields essentially four wet periods where both systems are relatively well constrained. These periods correspond with the Tioga I, Tioga III, Tioga IV and Recess Peak glacial advances in Bishop Creek. To reconstruct the climatic conditions that existed during those periods, we display these constraints by positioning them along the corresponding contours of a subset



(Figure 7-3) of the combined response surfaces shown in Figure 7-1. The area of intersection of the corresponding glacier and lake contours defines the range of climatic conditions that could produce the two systems at the observed extents. Because of the large contrast in the slope of those contours, the area generally defines a very narrow range of likely precipitation and temperature changes.

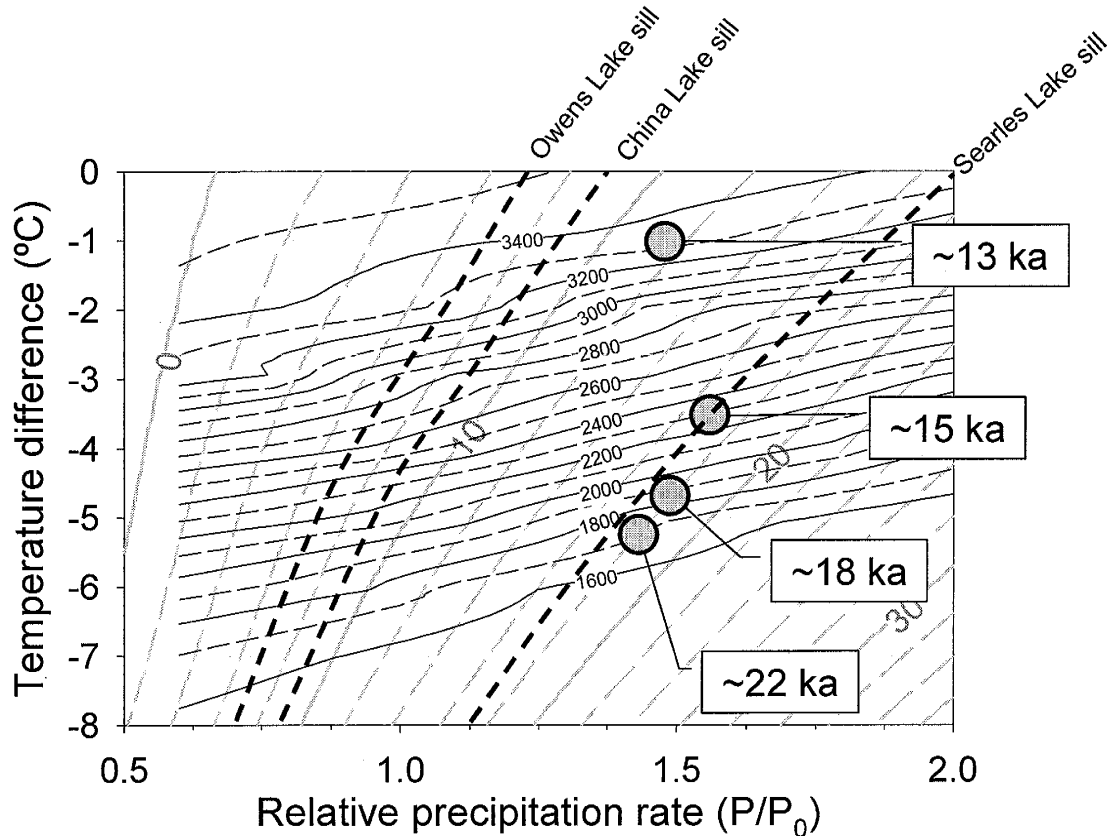


Figure 7-3. Overlay of the Bishop Creek glacier terminus position response surface (thin black, subhorizontal, contour lines labeled with terminus elevation in meters) and the Owens Valley lake system response surface (cumulative lake surface area contours (thick gray lines). Heavy black dashed lines indicate cumulative lake surface areas at sills of Owens, China and Searles Lakes. Temperature and precipitation reference ( $P_0$ ) conditions refer to modern climate.

This discussion has heretofore neglected the not insignificant uncertainties involved in our estimates of the response of the glacial and lacustrine systems to climate change. Systematic errors in our calculations of glacier response include (1) neglecting the feedback between the surface energy balance and the surface itself, due to addition of glacial ice to the existing topography and (2)

application of initial conditions that lead to slight underestimation of ablation rates. Together these effects lead to an underestimation of the climate change needed to maintain a certain glacier. For the Tioga maximum glaciers in Bishop Creek, an additional  $0.75^{\circ}\text{C}$  temperature depression, or  $\sim 40\%$  increase in precipitation would be needed (Table 6-2). Assuming the error is directly proportional to glacial extent, the necessary corrections for the Tioga IV and Recess Peak advances are  $-0.6^{\circ}\text{C}$  or  $\sim +30\%$  precipitation, and  $-0.1^{\circ}\text{C}$  or  $\sim +5\%$  precipitation, respectively. We can represent these systematic errors with a corresponding offset in the glacier contours that represent the periods of known glacial extent. This slightly alters the paleoclimatic estimates of precipitation and temperature derived from the intersecting lake and glacier contours (Figure 7-4). Potential differences in second-order climatic variables, such as windiness and cloudiness, which might have attended the last glacial period, contribute significant uncertainty to our paleoclimate estimates. Based on the results of our preliminary uncertainty analysis, it appears that one standard error in temperatures estimated using the glacier model is on the order of  $1^{\circ}\text{C}$  or, equivalently, a  $\sim 50\%$  change in the relative precipitation rate. These uncertainties are shown as error bars on the precipitation and temperature combinations that correspond to intersecting lake and glacier contours (Figure 7-4).

Additional uncertainty stems from our model of the response of lake surface area to climate change in the Owens Valley and to the uncertainty in our lake level chronology. At this point we have not conducted similar sensitivity tests with the water balance model to estimate the effects of uncertain parameters. That analysis is not warranted at this time primarily because the greater uncertainties associated with it stem from the assumptions of the model itself, rather than in the few parameters included in it. The model we have applied is perhaps most notable for its lack of input parameters and its usefulness may be primarily as an alert to the potential simplicity of the system. Additional modeling, using more sophisticated basin water balance models, is needed to examine whether the predictions of our simpler model are reasonable. We also note that both the timing and

magnitude of events in the lake surface area chronology of the Owens Valley are considerably less well-constrained than the glacial chronology. For these reasons, we have not attempted to illustrate in Figure 7-4 the uncertainties associated with the lacustrine system.

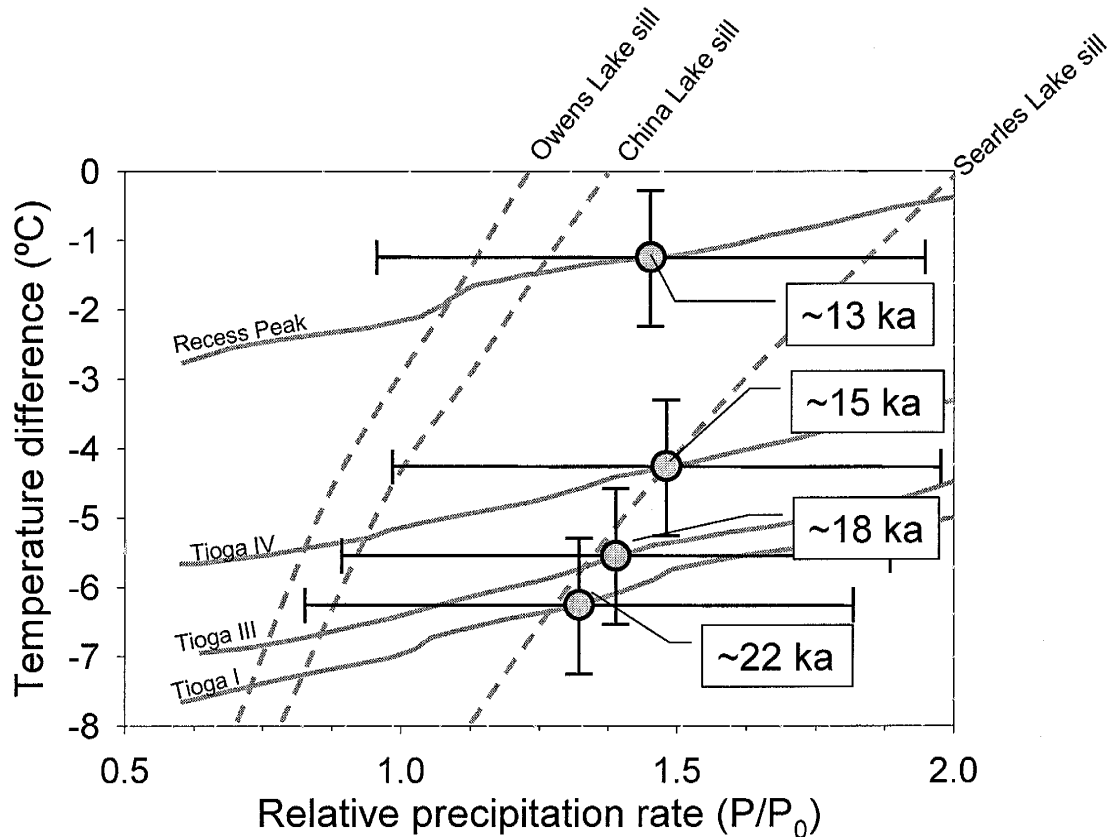


Figure 7-4. Total lake surface area contours (dashed lines) corresponding to various sills in the system, and glacier terminus elevation contours (solid lines) corresponding to four of the last five recorded advances in Bishop Creek. The latter have been adjusted to account for systematic errors in the glacier model. Circles and corresponding ages indicate the intersections of contours describing contemporaneous events in the lake-surface area and glacial chronologies. They therefore describe the temperature and precipitation combinations that could satisfy both constraints. Error bars represent one sigma errors in the temperature and precipitation estimates derived from the glacier model.

From the contour intersections in Figure 7-4, we can deduce both the temperature and precipitation changes that accompanied changes in the water balance of the Owens Valley glaciers and lakes during the last ~20 ka. The most striking result is that the glacial-pluvial period appears to have been more the result of lower temperatures than of increased precipitation. Stages I and III of

the Tioga glaciation appear to have been characterized by temperature depressions of approximately 5.5°C and 6.5°C, respectively, and a precipitation increase of only ~30 - 50%. Approximately 3,000 years after the Tioga III moraines were constructed, the glaciers in Bishop Creek had taken position upcanyon at the confluence of the Middle and South Forks, ~9 km and 350 m higher in elevation. Highest levels in the lake system, on the other hand, appear to have been little different; the change in climatic conditions therefore appears to have been primarily a result of warming, by approximately 2°C. The slight increase in precipitation from the Tioga III to the Tioga IV (from ~40% to ~60%) reflects our interpretation that the cumulative lake surface area was much the same at both these times. This may or may not reflect the average conditions that existed during the Tioga IV period but even relatively large differences in the lake area would not substantially alter the amount of warming implied. Although Searles Lake continued to receive significant inflow during the next few thousand years, the glaciers retreated dramatically after ~15 ka and the last moraines of the latest Pleistocene are the Recess Peak deposits (~13 ka) that reflect a glacial period much closer to modern conditions than those of the last glacial maximum. From Figure 7-3, we infer that conditions during the Recess Peak advance differed more in precipitation than in temperature, comprising a temperature depression of about 1°C and a precipitation rate about 50% greater than at present.

---

## CHAPTER 8 - IMPLICATIONS AND DISCUSSION

---

Considering the uncertainties and systematic errors discussed above, the LGM temperature depression estimate derived from this analysis is approximately  $5\frac{1}{2}^{\circ}$  to  $6\frac{1}{2}^{\circ}\text{C}$ , slightly less than that estimated by Dohrenwend ( $-7^{\circ}\text{C}$ ) [1984]. Much of the difference appears to stem from our conclusion that precipitation rates were 20 to 40% higher than modern precipitation rates. With no change in precipitation, our coupled snow/ice energy and mass balance model and glacier flow model would also require a change of  $\sim -7^{\circ}\text{C}$  to produce the LGM glacier in Bishop Creek. Though slightly less than the estimated depression of Dohrenwend, the paleotemperature estimate of this study is entirely consistent with reconstructions based on paleoecological evidence. The closest of these studies to the Sierra Nevada are an estimate based on plant remains in ancient packrat middens from the Colorado River in northern Arizona ( $-4.8$  to  $-6.1^{\circ}\text{C}$  [Cole, 1990]) and a pollen and macrofossil study of Potato Lake in central Arizona ( $-5.2^{\circ}\text{C}$  [Anderson, 1993]). Though those estimates are subject to considerable uncertainty due to the assumptions required to convert the observations to temperatures [Stute *et al.*, 1992], they are supported by noble gas paleothermometry studies of groundwater in Texas [Stute *et al.*, 1995] and New Mexico [Stute *et al.*, 1995]. Together those studies suggest that LGM temperature depression in the southwestern U.S. was uniformly about  $5^{\circ}$  to  $6^{\circ}\text{C}$ .

Previous authors have suggested that temperature and precipitation should be somewhat interdependent and such a relationship could potentially explain at least part of the increased wetness of the pluvial period. Brakenridge [1978] argued that colder conditions in the Great Basin would be expected to decrease the overall intensity of the hydrologic cycle and temperature depression should therefore be accompanied by a decrease in precipitation. Mifflin and Wheat [1979], on the other hand, noted an inverse correlation between precipitation and temperature in basins in Nevada. They thus concluded that temperature depression would likely be accompanied by an increase in

precipitation. Although the arguments are not unreasonable, they seem to be based on oversimplified models of the global water cycle. Several studies [eg. Hostetler and Benson, 1990] have argued that a southward shift in the jet stream was the source of additional moisture in the Great Basin during the Pleistocene and it seems likely that significant changes in temperature as well as temperature gradients across the continent would result in some shift in position or intensity of the dominant storm tracks in the region. The results of this study argue against a simple interdependence of the primary climatic variables, at least during the last ~20 kyr. Much of the change to the warmer climate that characterizes the Holocene, for example, seems to have occurred between ~18 ka and 13 ka, a period in which Searles Lakes continued to regularly reach its maximum level, albeit somewhat sporadically. The final change to Holocene conditions in the Owens Valley thus seems to be defined by a final transition to drier conditions that was not accompanied by dramatic warming. The glacial record indicates that the greatest warming in the basin was concurrent with the beginning of the Bolling/Allerod, at the end of Tioga stage IV.

Our temperature and precipitation estimates for the last deglaciation are based on combined analysis of lacustrine and glacial records. They are thus subject to uncertainties in the estimates of both the glacial and lacustrine extents as well as in the model predictions of their climate sensitivity. Aside from questions about the precise timing and correspondence of changes in these systems, the greater uncertainty in our reconstruction of the lacustrine and glacial histories lies in the lake level history. The position of the Tioga III terminus position, for example, is well constrained in Bishop Creek but the corresponding lake level, assumed here to be slightly above the sill at Searles Lake, is not well constrained. Combined with the shape of the response surfaces of the lakes and glaciers, the greater uncertainty in the lacustrine history suggests that our paleoprecipitation estimate is less well constrained than the paleotemperature estimate. Changes in the estimated lake level of  $\pm 20\%$ , for example, would imply a range of temperature depression between  $\sim -4.5$  and  $-6.2^\circ\text{C}$ . The

corresponding range in the estimated relative precipitation increase is  $\sim -10\%$  to  $+90\%$ . For comparison, the standard deviations of annual average temperature and precipitation at Bishop are  $1.6^{\circ}\text{C}$  and  $7\text{ cm}$  ( $\sim 60\%$  of average annual precipitation), respectively. That the latter range is not much greater than the standard deviation of average annual precipitation in the area underscores one of the most significant conclusions of this study, that modest precipitation increases, with or without a corresponding decrease in temperature, are fully capable of producing the lakes of the pluvial era.

Although our model for describing basin and lake response to climate change is probably overly simplistic, its predictions of basin sensitivity are supported in several ways. First, simple theoretical arguments show that arid basin streamflow should display an amplified response to changes in precipitation. This effect has been observed in historical records of streamflow and precipitation variations in several mountainous basins in the western U.S., though the degree of amplification is typically less than that predicted here. Second, the magnitude of the runoff response to precipitation predicted by the simple water balance model we applied agrees well with the observed relationship between precipitation, temperature and runoff in basins across the United States [Langbein, 1949, 1962]. That agreement improves when we apply the relationship on a spatially distributed basis and incorporate primary riparian effects. Third, the glacier model for Bishop Creek incorporates a careful accounting of the effect of changes in precipitation on snow mass and energy balance, including basin-specific estimates of monthly precipitation distribution, temperature-based partitioning of precipitation into rain and snow, and the related energy advection. The model should, therefore, present a relatively robust estimate of glacier sensitivity to precipitation. In this case, it clearly indicates that only a narrow range of modest precipitation increases are consistent with both the Tioga maximum glacier and other estimates of LGM temperature depression.

---

## CHAPTER 9 - CONCLUSIONS

---

The principal aim of this study has been to develop a means of combining information from glacial and lacustrine records to produce improved estimates of paleoclimatic conditions. Toward that end, we have developed alpine glacier and terminal lake system models that attempt to capture, using physically based equations, the primary relationships between their water balance and climate. We take a holistic approach in using these models to reconstruct paleoclimate from the geologic record of glacial and lacustrine changes. Recognizing that the two systems respond quite differently to the primary climatic variables, we use their combined constraints to construct the specific history of changes in both temperature and precipitation that best reconciles both features of the basin's paleohydrology. In this study, we demonstrate this novel approach using the paleohydrologic record of the Owens Valley to reconstruct the temperature and precipitation changes that characterized the end of the last glacial period. We find that temperature depression during the last glacial maximum was approximately 6°C and that precipitation was probably on the order of 20% to 40% greater than at present. The estimated temperature depression is consistent with paleoecological and noble gas paleothermometry estimates of LGM temperature depression in the southwestern United States. Following the LGM, temperatures increased by about 4°C between ~18 ka and 12 ka, with the most dramatic warming occurring at about 15 ka, coincident with the onset of the Bolling/Allerod warm interval. At the same time, precipitation seems to have been more or less maintained at a rate roughly 20-40% greater than at present until the very end of the Pleistocene, at ~10 ka. We conclude that the transition to the Holocene in the Owens Valley was marked more by a final decrease in precipitation rather than by a dramatic final warming.

### RECOMMENDATIONS FOR FURTHER RESEARCH

One of the more significant conclusions of this study is that precipitation during the LGM was



probably no more than 50% greater than today and that this, more than the accompanying temperature change, was the mechanism for the dramatic increase in lake area in the Owens Valley and probably throughout the Great Basin. This result is based largely on a relatively simple, Thornthwaite-type, water balance model of the Owens Valley that predicts a strongly amplified runoff response to precipitation. Though simplistic, the precipitation-temperature-runoff relationship it describes is very similar to that observed among modern basins in the U.S [Langbein, 1949, 1962], and the amplified sensitivity to precipitation is consistent with theoretical analysis of the potential climatic sensitivity of runoff in arid basins [Wigley and Jones, 1985]. This is intriguing in that it suggests that our relatively simple model adequately describes the relationship between climate and runoff in arid basins. Testing that supposition, using more sophisticated distributed-parameter water balance models, is among our highest priorities for further study of the climatic changes associated with the pluvial period in the Great Basin.

While we hope that this research ultimately leads to improvements in predictive models of basin evapotranspiration and runoff response, we believe that by itself the glacier model presented here stands as a significant advance in our ability to interpret the glacial record. The model was specifically designed to incorporate the effects of topography on both surface energy balance and the flow of ice in mountainous terrain and is, to our knowledge, the first attempt to take this detailed approach to modeling the alpine glaciers of the Pleistocene. The model offers a unique opportunity to examine the relationship between glacial extent and climate across a broad range of climatic conditions, which is precisely what is needed to relate the climatic conditions associated with the large glaciers of the last glacial period to the small cirque glaciers that survive under the modern climate. There are, however, several matters that should be addressed in future applications of the model. First, it has not been validated by comparison with extant glaciers of significant size. Simulation of a modern glacier of a kilometer or more in length, where relatively detailed meteorological data are available,

should demonstrate whether the flow equations are sufficient to describe the critical features of alpine glaciers. Also, as discussed in Section 6, simulations of specific glacial advances in Horton Creek require significantly different climatic conditions than those that yield the corresponding glacial events in Bishop Creek. This suggests either that climate is highly variable over short distances in the Sierra Nevada or that other influences are effecting the apparent differences in the behavior of the Horton Creek and Bishop Creek glaciers. These questions might be answered by consideration of, for example, the relative amount of glacial deposition that has occurred in those basins. Our model provides a useful tool to investigate such questions and solution of that puzzle should either lead to improvements in this modeling approach or to an improved understanding of the controls on glacier size and distribution at the basin-scale.

---

## REFERENCES

---

- Alley, W. M. (1984). "On the treatment of evapotranspiration, soil moisture accounting, and aquifer recharge in monthly water balance models." Water Resources Research **20**: 1137-1149.
- Anderson, E. A. (1968). "Development and testing of snow pack energy balance equations." Water Resources Research **4**: 19-37.
- Anderson, E.A., 1976. A point energy and mass balance model of a snow cover. Technical Report NWS 19, National Oceanic and Atmospheric Administration, Washington, DC.
- Arnold, N. S., I. C. Willis, M. J. Sharp, K. S. Richards and W. J. Lawson (1996). "A distributed surface energy-balance model for a small valley glacier. I. Development and testing for Haut Glacier d'Arolla, Valais, Switzerland." Journal of Glaciology **42**: 77-89.
- Beatty, C. B. (1975). "Sublimation or melting: Observations from the White Mountains, California and Nevada." Journal of Glaciology **14**: 275-286.
- Benson, L. (1986). The sensitivity of evaporation rate to climate change - results of an energy-balance approach. Denver, U.S. Geological Survey Water-Resources Investigations Report 86-4148: 40 pp.
- Benson, L. V., J. W. Burdett, M. Kashgarian, S. P. Lund, F. M. Phillips and R. O. Rye (1996). "Climatic and hydrologic oscillations in the Owens Lake Basin and Adjacent Sierra Nevada, California." Science **274**: 746-751.
- Benson, L. V., D. R. Currey, R. I. Dorn, K. R. Lajoie, C. G. Oviatt, S. W. Robinson, G. I. Smith and S. Stine (1990). "Chronology of expansion and contraction of four Great Basin lake systems during the past 35,000 years." Palaeogeography, Palaeoclimatology, Palaeoecology **78**: 241-286.
- Bergonzini, L., F. Chalé, and F. Gasse (1997). "Paleoevaporation and paleoprecipitation in the Tanganyika Basin at 18,000 years B.P. inferred from hydrologic and vegetation proxies." Quaternary Research **47**: 295-305.
- Birman, J. H. (1964). "Glacial geology across the crest of the Sierra Nevada." Geological Society of America Special Paper **75**: 80 pp.
- Blackwelder, E. (1931). "Pleistocene glaciation in the Sierra Nevada and Basin ranges." Bulletin of the Geological Society of America **42**: 865-922.
- Brakenridge, G. R. (1978). "Evidence for a cold, dry full-glacial climate in the American Southwest." Quaternary Research **9**: 22-40.

- Burbank, D. W. (1991). "Late Quaternary snowline reconstructions for the southern and central Sierra Nevada, California and a reassessment of the "Recess Peak Glaciation"." Quaternary Research **36**: 294-306.
- Clark, D. H. and A. R. Gillespie (1997). "Timing and significance of late-glacial and Holocene cirque glaciation in the Sierra Nevada, California." Quaternary International **38-9**: 21-38.
- Daly, C., R.P. Neilson, and D.L. Phillips (1994). A statistical-topographic model for mapping climatological precipitation over mountainous terrain. Journal of Applied Meteorology **33**: 140-158.
- Daly, C., G.H. Taylor, and W.P. Gibson (1997). The PRISM approach to mapping precipitation and temperature. In reprints: 10th Conf. on Applied Climatology, Reno, NV, American Meteorological Society.
- Daly, C., R. P. Neilson and D. L. Phillips (1994). "A statistical-topographic model for mapping climatological precipitation over mountainous terrain." Journal of Applied Meteorology **33**: 140-158.
- Danskin, W. R. (1998). Evaluation of the hydrologic system and selected water-management alternatives in the Owens Valley, California. Reston, Va., U.S. Geological Survey Water-Supply Paper **2370-H**: 175 pp.
- Dingman, L. (1993). Physical Hydrology. Englewood Cliffs, NJ, Prentice-Hall, 575 pp.
- Dohrenwend, J. C. (1984). "Nivation landforms in the western Great Basin and their paleoclimatic significance." Quaternary Research **22**: 275-288.
- Duell, L. F. W. (1990). Estimates of evapotranspiration in alkaline scrub and meadow communities of Owens Valley, California, using the Bowen-ratio, Eddy-correlation, and Penman-combination methods. Denver, Co, U.S. Geological Survey Water-Supply Paper **2370-E**.
- Duell, L. F. W. (1994). "The sensitivity of Northern Sierra Nevada streamflow to climate change." Water Resources Bulletin **30**: 841-859.
- Fastook, J. and J. E. Chapman (1989). "A map-plane finite element model: Three modeling experiments." Journal of Glaciology **35**: 48-52.
- Flaschka, I., C. W. Stockton and W. R. Boggess (1987). "Climatic variation and surface water resources in the Great Basin region." Water Resources Bulletin **23**: 47-57.
- Friedman, I. and G. I. Smith (1976). "Studies of Quaternary saline lakes - II. Isotopic and compositional changes during desiccation of the brines in Owens Lake, California, 1969-1971." Geochimica et Cosmochimica Acta **40**: 501-511.
- Friedman, I., G. I. Smith, J. D. Gleason, A. Warden and J. M. Harris (1992). "Stable isotope composition of waters in southeastern California 1. Modern precipitation." Journal of Geophysical Research **97**: 5795-5812.

Gale, H. S. (1914). Notes on the Quaternary lakes of the Great Basin with special reference to the deposition of potash and other salines. In: Contributions to Economic Geology, 1912. Part I – Metals and Nonmetals except Fuels. U.S. Geological Survey Bulletin 540-N: 399-406.

Galloway, R. W. (1970). "The full-glacial climate in the southwestern United States." Annals of the Association of American Geographers **60**: 245-256.

Gat, J. R. (1995). Stable isotopes of fresh and saline lakes. Physics and Chemistry of Lakes. A. Lerman, D. Imboden and J. Gat. New York, Springer-Verlag: 139-162.

Gosse, J. C. and F. M. Phillips (2001). "Terrestrial in situ cosmogenic nuclides: theory and application." Quaternary Science Reviews **20**: 1475-1560.

Greuell, W. and R. Böhm (1998). "2 m temperatures along melting mid-latitude glaciers, and implications for the sensitivity of the mass balance to variations in temperature." Journal of Glaciology **44**: 9-20.

Greuell, W. and J. Oerlemans (1986). "Sensitivity studies with a mass balance model including temperature profile calculations inside the glacier." Zeitschrift Gletscherkunde Glazialgeologie **22**: 101-124.

Hay, J. E. and B. B. Fitzharris (1988). "A Comparison of the Energy-Balance and Bulk-Aerodynamic Approaches for Estimating Glacier Melt." Journal of Glaciology **34**: 145-153.

Hollett, K. J., W. R. Danskin, W. F. McCaffrey and C. L. Walti (1991). Geology and Water Resources of Owens Valley, California. Denver Co, U.S. Geological Survey Water-Supply Paper 2370-B.

Hostetler, S. W. (1995). Hydrological and thermal response of lakes to climate: description and modeling. Physics and Chemistry of Lakes. A. Lerman, D. M. Imboden and J. R. Gat. New York, Springer-Verlag: 334 pp.

Hostetler, S. and L. Benson (1990). "Paleoclimatic implications of highstand Lake Lahontan derived from models of evaporation & lake level." Climate Dynamics **4**: 207-217.

Hostetler, S. W. (1991). "Simulation of lake ice and its effect on the late-Pleistocene evaporation rate of Lake Lahontan." Climate Dynamics **6**: 43-48.

Hostetler, S. W. and L. V. Benson (1994). "Stable isotopes of oxygen and hydrogen in the Truckee River - Pyramid Lake surface-water system. 2. A predictive model of  $\delta^{18}\text{O}$  and  $\delta^2\text{H}$  in Pyramid Lake." Limnology and Oceanography **39**: 356-364.

Huybrechts, P., P. d. Nooze and H. Decleir (1989). Numerical modeling of Glacier D'Argentiere and its historic front variations. Glacier Fluctuations and Climatic Change. J. Oerlemans. Dordrecht, Reidel: 373-389.

Iqbal, M. (1983). An Introduction to Solar Radiation. New York, NY, Academic Press.

Johannesson, T., C. Raymond, and E. Waddington (1989). "Time-scale for adjustment of glaciers to changes in mass balance." Journal of Glaciology **35**: 355-369.

Kattleman, R. and K. Elder (1991). "Hydrological characteristics and water balance of an alpine basin in the Sierra Nevada." Water Resources Research **27**: 1553-1562.

Klein, W. H. (1948). "Calculation of solar radiation and the solar heat load on man." Journal of Meteorology **5**: 119-129.

Knopf, A. and E. Kirk (1918). A geologic reconnaissance of the Inyo range, and the eastern slope of the southern Sierra Nevada, California, by Adolph Knopf, with a section on the stratigraphy of the Inyo range, by Edwin Kirk. Washington, Govt. Print. Office, U.S. Geological Survey Professional Paper 110: 130 pp.

Kondrat'ev, K. Y., Ed. (1973). Radiation Characteristics of the Atmosphere and the Earth's Surface, New Delhi, Amerind Pub. Co., NASA TTF-678.

Konrad, S. K. and D. H. Clark (1998). "Evidence for an early Neoglacial glacier advance from rock glaciers and lake sediments in the Sierra Nevada, California, USA." Arctic and Alpine Research **30**: 272-284.

Kuhn, M. (1979). "On the Computation of Heat Transfer Coefficients from Energy-Balance Gradients on a Glacier." Journal of Glaciology **22**: 263-272.

Kutzbach, J. E. (1980). "Estimate of past climate at paleolake Chad, North Africa, based on a hydrological and energy balance model." Quaternary Research **14**: 210-223.

Jeton, A. E. and J. L. Smith (1993). "Development of watershed models for two Sierra Nevada basins using a geographic information system." Water Resources Bulletin **29**: 923-932.

Jeton, A. E. and J. L. Smith (1996). Potential effects of climate change on streamflow, eastern and western slopes of the Sierra Nevada, California and Nevada, U.S. Geological Survey: 60 pp.

Johannesson, T., C. Raymond, and E. Waddington (1989). "Time-scale for adjustment of glaciers to changes in mass balance." Journal of Glaciology **35**: 355-369.

Langbein, W. B. and others (1949). Annual runoff in the United States, U.S. Geological Survey Circular 52: 13 pp.

Langbein, W. B. (1962). "The water supply of arid valleys in intermountain regions in relation to climate." Bulletin of the International Association of Scientific Hydrology **7**: 34-39.

Leydecker, A. and J. M. Melack (1999). "Evaporation from snow in the central Sierra Nevada of California." Nordic Hydrology **30**: 81-108.

Lerman, A.; D. Imboden and J. Gat Eds. (1995). Physics and Chemistry of Lakes. New York, Springer-Verlag.

Lin, J. C., W. S. Broecker, S. R. Hemming, I. Hajdas, R. F. Anderson, G. I. Smith, M. Kelley and G. Bonani (1998). "A reassessment of U-Th and <sup>14</sup>C ages for late-glacial high-frequency hydrological events at Searles Lake, California." Quaternary Research **49**: 11-23.

- Male, D. H. and R. J. Granger (1981). "Snow surface energy exchange." Water Resources Research **17**: 609-627.
- Malmstrom (1969). "A new approach to the classification of climate." The Journal of Geography **68**: 351-357.
- Marks, D. and J. Dozier (1992). "Climate and energy exchange at the snow surface in the alpine region of the Sierra Nevada, 2. Snow cover energy balance." Water Resources Research **28**: 3043-3054.
- Marks, D., J. Dozier and R. E. Davis (1992). "Climate and energy exchange at the snow surface in the alpine region of the Sierra Nevada, 1. Meteorological measurements and monitoring." Water Resources Research **28**: 3029-3042.
- Matthes, F. E. (1934). "Ablation of snowfields at high altitudes by radiant solar heat." Transactions of the American Geophysical Union: 380-385.
- Meierding, T. C. (1982). "Late Pleistocene glacial equilibrium-line altitudes in the Colorado Front Range: A comparison of methods." Quaternary Research **18**: 289-310.
- Mifflin, M. D. and M. M. Wheat (1979). Pluvial lakes and estimated pluvial climates of Nevada. Reno, Nv, Nevada Bureau of Mines and Geology Bulletin **94**.
- Mishra, S. (2002). "Dealing with uncertainty in environmental model predictions." Eos Trans. AGU: 568.
- Oerlemans, J. (1988). "Simulation of historic glacier variations with a simple climate-glacier model." Journal of Glaciology **34**: 333-341.
- Oerlemans, J. (1989). On the response of valley glaciers to climatic change. Glacier Fluctuations and Climatic Change. J. Oerlemans. Dordrecht, Reidel: 353-371.
- Oerlemans, J. (1992). "Climate sensitivity of glaciers in southern Norway: application of an energy balance model to Nigardsbreen, Hellstugubreen, and Alftobreen." Journal of Glaciology **38**: 223-232.
- Oerlemans, J. (1993). "A model for the surface balance of ice masses: part 1. Alpine glaciers." Zeitschrift fur Gletscherkunde und Glazialgeologie **27/28**: 63-83.
- Oerlemans, J. (2000). "Analysis of a 3 year meteorological record from the ablation zone of Morteratschgletscher, Switzerland: energy and mass balance." Journal of Glaciology **46**: 571-579.
- Oerlemans, J. and N. C. Hoogendoorn (1989). "Mass-balance gradients and climatic change." Journal of Glaciology **35**: 399-405.
- Oerlemans, J. and W. H. Knap (1998). "A 1 year record of global radiation and albedo in the ablation zone of Morteratschgletscher, Switzerland." Journal of Glaciology **44**: 231-238.

Orndorff, R. L. and R. G. Craig (1994). Snowfall and snowmelt estimates for modern and last glacial conditions within the Owens Valley, California. Western Snow Conference, Santa Fe, New Mexico.

Paterson, W. S. B. (1994). The Physics of Glaciers. Oxford, Pergamon, 480 pp.

Pfeffer, W. T., C. Sassolas, D.B. Bahr, and M.F. Meier (1998). "Response time of glaciers as a function of size and mass balance: 2. Numerical experiments." Journal of Geophysical Research **103**: 9777-9782.

Pfeffer, W. T., M. Dyurgerov, M. Kaplan, J. Dwyer, C. Sassolas, A. Jennings, B. Raup and W. Manley (1997). "Numerical modeling of late Glacial Laurentide advance of ice across Hudson Strait: Insights into terrestrial and marine geology, mass balance, and calving flux." Paleoceanography **12**: 97-110.

Phillips, F. M., A. R. Campbell, C. Kruger, P. Johnson, R. Roberts, E. Keyes (1992). A reconstruction of the lake water balance in western United States lake basins to climatic change, Volume I. Las Cruces, New Mexico Water Resources Research Institute Report No. 269: 167 pp.

Phillips, F. M., A. R. Campbell, C. Kruger, P. Johnson, R. Roberts, E. Keyes (1992). A reconstruction of the lake water balance in western United States lake basins to climatic change, Volume II. Las Cruces, New Mexico Water Resources Research Institute Report No. 269.

Phillips, F. M., A. R. Campbell, G. I. Smith and J. L. Bischoff (1994). "Interstadial climatic cycles: A link between western North America and Greenland?" Geology **22**: 1115-1118.

Phillips, F. M. and M. A. Plummer (1996). "CHLOE: A program for interpreting *in-situ* cosmogenic nuclide data for surface exposure dating and erosion studies." Radiocarbon (Abstr. 7th Int. Conf. Accel. Mass Spectrom. **38**: 98-99.

Phillips, F. M., M. G. Zreda, L. V. Benson, M. A. Plummer, D. Elmore and P. Sharma (1996). "Chronology for fluctuations in late Pleistocene Sierra Nevada Glaciers and Lakes." Science **274**: 749-751.

Plummer, M. A., and F. M. Phillips (1996). Detailed deglacial chronology for the eastern Sierra Nevada. Geological Society of America Abstracts with Programs **28**: 435.

Plummer, M. A., and F. M. Phillips (1999). Combined Simulation of Alpine Glaciers and Closed-Basin Lakes: The key to determining the long-term temperature and precipitation changes driving fluctuations in the alpine glaciers. Geological Society of America Abstracts with Programs **31**: A-418.

Porter, S. C., K. L. Pierce and T. D. Hamilton (1983). Late Pleistocene glaciation in the western United States. Late Quaternary Environments of the United States. S. C. Porter. Minneapolis, University of Minnesota Press: 71-111.

Rango, A. and J. Martinec (1995). "Revisiting the degree-day method for snowmelt computations." Water Resources Bulletin **31**: 657-669.

Risbey, J. S. and D. Entekhabi (1996). "Observed Sacramento Basin streamflow response to precipitation and temperature changes and its relevance to climate impact studies." Journal of Hydrology **184**: 209-223.



Roberts, D. W., R. F. Fisher, J. M. Long and S. N. Jack (1993). The leaf area allocation model. Final report for EPA Cooperative Agreement #817539.

Schmeits, M. J. and J. Oerlemans (1997). "Simulation of the historical variations in length of Unterer Grindelwaldgletscher, Switzerland." Journal of Glaciology **433**: 152-164.

Shanahan, T. and M. Zreda (2000). "New Constraints on the Ages of Old Moraines: The Impact of Erosion on Surface Exposure Age Distributions." Eos Transactions. AGU 81: Fall Meet. Supplement, Abstract U21A-12.

Schlosser, E. (1997). "Numerical simulation of fluctuations of Hintereisferner, Otztal Alps, since AD 1850." Annals of Glaciology **24**: 199-202.

Schumm, S. A. (1965). Quaternary Paleohydrology. The Quaternary of the United States. H. E. Wright and D. G. Frey. Princeton, NJ, Princeton University Press: 922 pp.

Sharp, R. P. (1951). "Melting versus evaporation in the Sierra Nevada, California." Journal of Glaciology **1**: 583.

Sharp, R. P. (1969). "Semiquantitative differentiation of glacial moraines near Convict Lake, Sierra Nevada, California." Journal of Geology **77**: 68-91.

Sharp, R. P. and J. H. Birman (1963). "Additions to classical sequence of Pleistocene glaciations, Sierra Nevada, California." Geological Society of America Bulletin **74**: 1079-1086.

Smith, G. I. (1987). Searles Valley, California: Outcrop evidence of a Pleistocene lake and its fluctuations, limnology, and climatic significance. Geological Society of America Centennial Field Guide - Cordilleran Section, Geological Society of America.

Smith, G. I. and F. A. Street-Perrott (1983). Pluvial lakes of the western United States. Late-Quaternary Environments of the United States. S. C. Porter. Minneapolis, University of Minnesota Press. 190-212.

Stuiver, M., P. J. Reimer and T. F. Braziunas (1998). "High-precision radiocarbon age calibration for terrestrial and marine samples (AD 1950-9700 BC)." Radiocarbon **40**: 1127-1151.

Stute, M., J. F. Clark, P. Schlosser, W. S. Broecker and G. Bonani (1995). "A 30,000 yr continental paleotemperature record derived from noble gases dissolved in groundwater from the San Juan Basin, New Mexico." Quaternary Research **43**: 209-220.

Stute, M., P. Schlosser, J. F. Clark and W. S. Broecker (1992). "Paleotemperatures in the southwestern United States derived from noble gas temperatures." Science **256**: 1000-1003.

Street-Perrott, F. A., Y. Huang, R. A. Perrott, G. Eglinton, P. Barker, L. Ben Khelifa, D. D. Harkness and D. O. Olago (1997). "Impact of lower atmospheric carbon dioxide on tropical mountain ecosystems." Science **278**: 1422-1426.

Stroeve, A., R. v. d. Wal and J. Oerlemans (1989). Historic front variations of the Rhone Glacier: simulation with an ice flow model. Glacier Fluctuations and Climatic Change. J. Oerlemans. Dordrecht, Reidel: 391-405.

Thornthwaite, C. W. (1948). "An approach toward a rational classification of climate." Geographical Review **38**: 55-94.

Thornthwaite, C. W. and J. R. Mather (1955). The water balance. Philadelphia, PA, Drexel Institute of Technology, Climatological Laboratory Publication No. 8.

Tonnessen, K. A. (1991). "The Emerald Lake Watershed Study; introduction and site description." Water Resources Research **27**: 1537-1539.

Wigley, T. M. L. and P. D. Jones (1985). "Influences of precipitation changes and direct CO<sub>2</sub> effects on streamflow." Nature **314**: 149-152.

Williams, A. E. and D. P. Rodoni (1997). "Regional isotope effects and application to hydrologic investigations in southwestern California." Water Resources Research **33**: 1721-1729.

Winograd, I. J., T. B. Coplen, J. M. Landwehr, A. C. Riggs, K. R. Ludwig, B. J. Szabo, P. T. Kolesar and K. M. Revesz (1992). "Continuous 500,000-year climate record from vein calcite in Devils Hole, Nevada." Science **258**: 255-260.

Zreda, M. G. and F. M. Phillips (1995). "Insights into alpine moraine development from cosmogenic <sup>36</sup>Cl buildup dating." Geomorphology **14**: 149-156.

## APPENDICES

APPENDIX A

TRANSIENT ISOTOPE  
CALCULATIONS WORKSHEET

---

The isotopic composition and evolution of a closed-basin lake and the carbonate precipitated in it can be calculated from relatively simple water and isotope balance equations if the parameters in those equations are known or can be reasonably estimated.

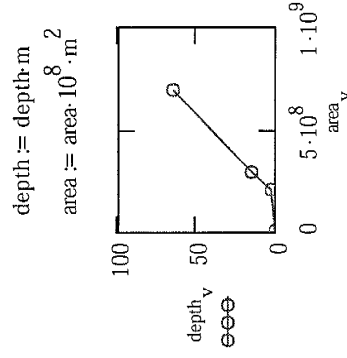
Because net evaporation from the lake depends on the surface area of the lake while changes in storage affect the volume, we need a relationship between volume and surface area. The following data for Owens Lake are taken from appendix P of volume 2 of WRRI #269:

## Owens Lake Surface Area - Volume relationship:

$$v := 1..4 \quad \text{depth}_v := \text{area}_v :=$$

0	2.4	14.0	64.0
---	-----	------	------

0	2.0	2.9	6.94
---	-----	-----	------



$$\text{vol} := \frac{\text{area} \cdot \text{depth}}{3}$$

$\text{vol}_V =$	$0 \text{ m}^3$
	$1.6 \cdot 10^8$
	$1.353 \cdot 10^9$
	$1.481 \cdot 10^{10}$

$$\text{bedslope} := \left( \frac{\pi \cdot \text{depth}^2}{\text{area}} \right)^{\frac{1}{2}}$$

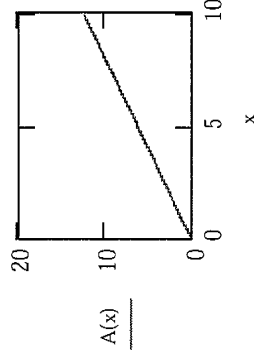
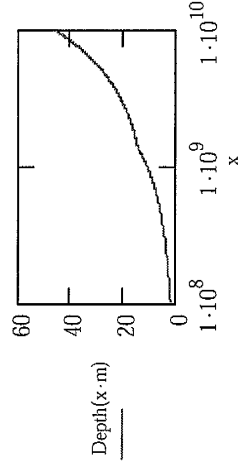
$$\text{bedslope} = \begin{pmatrix} 0 \\ 0.03 \\ 0.146 \\ 0.431 \end{pmatrix} \%$$

☐ Alternatively, use Searles data

Functions to calculate depth from lake surface area and vice-versa:

$$\text{Depth}(V) := \text{linterp}(\text{vol}, \text{depth}, V)$$
$$A(V) := \text{interp}(\text{vol}, \text{area}, V)$$

Example calculations:  $\text{Depth}(1.6 \cdot 10^8 \cdot \text{m}^3) = 2.4 \text{ m}$

$$A(1.6 \cdot 10^8 \cdot \text{m}^3) = 2 \times 10^8 \text{ m}^2$$


Need to limit maximum surface area here?

The isotopic composition of the lake is governed by the composition of the inflow, ambient vapor, and the rate of evaporation and isotopic enrichment via evaporation. Here we use the Hosteteler-Benson form of the Craig-Gordon (1965) governing equation for isotope balance:

$$\delta_L(f_{air}, \delta_L) = \frac{\alpha^a \cdot \delta_L - h \cdot f_{air} \cdot \delta_A - \varepsilon(\Delta\varepsilon)}{(1 - f_{air} \cdot h) + \Delta\varepsilon}$$

**Isotope balance equation parameters (adjustable parameters are highlighted in yellow):**

Variation of the equilibrium fractionation factor with temperature (after Friedman et al., ):

$$\varepsilon_F(T) := \exp\left(\frac{1.534 \cdot 10^6 \cdot T^{-2} - 3.206 \cdot 10^3 \cdot T^{-1} + 2.664}{10^3}\right) - 1$$

Eqm enrichment factor	$\varepsilon^a := \varepsilon_F(273 + 28)$	$\varepsilon^a \cdot \text{prml} = 8.984 \times 10^{-6}$
Eqm fractionation factor (<1)	$\alpha^a := 1 - \varepsilon^a$	$\alpha^a = 0.991$
Kinetic enrichment factor	$\Delta\varepsilon := 0.005$	(mean observed in CGH experiments)
Total enrichment factor	$\varepsilon(\Delta\varepsilon) := \varepsilon^a + \Delta\varepsilon$	$\varepsilon(\Delta\varepsilon) = 0.014$
Vapor P of free air relative to sat P at surface	$h := 0.11$	
Fraction of air from outside basin	$f_{air} := 0.1$	
Isotopic enrichment of air (relative to std.)	$\delta_A := -15 \cdot \text{prml}$	
Isotopic composition of inflow	$\delta_{in} := -16.3 \cdot \text{prml}$	
Isotopic composition of precipitation	$\delta_p := -12 \cdot \text{prml}$	

**The working Hosteteler - Benson isotope equation**

$$\delta_L(f_{air}, \delta_L) := \frac{\alpha^a \cdot \delta_L - h \cdot f_{air} \cdot \delta_A - \varepsilon(\Delta\varepsilon)}{(1 - f_{air} \cdot h) + \Delta\varepsilon}$$

The water and isotope balance equation for the lake is described by the following differential equation:

$$V \left[ \frac{d(\delta_l)}{dt} \right] = \left[ \left[ Q_{in} \delta_{in} + A \left( P \delta_p - E \delta_E (f_{air} \delta_l) \right) \right] - Q_{out} \delta_l \right] - \left[ \left[ Q_{in} + A (P - E) \right] - Q_{out} \right] \delta_l$$

Water balance parameters for the lake and basin:

Inflow rate from basin runoff	$Q_{in} := 48.5 \cdot m^3 \cdot sec^{-1}$	Modern inflow is close to 13.5 m3 sec-1	$E := Adj \cdot E^*$
Evaporation rate from lake surface	$E := 1.54 \cdot m \cdot yr^{-1}$		
Precipitation on lake surface	$P := 6 \cdot cm \cdot yr^{-1}$		

**Outflow** is zero until lake is at maximum volume; then outflow equals inflow minus the evaporative loss from the full lake

$$Q_{out}(Volume, Q_{in}) := \text{if} \left[ Volume < vol_4, 0 \cdot m^3 \cdot sec^{-1}, Q_{in} + (P - E) \cdot area_4 \right]$$

Initial conditions:

Lake volume	$V_1 := vol_3$
Surface area	$A(V_1) = 2.9 \times 10^8 \cdot m^2$
Isotopic composition	$\delta_{l_1} := -2.3 \cdot permil$
Initial inflow rate	$(E - P) \cdot A(V_1) = 13.601 \cdot m^3 \cdot sec^{-1}$

► Random inflow function

▼ Step change inflow function

$$\Delta t := 1 \cdot \text{yr}$$

$$t_{\max} := 300 \cdot \text{yr}$$

$$I := \frac{t_{\max}}{\Delta t}$$

$$I = 300$$

$$i := 1..I$$

$$t_i := \Delta t \cdot i$$

Index for the inflow must be one more than the d index which is one more than the volume index.

$$i_{\text{plus}} := 1..I + 1$$

Number of years between changes

$$\text{period} := 100$$

A function that converts index i to a heaviside step

$$\text{pattern}(x) := \text{mod}\left(\left\lceil \frac{x}{\text{period}} \right\rceil, 2\right)$$

Lower inflow rate

$$Q_{\min} := \text{Adj} \cdot 14 \cdot \text{m}^3 \cdot \text{sec}^{-1}$$

$$Q_{\min} := \text{Adj} \cdot 30 \cdot \text{m}^3 \cdot \text{sec}^{-1}$$

$$Q_{\min} = 14 \cdot \text{m}^3 \cdot \text{sec}^{-1}$$

Higher inflow rate

$$Q_{\max} := \text{Adj} \cdot 2 \cdot 14 \cdot \text{m}^3 \cdot \text{sec}^{-1}$$

$$Q_{\max} := \text{Adj} \cdot 60 \cdot \text{m}^3 \cdot \text{sec}^{-1}$$

$$Q_{\max} = 28 \cdot \text{m}^3 \cdot \text{sec}^{-1}$$

The heaviside step function for inflow rate

$$Q_{i_{\text{plus}}} := \text{if}(\text{pattern}(i_{\text{plus}}) < 0.5, Q_{\min}, Q_{\max})$$

► Step change inflow function



The water balance of the lake controls both the surface area of the lake and the isotopic composition. To simulate changes in lake volume during in response to changes in inflow and/or evaporation rates, we use an explicit finite difference approximation to solve the governing differential equation.

**Lake volume** as a function of 'time.' If volume exceeds volume at sill, the volume is the sill volume, otherwise, it expands or contracts.

$$V_{i+1} := \text{if} \left[ V_i + \left[ Q_{\text{in}_{i+1}} + A(V_i) \cdot (P - E) - Q_{\text{out}}(V_i, Q_{\text{in}_i}) \right] \cdot \Delta t < \text{vol}_4, V_i + \left[ Q_{\text{in}_{i+1}} + A(V_i) \cdot (P - E) - Q_{\text{out}}(V_i, Q_{\text{in}_i}) \right] \cdot \Delta t, \text{vol}_4 \right]$$

$$\text{Vol}_i := \frac{V_{i+1} + V_i}{2} \quad \text{Vol} := V$$

The change in the isotope balance is coupled to the water balance equation. This is the differential equation describing changes in isotopic composition over time.

$$\frac{d\delta_{\text{lake}}(\delta_{\text{lake}}, \text{Volume}, Q_{\text{in}})}{dt} := \frac{\left[ Q_{\text{in}} \cdot \delta_{\text{in}} + A(\text{Volume}) \cdot (P \cdot \delta_p - E \cdot \delta_E(f_{\text{air}}, \delta_{\text{lake}})) \right] - Q_{\text{out}}(\text{Volume}, Q_{\text{in}}) \cdot \delta_{\text{lake}} - \left[ Q_{\text{in}} + A(\text{Volume}) \cdot (P - E) \right] - Q_{\text{out}}(\text{Volume}, Q_{\text{in}}) \cdot \delta_{\text{lake}}}{\text{Volume}}$$

☑ RKF terms

$$\text{RK1}(\delta_{\text{lake}}, \text{Volume}, Q_{\text{in}}) := \frac{d\delta_{\text{lake}}(\delta_{\text{lake}}, \text{Volume}, Q_{\text{in}})}{dt}$$

$$\text{RK2}(\delta_{\text{lake}}, \text{Volume}, Q_{\text{in}}) := \frac{d\delta_{\text{lake}}}{dt} \left( \delta_{\text{lake}} + \frac{\Delta t}{2} \cdot \text{RK1}(\delta_{\text{lake}}, \text{Volume}, Q_{\text{in}}), \text{Volume}, Q_{\text{in}} \right)$$

$$\text{RK3}(\delta_{\text{lake}}, \text{Volume}, Q_{\text{in}}) := \frac{d\delta_{\text{lake}}}{dt} \left( \delta_{\text{lake}} + \frac{\Delta t}{2} \cdot \text{RK2}(\delta_{\text{lake}}, \text{Volume}, Q_{\text{in}}), \text{Volume}, Q_{\text{in}} \right)$$

$$\text{RK4}(\delta_{\text{lake}}, \text{Volume}, Q_{\text{in}}) := \frac{d\delta_{\text{lake}}}{dt} \left( \delta_{\text{lake}} + \Delta t \cdot \text{RK3}(\delta_{\text{lake}}, \text{Volume}, Q_{\text{in}}), \text{Volume}, Q_{\text{in}} \right)$$

☑ RKF terms

The Runge-Kutta solution for isotopic composition of the lake water:

$$\delta_{i+1} := \delta_i + \Delta t \cdot \frac{d\delta_i(\delta_i, Vol_i, Q_{in_i}) + 2 \cdot RK2(\delta_i, Vol_i, Q_{in_i}) + 2 \cdot RK3(\delta_i, Vol_i, Q_{in_i}) + RK4(\delta_i, Vol_i, Q_{in_i})}{6}$$

Although carbonate of isotopic composition x is deposited continuously, sampling and analysis of the carbonate sediments must average over some time period represented. I've tried to represent that here with an estimation of the period averaged in the sample,  $t_{samp}$ . The interval between samples in the Owens Lake OL-90-2 core data on the NGDC website is 10-40 years and the samples were continuous.

Largest value of i      I = 300

Years averaged in each sample       $t_{samp} := 25$

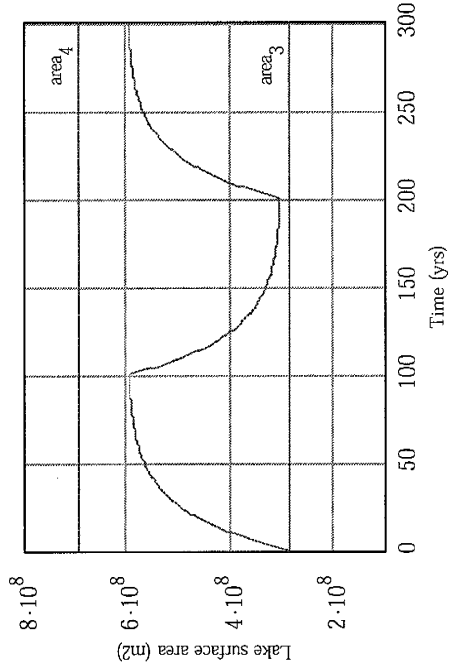
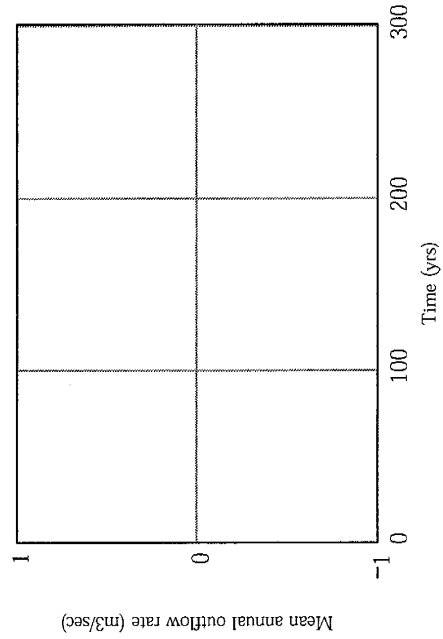
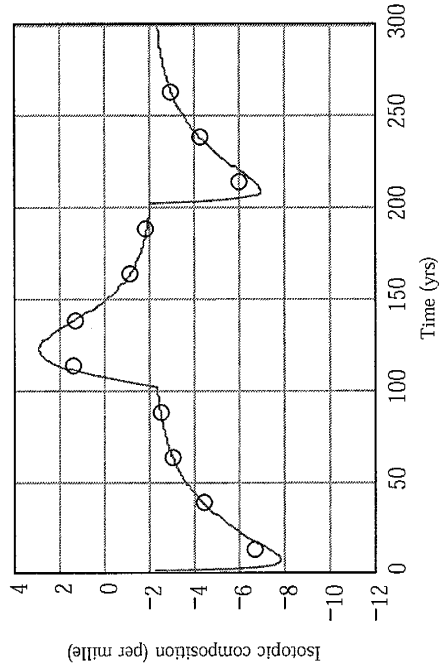
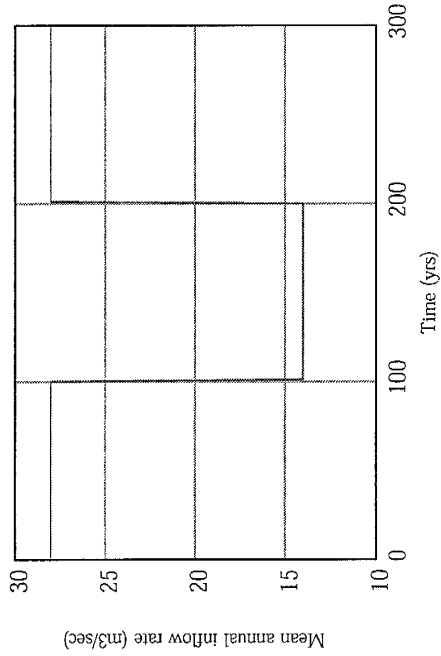
Maximum index value for sampling of the i layers       $J := \text{ceil} \left[ \frac{t_{max}}{t_{samp}} \cdot \text{yr} \right] - 1$       J = 11

Check that j \*  $t_{samp}$  is less than max i      J \*  $t_{samp} = 275$

Index for sampled version of the i values      j := 1..J

Equation for averaging isotopic composition over the sampling period

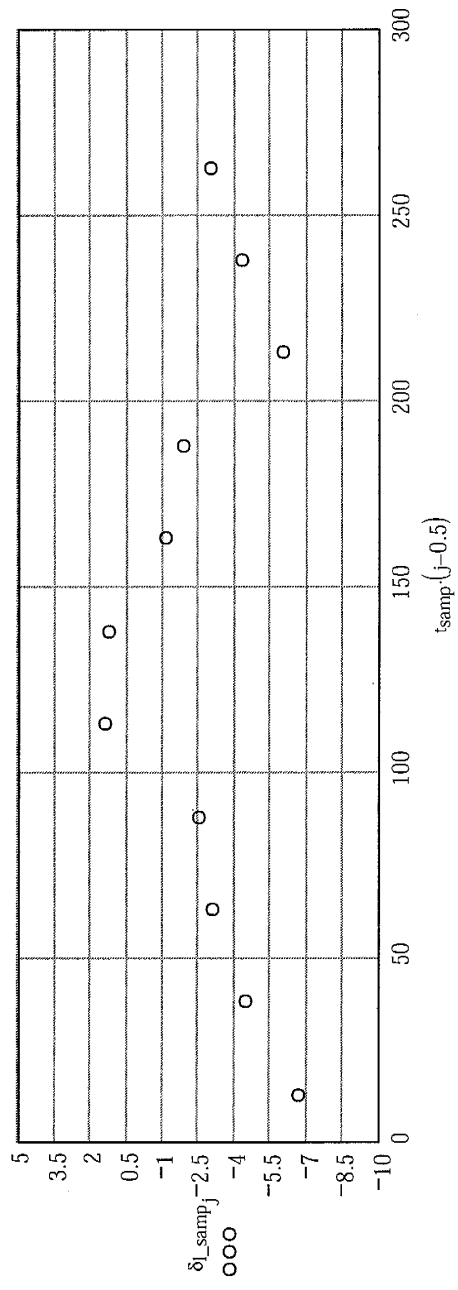
$$\delta_{i\_samp,j} := \sum_{i=1+(j-1) \cdot t_{samp}}^{j \cdot t_{samp}} \frac{\delta_i}{\text{prml} \cdot t_{samp}}$$



$period = 100$        $Q_{max} = 28 \text{ m}^3 \text{ sec}^{-1}$        $\frac{Q_{max}}{Q_{min}} = 2$   
 $t_{smp} = 25$        $Q_{min} = 14 \text{ m}^3 \text{ sec}^{-1}$

Adj = 1





▢ Constants, conversions, ...

APPENDIX B

ROCK SAMPLE  
PROCESSING FOR  $^{36}\text{Cl}$   
ANALYSIS

---

## **1. Rock preparation**

### **1.1. *Initial cleaning***

- 1.1.1. Thoroughly clean the surface of the rock, removing any moss, lichen, dirt, or other organic matter.

### **1.2. *Rock crushing***

- 1.2.1. Crush the rock into pieces of approximately 1-2 cm in size. For lava flow samples only the top 5-7 cm of the sample should be used. If the sample is thicker than this, trim off the lower part with a rock chisel or other necessary tools. **You will want to select a piece of the rock for thin section and grain size analysis.** Preferably, this piece should **not** be taken from the surface and should be large enough for analysis (~1" x 1" x .5") (This is generally no problem with larger samples).

## **2. TEMA Mill: Grinding and Sieving**

### **2.1. *TEMA Mill (Shatterbox)***

- 2.1.1. Final grinding of the sample should be done using the TEMA shatterbox.
- 2.1.2. Grind the 1-2 cm pieces crushed earlier.

## 2.2. *Sieving*

- 2.2.1. Transfer the ground sample to a 150-micron mesh sieve.
- 2.2.2. Collect the < 150-micron fraction (fine) in the pan located with the sieves. Transfer the > 150-micron fraction (coarse) to a piece of the wax paper and the fine fraction to an additional piece of wax paper. The ratio of coarse to fine should be approximately 50/50 by weight. If the fine ratio is too high, the sample should be ground for less time. If grinding for less time leaves too many large pieces, the coarse fraction can be briefly reground, but not re-sieved.

## 3. **Leaching sample**

### 3.1. *Leaching solution*

- 3.1.1. The > 150-micron fraction of the sample should be leached in 3% nitric acid to remove meteoric chloride and secondary carbonate. If the sample material to be analyzed is carbonate, it should be leached in 18 MΩ DI water.

### 3.2. *Sample leaching*

- 3.2.1. Label large glass beakers (1 liter) (washed, then rinsed thoroughly in 18 MΩ DI water) and transfer the ground samples to the beakers. If the samples are very large (i.e. greater than 300 g) you might consider using 2 separate beakers for the sample.
- 3.2.2. Add a volume of 3% HNO<sub>3</sub> about equal to the sample volume. (Add a very small amount of 3% nitric acid at first and note the reaction of the sample. Then add the rest to equal the sample volume). Stir the sample with a **clean** stir rod or swirl the sample around to assure that it is completely wetted. **NOTE: any bubbling behavior should be noted in your lab book** (this is usually the result of a high concentration of carbonate in the rock sample and, if significant, may require a second leaching, or more).
- 3.2.3. After stirring the sample, add additional 3% nitric acid equal to 3 - 4 times the sample volume. The acid should be added more slowly to samples that reacted or bubbled strongly when the first acid aliquot was added, in order to prevent bubbling over.



- 3.2.4. Stir each sample several times with a **clean** stir rod and cover the beaker with a clean watchglass.
- 3.2.5. The samples should be allowed to leach for 8 - 12 hours. If possible, stir the samples once or twice during leaching.
- 3.2.6. If a sample reacted particularly vigorously, add an additional small amount of 3% nitric acid about half way through leaching, in case the existing acid has been neutralized.

### 3.3. *Rinsing leached sample*

- 3.3.1. When leaching is complete, pour the solution, but not the sample, down the drain (turn the faucet on to facilitate any further dilution of the acid and to rinse everything down thoroughly). **NOTE:** the fine powder on top can usually be rinsed down the drain. You typically just want the grains.
- 3.3.2. Rinse the sample once with 18 M $\Omega$  DI water, pouring the rinse down the drain.
- 3.3.3. After the first rinse, add a small volume of 3% nitric acid. If bubbling occurs, the sample will have to be leached again by following the steps in 3.2.
- 3.3.4. For samples that do not react or bubble further, rinse the sample with a 1% sodium hydroxide (NaOH) solution.
- 3.3.5. Add the NaOH in approximately 100 ml aliquots, stirring thoroughly between additions, until the pH of the solution is between 7 and 9 (use pH paper). **NOTE:** You may want to only add 50 ml of NaOH, and then small (~ 10 ml) aliquots until the pH is between 7 and 9. **Stir thoroughly between additions.** Pour the NaOH down the drain, and then rinse the sample in 18 M $\Omega$  DI water 2 - 3 times (or more) until the pH is around 5 or 6.
- 3.3.6. Cover the beakers with watchglasses and place the rinsed samples in the oven until dry. This may take 12 hours to 3 days depending on the size of the sample and the temperature of the oven. You do not want the sample to boil. If possible stir the samples once or twice with a clean stir rod at some point during the drying process.

### **3.4. Weigh and bag samples**

- 3.4.1. Remove the dried samples from the oven and allow them to cool.
- 3.4.2. If the sample size allows, place about 40 grams of sample (obtained using the "cone and quarter" technique, see section 3.5) in a labeled whirlpack bag. This sample will later be ground in the TEMA to a fine powder for analysis by XRF, PGES, and total Cl. Put the rest of the sample in an additional labeled whirlpack bag.
- 3.4.3. XRF needs a minimum of 10 grams but would like to have 20. PGES analysis of B and Gd (XRAL lab) needs a minimum of 5 grams but would like to have 10. Total Cl requires just a few milligrams, but it is nice to have 3 to 5 grams. So, set aside 40 grams if the sample size is large enough, otherwise all that you think you can spare, keeping the above minimum values in mind.

### **3.5. Cone and quarter technique**

- 3.5.1. Dump the sample onto a clean piece of wax paper, forming a cone shaped pile.
- 3.5.2. Mark the cone shaped pile with a clean spatula or scoopula dividing it into approximately equal quarters.
- 3.5.3. Remove your sample from one of the quarters so as to have a general mix of the entire sample, not just what's on top.

### **3.6. Grinding sample in TEMA mill for chemical analysis**

- 3.6.1. Rinse an appropriate number of 20 ml scintillation vials and small glass vials with 18 M $\Omega$  DI water. (Usually 2 scintillation vials and 1 small glass vial per sample). Dry the vials in the oven at an appropriate temperature.
- 3.6.2. Add the entire sample (the 40 grams that was labeled to grind for analysis) to the clean vessel and grind until the sound changes from a clanking sound to a high pitched sound. The sample should now be a very fine powder.
- 3.6.3. Weigh approximately 20 grams into one of the scintillation vials (for XRF), 10 grams into the other (for PGES) and 5

grams into a small glass vial (for total Cl). When transferring into the vials use the "cone and quarter" technique (section 3.5).

#### 4. Determination of approximate chlorine concentration

In this procedure an approximate total chlorine concentration is determined using a specific ion electrode in order to calculate the size of sample to be processed and the amount of  $^{35}\text{Cl}$  carrier to be added. The dissolution of the sample is accomplished by placing a small amount of sample in the outer ring of the Teflon cell and a reducing solution in the inner ring of the Teflon cell. An oxidizing solution is then placed in the outer ring of the cell being careful that the oxidizing solution and sample do not make contact until the lid has been securely placed on the cell.

##### 4.1. *Cleaning the Teflon diffusion cells (two step process)*

- 4.1.1. **First solution:** combine 300 ml  $\text{H}_2\text{SO}_4$  with 10.5 ml of saturated  $\text{K}_2\text{Cr}_2\text{O}_7$  solution in a 600 ml acid washed beaker. The  $\text{K}_2\text{Cr}_2\text{O}_7$  solution should be put in the beaker first, and then the acid should be added **SLOWLY**. This solution is dark brown when first prepared, and can be used until it becomes green.
- 4.1.2. Put the first solution on the hotplate until it is too hot to touch (~ 1/2 hour at a setting of 7 or 8). When this is hot enough remove it from the hotplate and fill each diffusion cell with the hot solution until the center ring is completely covered. Place the lids on the cells. While holding the lids on, invert the cells back and forth several times, then place them under the hood right side up and leave for 10-15 minutes. (**NOTE:** the lids fit easier if you place them on each cell immediately after filling the cell)
- 4.1.3. **Second solution:** heat 300 ml of  $\text{HNO}_3$  in a 500 ml beaker on the hotplate as above. When it is close to boiling, add 50 ml of  $\text{H}_2\text{O}_2$ . Add the hydrogen peroxide very slowly to prevent boil over.
- 4.1.4. Empty the first solution back into the beaker and rinse the cell and lid in 18 M $\Omega$  DI water very thoroughly.
- 4.1.5. After all the cells have been emptied and rinsed, fill each cell with the second solution, making sure the center ring is covered completely. While holding the lid on, invert each cell

several times and place on the hood floor right side up for 10-15 minutes.

- 4.1.6. Rinse each cell thoroughly in 18 MΩ DI water. Place the cells on a piece of clean lab paper on the counter.

#### **4.2. *Preparing the oxidizing and reducing solutions***

- 4.2.1. **Reducing solution:** Add 5.8 g of KOH pellets to a tared plastic tube with a lid. Retare. Add 0.29 g of Na<sub>2</sub>SO<sub>3</sub> to the mixture. Retare. Add 31 g of 18 MΩ DI water. Replace the lid, **shake the solution** and put aside.
- 4.2.2. **Oxidizing solution:** Using a 100-ml Teflon beaker. Place it on the balance and tare. Add 0.4 g of KMnO<sub>4</sub>. Retare. Carefully add 5.6 g of 18 MΩ DI water, trying to rinse the sides of the beaker as you do. Place the beaker on the orbital shaker. Add 1.85 ml of 50% H<sub>2</sub>SO<sub>4</sub>. Turn the shaker on and leave it for a few minutes. Remove the beaker and place it under the hood. Add 32 ml of HF to the Teflon beaker.

#### **4.3. *Loading the Cells***

- 4.3.1. **Conditioning cell:** The first cell is used to condition the electrode, and should have no sample loaded.
- 4.3.2. **Standards:** Standards are used to calibrate the electrode and determine a slope from which the concentration of the samples can be determined. The number and concentration of standards run with each sample set depends on the concentration of Cl in the samples. For complete unknowns, run a 10 ppm, 100 ppm, 250 ppm and a 500 ppm liquid standard.
  - 4.3.2.1. Measure 0.2000 g ( $\pm 0.0004$  g) of standard solution into the outer ring of the diffusion cell and record the exact mass. The standard solution should form a bead in the outer ring of the cell.
  - 4.3.2.2. Prop the cell on the hood shelf with the bead of standard on the uphill side. (You want to prevent premature mixing with oxidizing solution)

- 4.3.3. **Samples:** Place the lid on the stainless hood shelf and place the diffusion cell on the balance. Write down the empty cell weight and tare the balance. Using an 18 M $\Omega$  DI water rinsed and dried spatula, add 0.2000 g ( $\pm$  0.0004 g) of leached, powder sample to the outer ring. With the spatula, spread the sample over  $\sim$ 160 degrees in the outer ring, and then record the exact final mass. Place the cell on the hood shelf with the sample on the uphill side.
- 4.3.4. **Adding Solutions:** When all of the standards and samples have been loaded, put 2.5 ml of reducing solution into the inner ring of the diffusion cells. Then, measure 3 ml of oxidizing solution into the downhill part of the outer ring. You do not want the oxidizing solution to come into contact with the sample.
- 4.3.5. **Shaker:** Place the lids on the cells and carefully carry them to the orbital shaker. Place all of the cells on the shaker, checking the lids occasionally by pressing down on them to make sure they are sealed properly. Tighten the bars, recheck the lids, set the speed of the orbital shaker  $\sim$  100 and shake the cells for 16 to 20 hours. **Mark the start time and date.**

#### 4.4. *Cl determinations*

- 4.4.1. We currently use a portable Beckman meter and an Orion model 96-17BN combination chloride electrode. It is important to remember that this method will only give an estimate of the total chloride present, which is sufficient for determining the amount of sample needed to be dissolved. AMS/IDMS is used for the actual chloride analysis.
- 4.4.2. **Electrode conditioning:** Turn the orbital shaker off and note the time on the Cl log sheet. Retrieve the conditioning cell and place it on the hood shelf. Open the lid of the cell and using 18 M $\Omega$  DI water in a squeeze bottle rinse the lid into the HF waste bucket.
- 4.4.2.1. Using a small Teflon dropper Carefully remove the droplets on the separation ring between the inner and outer portions of the cell, placing the removed droplets in the HF waste bucket.
- 4.4.2.2. With the small Teflon dropper, pipette off the purple solution in the outer ring and place in the HF waste

bucket. Run the dropper around the outer wall of the inner ring and the inner wall of the outer ring removing any adhering droplets of the purple solution

4.4.2.3. Carefully rinse the outer ring of the cell with 18 MΩ DI water and pipette this solution off.

4.4.2.4. Carefully tip the cell until the solution in the inner ring is close to the top of the inner ring and rotate the cell allowing the solution to collect any adhering drops on the inner portion of the separation ring and incorporating them into the inner solution.

4.4.2.5. Carefully move the cell to the counter and place the electrode in the inner ring conditioning solution. The electrode should not touch the bottom of the cell, but should be completely immersed in solution.

4.4.3. **Determinations:** When the time is almost up for the conditioning cell, take the next cell off the shaker and move it to the hood. Rinse the lid and remove the purple solution as described above. **(The procedure for standards and samples are the same).** **NOTE:** The chlorine is in the inner reducing solution and the mass needs to be accurately measured.

4.4.3.1. Remove the purple solution and rinse the cell as described above.

4.4.3.2. Take the cell to the balance and weigh it to determine the total mass.

4.4.3.3. While this cell is on the balance, take the final reading from the conditioning cell and **\*write it down\*** on the CI log sheet.

4.4.3.4. Retrieve the cell from the balance, being sure to **record the final mass of the cell** on the paper used earlier to record the empty mass.

4.4.3.5. Place the electrode in the center solution as before.

4.4.3.6. Retrieve the next cell from the orbital shaker and repeat the process until all cells have been done being sure to **write the stable reading down before removing the electrode.**

4.4.3.7. When all the readings have been taken, subtract the empty cell mass from the final cell mass to determine the final mass and record this on the CI log sheet.

**NOTE:** Be consistent with the time between readings (i.e. the amount of time the sample or standard is exposed to the atmosphere (evaporation)).

#### **4.5. Calculation of CI content**

4.5.1. **CHLOE:** On the input page fill in the appropriate data concerning the sample name and location. Also fill in the information received from XRF concerning major elements, U and Th. Also fill in the elevation, latitude and longitude information. On the shielding page fill in any appropriate information concerning shielding, if required. The ppm of CI is determined using "Lab Calcs" (Sect. 4.5.3 part 4.5.3.1).

4.5.1.1. Go to the "theoretical" page of CHLOE, enter the estimated exposure age of the sample, and write down the estimated  $^{36}\text{Cl}/^{35}\text{Cl}$  ratio (R/S ratio) that is calculated by CHLOE.

#### **4.5.2. Saving the worksheet**

4.5.2.1. On the input sheet of CHLOE select the **"save data"** button. A screen titled **"Use the following workbook"** will appear.

4.5.2.2. You will be prompted to "Open another workbook" or "Create a new workbook". If a workbook already exists that is appropriate for the sample you can open it by single clicking on "Open another workbook" and then selecting the workbook that you want to open from its location. Otherwise, create a new workbook by single clicking on "Create a new workbook". A screen will appear prompting the user to enter a title. Title the workbook so as to be able to readily identify it should you need to reopen it at a later date. Single click OK.

4.5.2.3. On the "Use the following workbook" screen, select the "down" arrow and then the name of the workbook you just created. Single click OK.

4.5.2.4. A "Enter name of sheet" screen will appear. Enter a name for the sheet. (Usually the sample name and number will automatically appear. This was entered in the Sample ID, Name box on the input sheet of CHLOE). Select OK and the workbook will be saved.

4.5.2.5. To Import data from a previously saved workbook, single click "Import data", select the down arrow if the workbook is already open, otherwise select open a workbook, and select the workbook from the location it is stored at. Select the sheet or sample that you wish to import data for. Single click OK.

4.5.3. **LABCALCS: On the Cl determination page**, fill in the appropriate boxes concerning the ppm of the standards, initial and final masses and millivolt readings. Do the same for the samples.

4.5.3.1. Try to select standards that are on either side of the sample in question by selecting and deselecting the appropriate boxes next to each. Observe the ppm concentration of each sample and record the appropriate concentration for each. (Also, look at the bottom of the graph and record the  $R^2$  value)

4.5.3.2. **On the SPIKE addition page**: at the top of the page fill in the box concerning ppm concentration and the box concerning estimated  $^{36}\text{Cl}/\text{Cl}$  ratio (obtained from CHLOE). **Read the information included on the side of the charts.**

4.5.3.3. The values highlighted in **green** meet all the constraints and will most often be used though they are not necessarily optimal for that parameter.

4.5.3.4. The values highlighted in **red** do not meet the constraints.

4.5.3.5. Basically, first you want the Stable/Stable ratio (S/S) to be close to six (6). Second, you want to maximize the  $^{36}\text{Cl}/\text{Cl}$  ratio (R/S). Third, maximize the AgCl mass recovered, preferably at least 10 mg.

## 5. Chloride extraction for $^{36}\text{Cl}$ analysis

### 5.1. Initial sample dissolution



- 5.1.1. Large (1 liter) Teflon bottles are used for the initial stages of sample dissolution for most samples. Before using, these need rinsed in  $\text{NH}_4\text{OH}$ , 18 M $\Omega$  DI water, hot  $\text{HNO}_3$ , then thoroughly rinsed in 18 M $\Omega$  DI water. **NOTE:** if the sample size is 20 -30 grams, you might consider using a 250-ml Teflon bottle.
- 5.1.2. The amount of sample dissolved and spike used will depend on the sample composition and age. Use the **LabCalcs** Excel Workbook to determine the appropriate masses of rock to dissolve and spike to add.
- 5.1.3. Exactly weigh the appropriate amount of sample into the Teflon bottle using the cone-and-quarter technique (section 3.5). Record the sample weight in your logbook. Add 18 M $\Omega$  DI water at a ratio of 1:1 with the sample weight. Swirl the sample.
- 5.1.4. Weigh the amount of spike determined from the LabCalcs program into an acid-washed 10-ml beaker. Record the mass, concentration, and the identification code of the spike in your lab book. Add the spike to the sample and rinse the beaker several times with 18 M $\Omega$  DI water, adding the rinse to the sample also. Swirl the sample.
- 5.1.5. Prepare a cold water bath for each sample so that the following reaction can be slowed if it begins to proceed too rapidly.
- 5.1.6. **(NOTE: All of the remaining steps in this section must be performed under the hood)** HF is a very hazardous weak acid and caution should be exercised when using. Pay particular attention to inhalation of vapors and any spills and splashes should be cleaned up immediately. Always wear appropriate clothing, lab coat, goggles, and gloves when using.
- 5.1.7. In a Teflon separatory funnel measure and add  $\text{HNO}_3$  at a ratio of 1:2 of the sample weight (volume to weight), and add HF in a 2½:1 ratio to the sample weight. Add both solutions to the funnel and then drip them into the Teflon bottle containing the sample. This solution needs to be **dripped** into the Teflon bottle slowly because of the possibility of violent reaction with silicates. Position the separatory funnel and Teflon bottle so that the water bath may be added if needed.

- 5.1.8. **Swirl the samples often.** If lots of bubbling takes place, or if a bottle becomes hot enough for the Teflon to soften, place the bottle in the cold water bath for a few minutes. The drip rate must be very slow initially, but can be speeded up as more solution is added (watch the temperature). The drip rate may also depend on the sample type; i.e. the solution may need to be added to granite samples more slowly.
- 5.1.9. Once all of the solution has been dripped into the samples, cap the bottles and then loosen the caps approximately 1/4 turn. Place the Teflon bottle on a hot plate under the hood at a low setting (the hot plate should be warm to the touch but not hot). Repeat this process for each sample. The dissolution may take as long as 48 to 72 hours but should be checked every 12 hours or so. The samples should be swirled periodically. Some samples dissolve overnight.
- 5.1.10. If silica gel deposits on the walls of the bottle add an additional 10-20 ml aliquot of HF, depending on the sample size. Swirl the samples after the addition of HF.

## **5.2. Separation of Cl from dissolved rock by precipitation of AgCl**

- 5.2.1. After complete dissolution, transfer the solution and solid into 250-ml Teflon bottles that have been cleaned as described above for 1 liter bottles.
- 5.2.2. Centrifuge the bottles at ~2500 rpm for at least 10 minutes.
- 5.2.3. Decant the **solution** into a Teflon beaker that has been cleaned as described above for 1 liter bottles. **NOTE:** if the sample is small; transfer to a clean labeled 250 ml Teflon bottle instead of a Teflon beaker.
- 5.2.4. Add 10 ml of 0.2 M  $\text{AgNO}_3$  to the solution in the Teflon beaker, or bottle, using an acid washed 10-ml beaker (this doesn't have to be exact). Cover the Teflon beakers with Teflon covers or loosely cap the bottles, place on a warm hot plate (setting of 1-3), and leave for approximately 12 hours (overnight).

## **5.3. Purification of AgCl**

- 5.3.1. Transfer the solution and precipitate into 250-ml Teflon bottles, that have been cleaned as described above, and centrifuge each bottle. Transfer the liquid from the 250 ml

bottles into a waste bucket and the precipitate into acid washed 50-ml centrifuge tubes, using 18 M- $\Omega$  DI water to facilitate the transfer.

- 5.3.2. Balance the tubes using 18 M- $\Omega$  DI water and cover with parafilm. Centrifuge for at least 10 minutes at approximately 2000 rpm.
- 5.3.3. Decant the solution into the HF waste bucket used previously. Rinse the samples in 18 M- $\Omega$  DI water, balance the tubes, cover with parafilm, and centrifuge again.
- 5.3.4. Decant the water down the drain in the sink. Add enough  $\text{NH}_4\text{OH}$  (a few ml) to dissolve the white powder sample containing the AgCl (Strange looking precipitate may form here). Add the  $\text{NH}_4\text{OH}$  a small amount at a time, swirling the tube after each addition. Do not add more than you need to dissolve the powder. **NOTE:** you may need to use an acid washed, glass stir rod on some samples to assure that the chloride is in solution.
- 5.3.5. Balance the tubes (using  $\text{NH}_4\text{OH}$ ), cover with parafilm, and centrifuge for at least 10 minutes
- 5.3.6. Decant the liquid, containing the chloride, into another 50-ml glass centrifuge tube that has been cleaned as described above. Add concentrated  $\text{HNO}_3$  slowly from the squeeze bottle (**CAUTION: reaction may be violent at first**) until AgCl precipitate begins to form (liquid turns milky white). The tube should be about  $\frac{1}{2}$  full when completed. Balance the tubes using  $\text{HNO}_3$ , cover with parafilm, and centrifuge for at least 10 minutes.
- 5.3.7. Dump the solution down the drain with the faucet running, being careful not to lose any precipitate.
- 5.3.8. Rinse the sample in 18 M- $\Omega$  DI water, balance, and centrifuge again.

#### **5.4. Sulfur removal**

- 5.4.1. Pour off the solution, and as described in step 5.3.4, add enough  $\text{NH}_4\text{OH}$  to dissolve the AgCl sample (a few ml). Balance the tubes using  $\text{NH}_4\text{OH}$ , then add 1 ml of  $\text{Ba}(\text{NO}_3)_2$ , to precipitate  $\text{BaSO}_4$ . Cover the tubes with parafilm and

leave the solution for at least 8 hours. (24 to 48 hours is preferable for the initial sulfur removal step if time allows)

**5.4.2.** Centrifuge the sample for at least 10 minutes at approximately 2000 rpm (longer centrifuge times sometimes aids in removal of the solution). **Carefully** remove the solution with a clean glass pipette. (The pipettes should be rinsed in dilute nitric and then 18 M $\Omega$  DI water). If the “clump” of precipitate in the bottom of the tube begins to come apart, re-centrifuge the sample. Eventually it will stay in one coherent mass in the bottom of the tube. The solution may be placed in a 10 ml test tube that has been cleaned as described above if the sample is small, otherwise use 50-ml tubes.

**5.4.3.** Add enough HNO<sub>3</sub> to precipitate AgCl, (**CAUTION: reaction may be violent at first**) balance the tubes using HNO<sub>3</sub>, and cover with parafilm. Let stand for 2 hours, then centrifuge and pour off the acidic solution (down the drain). Rinse the AgCl sample in 18 M- $\Omega$  DI water and centrifuge again. **Repeat the sulfur removal procedures at least once more. If the sample is suspected of having a high sulfur content, repeat the procedure 3 times.** (<sup>36</sup>S is an isobar of <sup>36</sup>Cl and interferes with AMS analysis)

**5.4.4.** When all the sulfur has been removed, rinse the sample which has been precipitated in HNO<sub>3</sub> at least 3 times in 18 M- $\Omega$  DI water, centrifuging each time. The pH of the final solution should be about 7. Store the clean sample in 18 M- $\Omega$  DI water in a tightly covered test tube (parafilm) in a dark place until it needs to be sent away, **however**, drying the sample and putting it into a labeled vial is preferred (section 5.5).

## **5.5. Preparation for shipping**

**5.5.1.** Label a set of watch glasses that have been cleaned as described earlier. Decant as much water from the tubes as possible. Pour each sample into its prelabeled watchglass using 18 M- $\Omega$  DI water to facilitate complete transfer. Very carefully remove excess water from the watch glass with a clean glass pipette. Prepare and label pieces of aluminum foil that are large enough to cover the watch glasses. Very carefully, cover the watch glass with the aluminum foil. Very carefully, place samples in the oven for ~24 hours at a temperature of ~60°C.

- 5.5.2. Label appropriately as many small sterile vials as necessary.
- 5.5.3. Fold a weighing paper in half along both axes. Calibrate the digital balance then weigh and tare the weighing paper. Very carefully transfer the sample from the watch glass to the weighing paper. Weigh each sample, using a new weighing paper each time, and record the weight in your lab book. Carefully transfer the sample from the weighing paper into the appropriately labeled sterile vial as it is weighed. Cap the vial tightly and tape the lid around the circumference with scotch tape.
- 5.5.4. Store the vials in a ziplock bag until ready to send them to be analyzed.

# APPENDIX C

## Observed and Estimated Meteorological Data

---

# Long-term means for Bishop National Climatic Data Center

BISHOP, CALIFORNIA

NORMALS, MEANS, AND EXTREMES

LATITUDE: 37° 22' N LONGITUDE: 118° 22' W ELEVATION: FT. GRND 4110 BARO 4113 TIME

ZONE: PACIFIC WBAN: 23157

	(a)	JAN	FEB	MAR	APR	MAY	JUN	JUL	AUG	SEP	OCT	NOV	DEC	YEAR
<b>TEMPERATURE (Deg. F)</b>														
Normals														
-Daily Maximum		53.5	58.5	63.4	71.1	80.6	90.5	97.2	94.9	86.8	76.3	62.4	53.8	74.1
-Daily Minimum		22.0	26.3	30.2	35.7	43.8	51.2	56.1	54.2	46.9	37.4	27.8	21.7	37.8
-Monthly		37.8	42.4	46.8	53.4	62.2	70.9	76.7	74.6	66.8	56.9	45.2	37.8	56.0
Extremes														
-Record Highest	48	77	81	87	93	101	109	109	107	112	97	84	78	112
-Year		1948	1986	1966	1989	1951	1954	1972	1993	1995	1980	1988	1958	SEP 1995
-Record Lowest	48	-7	-2	9	15	25	29	34	37	26	16	5	-8	-8
-Year		1982	1969	1971	1953	1964	1988	1987	1959	1986	1970	1958	1990	DEC 1990
<b>NORMAL DEGREE DAYS</b>														
Heating (base 65 Deg. F)		843	633	564	361	140	16	0	0	51	265	594	843	4310
Cooling (base 65 Deg. F)		0	0	0	13	53	193	363	298	105	14	0	0	1039
<b>% OF POSSIBLE SUNSHINE</b>														
<b>MEAN SKY COVER(tenths)</b>														
Sunrise - Sunset	29	5.3	5.0	4.7	4.3	4.1	2.6	2.4	2.2	1.9	2.9	4.1	4.5	3.7
<b>MEAN NUMBER OF DAYS:</b>														
Sunrise to Sunset														
-Clear	29	11.5	11.0	13.0	13.7	14.8	20.2	21.9	22.9	23.2	19.7	14.9	14.3	201.0
-Partly Cloudy	29	8.0	7.5	8.9	9.0	9.8	6.8	6.7	6.0	4.7	6.7	7.9	7.4	89.3
-Cloudy	29	11.6	9.8	9.0	7.3	6.4	3.0	2.4	2.2	2.1	4.7	7.2	9.3	75.0
Precipitation														
.01 inches or more	48	4.0	3.4	3.2	2.4	2.7	1.5	2.0	1.6	1.9	1.6	2.4	3.0	29.5
Snow, Ice Pellets, Hail														
1.0 inches or more	48	1.0	0.3	0.2	0.1	0.*	0.0	0.0	0.0	0.0	0.*	0.1	0.5	2.3
Thunderstorms	21	0.0	0.0	0.0	0.2	1.2	1.3	4.7	2.7	0.9	0.4	0.1	0.0	11.5
Heavy Fog Visibility														
1/4 mile or less	21	0.1	0.0	0.0	0.*	0.0	0.0	0.0	0.0	0.0	0.0	0.1	0.1	0.3
Temperature Deg. F														
-Maximum														
90 Deg. F and above	48	0.0	0.0	0.0	0.4	4.9	18.4	29.1	26.7	13.9	1.4	0.0	0.0	94.8
32 Deg. F and below	48	0.6	0.1	0.0	0.0	0.0	0.0	0.0	0.0	0.0	0.0	0.0	0.3	1.0
-Minimum														
32 Deg. F and below	47	29.4	24.2	20.0	8.1	1.0	0.1	0.0	0.0	0.3	6.3	23.5	29.4	142.4
0 Deg. F and below	47	0.2	0.*	0.0	0.0	0.0	0.0	0.0	0.0	0.0	0.0	0.0	0.2	0.4
<b>AV. STATION PRES. (mb)</b>														
	11	875.2	874.7	871.0	871.5	870.8	871.6	873.0	873.1	873.5	875.1	875.4	876.5	873.4
<b>RELATIVE HUMIDITY (%)</b>														
Hour 04						74	65	55	53	53	51	60	75	
Hour 10 (Local Time)	41	50	41	31	23	22	19	20	20	22	25	35	45	29
Hour 16	32	35	27	21	16	16	13	14	13	14	18	26	34	21
Hour 22						57	44	35	32	33	39	49	65	
<b>PRECIPITATION (in.)</b>														
Water Equivalent														
-Normal		1.11	0.95	0.39	0.26	0.29	0.18	0.23	0.18	0.24	0.13	0.57	0.84	5.37
-Maximum Monthly	48	8.93	6.01	2.94	2.26	1.30	1.29	1.47	0.64	1.28	1.58	2.59	5.79	8.93
-Year		1969	1969	1991	1956	1962	1982	1976	1983	1994	1957	1960	1966	JAN 1969
-Minimum Monthly	48	0.00	T	0.00	0.00	0.00	0.00	0.00	0.00	0.00	0.00	0.00	0.00	0.00

-Year		1976	1967	1972	1973	1983	1981	1982	1980	1974	1973	1976	1975	MAY 1983
-Maximum in 24 hrs	48	3.32	3.64	1.79	1.58	0.95	0.72	0.86	0.46	1.25	1.05	1.79	3.35	3.64
-Year		1952	1969	1995	1982	1953	1982	1976	1977	1994	1957	1950	1966	FEB 1969
Snow, Ice Pellets, Hail														
-Maximum Monthly	47	23.2	31.9	14.5	8.8	2.3	0.0	0.0	0.0	T	1.8	3.9	13.2	31.9
-Year		1969	1969	1952	1956	1964				1955	1978	1964	1967	FEB 1969
-Maximum in 24 hrs	47	18.0	14.2	7.5	8.8	2.3	0.0	0.0	0.0	T	1.8	3.9	6.7	18.0
-Year		1969	1976	1952	1956	1964				1955	1978	1964	1967	JAN 1969
<b>WIND</b>														
Mean Speed (mph)					6.7	8.7	8.1	7.6	7.3	7.0	73	6.6	6.4	
Prevailing Direction through 1964														
Fastest Mile														
-Direction(!)														
-Speed(mph)	9	51	52	59	60	58	60	55	75	53	56	56	66	75
-Year		1983	1975	1977	1980	1979	1975	1980	1976	1982	1979	1975	1975	AUG 1976
Peak Gust														
-Direction(!)														
-Speed(mph)														
-Date														

- Length of Record in Years, although individual months may be missing.

0.\* or \* - The value is between 0.0 and 0.05.

Normals - Based on the 1961 - 1990 record period.

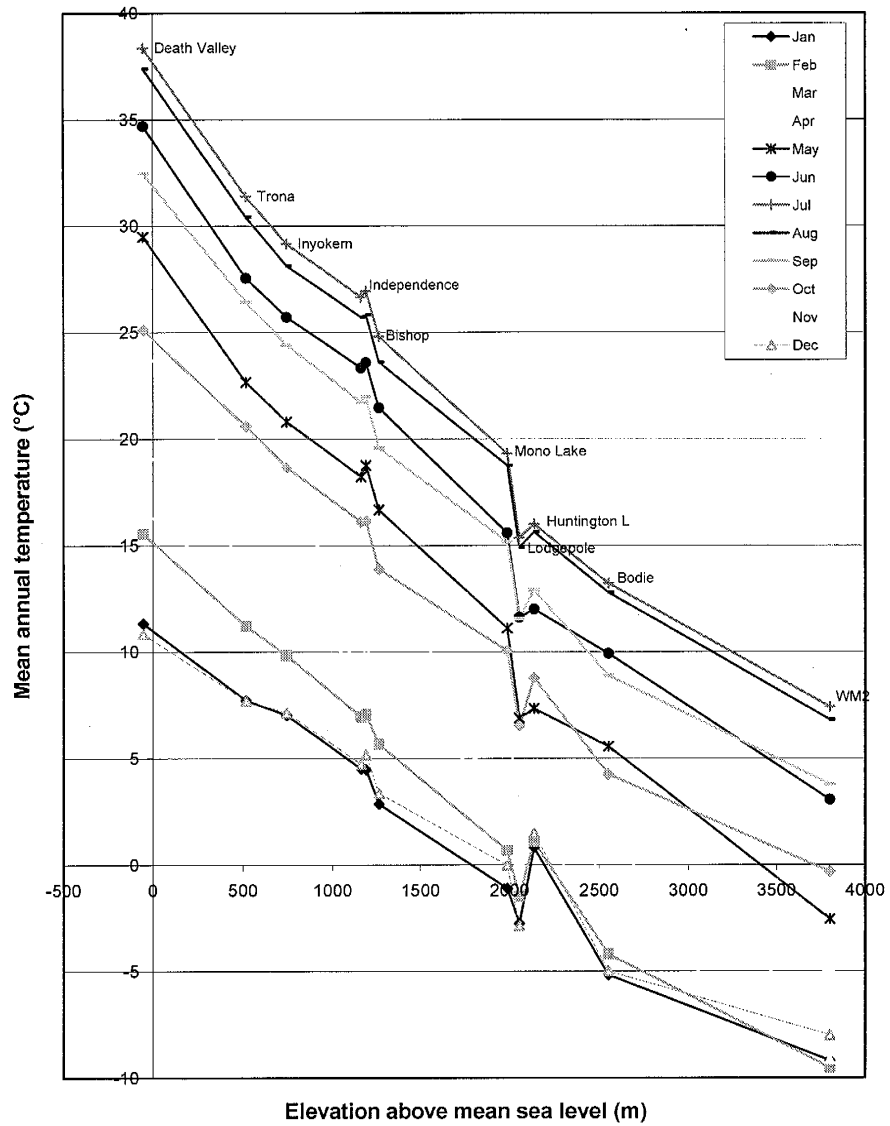
Extremes - Dates are the most recent occurrence.

Wind Dir.- Numerals show tens of degrees clockwise from true north. "00" indicates calm.

Resultant Directions are given to whole degrees.

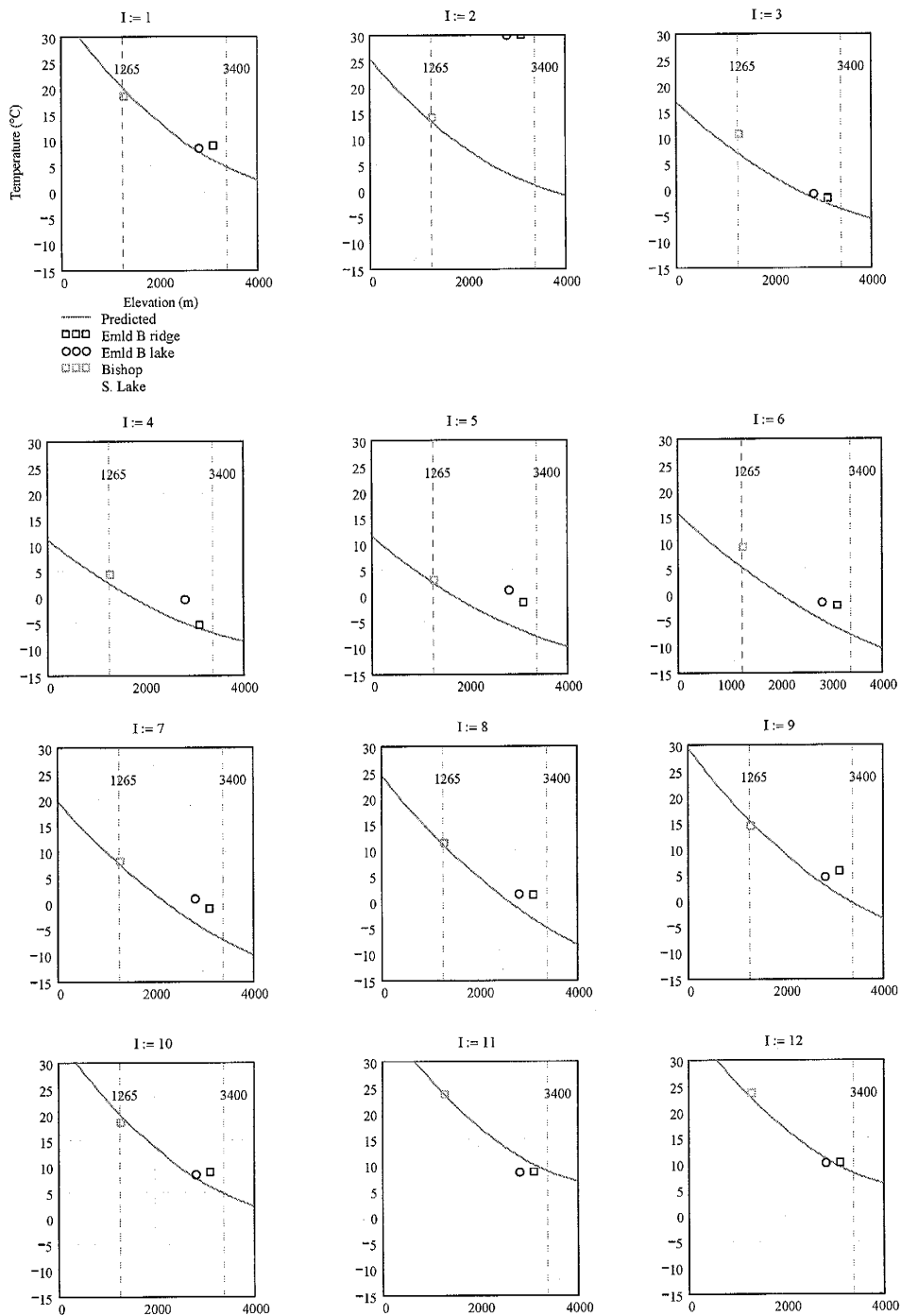


GRAPH OF MEAN MONTHLY TEMPERATURES FROM NCDC STATIONS IN  
THE OWENS VALLEY REGION

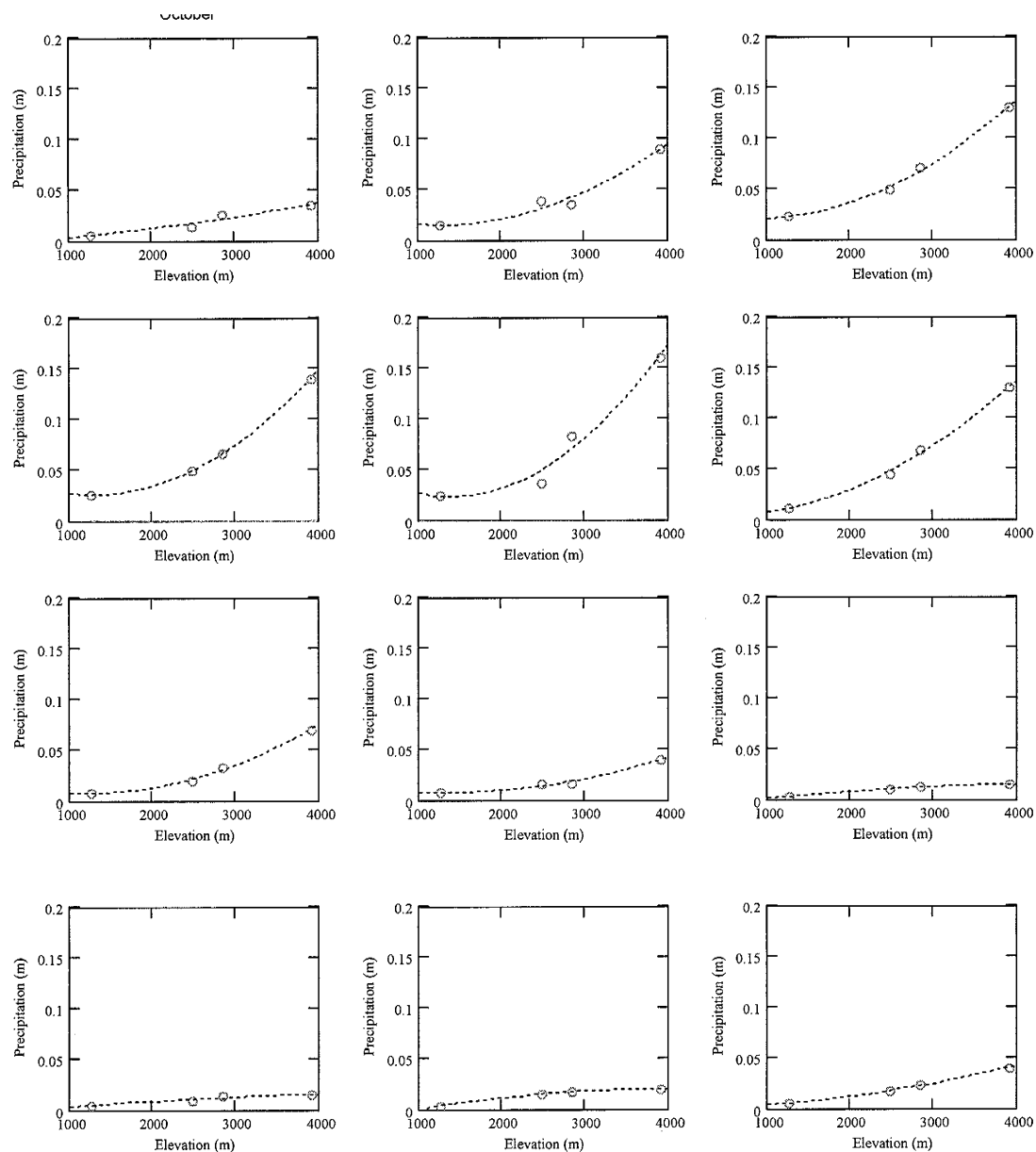


# MODELED MONTHLY MEAN TEMPERATURE – ELEVATION RELATIONSHIP FOR THE BISHOP CREEK AREA

Month no. 1 is October, beginning of the water year



# MODELED MONTHLY MEAN PRECIPITATION – ELEVATION RELATIONSHIP FOR THE BISHOP CREEK AREA



# APPENDIX D

## Solar Angles Calculation Worksheet

---

**Worksheet to calculate solar angles for a prescribed set of times in a day, taking into account the orbital variations known as the Milankovitch effects:**

Indices for, respectively, approximation summations; day of year graphs, and long time scale for orbital effects graphs:

$$j := 1, 10.. 365$$

Conversions & constants  $\text{kyr} := 1000 \cdot \text{yr}$

Angular velocity for azimuth and zenith angle calculations:  $\omega_v := 0.2618 \cdot \frac{\text{rad}}{\text{hr}}$

Solar constant  $S_0 := 1367 \cdot \text{watt} \cdot \text{m}^{-2}$

Time of year (radians)  $\Gamma(J) := \frac{2 \cdot \pi \cdot (J - 1)}{365.25}$   $\Gamma(182) = 3.114$

☒ Orbital parameters & plots

Data for the orbital changes in the astronomical parameters affecting insolation are taken from Berger and Loutre, 1991.

OrbitData :=



D:\..\orbit91.prn

$t := \text{OrbitData}^{\langle 1 \rangle}$   $K := \text{length}(t)$   $K = 400$   $k := 1.. K$   $tset_k := 1 - k$

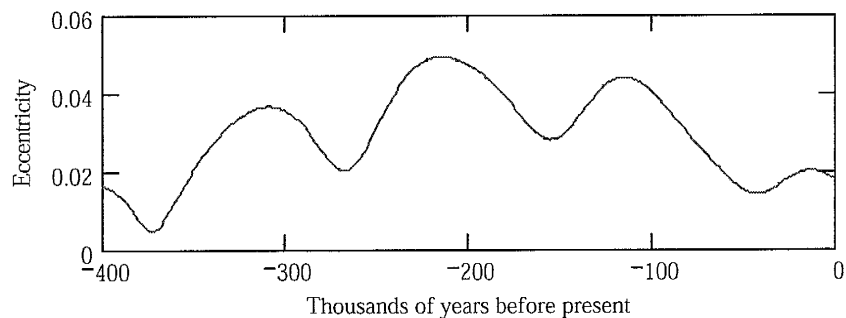
$\text{Eccent} := \text{OrbitData}^{\langle 2 \rangle}$

$\text{Omega} := \text{OrbitData}^{\langle 3 \rangle}$

$\text{Obliq} := \text{OrbitData}^{\langle 4 \rangle}$

$\text{CPP} := \text{OrbitData}^{\langle 5 \rangle}$

**Eccentricity**



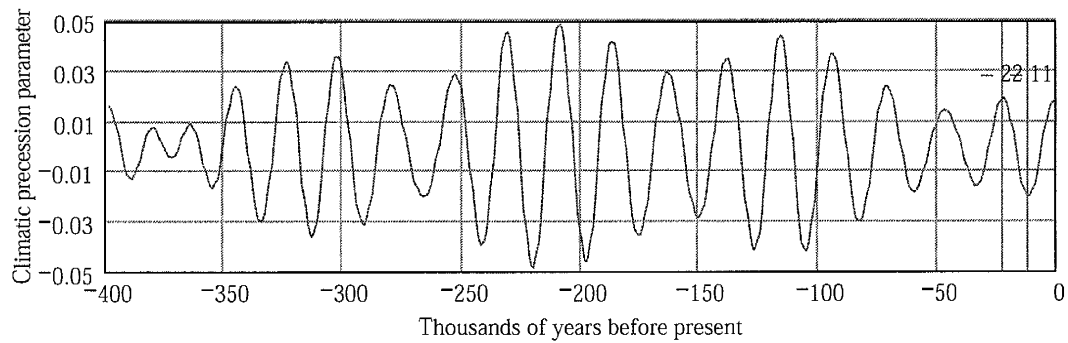
A function to interpolate eccentricity between integer kyr values:

$\text{ecc}(t) := \text{linterp}(\text{reverse}(tset), \text{reverse}(\text{Eccent}), t)$

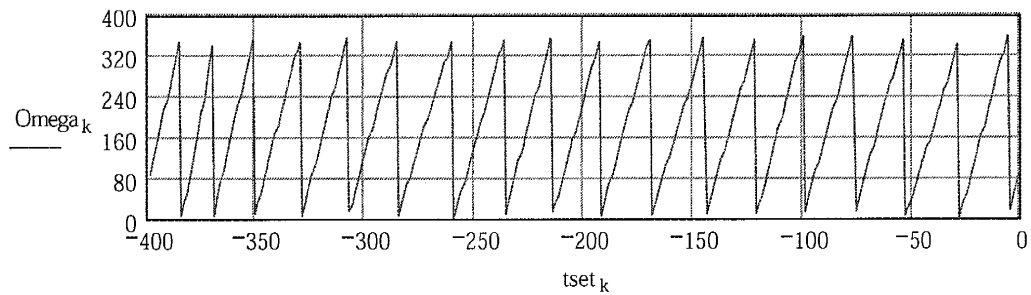
$\text{ecc}(0) = 0.017$

$\text{ecc}(-12.5) = 0.02$

Plot of the climatic precession parameter, for reference; it is not needed in the calculations.



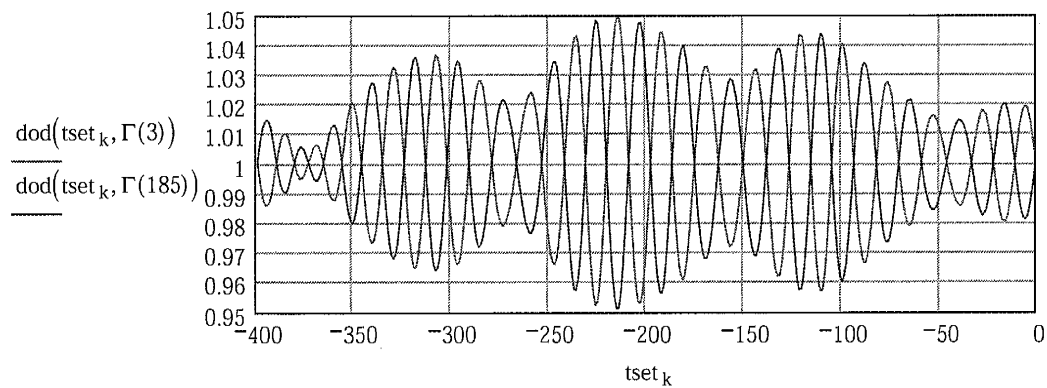
**The longitude of perihelion measured from the moving vernal equinox**  $\Omega_{a_1} = 101.37$

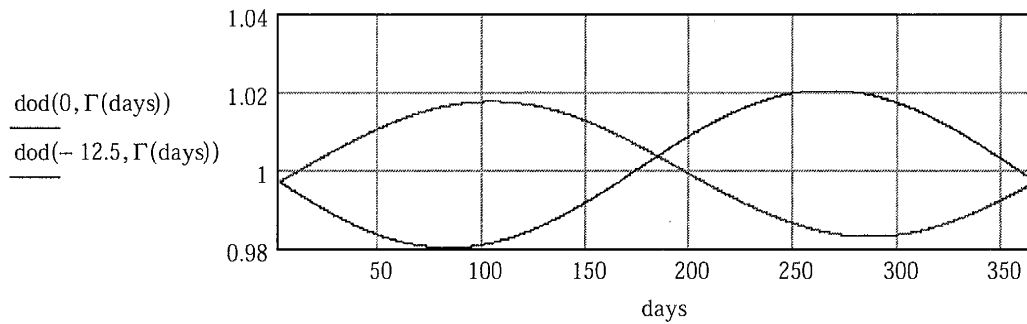


Ratio of mean Earth-Sun distance to actual Earth-Sun distance (insolation is proportional to square of this).

$$\text{dod}(t, \theta) := \frac{1 + \text{ecc}(t) \cdot \cos(\theta - \Omega_{a_{\text{floor}(|t|)+1} \cdot \text{deg}})}{1 - (\text{ecc}(0))^2}$$

$\text{dod}(0, \Gamma(1)) = 0.997$   
 $\text{dod}(-12, \Gamma(1)) = 0.997$





### Eccentricity correction

An approximation (from Dingman appendix) for the eccentricity correction today.

$$E_{\text{naught}}(G) := 1.00011 + 0.034221 \cdot \cos(G) + 0.00128 \cdot \sin(G) + 0.000719 \cdot \cos(2 \cdot G) + 0.000077 \cdot \sin(2 \cdot G)$$

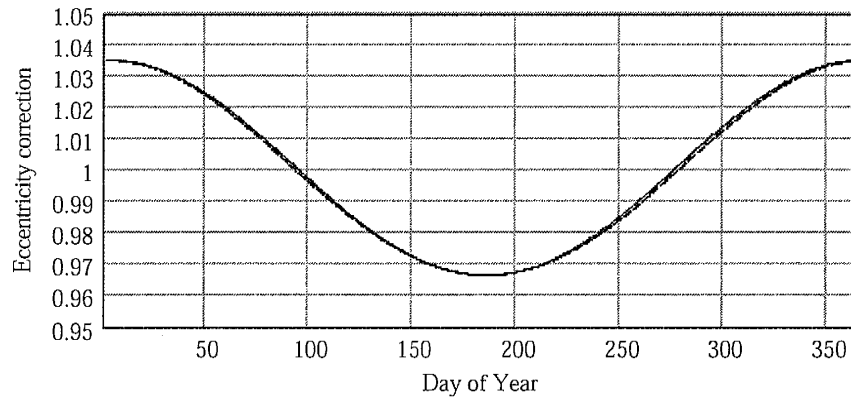
The eccentricity correction is the adjustment to the solar constant for the distance to sun relative to the mean Earth-Sun distance for the modern eccentricity (it is a squared term because radiation is proportional to square of inverse distance. This uses the angle of perihelion measured from the moving vernal equinox but since we want the earth-sun distance correction for a period that starts on Jan 1, we shift the phase by the angular distance between Jan 1 and the vernal equinox. Based on comparison of the unshifted value with the correction, the dod date needs to be shifted forward by 47 days, or

$$\Gamma(101) = 98.563 \text{ deg}$$

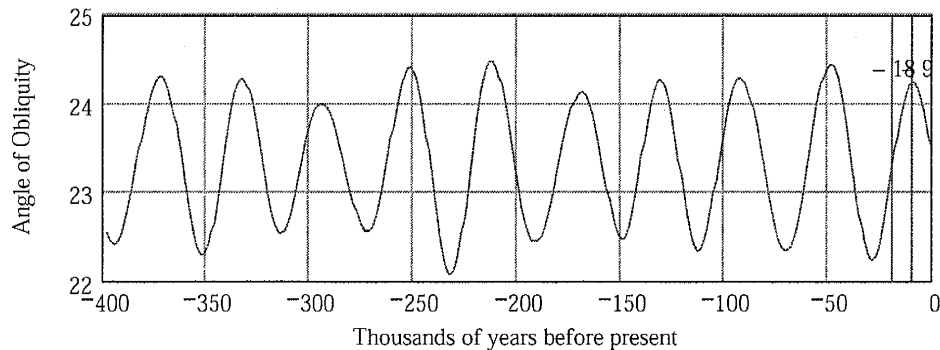
**Eccentricity correction**  $(r_o/r)^2$ :

$$Eo(t, J) := \text{dod}(t, \Gamma(J + 101))^2$$

year = 0



### Obliquity



$$\varepsilon(t) := \text{linterp}(\text{reverse}(\text{tset}), \text{reverse}(\text{Obliq}), t)$$

$$\varepsilon(-0) = 23.446$$

Values required for further sun position calculations:

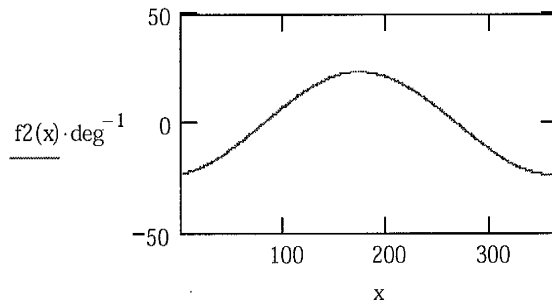
$$\varepsilon(\text{year}) = 23.446 \quad (\text{obliquity})$$

### Sun position and radiant flux calculations from Dingman, 1993.

The following expression provides a good approximation to declination assuming modern day obliquity.

$$\text{Solar declination: } f2(J) := \left( \begin{array}{l} 0.006918 - 0.399912 \cdot \cos(\Gamma(J)) \dots \\ + 0.070257 \cdot \sin(\Gamma(J)) \dots \\ + -0.006758 \cdot \cos(2 \cdot \Gamma(J)) + 0.000907 \cdot \sin(2 \cdot \Gamma(J)) \dots \\ + -0.002697 \cdot \cos(3 \cdot \Gamma(J)) + 0.00148 \cdot \sin(3 \cdot \Gamma(J)) \end{array} \right)$$

To extend it back in time we'll normalize to the max obliquity of the above expression and multiply result by actual obliquity.



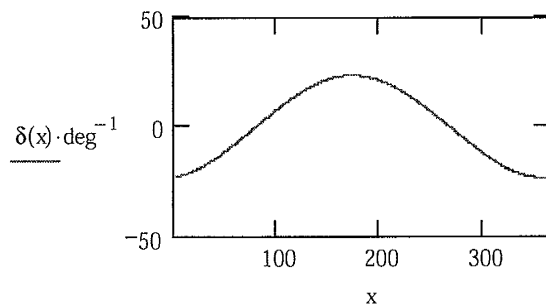
$$\text{root}\left(\frac{d}{dx} f2(x), x, 300, 365\right) = 356.53$$

$$\text{root}\left(\frac{d}{dx} f2(x), x, 100, 300\right) = 173.127$$

$$f2(356.287) \cdot \text{deg}^{-1} = -23.426$$

$$f2(173.009) \cdot \text{deg}^{-1} = 23.456$$

$$\delta(J) := f2(J) \cdot \frac{\varepsilon(\text{year}) \cdot \text{deg}}{23.456 \cdot \text{deg}}$$



Orbital parameters & plots

**Zenith** angle:

(measured from vertical)

$$ZA(\delta, t) := \text{acos}(\sin(\text{lat}) \cdot \sin(\delta) + \cos(\text{lat}) \cdot \cos(\delta) \cdot \cos(\omega \cdot t \cdot \text{hr}))$$

**Azimuthal** angle argument:

$$\arg(d_n, t_h) := \frac{\sin(\delta(d_n)) \cdot \cos(\text{lat}) - \cos(\delta(d_n)) \cdot \sin(\text{lat}) \cdot \cos(\omega \cdot t_h \cdot \text{hr})}{\sin(ZA(\delta(d_n), t_h))}$$



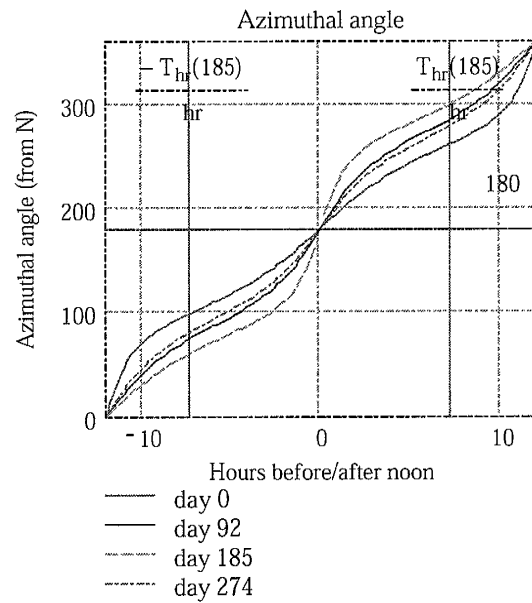
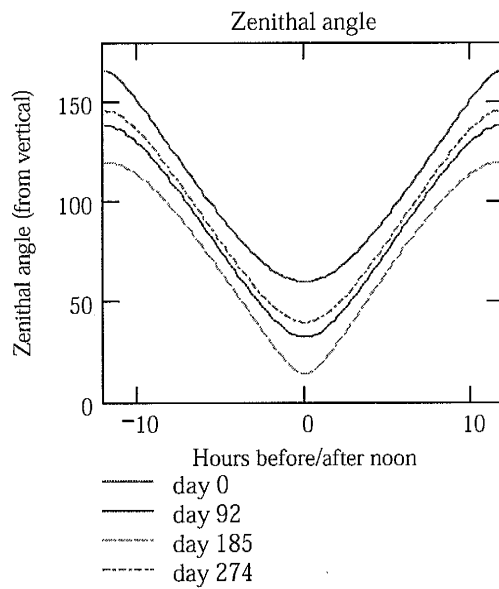
**Azimuthal angle** (measured from N):  $\phi_p(d_n, t_h) := \text{if}(|\arg(d_n, t_h)| > 1, \pi \text{rad}, \text{acos}(\arg(d_n, t_h)))$   
 (the if statement here corrects for precision problems which produce an acos argument that is slightly greater than one)

Convert azimuth angle to compass direction:  $\Phi(d_n, t_h) := \text{if}(t_h > 0, 2\pi - \phi_p(d_n, t_h), \phi_p(d_n, t_h))$

Time of sunrise (hours before solar noon):  $T_{hr}(J) := \left| \frac{-\text{acos}(-\tan(\delta(J)) \cdot \tan(\text{lat}))}{\omega v} \right|$

$$T_{hr}(0) = 4.749 \text{ hr}$$

$t := -12, -11.8..12$



▼ Opt Path - secant & Kastens

Relative optical path (normalized to sun at zenith) can be calculated from the secant approximation, assuming a plane-parallel atmosphere.

$$M_{\text{opt\_sec}}(\theta) := \text{if} \left( \theta < \frac{\pi}{2}, \sec(\theta), 100 \right)$$

$$M_{\text{opt\_sec}}(\text{ZA}(\delta(0), 0)) = 2.007$$

or from Kasten's formula [Dozier and Outcalt 1979]:

$$M_{\text{opt\_Kastens}}(\theta) := \frac{1}{\left[ \cos(\theta) + 0.15 \cdot (\theta + 3.885 \cdot \text{deg})^{-1.253} \right]} \quad ??$$

$$M_{\text{opt\_Kastens}}(\text{ZA}(\delta(0), 0)) = 1.59$$

▲ Opt Path - secant & Kastens

Relative optical path (normalized to sun at zenith), assuming a plane-parallel atmosphere, can be calculated from the secant approximation but here we use an approximation that is slightly better when sun is close to horizon (from Kondratyev [1973] but could be switched to calcs from lqbal to have a consistent source).

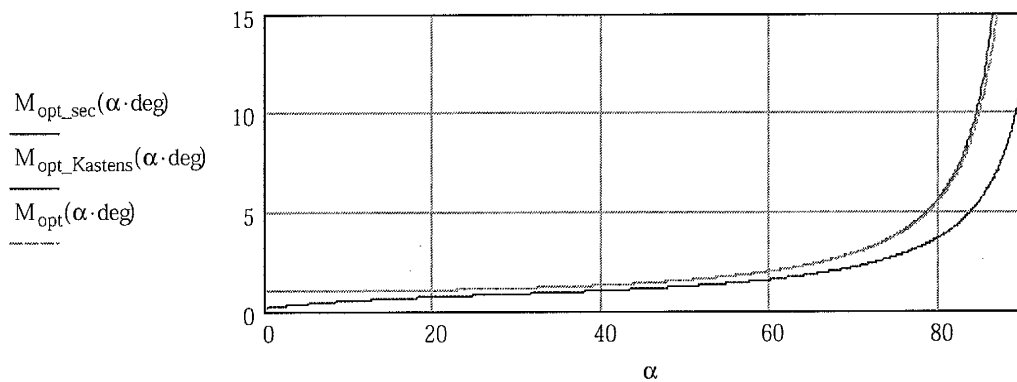
*Note that pressure correction is not made here. These values are passed to other routines where elevation information is available.*

Needed constants are the radius of the earth,  $r$ ,  
the scale height of the atmosphere,  $H$ :  $r_{\text{Earth}} := 6366 \cdot 10^3$   $H_{\text{scale}} := 8 \cdot 10^3$

$$M_{\text{opt}}(\alpha) := \text{if} \left[ \alpha < \frac{\pi}{2}, \frac{1}{H_{\text{scale}}} \cdot \left( \sqrt{r_{\text{Earth}}^2 \cdot \cos(\alpha)^2 + 2 \cdot r_{\text{Earth}} \cdot H_{\text{scale}} + H_{\text{scale}}^2} - r_{\text{Earth}} \cdot \cos(\alpha) \right), 100 \right]$$

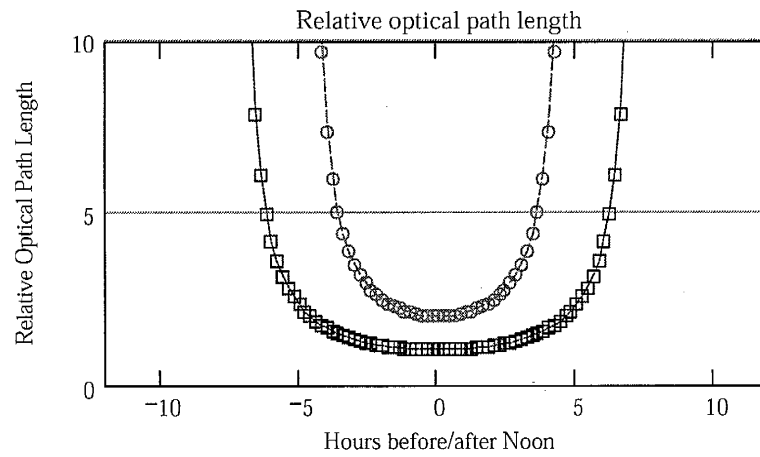
$$M_{\text{opt}}(\text{ZA}(\delta(0), 0)) = 2.004$$

▼ Optical path length comparisons



▲ Optical path length comparisons

Plots of relative optical path length. The lines are the simple secant approximation used in the Arcview script. The symbols are more accurate approximations.



Average optical path length for a day

$$M_{\text{optavg}}(J) := \frac{\int_0^{T_{\text{hr}}(J) - 0.1} M_{\text{opt}}(\text{ZA}(\delta(J), t)) dt}{T_{\text{hr}}(J) \cdot \text{hr}^{-1} - 0.1}$$

$M_{\text{optavg}}(0) = 4.53$   
 $M_{\text{optavg}}(182) = 2.971$

Instantaneous extraterrestrial radiant flux on a horizontal plane:

$$f(J, t) := S_0 \cdot E_0(t, J) \cdot (\cos(\delta(J)) \cdot \cos(lat) \cdot \cos(\omega \cdot t \cdot hr) + \sin(\delta(J)) \cdot \sin(lat))$$

$$k_{ET}(J, t) := \text{if}(f(J, t) > 0, f(J, t), 0)$$

Daily integrated average extraterrestrial radiant flux on a horizontal plane:

$$K_{ET}(t, J) := \frac{1}{24 \cdot hr} \left[ 2 \cdot S_0 \cdot E_0(t, J) \cdot \left( \cos(\delta(J)) \cdot \cos(lat) \cdot \frac{\sin(\omega \cdot T_{hr}(J))}{\omega} + T_{hr}(J) \cdot \sin(\delta(J)) \cdot \sin(lat) \right) \right]$$

$$K_{ET}(\text{year}, 10) = 189.087 \text{ m}^{-2} \text{ watt}$$

Output to include:

Years beyond present (past is negative)

Month number (starting from October for water year calculations)

Hours of daylight

Daily integrated average extraterrestrial radiant flux on a horizontal plane (watts/m<sup>2</sup>)

Earth-sun distance correction (dimensionless)

Prescribed number of Azimuth angles (radians, measured from North)

Prescribed number of Zenith angles (radians, measured from vertical)

Relative optical path length corresponding to each zenithal angle

---

Adjustable parameters:  $\text{lat} \equiv 37 \cdot \text{deg}$   $\text{year} \equiv -0$  (kyr)  $\epsilon(\text{year}) = 23.446$

Month index:  $\text{mnth} := 1..12$

Month of water year (Oct start):  $\text{Wmnth}(\text{mnth}) := \text{if}(\text{mnth} > 9, \text{mnth} - 9, \text{mnth} + 3)$

Day of month used for calcs:  $\text{cday}_{\text{mnth}} := \text{mnth} \cdot \frac{365}{12} - \frac{365}{24}$

Hour of day index:  $I = 7$   $i := 1..I$

Produce angles on this time interval  $\text{interval}_{\text{mnth}} := \frac{2 \cdot T_{\text{hr}}(\text{cday}_{\text{mnth}}) \cdot \text{hr}^{-1}}{I}$

Angles are output at these times  
(relative to noon)  $\text{time}_{\text{mnth}, i} := \text{interval}_{\text{mnth}} \cdot \left(i - \frac{1}{2}\right) - T_{\text{hr}}(\text{cday}_{\text{mnth}}) \cdot \text{hr}^{-1}$

Avg daily integrated extraterrestrial  
radiant flux:  $\text{Hor}_{\text{mnth}} := K_{\text{ET}}(\text{year}, \text{cday}_{\text{mnth}})$

Azimuth output (**degrees**):  $\text{azimuth}_{\text{mnth}, i} := \phi(\text{cday}_{\text{mnth}}, \text{time}_{\text{mnth}, i}) \cdot \text{deg}^{-1}$

Zenith angles output (**degrees**) &  
measured from the **horizontal**:  $\text{zenith}_{\text{mnth}, i} := \left(\frac{\pi}{2} - \text{ZA}(\delta(\text{cday}_{\text{mnth}}), \text{time}_{\text{mnth}, i})\right) \cdot \text{deg}^{-1}$

Relative optical path length might also  
be output:  $\text{opt\_path}_{\text{mnth}, i} := M_{\text{opt}}(\text{ZA}(\delta(\text{cday}_{\text{mnth}}), \text{time}_{\text{mnth}, i}))$

Average optical path length:  $\text{avg\_opt\_path}_{\text{mnth}} := M_{\text{optavg}}(\text{cday}_{\text{mnth}})$

Output data

mnth =

1
2
3
4
5
6
7
8
9
10
11
12

cday =

	1
1	15.208
2	45.625
3	76.042
4	106.458
5	136.875
6	167.292
7	197.708
8	228.125
9	258.542
10	288.958
11	319.375
12	349.792

$E_o(\text{year}, \text{cday}_{\text{mnth}}) =$

1.035
1.026
1.011
0.993
0.978
0.968
0.967
0.975
0.99
1.008
1.024
1.034

$T_{\text{hr}}(\text{cday}_{\text{mnth}}) =$

4.865
5.327
5.917
6.508
7.008
7.264
7.145
6.722
6.161
5.569
5.036
4.741

hr

Hor =

	1
1	195.506
2	257.162
3	339.362
4	413.732
5	463.517
6	483.047
7	471.861
8	431.619
9	366.535
10	287.312
11	215.82
12	179.729

$\text{m}^{-2} \text{ watt interval} =$

	1
1	1.39
2	1.522
3	1.691
4	1.859
5	2.002
6	2.075
7	2.042
8	1.92
9	1.76
10	1.591
11	1.439
12	1.355

time<sup>T</sup> =

	1	2	3	4	5	6	7	8	9	10
1	-4.17	-4.566	-5.072	-5.578	-6.006	-6.226	-6.125	-5.761	-5.281	-4.773
2	-2.78	-3.044	-3.381	-3.719	-4.004	-4.151	-4.083	-3.841	-3.521	-3.182
3	-1.39	-1.522	-1.691	-1.859	-2.002	-2.075	-2.042	-1.92	-1.76	-1.591
4	0	0	0	0	0	0	0	0	0	0
5	1.39	1.522	1.691	1.859	2.002	2.075	2.042	1.92	1.76	1.591
6	2.78	3.044	3.381	3.719	4.004	4.151	4.083	3.841	3.521	3.182
7	4.17	4.566	5.072	5.578	6.006	6.226	6.125	5.761	5.281	4.773

	1	2	3	4	5
1	123.5	138.8	157.8	$180-1.2i \cdot 10^{-6}$	202.2
2	113.6	130.3	152.3	180	207.7
3	99.8	117.6	142.9	$180-1.7i \cdot 10^{-6}$	217.1
4	85.7	103.5	129.9	$180-1.2i \cdot 10^{-6}$	230.1
5	74.5	91.6	116.1	$180-2.7i \cdot 10^{-6}$	243.9
6	69.2	85.8	108.3	180	251.7
7	71.6	88.5	111.9	$180+2.7i \cdot 10^{-6}$	248.1
8	80.8	98.3	124.3	180	235.7
9	94	111.8	138	180	222
10	108.1	125.3	148.9	$180-1.2i \cdot 10^{-6}$	211.1
11	120	135.8	156	$180-1.2i \cdot 10^{-6}$	204
12	126	140.8	159.1	$180-1.2i \cdot 10^{-6}$	200.9

azimuth =

	1	2	3	4	5	6	7
1	7.2	19.7	28.5	31.8	28.5	19.7	7.2
2	8.6	24	35.5	39.9	35.5	24	8.6
3	10.1	29.2	44.8	51.4	44.8	29.2	10.1
4	11	33.1	53.1	63	53.1	33.1	11
5	11.3	35	58.2	72.1	58.2	35	11.3
6	11.2	35.4	60	76.3	60	35.4	11.2
7	11.3	35.3	59.3	74.4	59.3	35.3	11.3
8	11.2	34.1	55.5	67	55.5	34.1	11.2
9	10.5	31	48.4	56.2	48.4	31	10.5
10	9.2	26.3	39.3	44.5	39.3	26.3	9.2
11	7.7	21.3	31	34.7	31	21.3	7.7
12	6.8	18.6	26.8	29.8	26.8	18.6	6.8

zenith =

mnth = opt\_path =

1	7.694	2.945	2.089	1.896	2.089	2.945	7.694
2	6.54	2.447	1.72	1.557	1.72	2.447	6.54
3	5.612	2.045	1.419	1.28	1.419	2.045	5.612
4	5.153	1.827	1.25	1.122	1.25	1.827	5.153
5	5.037	1.742	1.176	1.051	1.176	1.742	5.037
6	5.053	1.723	1.154	1.029	1.154	1.723	5.053
7	5.04	1.73	1.163	1.038	1.163	1.73	5.04
8	5.077	1.781	1.212	1.086	1.212	1.781	5.077
9	5.373	1.936	1.337	1.203	1.337	1.936	5.373
10	6.094	2.255	1.577	1.426	1.577	2.255	6.094
11	7.218	2.739	1.936	1.756	1.936	2.739	7.218
12	8.08	3.114	2.213	2.011	2.213	3.114	8.08

Wmnth(mnth) =

4
5
6
7
8
9
10
11
12
1
2
3

Define the parameters that will be output for each month:

I = 7      k := 1..7

OutMatrix<sub>1,k</sub> :=

"Mnth"
"E-S corr"
"daylength (hr)"
"Max Rad"
"Angles Int"
"AvgOPath"
"blank"

OutMatrix<sub>mnth+1,1</sub> := mnth

OutMatrix<sub>mnth+1,2</sub> := Eo(year, cday<sub>mnth</sub>)

OutMatrix<sub>mnth+1,3</sub> := 2 · T<sub>hr</sub>(cday<sub>mnth</sub>) · hr<sup>-1</sup>

OutMatrix<sub>mnth+1,4</sub> := Hor<sub>mnth</sub> · watt<sup>-1</sup> · m<sup>2</sup>

OutMatrix<sub>mnth+1,5</sub> := interval<sub>mnth</sub>

OutMatrix<sub>mnth+1,6</sub> := avg\_opt\_path<sub>mnth</sub>

OutMatrix =

	1	2	3	4	5
1	"Mnth"	"E-S corr"	"daylength (hr)"	"Max Rad"	"Angles Int"
2	1	1.035	9.731	195.506	1.39
3	2	1.026	10.655	257.162	1.522
4	3	1.011	11.834	339.362	1.691
5	4	0.993	13.015	413.732	1.859
6	5	0.978	14.015	463.517	2.002
7	6	0.968	14.528	483.047	2.075
8	7	0.967	14.291	471.861	2.042
9	8	0.975	13.443	431.619	1.92
10	9	0.99	12.322	366.535	1.76
11	10	1.008	11.138	287.312	1.591
12	11	1.024	10.072	215.82	1.439
13	12	1.034	9.483	179.729	1.355

Output data

Write the data to a file:

Separator<sub>k</sub> := 0

WRITEPRN("SolarAngles") := OutMatrix<sup>T</sup>

APPENDPRN("SolarAngles") := Separator<sup>T</sup>

APPENDPRN("SolarAngles") := azimuth<sup>T</sup>

APPENDPRN("SolarAngles") := Separator<sup>T</sup>

APPENDPRN("SolarAngles") := zenith<sup>T</sup>



☑ Error in the avg irrads approx

The finite difference approx to the daily average extraterrestrial flux for a flat surface is

$$\text{HorSum}_{\text{mnth}} := \left( \sum_i k_{\text{ET}}(\text{cday}_{\text{mnth}}, \text{time}_{\text{mnth}, i}) \cdot \text{interval}_{\text{mnth}} \cdot \text{hr} \right) \text{day}^{-1}$$

The percent difference between the summation and the analytical sol'n for the daily average ET flux is less than 1 percent with seven terms in the approximation:

No. of terms: I = 7

$$\left( \frac{\text{HorSum} - \text{Hor}}{\text{Hor}} \right)^T =$$

	1	2	3	4	5	6	7	8	9	10	%
1	0.204	-0.567	-0.784	-0.487	0.118	1.314	2.408	2.35	2.501	2.189	

☑ Error in the avg irrads approx

We can use the daily average extraterrestrial irradiance to determine how much irradiance changes with latitude, to estimate, for example, whether or not a latitude dependence needs to be included for the energy balance of a large basin like the Owens River basin. The current calculation is for lat = 37 deg. The other column of data is saved output from a calculation for 38 degrees. The difference is expressed as percent difference:

Hor <sub>36</sub> :=	202.178	Hor =	m <sup>-2</sup> watt	→	Hor <sub>36</sub> · m <sup>-2</sup> · watt - Hor	=	%
	265.154						
	348.308						
	422.29						
	469.853						
	486.055						
	471.956						
	430.43						
	366.045						
	288.926						
	219.678						
	185.154						

	1
1	195.506
2	257.162
3	339.362
4	413.732
5	463.517
6	483.047
7	471.861
8	431.619
9	366.535
10	287.312
11	215.82
12	179.729

	1
1	3.4
2	3.1
3	2.6
4	2.1
5	1.4
6	0.6
7	0
8	-0.3
9	-0.1
10	0.6
11	1.8
12	3

# APPENDIX E


## Snow and Energy Balance Model Calculation Worksheet

---

**SNOW- & ENERGY BALANCE AS A FUNCTION OF ELEVATION**

This worksheet performs the same snow/energy balance calculations as the "mass & energy balance" model implemented in Arcview for a surface. It reads the same input file. The only difference is that radiation calculations are slightly streamlined because they are not influenced by topography. The radiation calcs are therefore somewhat streamlined, using integral-based calculations of daily extraterrestrial radiation for a flat surface, rather than a summation of irradiances over time. The end result of all these calculations, as calculated in a short program at the bottom of the page, is the "regional ELA" for the prescribed change in temperature and precipitation (set in highlighted regions at bottom of page). Those calculations can be run through once, or twice or more to see how antecedent conditions affect the result.

The source document for the regression data is referenced here. The same document writes output that is used by the Energy & Mass Balance model written in ArcView.

 Reference:D:\Mathcad calcs\M&E balance input calcs\BpCr climate regressions - no writeout.mcd(R)

A subscript for the months of the year (here we start in October):

$i := 1..12$

**Constants to use for checking calculations:**

Particular elevations:	$Z_{Bish} := 1265$	$Z_{Emerald} := 2950$
Example elevations:	$Z_A := 2000$	$Z_B := 3000$
Month:	$I := 1$	
Windspeed:	$W_A := 5$	
Year:	$Yr_A := 0$	
Albedo:	$alb_A := 0.4$	$alb_B := 0.7$
Months for plotting data:	$Mo_A := 1$	$Mo_B := 9$

z =	
	0
	500
	1·10 <sup>3</sup>
	1.5·10 <sup>3</sup>
	2·10 <sup>3</sup>
	2.5·10 <sup>3</sup>
	3·10 <sup>3</sup>
	3.5·10 <sup>3</sup>
	4·10 <sup>3</sup>
	4.5·10 <sup>3</sup>
	5·10 <sup>3</sup>

RH =

	1
1	0.356
2	0.59
3	0.68
4	0.633
5	0.58
6	0.57
7	0.52
8	0.42
9	0.321
10	0.33
11	0.27
12	0.39

Wind =

	1
1	3
2	3
3	3
4	3
5	3
6	3
7	3
8	3
9	3
10	3
11	3
12	3

Tσ=

	1
1	1.478
2	1.589
3	1.8
4	2.256
5	1.894
6	1.75
7	1.933
8	1.744
9	1.456
10	1.022
11	1.017
12	1.222

Cld =

	1
1	0.29
2	0.41
3	0.45
4	0.53
5	0.5
6	0.47
7	0.43
8	0.41
9	0.26
10	0.24
11	0.22
12	0.19

Elevation range for plotting:

Ndex := 20

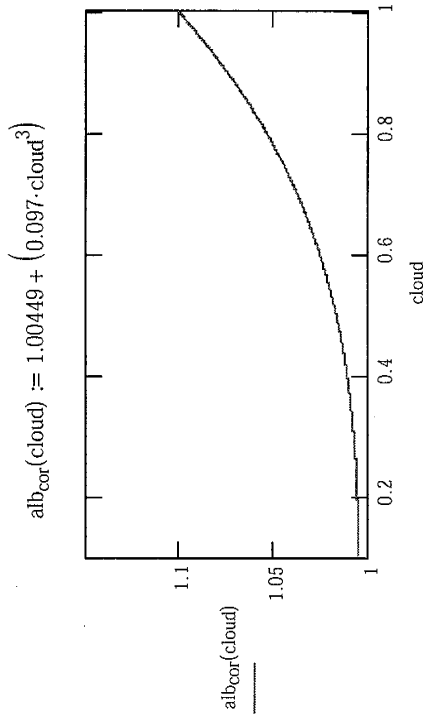
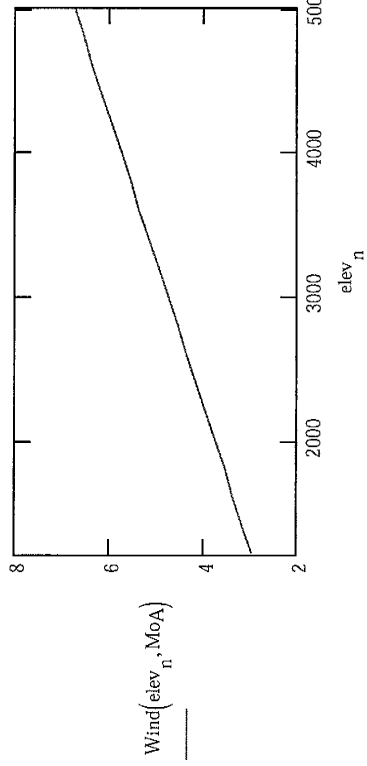
n := 1.. Ndex

elev<sub>n</sub> := 1000 + n· $\frac{4000}{Ndex}$

minZ := min(elev)

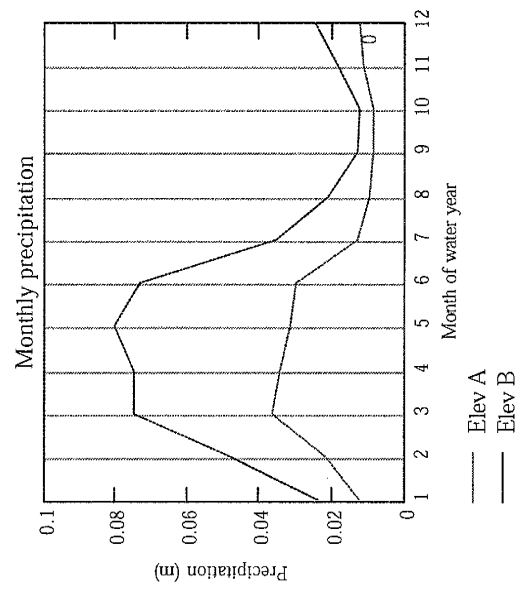
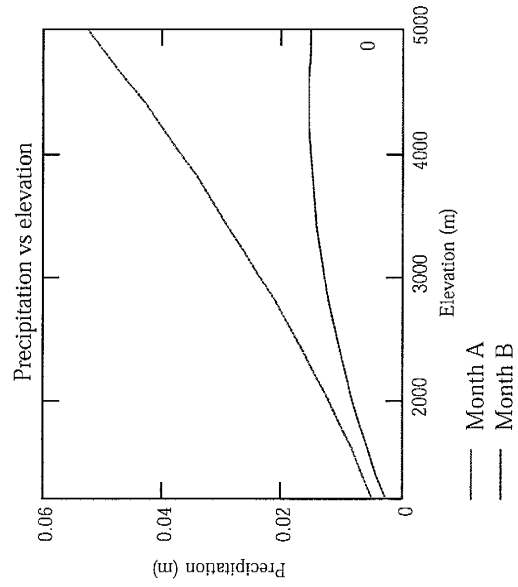
maxZ := max(elev)

$$\text{Wind}(z, \text{mo}) := \text{Wind}_{\text{mo}} + (z - Z_{\text{Bish}}) \cdot 0.001$$



☑ Precipitation

$$P(z, \text{mo}) := \left[ R_p \cdot \sum_{i=1}^3 z^{i-1} \cdot (P_{\text{coeff}})^{i-1} \right] \cdot m$$



☑ Precipitation

11/8/2002

Predict mass balance vs Elev with adjusted T.mcd

Annual precipitation

Annual precipitation by summing the monthly polynomial coefficients.

$$P_{ann}(z) := R_p \cdot \sum_{i=1}^3 z^{i-1} \cdot \sum_{mo=1}^{12} (Pcoeff_{mo,i})_{mo}$$

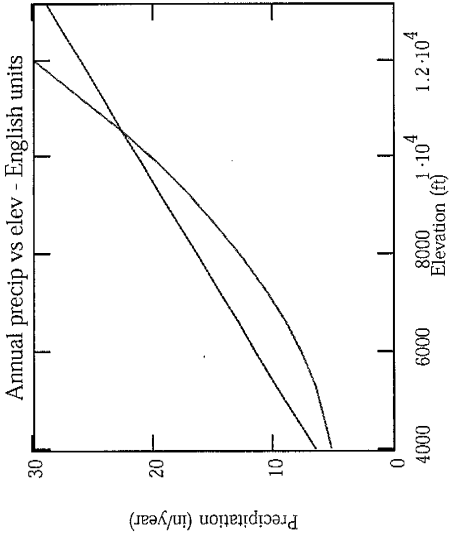
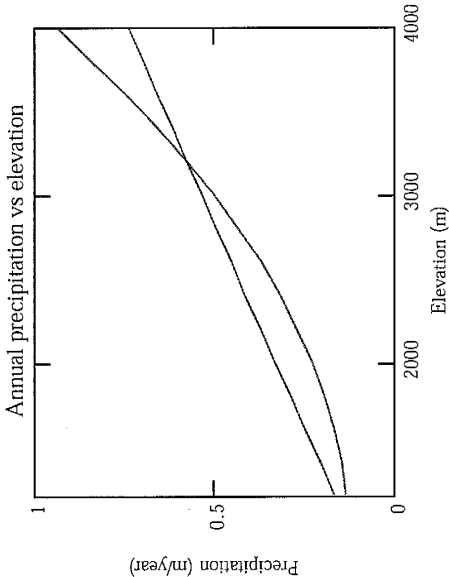
$$i_{poly} := 1..3$$

$$\sum_{mo=1}^{12} Pcoeff_{mo,i_{poly}} =$$

	0.193
	-1.529·10 <sup>-4</sup>
	8.491·10 <sup>-8</sup>

Annual precip from USGS Report 2370-H [Danskin, 1998]

$$P_{USGS}(z) := 0.00245 \cdot z \cdot \frac{m}{ft} - 3.205$$

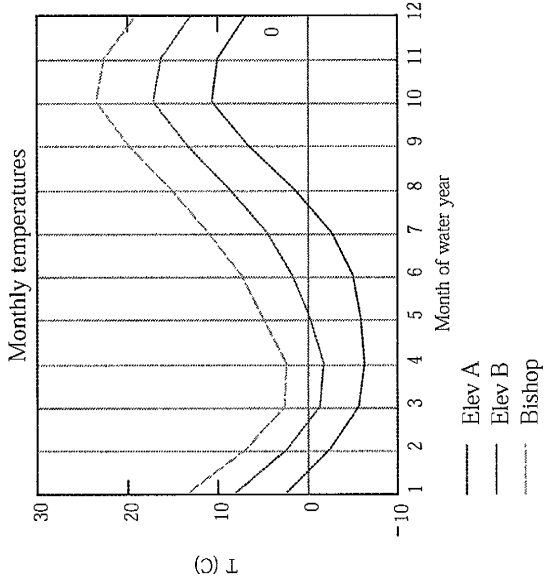
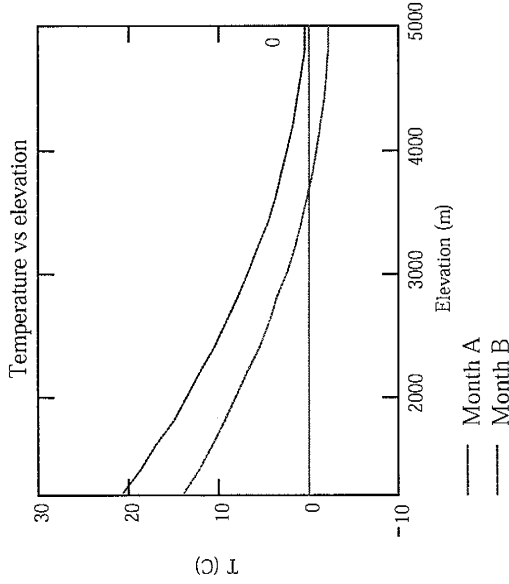


Annual precipitation

Temperature

$$T(z, mo) := \left( L_{coeff}^{(1)} \right)_{mo} + \left[ z \cdot \left( L_{coeff}^{(2)} \right) \right]_{mo} + \left[ z^2 \cdot \left( L_{coeff}^{(3)} \right) \right]_{mo} + \Delta T$$

$$Kelv(z, mo) := T(z, mo) + 273.16$$



$$\Delta T = 0$$

$$R_p = 1$$

```

Buv0(z, mo) :=
Temp ← T(z, mo)
indx1 ← mod(mo + 10, 12) + 1
indx2 ← mod(mo, 12) + 1
SumFrac ← 0
SumTemp ← 0
for j ∈ 1..2
    OtherTemp ← T(z, indxj)
    MidTemp ← 0.5(Temp + OtherTemp)

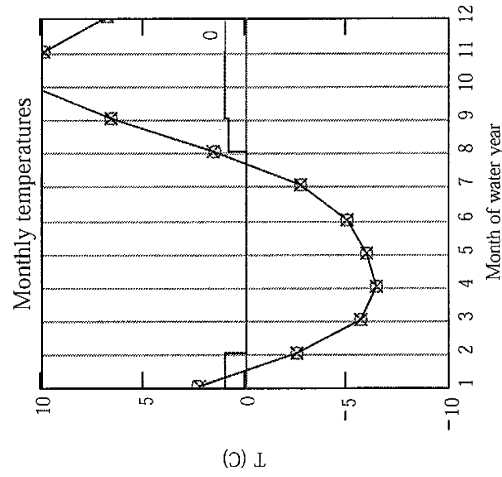
```

$$\begin{aligned}
 & \text{Max} \leftarrow \max(\text{Temp}, \text{MidTemp}) \\
 & \text{Min} \leftarrow \min(\text{Temp}, \text{MidTemp}) \\
 & \text{TempBuv} \leftarrow 0.5 \cdot (\text{MidTemp} + \text{Temp}) \\
 & \text{FracCalc} \leftarrow 0.5 \cdot \left( \frac{\text{Max}}{\text{Max} - \text{Min}} \right) \\
 & \text{TempCalc} \leftarrow \frac{\text{Max}}{2} \\
 & \text{iFrac} \leftarrow \begin{cases} 0.5 & \text{if } \text{Min} > 0 \\ 0 & \text{if } \text{Max} < 0 \end{cases} \\
 & \text{FracCalc} \text{ otherwise} \\
 & \text{iTemp} \leftarrow \begin{cases} \text{TempBuv} & \text{if } \text{Min} > 0 \\ 0 & \text{if } \text{Max} < 0 \end{cases} \\
 & \text{TempCalc} \text{ otherwise} \\
 & \text{SumFrac} \leftarrow \text{SumFrac} + \text{iFrac} \\
 & \text{SumTemp} \leftarrow \text{SumTemp} + \text{iTemp} \cdot \text{iFrac} \\
 & \left( \begin{matrix} \text{SumTemp} \\ \text{SumFrac} \end{matrix} \right)
 \end{aligned}$$



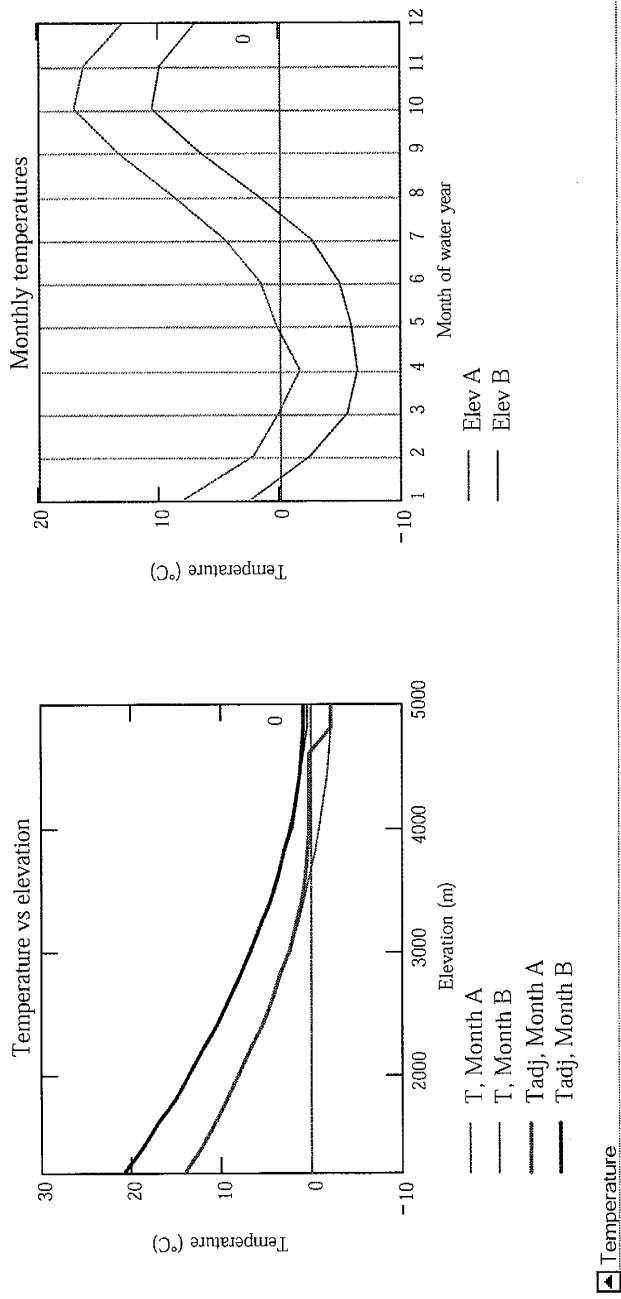
Now adjust temperatures of those months for which only part of the month is above zero to reflect the average temp for the fraction of the month that is above zero.

$$T_{adj}(z, mo) := \text{if}[(Buv0(z, mo)_2 = 1) \vee (Buv0(z, mo)_2 = 0)], T(z, mo), Buv0(z, mo)_1]$$



$i =$	$T(Z_B, i) =$	$Buv0(Z_B, i)_1 =$	$Buv0(Z_B, i)_2 =$	$T_{adj}(Z_B, i) =$
1	2.359	2.291	0.979	2.291
2	-2.571	0	0	-2.571
3	-5.76	0	0	-5.76
4	-6.496	0	0	-6.496
5	-6.034	0	0	-6.034
6	-5.09	0	0	-5.09
7	-2.749	0	0	-2.749
8	1.46	1.619	0.847	1.619
9	6.545	6.403	1	6.545
10	10.495	9.92	1	10.495
11	9.843	9.536	1	9.843
12	6.736	6.578	1	6.736

The adjusted temperature looks a little different:



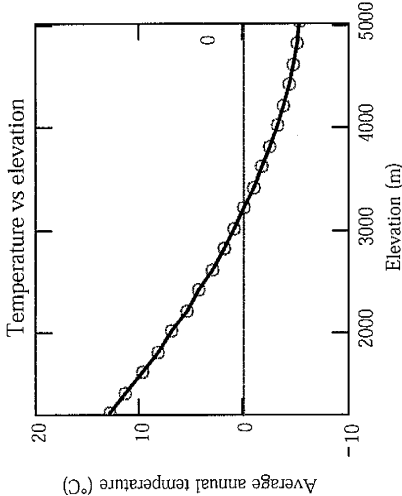
▼ Avg annual temperature

Average annual temperature, WITH CLIMATIC ADJUSTMENT:

$$T_{ann}(z) := \frac{1}{12} \left( \sum_i T(z,i) \right)$$

Avg. annual temperature WITHOUT CLIMATIC ADJUSTMENT  
via summing the monthly polynomial coefficients and dividing  
by 12.

$$T_{ann\_poly}(z) := \sum_{i=1}^3 z^{i-1} \cdot \frac{1}{12} \cdot \left[ \sum_{mo=1}^{12} (L_{coeff}^{(i)})_{mo} \right]$$



Coefficients for the avg annual temp function:

$$i_{poly} := 1..3$$

$$\frac{1}{12} \cdot \sum_{mo=1}^{12} L_{coeff}_{mo,i_{poly}} =$$

24.424
-0.011
9.618 · 10 <sup>-7</sup>

▼ Avg annual temperature

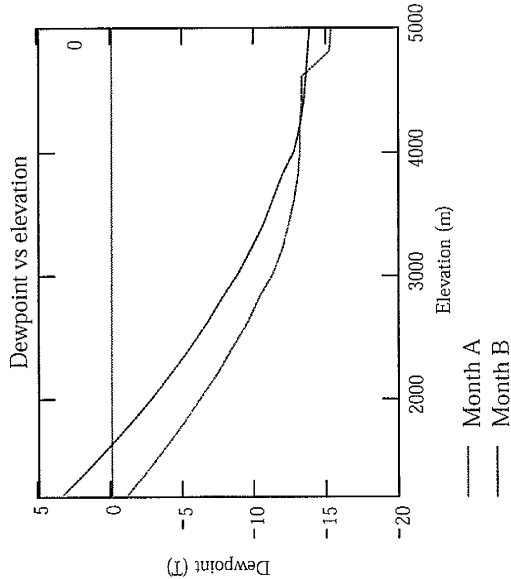
▼ Dewpoint

$$A := 17.3 \quad B := 237.3$$

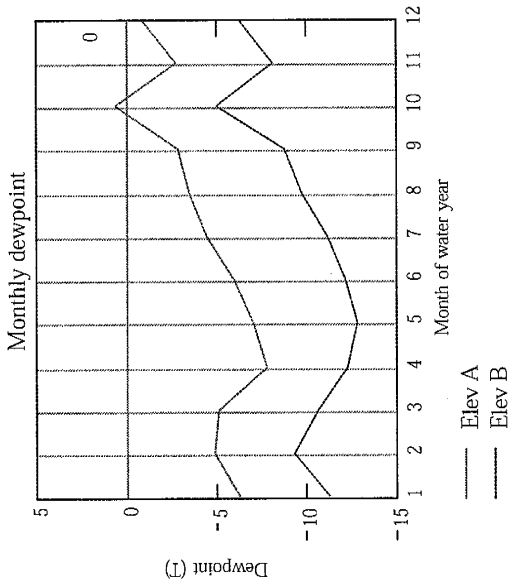
$$T_{\text{dew}}(\text{RH}, T) := \frac{B \cdot \left( \ln(\text{RH}) + \frac{A \cdot T}{T + B} \right)}{A - \left( \ln(\text{RH}) + \frac{A \cdot T}{T + B} \right)}$$

$$T_{\text{dew}}(\text{RH}, T) := \frac{B}{\left( \ln(\text{RH}) + \frac{A \cdot T}{T + B} \right) - 1}$$

$$T_d(Z, \text{mo}) := T_{\text{dew}}(\text{RH}_{\text{mo}}, T_{\text{adj}}(Z, \text{mo}))$$



▼ Dewpoint



▼ Solar rad - sun pos'n link

11/8/2002

E-11

Predict mass balance vs Elev with adjusted T.mcd

➔ Reference:D:\Mathcad calcs\M&E balance input calcs\Sun position with orbital effects - final - no writeout.mcd(R)

lat = 37 deg      year = 0

The above file introduces the range subscript mnth:

It also defines the range subscript i; we redefine it here cuz we need it to range from 1 to 12      i := 1..12

	1
1	195.506
2	257.162
3	339.362
4	413.732
5	463.517
6	483.047
7	471.861
8	431.619
9	366.535
10	287.312
11	215.82
12	179.729

Hor =  $\frac{1}{m^2}$  watt

M<sub>optavg</sub>(cday mnth) =

4.344
3.748
3.266
3.026
2.964
2.971
2.965
2.986
3.141
3.517
4.099
4.543

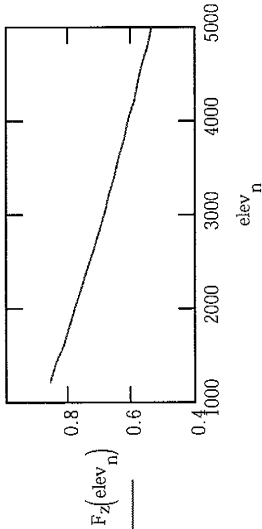
M<sub>opt\_path\_mnth</sub> := M<sub>optavg</sub>(cday mnth)

The solar radiation data is written for month of the calendar year; convert that to month of water year:


$$\begin{aligned} \text{Rearrange}(X) &:= \begin{cases} \text{for } i \in 1..12 \\ \quad j \leftarrow \begin{cases} i+9 & \text{if } i < 4 \\ i-3 & \text{if } i > 3 \end{cases} \\ \quad \text{Temp}_i \leftarrow X_j \end{cases} \\ K_{ET} &:= \text{Rearrange}(\text{Hor}) \\ M_{\text{opt\_path}} &:= \text{Rearrange}(M_{\text{opt\_path}}) \end{aligned}$$

**Optical path length correction for elevation:**

$$H_{\text{scale}} := 8000 \qquad F_z(z_{\text{elev}}) := \exp\left(\frac{-z_{\text{elev}}}{H_{\text{scale}}}\right)$$



$$M_{\text{opt}}(z, \text{mo}) := F_z(z) \cdot M_{\text{opt\_path\_mo}}$$

 [Solar rad - sun pos'n link](#)

▼ Direct irradiance

**Calculation of DIRECT irradiance on a horizontal surface:**

Dewpoint temp (C) of surface,  $T_d$ , is given by a function

Attenuation due to dust:  $\gamma_{\text{dust}} := 0.03$

Precipitable water content of atmosphere (empirically):  
(pressure correction term added)

$$W_p(z, \text{mo}) := F_2(z) \cdot 1.12 \cdot \exp(0.0614 \cdot T_d(z, \text{mo}))$$

Constants for calculation of transmissivity due to water ...:

$$a_{sa}(z, \text{mo}) := -0.124 - 0.0207 \cdot W_p(z, \text{mo})$$

$$b_{sa}(z, \text{mo}) := -0.0682 - 0.0248 \cdot W_p(z, \text{mo})$$

Transmissivity due to water vapor:

$$\tau_{sa}(z, \text{mo}) := \exp(a_{sa}(z, \text{mo}) + b_{sa}(z, \text{mo}) \cdot M_{\text{opt}}(z, \text{mo}))$$

Fudge factor to increase trans with elevation

$$F_{\text{udge}}(z) := \exp\left(\frac{z}{7 \cdot 10^4}\right)$$

This adjustment is aimed at better matching the Klein [1948] data. Should maybe just use the transmissivity polynomial of Klein and skip all the other calcs for tau.

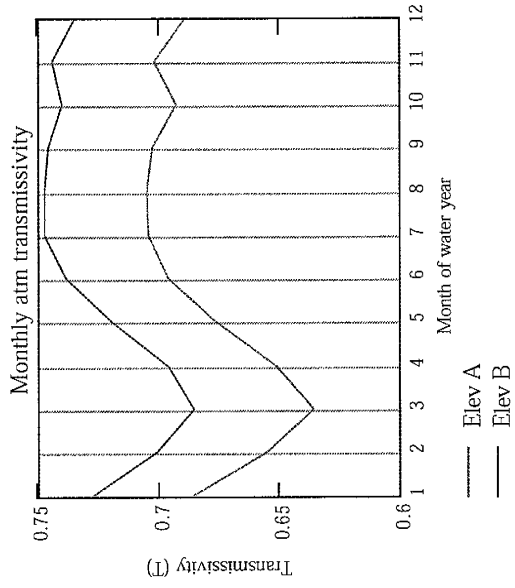
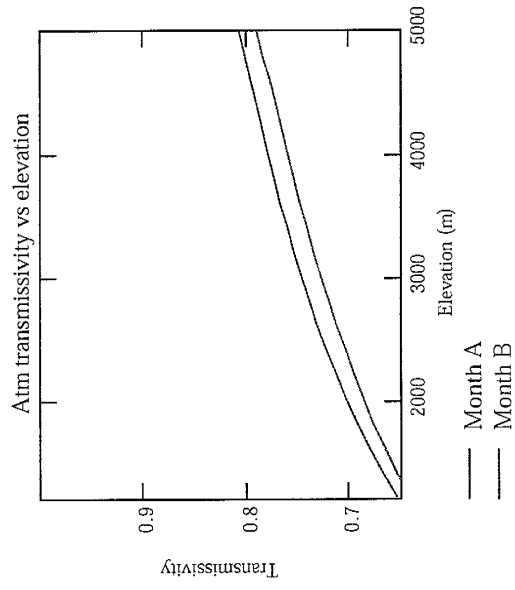
Total transmissivity for direct radiation:

$$\tau(z, \text{mo}) := (\tau_{sa}(z, \text{mo}) - \gamma_{\text{dust}}) \cdot F_{\text{udge}}(z)$$

Daily average flux:

$$K_{\text{dir}}(z, \text{mo}) := (\tau(z, \text{mo}) \cdot K_{\text{ET}})_{\text{mo}}$$

$$\frac{1}{(7 \cdot 10^4)} = 1.429 \times 10^{-5}$$



◀ Direct irradiance

▶ Atm transmissivity comparison



☑ Diffuse & backscattered

**Calculation of DIFFUSE radiant flux on a horizontal surface:**

Constants for calculation of transmissivity due to water ...:  $a_s(z, mo) := -0.0363 - 0.0084 \cdot W_p(z, mo)$   
 $b_s(z, mo) := -0.0572 - 0.0173 \cdot W_p(z, mo)$   
 Atm. transmissivity due to water content:  $\tau_s(z, mo) := \exp(a_s(z, mo) + b_s(z, mo) \cdot M_{opt}(z, mo))$   
 Total attenuation of solar beam producing diffuse radiation:  $\gamma_s(z, mo) := 1 - \tau_s(z, mo) + \gamma_{dust}$   
 Daily average flux:  $K_{diff}(z, mo) := 0.5 \cdot \gamma_s(z, mo) \cdot K_{ET, mo}$

**Calculation of BACKSCATTERED radiant flux to a horizontal surface:**

Daily average flux:  $K_{bs}(alb, z, mo) := \left[ 0.5 \cdot \gamma_s(z, mo) \cdot alb \cdot (K_{dir}(z, mo) + K_{diff}(z, mo)) \right]$

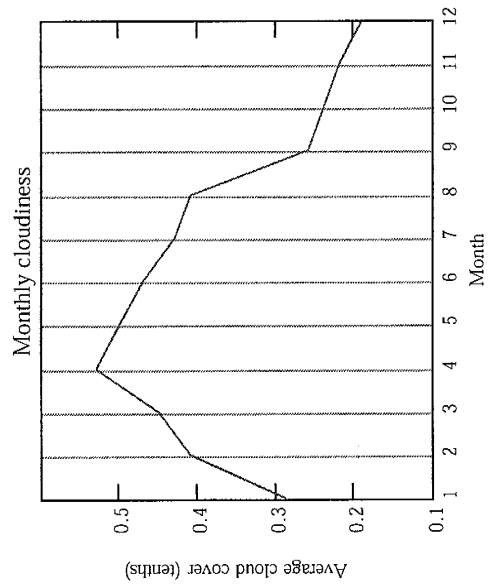
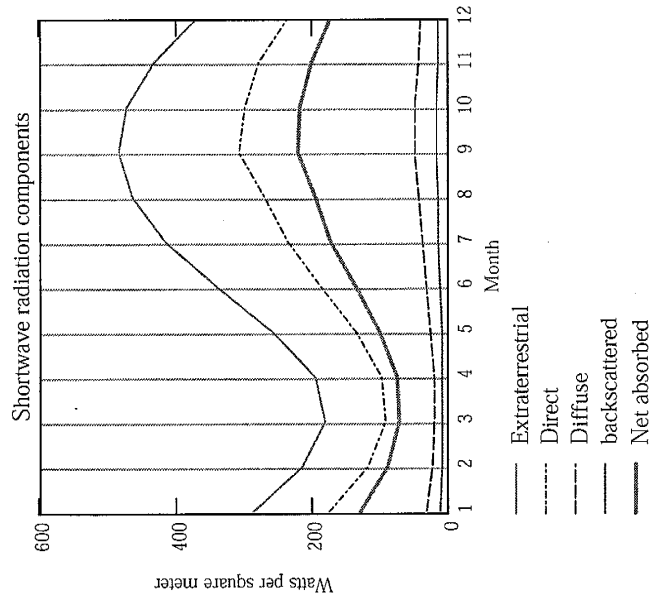
**Oerleman's transmissivity reduction due to cloudiness (expressed in tenths):**  $\tau_c(z, n) := 1 - (0.41 - 0.000065 \cdot z) \cdot n - 0.37 \cdot n^2$

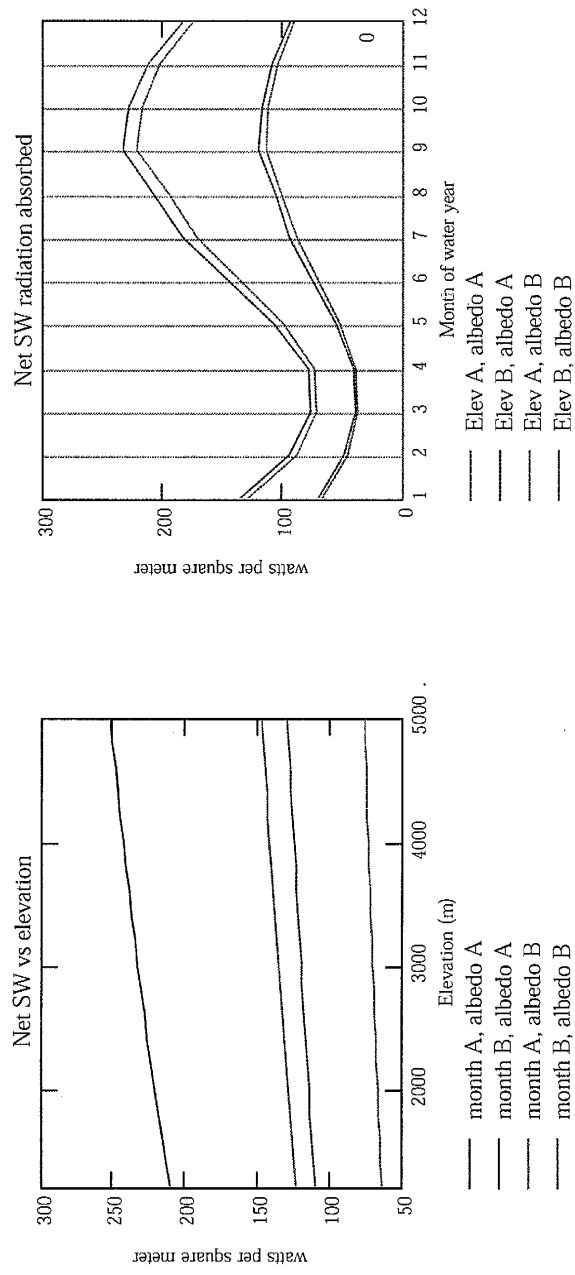
☑ Diffuse & backscattered

☑ Cloudiness & Net SW

**Now add cloudiness factors to the radiation calculations (using equations of Oerlemans):**

$K_{dirC}(z, mo) := \tau_c(z, Cld_{mo}) \cdot \tau(z, mo) \cdot K_{ET, mo}$   
 $K_{diffC}(z, mo) := 0.5 \cdot \gamma_s(z, mo) \cdot \tau_c(z, Cld_{mo}) \cdot K_{ET, mo}$   
 $K_{bsC}(z, mo, albedo) := 0.5 \cdot \gamma_s(z, mo) \cdot albedo \cdot (K_{dirC}(z, mo) + K_{diffC}(z, mo))$   
 $SW_{net}(z, mo, albedo) := (1 - albedo) \cdot (K_{diffC}(z, mo) + K_{diffC}(z, mo) + K_{bsC}(z, mo, albedo))$





Cloudiness & Net SW

▼ Snow vs Rain

For this we need the standard deviation of the variance of the monthly temperature; for lack of more data we'll assume its constant across the elevation range of interest. The following program calculates the probability that the value of variable that is normally distributed is below a given value,  $Z$ .  $J$  is the number of terms in the summation that represents the integration.

$$\begin{aligned} \text{Prob}(Z, J) &\equiv \begin{aligned} &U \leftarrow |Z| \\ &Y \leftarrow U^2 \\ &I \leftarrow U \\ &\text{for } j \in 1..J \\ &\quad \left| \begin{aligned} &U \leftarrow -U \cdot Y \cdot \frac{(2 \cdot j - 1)}{[2 \cdot j \cdot (2 \cdot j + 1)]} \\ &I \leftarrow I + U \end{aligned} \right. \\ &I \leftarrow \frac{I}{\sqrt{2 \cdot \pi}} \\ &P \leftarrow \begin{cases} 0.5 - I & \text{if } Z < 0 \\ 0.5 + I & \text{otherwise} \end{cases} \\ &P \leftarrow \begin{cases} 1 & \text{if } P > 1 \\ 0 & \text{if } P < 0 \end{cases} \end{aligned} \end{aligned}$$

$$T_{\text{crit}} := 2$$

$$\text{SnowFrac}(z, \text{mo}) := \text{Prob} \left( \frac{T_{\text{crit}} - T_{\text{adj}}(z, \text{mo})}{T_{\sigma_{\text{mo}}}}, 14 \right)$$

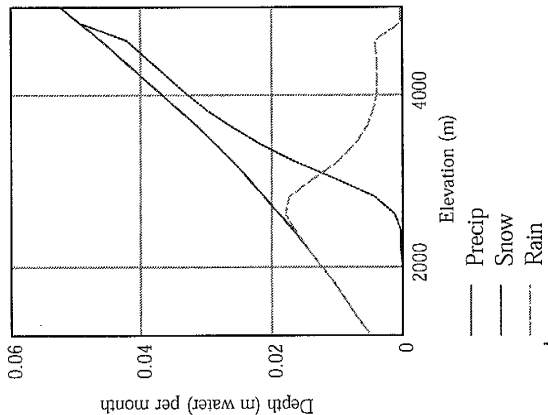
$$\text{Ice}(z, \text{mo}) := \text{SnowFrac}(z, \text{mo}) \cdot P(z, \text{mo})$$

$$\text{Rain}(z, \text{mo}) := (1 - \text{SnowFrac}(z, \text{mo})) \cdot P(z, \text{mo})$$

$T_{\text{adj}}(Z_A, i)$	7.857
	2.223
	0.017
	-1.841
	0.119
	1.532
	4.495
	8.587
	13.343
	16.984
	16.209
	12.798

$T_{\sigma_i}$	1.478
	1.589
	1.8
	2.256
	1.894
	1.75
	1.933
	1.744
	1.456
	1.022
	1.017
	1.222

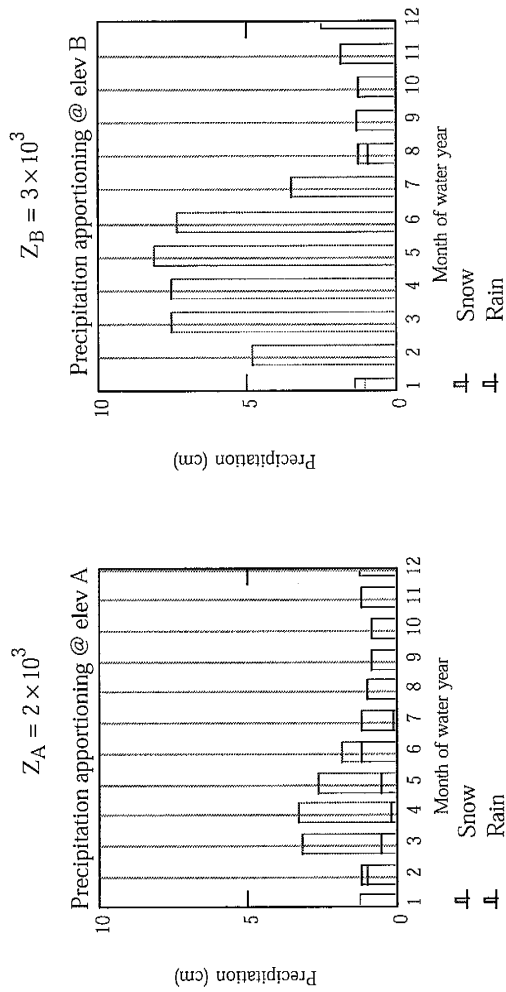
$\text{SnowFrac}(Z_A, i)$	0
	0.444
	0.865
	0.956
	0.84
	0.605
	0.098
	0
	0
	0
	0
	0



$\text{Ice}(Z_A, i) =$	0
	$9.421 \cdot 10^{-3}$
	0.031
	0.032
	0.026
	0.018
	$1.242 \cdot 10^{-3}$
	0
	0
	0
	0
	0

$\text{Rain}(Z_A, i) =$	0.012
	0.012
	$4.88 \cdot 10^{-3}$
	$1.502 \cdot 10^{-3}$
	$5.009 \cdot 10^{-3}$
	0.012
	0.011
	$9.759 \cdot 10^{-3}$
	$8.242 \cdot 10^{-3}$
	$8.163 \cdot 10^{-3}$
	0.011
	0.012

$P(Z_A, i) =$	0.012
	0.021
	0.036
	0.034
	0.031
	0.03
	0.013
	$9.759 \cdot 10^{-3}$
	$8.242 \cdot 10^{-3}$
	$8.163 \cdot 10^{-3}$
	0.011
	0.012



☐ Snow vs Rain

▢ Specific basin precip calcs

▢ Oerlemans LW radiation (unused)

Idso-Jackson-Ohmura Longwave

Stefan constant:  $\sigma := 5.7 \cdot 10^{-8} \cdot \text{watt} \cdot \text{m}^{-2}$

Emissivity for snow:  $\epsilon_{\text{snow}} := 0.99$

Idso-Jackson equation for atmospheric emissivity:  
[Male and Granger, 1981]

$$\epsilon_{\text{atm}}(T) := 1 - 0.261 \cdot \exp\left[-7.77 \cdot 10^{-4} \cdot (273 - T)^2\right]$$

Ohmura's [Arnold, 1996] expression for increase in longwave due to cloudcover (n) expressed in tenths:

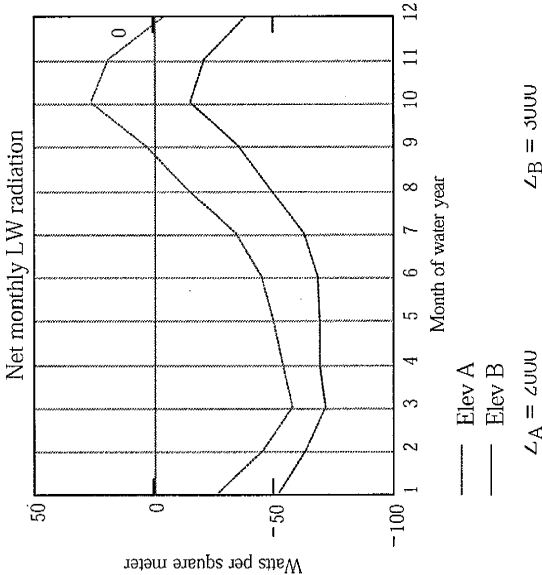
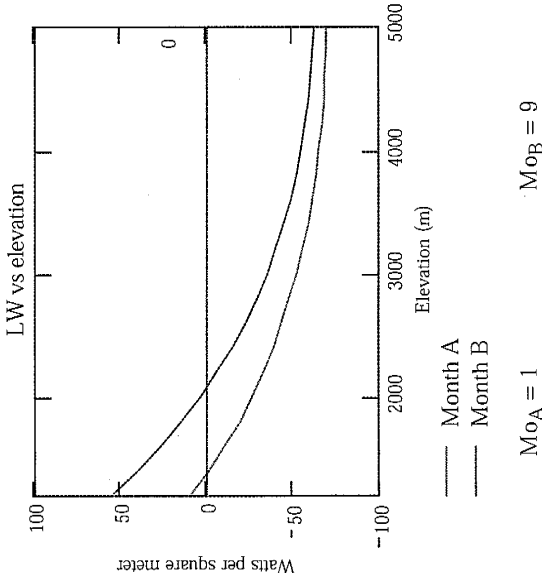
$$k_A := 0.26 \qquad F\epsilon_{\text{Ohm}}(n) := (1 + k_A \cdot n)$$

Resultant irradiation at the surface (watts/m<sup>2</sup>)  
Includes term for LW increase due to cloudiness:

$$L_{\text{inJ}}(T, n) := F\epsilon_{\text{Ohm}}(n) \cdot \epsilon_{\text{atm}}(T) \cdot \sigma \cdot T^4$$

$$LW_{\text{net}}(z, \text{mo}) := L_{\text{inJ}}(\text{Kelv}(z, \text{mo}), \text{Cld}_{\text{mo}}) - \epsilon_{\text{snow}} \cdot \sigma \cdot 273.16^4$$

$$LW_{\text{net}}(Z_A, 1) = -26.82 \frac{\text{kg}}{\text{s}^3}$$



### After Paterson [1994] (mostly):

The final function for sensible heat includes a 30% increase for ice versus snow. Low albedo is the trigger for calculating as if surface is ice:

$$\text{alb}_{\text{trig}} := 0.5$$

$$\text{alb}_{\text{ice\_mult}} := 1.3$$

$$c_p, \text{ specific heat capacity: } c_p := 1010 \cdot \text{joule} \cdot \text{kg}^{-1} \cdot \text{K}^{-1}$$

$$\text{Std. air density: } \rho_o := 1.29 \cdot \text{kg} \cdot \text{m}^{-3}$$

$$\text{Density calculation: } \rho_{\text{air}}(z) := F_z(z) \cdot \rho_o$$

$$\text{Transfer coefficient: } k_{\text{MD}} := 0.0015$$

$$\text{Adjusted upward when surface is ice: } k_{\text{bulk}}(\text{alb}) := \text{if}(\text{alb} < \text{alb}_{\text{trig}}, k_{\text{MD}} \cdot \text{alb}_{\text{ice\_mult}}, k_{\text{MD}})$$

$$\text{Fudge factor adjustment to temp: } T_{\text{offset}} := 2.1$$

$$\text{Temperature of ice surface: } T_s(T) := \text{if}(T > 0, 0, T)$$

$$\text{Bulk transfer latent heat flux equation: } H_P(T, u, z, \text{albedo}) := \rho_{\text{air}}(z) \cdot c_p \cdot k_{\text{bulk}}(\text{albedo}) \cdot \left( u \cdot \frac{\text{m}}{\text{sec}} \right) \cdot (T + T_{\text{offset}} - T_s(T)) \cdot \text{K}$$

$$\text{Written for monthly input: } H(z, \text{mo}, \text{albedo}) := H_P(T_{\text{adj}}(z, \text{mo}), \text{Wind}(z, \text{mo}), z, \text{albedo})$$

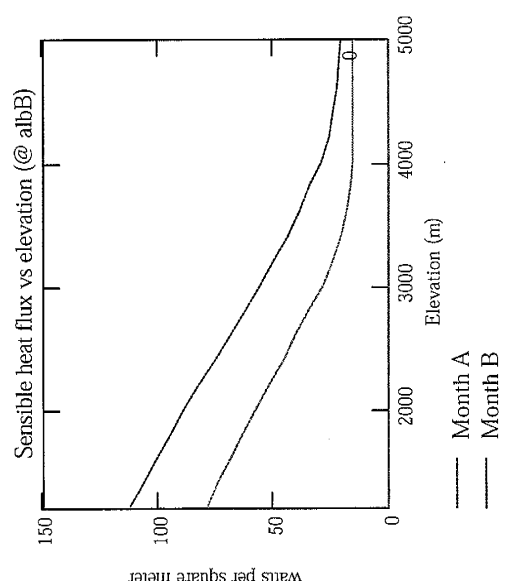
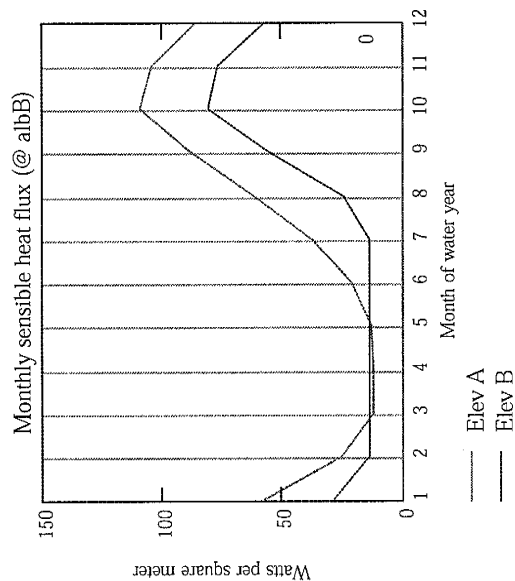
$$\rho_{\text{air}}(Z_{\text{Emerald}}) = 0.892 \frac{\text{kg}}{\text{m}^3}$$

$$T(1750, 10) = 19.022$$

$$H(1750, 10, \text{alb}_B) = 115.595 \frac{\text{watt}}{\text{m}^2}$$

$$\text{Wind}(1750, 10) = 3.485$$

$$\text{alb}_B = 0.7$$



$M_{oA} = 1$ 
 $M_{oB} = 9$

$Z_A = 2000$ 
 $Z_B = 3000$

Sensible heat flux



Latent heat flux

0 Kelvin:  $T' := 273.16$

Std air pressure:  $P_o := 1\text{-atm}$

$e_a$ , atm vapor pressure (Pa):  $e_a(T, RH) := RH \cdot p' \cdot \exp\left[19.85 \cdot \left(1 - \frac{T'}{T + T'}\right)\right]$  For T in Celsius

$e_s$ , surface vapor pressure (Pa):  $e_{\text{iceS}}(T) := \text{if}\left[T < 0, p' \cdot \exp\left[22.47 \cdot \left(1 - \frac{273.16}{T + T'}\right)\right], p'\right]$

Vapor pressure difference (Pa):  $de(T, RH) := e_a(T, RH) - e_{\text{iceS}}(T)$

Specific humidity difference  $dq(T, RH, z) := \frac{0.622}{F_z(z) \cdot P_o} \cdot de(T, RH)$  (kg/kg):

Note that the elevation dependence of air pressure here cancels with the same correction for the air density included in the ultimate latent heat energy calculation.

Energy involved in transfer:  $L(\text{grad}, T) := \text{if}(\text{grad} > 0.0 \wedge T > 0\text{-C}, L_v, L_v + L_f)$

Bulk transfer equation for latent heat flux (incorporates increase over ice as discussed above):

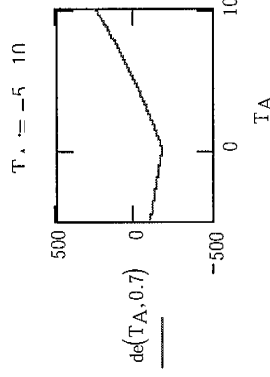
$$LvEvap(T, RH, u, z, \text{albedo}) := \rho_{\text{air}}(z) \cdot k_{\text{bulk}}(\text{albedo}) \cdot L(dq(T, RH, z), T) \cdot \left(u \cdot \frac{m}{\text{sec}}\right) \cdot dq(T, RH, z)$$

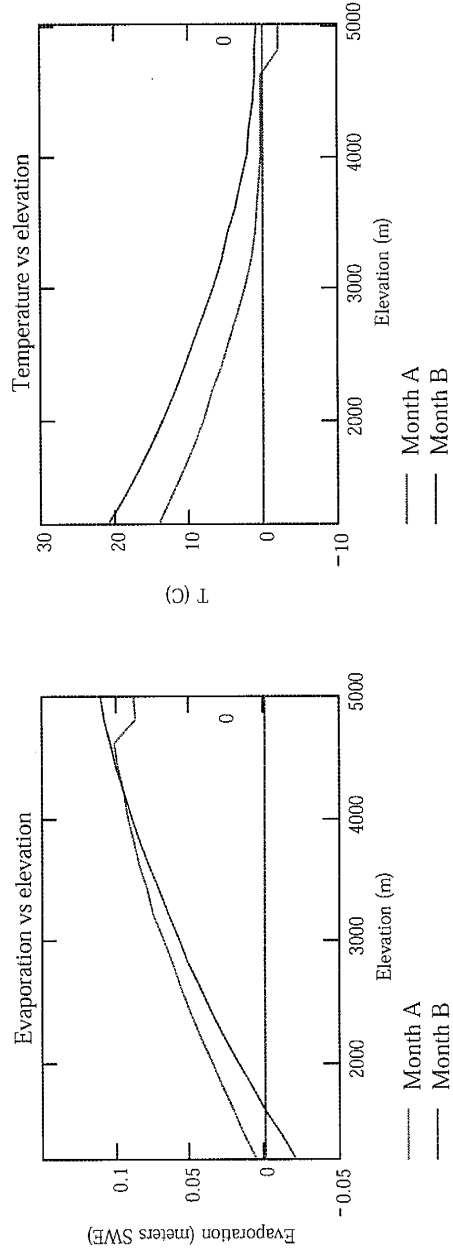
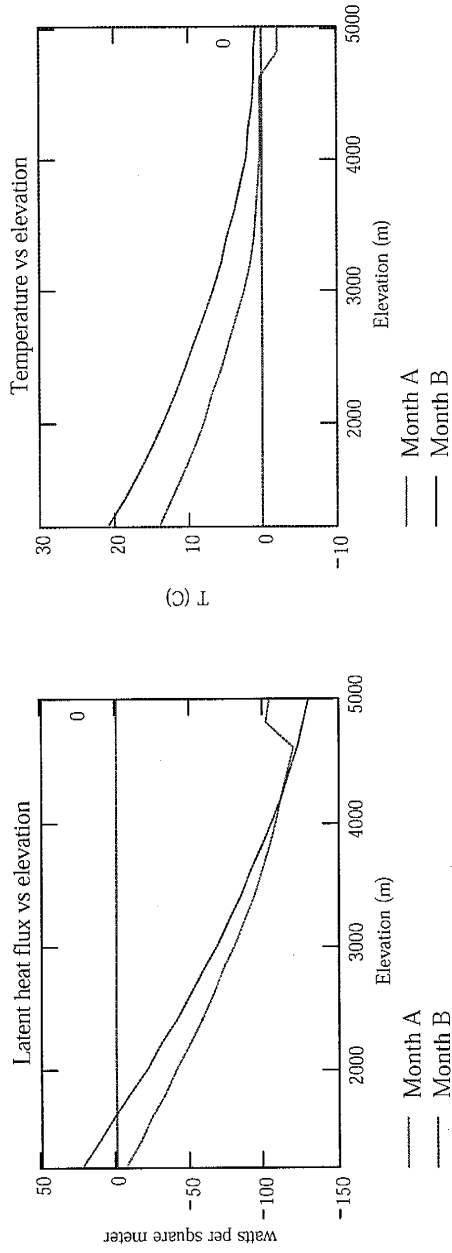
Same rewritten to minimize independent variables:

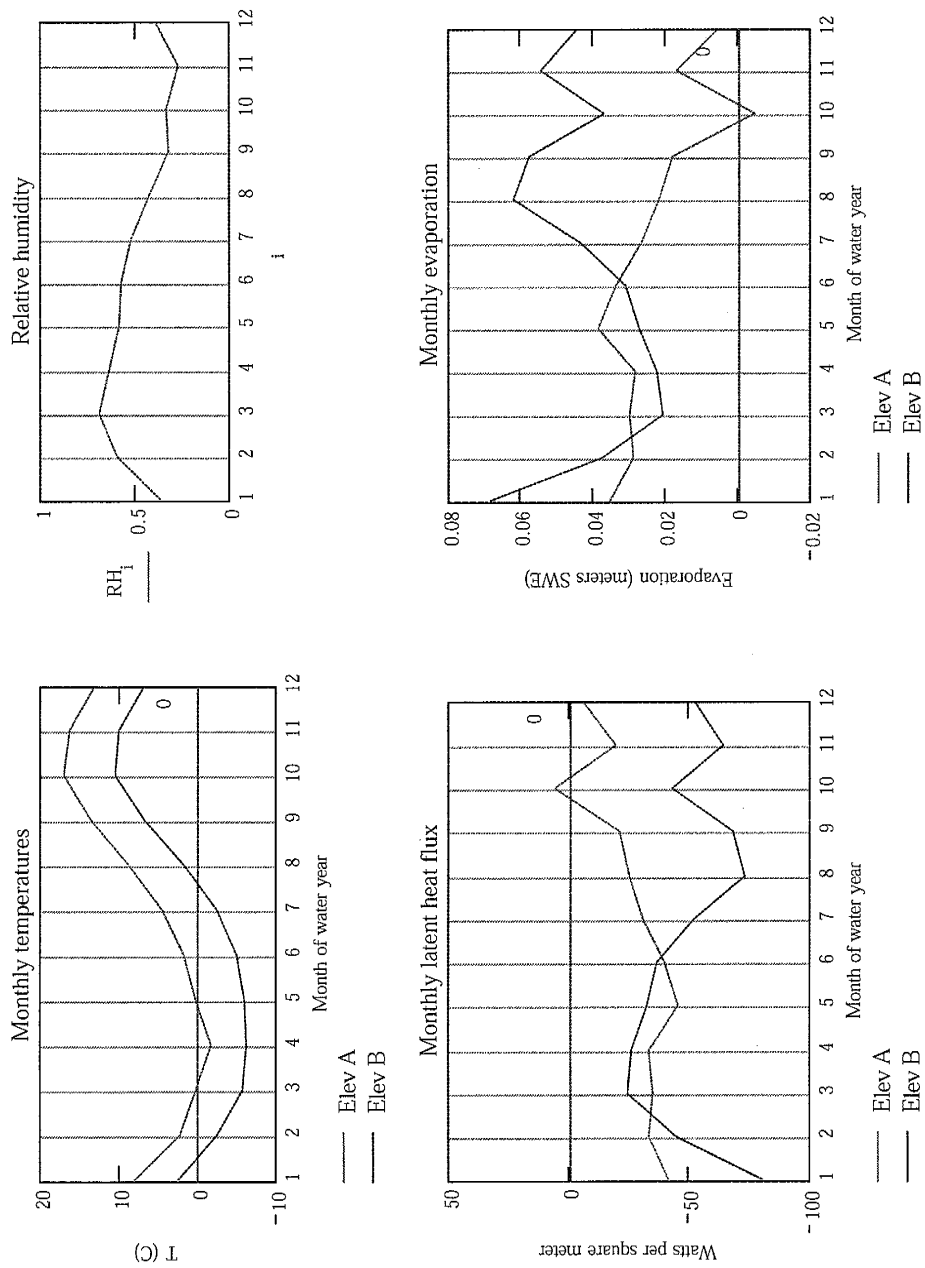
$$LvE(z, \text{mo}, \text{albedo}) := LvEvap(T_{\text{adj}}(z, \text{mo}), RH_{\text{mo}}, Wind(z, \text{mo}), z, \text{albedo})$$

Ice mass evaporated and/or sublimated (**m water**):

$$Evap(z, \text{mo}, \text{albedo}) := -LvE(z, \text{mo}, \text{albedo}) \cdot \text{SecPerMo} \cdot L(dq(T_{\text{adj}}(z, \text{mo}), RH_{\text{mo}}, z), T_{\text{adj}}(z, \text{mo}))^{-1} \cdot \rho_{\text{water}}^{-1}$$



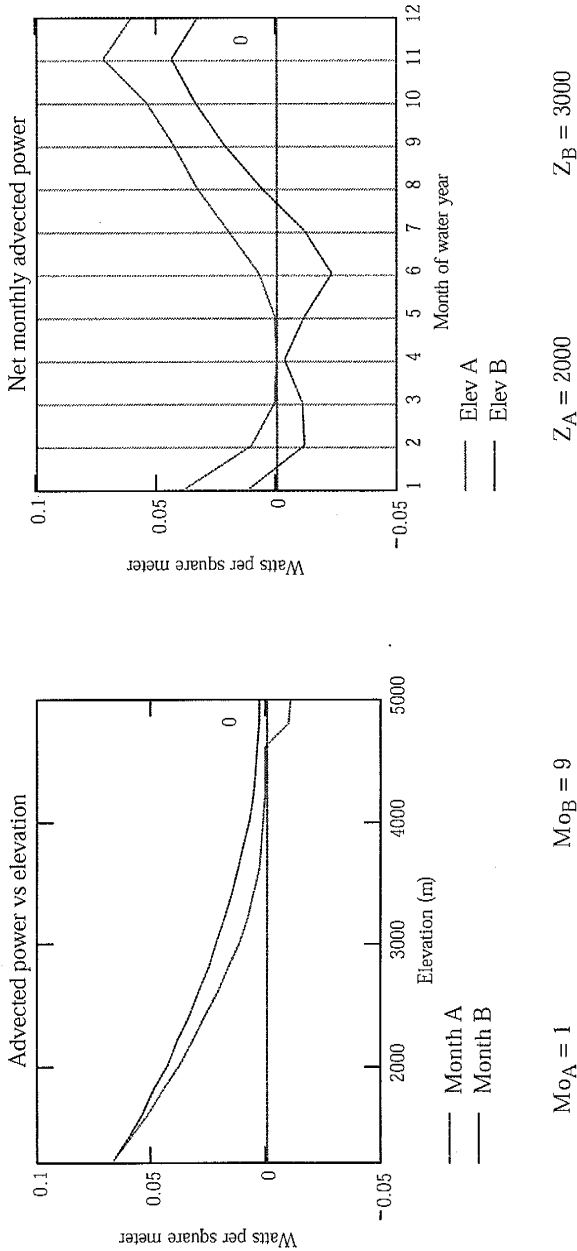




Latent heat flux

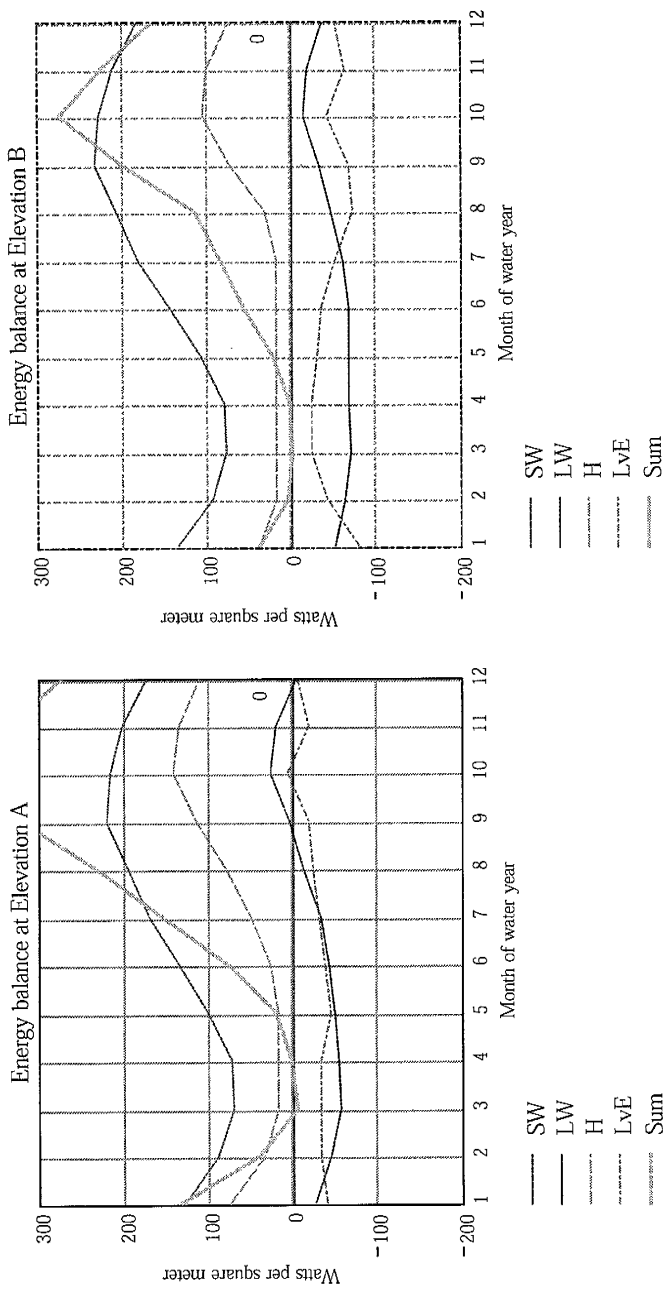
Advised via RAIN

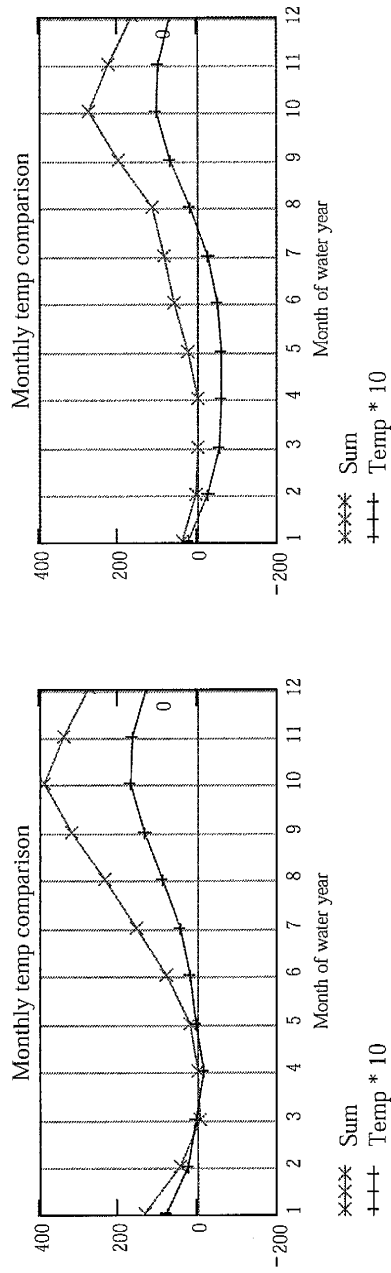
$$\text{Advec}(z, \text{mo}) := \frac{\text{Rain}(Z_A, \text{mo}) \cdot \rho_{\text{water}} \cdot T_{\text{adj}}(z, \text{mo}) \cdot K \cdot C_p}{30 \cdot \text{day}}$$



Advised via RAIN

$$\text{Sum}(z, \text{mo}, \text{albedo}) := \text{SWnet}(z, \text{mo}, \text{albedo}) + \text{LWnet}(z, \text{mo}) + \text{H}(z, \text{mo}, \text{albedo}) + \text{LvE}(z, \text{mo}, \text{albedo}) + \text{Advec}(z, \text{mo})$$





Monthly energy flux & melt

$$\text{Sum}(z, \text{mo}, \text{albedo}) := \text{SWnet}(z, \text{mo}, \text{albedo}) + \text{LWnet}(z, \text{mo}) + \text{H}(z, \text{mo}, \text{albedo}) + \text{LvE}(z, \text{mo}, \text{albedo}) + \text{Advvec}(z, \text{mo})$$

$$\text{Melt}(z, \text{mo}, \text{albedo}) := \max \left( \frac{\text{Sum}(z, \text{mo}, \text{albedo}) \cdot 30 \cdot \text{day}}{L_f \cdot \rho_{\text{water}}}, 0 \right)$$

$$\text{Ablate}(z, \text{mo}, \text{albedo}) := \text{Melt}(z, \text{mo}, \text{albedo}) + \text{Evap}(z, \text{mo}, \text{albedo})$$

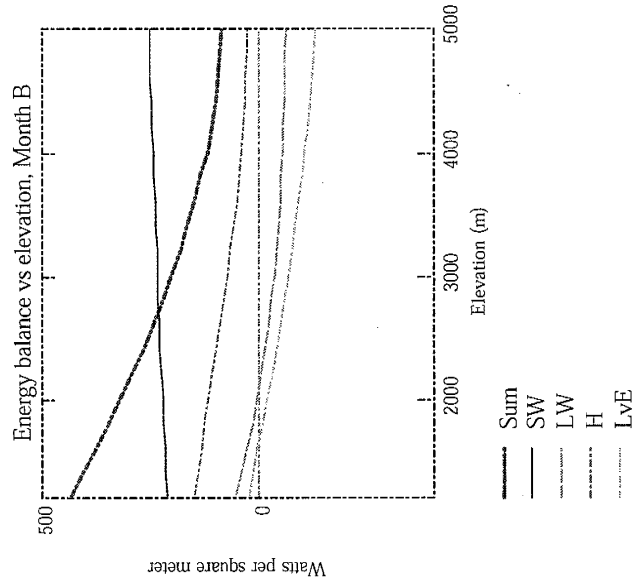
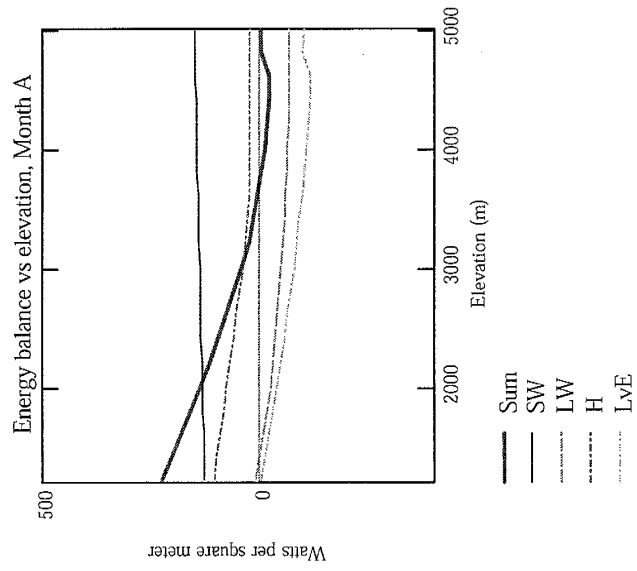
$\text{Sum}(Z_A, i, \text{alb}_A)$	$\text{Melt}(Z_A, i, \text{alb}_A)$	$\text{Evap}(Z_A, i, \text{alb}_A)$	$\text{Ablate}(Z_A, i, \text{alb}_A)$
133.082 $\frac{\text{kg}}{\text{s}}$	1.033 m	0.035 m	1.068 m
40.207 $\frac{\text{kg}}{\text{s}}$	0.312	0.028	0.341
-7.08	0	0.03	0.03
-0.191	0	0.028	0.028
19.332	0.15	0.038	0.188
76.87	0.597	0.034	0.63
153.562	1.192	0.026	1.218
232.576	1.805	0.021	1.826

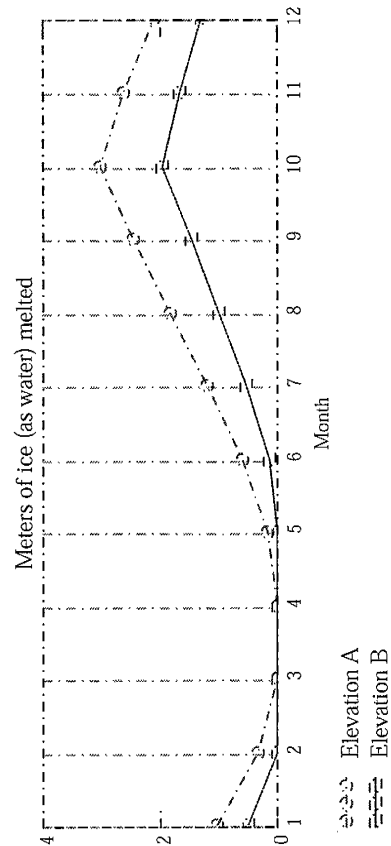
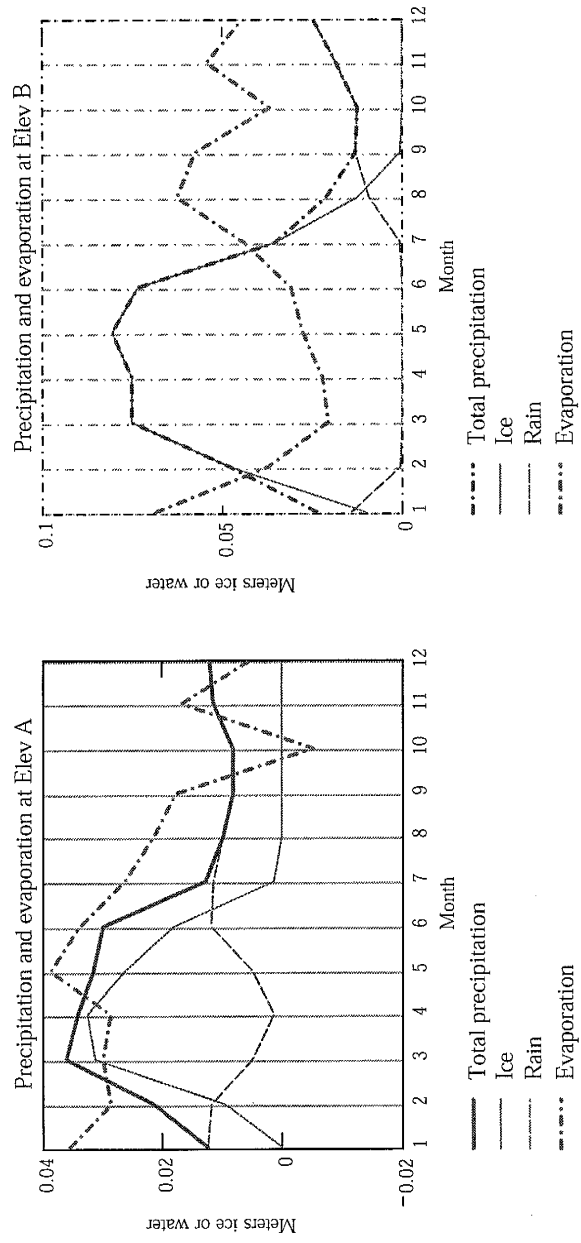
316.837
388.778
335.551
270.508

2.459
3.017
2.604
2.099

0.018
$-5.071 \cdot 10^{-3}$
0.017
$4.805 \cdot 10^{-3}$

2.477
3.012
2.621
2.104





Monthly energy flux & melt



$$\text{Avg\_SWnet}(z, \text{alb}) := \sum_{i=1}^{12} \frac{\text{SWnet}(z, i, \text{alb})}{12}$$

$$\text{Avg\_SWnet}(Z_A, \text{alb}_A) = 147.228 \frac{\text{kg}}{\text{s}}$$

$$\text{Avg\_LWnet}(z) := \sum_{i=1}^{12} \frac{\text{LWnet}(z, i)}{12}$$

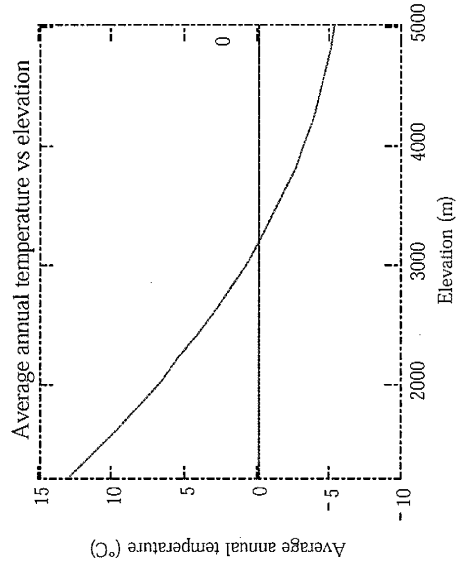
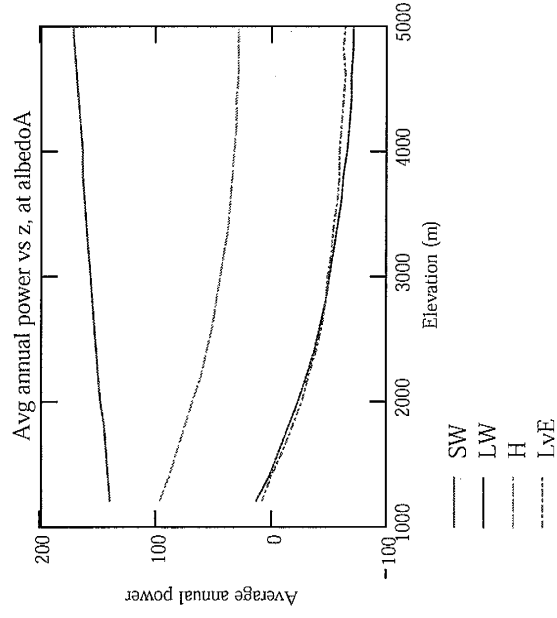
$$\text{Avg\_LWnet}(Z_A) = -23.87 \frac{\text{kg}}{\text{s}}$$

$$\text{Avg\_H}(z, \text{alb}) := \sum_{i=1}^{12} \frac{\text{H}(z, i, \text{alb})}{12}$$

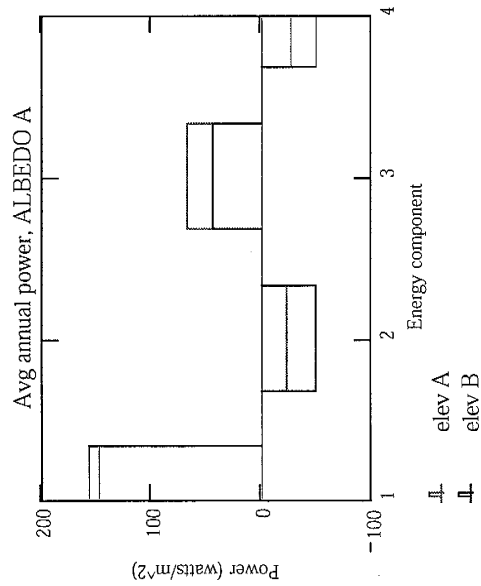
$$\text{Avg\_H}(Z_A, \text{alb}_A) = 67.353 \frac{\text{kg}}{\text{s}}$$

$$\text{Avg\_LvE}(z, \text{alb}) := \sum_{i=1}^{12} \frac{\text{LvE}(z, i, \text{alb})}{12}$$

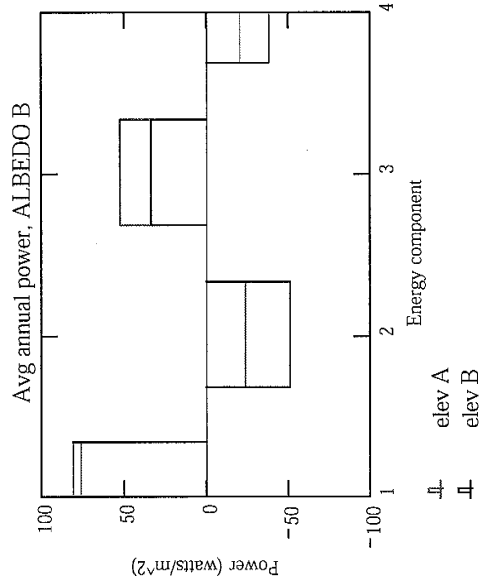
$$\text{Avg\_LvE}(Z_A, \text{alb}_A) = -27.402 \frac{\text{kg}}{\text{s}}$$



$$\begin{aligned}
 & \text{Avdex} := 1..4 & \text{AvgMatrix}(z, \text{alb}) := & \begin{pmatrix} \text{Avg\_SWnet}(z, \text{alb}) \\ \text{Avg\_LWnet}(z) \\ \text{Avg\_H}(z, \text{alb}) \\ \text{Avg\_LvE}(z, \text{alb}) \end{pmatrix}
 \end{aligned}$$



alb<sub>A</sub> = 0.4      alb<sub>B</sub> = 0.7  
 Z<sub>A</sub> = 2000      Z<sub>B</sub> = 3000



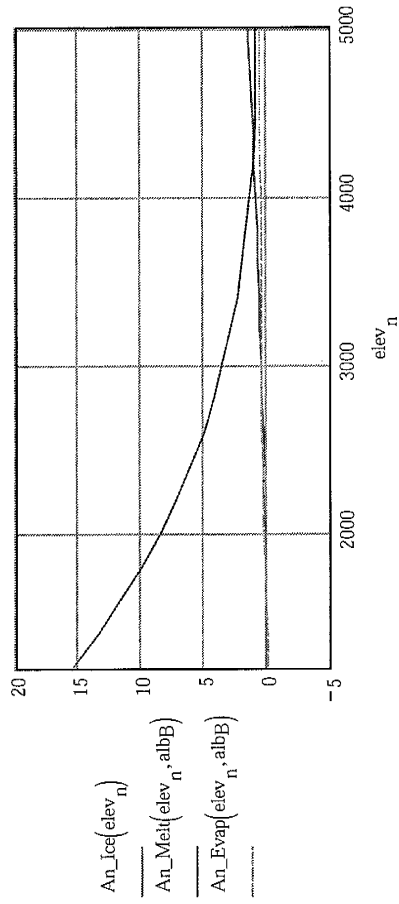
alb<sub>A</sub> = 0.4      alb<sub>B</sub> = 0.7  
 Z<sub>A</sub> = 2000      Z<sub>B</sub> = 3000

Net annual flux and melt

$$An\_Melt(z, alb) := \sum_{i=1}^{12} Melt(z, i, alb) \quad An\_Melt(Z_A, alb_A) = 15.267 \text{ m}$$

$$An\_Ice(z) := \sum_{i=1}^{12} Ice(z, i) \quad An\_Ice(Z_A) = 0.118 \text{ m}$$

$$An\_Evap(z, alb) := \sum_{i=1}^{12} Evap(z, i, alb) \quad An\_Evap(Z_A, alb_A) = 0.275 \text{ m}$$



$$\text{An\_Accum1}(z, \text{alb}) := \text{An\_Ice}(z) - \text{An\_Melt}(z, \text{alb})$$

$$\text{An\_Accum1}(Z_A, \text{alb}_A) = -15.149 \text{ m}$$

$$\text{HiAlb} := 0.7$$

$$\text{LoAlb} := 0.4$$

$$\text{An\_Accum2}(z, \text{Nmo}) :=$$

```

    alb ← LoAlb
    sum ← Ice(z, 1) - Melt(z, 1, alb)
    for i ∈ 1.. Nmo - 1
        j ← mod(i, 12) + 1
        alb ←  $\begin{cases} \text{HiAlb} & \text{if } \text{sum} > 0 \\ \text{LoAlb} & \text{otherwise} \end{cases}$ 
        alb ← alb · albcor(Cldj)
        sum ← 0 if j = 1
        accum ←  $\begin{cases} \text{Ice}(z, j) - \text{Evap}(z, j, \text{alb}) & \text{if } T_{\text{adj}}(z, j) < 0 \\ \text{Ice}(z, j) - \text{Melt}(z, j, \text{alb}) \cdot \text{Buv0}(z, j) - \text{Evap}(z, j, \text{alb}) & \text{otherwise} \end{cases}$ 
        sum ← sum + accum
    sum

```

$$\text{An\_Accum2}(Z_A, 12) = -15.234 \text{ m}$$

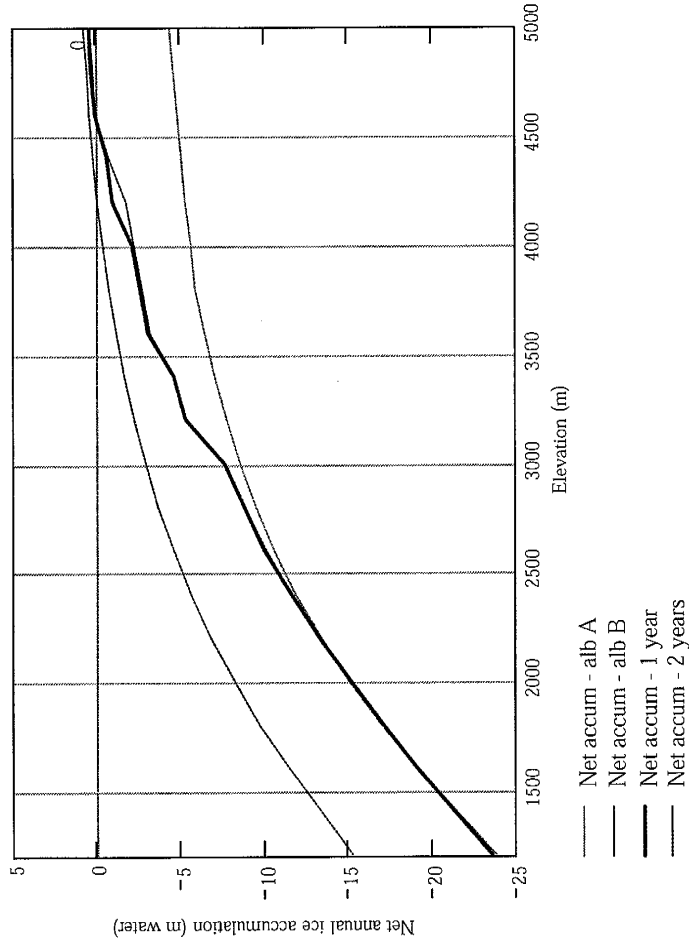
$$\text{An\_Accum2}(Z_A, 24) = \blacksquare$$

$$\text{An\_Accum2}(Z_A, 36) = \blacksquare$$

Net annual flux and melt

$$alb_A = 0.4$$

$$alb_B = 0.7$$



$$R_p \equiv 1$$

$$\Delta T \equiv -0$$

$$\text{ForInterp}_n \equiv \text{An\_Accum2}(\text{elev}_n, 12)$$

$$\text{ELA} \equiv \text{linterp}(\text{ForInterp}, \text{elev}, 0)$$

$$\text{ELA} = 4584$$

Modern ELA comes out to 4584 m after slight changes to LvE for sub vs evap function for L..  
 Modern ELA comes out to 4774 m with Idso-Jackson Ohmura longwave & bulktrans increase for LvE too.  
 Modern ELA comes out to ~5000 m with Idso-Jackson Ohmura longwave  
 Modern ELA comes out to 4175 m with Oerlemans longwave  
 ELA at 11 ka (greater summer inso) comes out to \_\_\_\_ m

Mutual dependence of T and accumulation at the ELA, according to Ohmura et al. [1992] (in Seltzer, 1994) is between  $2.5$  and  $3.3 \times 10^{-3} \text{ } ^\circ\text{C}/\text{mm}$ .

▼ Constants and conversions

$L_f$ , latent heat of fusion:	$L_f \equiv 3.34 \cdot 10^5 \cdot \text{joule} \cdot \text{kg}^{-1}$	$\text{mbar} \equiv 0.9869 \cdot 10^{-3} \cdot \text{atm}$
$L_v$ , latent heat of vaporization:	$L_v \equiv 2.8 \cdot 10^6 \cdot \text{joule} \cdot \text{kg}^{-1}$	$\text{mbar} = 99.998 \text{ Pa}$
Density of water:	$\rho_{\text{water}} \equiv 1000 \cdot \text{kg} \cdot \text{m}^{-3}$	
Days per month:	$\text{SecPerMo} \equiv \frac{365.25}{12} \cdot \text{day}$	
Gas constant:	$R_a \equiv 287 \cdot \text{m}^2 \cdot \text{sec}^{-2} \cdot \text{K}^{-1}$	
Standard water vapor pressure:	$p' \equiv 6.107 \cdot \text{mbar}$	
	$T' \equiv 273.16$	

▲ Constants and conversions

# APPENDIX F

## Glacier Flow Model Code

---

This is an explicit version of the code that uses matrices (rather than 1-D arrays) to compute the 5-point star finite difference equation for vertically integrated flow on an irregular surface. In general, pointers are assigned to reference array subsets, such as the N, S, E and W portions of the full matrix for the solution. At present, the code does not contain a routine to detect steady state.

#### Required input:

- A rectangular surface elevation grid
- A net accumulation grid (millimeters snow as water equivalent), with the same dimensions as the surface grid
- A NAMELIST-style parameter file to change flow, time, input, output and operation control

#### Optional input:

- An ice thickness map (meters) with the same dimensions as the surface elevation grid

#### Output:

- A rectangular grid of ice thickness with the same dimensions as the surface elevation grid
- A data file describing certain grid parameters at each time-step specified in the input parameter file

```

PROGRAM MatExp
implicit none
!implicit double precision (a-h,o-z)

!General stuff
character*12 temp, ClockDate, ClockTime
integer i, j, irow, icol, Npow, Mpow
Double precision Pmax, deltaT

!Input parameters
Logical ThickExists, PrintToScreen
Character*20 ElevFile, MassBalFile, ThickInFile, ThickOutFile, StepInfoFile
!File names
Integer NSteps, NoutFreq, MaxNSteps, NprintOutFreq
Integer Nc, Nr, deltaXY, NoDataVal
!Grid header

Real xllcorner, yllcorner
!Grid header
Double Precision Time, TimeMax, A, B, f, ThickToMeters
Double Precision Thresh, rhog, Aconst, Bconst, ThickInit

!Output stuff
Integer NonZeroCount, NegAccCount, LC(2), LL(2)
Double Precision Zlow, Volume, SurfSum, BalInt
Double Precision ChangeMax, MaxThick, BalMod, SumThick
Double Precision AccInt, ErrNeg, BigNeg

!Arrays
Integer, allocatable :: Diag(:,,:), test(:,,:)
Double Precision, allocatable :: Load(:,,:), PSum(:,,:), uOld(:,,:)
Double Precision, allocatable :: Ucorr(:,,:)

!Pointer target arrays
Integer, allocatable, target :: BCx(:,,:), BCy(:,,:)
Double Precision, allocatable, target :: Z_full(:,,:), u_full(:,,:), H_full(:,,:)
Double Precision, allocatable, target :: PX(:,,:), PY(:,,:)

!Pointers
Double Precision, pointer :: Z(:,,:), Z_w(:,,:), Z_e(:,,:), Z_n(:,,:), Z_s(:,,:)
Double Precision, pointer :: u(:,,:), u_w(:,,:), u_e(:,,:), u_n(:,,:), u_s(:,,:)
Double Precision, pointer :: H(:,,:), H_w(:,,:), H_e(:,,:), H_n(:,,:), H_s(:,,:)
Double Precision, pointer :: PX_w(:,,:), PX_e(:,,:), PY_n(:,,:), PY_s(:,,:)

NAMELIST /Params/ A,B,f,MaxNSteps,TimeMax,ThickInit,Thresh, &
NoutFreq,NPrintOutFreq,ThickExists,ThickToMeters,PrintToScreen

```



```

NAMELIST /FileNames/ ElevFile, MassBalFile, ThickInFile, ThickOutFile, StepInfoFile

!OPEN and READ PARAMETERS file with user adjustable constants
open(unit = 30,file = 'params.txt', status= 'old')
read (30,Params)
read (30,FileNames)

!OPEN and READ surface elevation grid for structure and grid constants
open(unit = 40,file =ElevFile, form ='formatted', status='old')
read (40,*) temp, Nc
read (40,*) temp, Nr
read (40,*) temp, xllcorner
read (40,*) temp, yllcorner
read (40,*) temp, deltaXY
read (40,*) temp, nodataval
rewind(40)      !Reset file access to beginning of actual data
do i = 1,6
    read (40,*)
end do

!CONSTANTS (units are generally MKS, except that flow constants
!           are input in terms of years so that timestep is in years)
mpow = 2          !Should be 2
npow = 3          !Should be 3
rhog = 8.826      !density of ice [900*kg*m^3] * grav. accel [9.8*m*sec^-2] = [8.826*kPa/m]
Aconst = (1.0/deltaXY**2)*(1-f)*(2*A/(npow+2))*rhog**npow
Bconst = (1.0/deltaXY**2)*f*B*(rhog)**mpow

!ALLOCATE space for arrays now that size is known
allocate ( Z_full(0:Nr+1,0:Nc+1), u_full(0:Nr+1,0:Nc+1), H_full(0:Nr+1,0:Nc+1))
allocate ( PX(1:Nr,1:Nc+1), BCx(1:Nr,1:Nc+1), PY(1:Nr+1,1:Nc), BCy(1:Nr+1,1:Nc) )
allocate ( Load(Nr, Nc), PSum(Nr, Nc), Diag(Nr, Nc), test(Nr, Nc) )
allocate ( uOld(0:Nr+1,0:Nc+1), uCorr(Nr,Nc) )
!Originally had uOld as simple allocatable array with dimensions of the actual grid
!Now it has the full dimensions so I can access all subsections

!Initialize some things
Z_full = 0.0
u_full = 0.0
H_full = 0.0
PX = 0.0
PY = 0.0
BCx = 0.0
BCy = 0.0

!Assign pointers to work with subsections of the full matrices
!These subsection pointers are used for the matrix calculations (INTERIOR POINTS)
u => u_full(1:Nr, 1:Nc)
H => H_full(1:Nr, 1:Nc)
Z => Z_full(1:Nr, 1:Nc)

!There is no pointer to interior of uOld_full. It must be addressed with indices!!!

!These subsection pointers are for conductance calculations
u_w => u_full(1:Nr, 0:Nc-1)
u_e => u_full(1:Nr, 2:Nc+1)
u_n => u_full(0:Nr-1, 1:Nc)
u_s => u_full(2:Nr+1, 1:Nc)

H_w => H_full(1:Nr, 0:Nc-1)
H_e => H_full(1:Nr, 2:Nc+1)
H_n => H_full(0:Nr-1, 1:Nc)
H_s => H_full(2:Nr+1, 1:Nc)

Z_w => Z_full(1:Nr, 0:Nc-1)
Z_e => Z_full(1:Nr, 2:Nc+1)
Z_n => Z_full(0:Nr-1, 1:Nc)
Z_s => Z_full(2:Nr+1, 1:Nc)

PX_w => PX(1:Nr, 1:Nc)
PX_e => PX(1:Nr, 2:Nc+1)
PY_n => PY(1:Nr, 1:Nc)
PY_s => PY(2:Nr+1, 1:Nc)

!OPEN the MASS BALANCE data file and read blanks to the start of the data

```

```

open(unit = 50,file = MassBalFile, form = 'formatted',status='old')
do i = 1,6
    read (50,*)
end do

!OPEN the THICKNESS data file if it exists
If (ThickExists) then
    open(unit = 60,err = 1000, file = ThickInFile, form='formatted',status='old')
    read (60,*) temp, Time
    TimeMax = Time + TimeMax      !Existing file already represents some time
    do i = 1,5
        read (60,*)
    end do
End if

!READ GRIDS into vectors
Do i = 1, Nr
    read (40,*)      (Z(i,j), j=1, Nc)
    read (50,*)      (Load(i,j), j=1, Nc)
    If (thickexists) then
        read (60,*)  (H(i,j), j=1, Nc)
    End if
End Do

!CLOSE files
close(unit = 30)
close(unit = 40)
close(unit = 50)
close(unit = 60)

!Write an ACTIVE NODE vector, 1 for ACTIVE nodes on the diag, 0 for non-active
!CONVERT MASSEAL millimeters to meters and from water to ice at same time
Where ( (int(Load)==NoDataVal).or.(int(Z)==NoDataVal) )
    Diag = 0
    Load = 0.0
    Z = 0.0
    !Replace NoDataVals in Load with zeros
    !Replace NoDataVals in Z with zeros
Elsewhere
    Diag = 1
    Load = Load / 900.0
End where

AccInt = sum( Load, mask=((Load > 0.0).and.(Diag==1)) )      !Surface-integrated
ACCUMULATION rate

!Create ice THICKNESS vector if it doesn't exist
If (.Not. thickexists) then
    Where (Load > 0.0)
        H = ThickInit
    Elsewhere
        H = 0.0
    End where
Else
    H = H * ThickToMeters * Diag      !Convert thickness to meters and elim nulls
End if

!Create arrays that can be used to apply watershed boundary conditions to the conductance
matrices
Where ( (Diag(1:Nr, 1:Nc-1)==0).or.(Diag(1:Nr, 2:Nc)==0) )
    BCx(1:Nr, 2:Nc) = 0
Elsewhere
    BCx(1:Nr, 2:Nc) = 1
End where
Where ( (Diag(1:Nr-1, 1:Nc)==0).or.(Diag(2:Nr, 1:Nc)==0) )
    BCy(2:Nr, 1:Nc) = 0
Elsewhere
    BCy(2:Nr, 1:Nc) = 1
End where

!Create Ice SURFACE vector
Where (Diag == 1)
    u = Z + H      !Should remain Zero everywhere else
End where

!Initialize values that are part of denominators to avoid div by zero at first timestep
NonZeroCount = 1

```

```

Psum = 1.0

!OPEN a file to write STEPping INFORMATION to
open(unit = 70,file = StepInfoFile)
WRITE (70, ' ("Integrated accumulation rate =", ES10.3)' ) AccInt
WRITE(70, *) "BalMod, BalInt & ErrNeg are all PERCENT of net accumulation"
WRITE(70, 502) "Time", "Stps", "dT", "BalMod", "BInt", "Volume", "Z_Low", "MaxThick", "ErrNg"

!Start of main loop that moves ahead in time =====
DO WHILE ( (time < timemax).and.(Nsteps < MaxNsteps) )

    !Store surface elevs for later comparison
    uOld(1:Nr, 1:Nc) = u

    !Create conductance matrix
    !Calculate the internode coefficients that go into the conductance matrix
    ! and create the pentadiagonal conductance matrix as a 5-column array

    !Calculate WEST part of CondX matrix
    !Ice can flow to bare ground but not vice versa
    Where ( abs(max(u_w, u) - max(Z_w, Z)) < 1.0E-10 )
        test = 0
    Elsewhere
        test = 1
    End where
    PX_w = test * (Bconst * ((H_w + H)/2)**(mpow+1) * (abs(u_w - u)/deltaxy)**(mpow-1)
+ &
        Aconst * ((H_w + H)/2)**(npow+2) * (abs(u_w -
u)/deltaxy)**(npow-1))
    PX = PX * BCx

    !Calculate NORTH part of CondY matrix
    !Ice can flow to bare ground but not vice versa
    Where ( abs(max(u_n, u) - max(Z_n, Z)) < 1.0E-10 )
        test = 0
    Elsewhere
        test = 1
    End where
    PY_n = test * (Bconst * ((H_n + H)/2)**(mpow+1) * (abs(u_n - u)/deltaxy)**(mpow-1)
+ &
        Aconst * ((H_n + H)/2)**(npow+2) * (abs(u_n -
u)/deltaxy)**(npow-1))
    PY = PY * BCy

    Where (Diag==1)
        PSum = PX_w + PX_e + PY_n + PY_s
    End where

    !Calculate the magnitude of the largest conductance
    !This is used to constrain the timestep size (it should be < 1/(2*PMax) ) for
    stability
    Pmax = max( maxval(PX), maxval(PY) )
    If (Pmax > 1) then
        !Calculate
        TIMESTEP SIZE *****
        deltaT = 0.5 * (1 / (2 * Pmax))
    Else
        deltaT = 0.01
    Endif
    Time = Time + deltaT
    NSteps = NSteps + 1
    !Update time
    !Update
    NumTimeSteps

    !Calculate the new ice surface elevation from the continuity equation
    u = ( (PX_w * u_w) + (PX_e * u_e) + &
        (PY_n * u_n) + (PY_s * u_s) - (PSum * u) + Load ) * deltaT + u

    !Before correcting places where ice surface is below ground, lets look at those
    places
    NegAccCount = count( mask=((Z-u) > Thresh).and.(Load > 0.0).and.(Diag==1)) )
    !How many
    BigNeg = maxval( Z - u, mask=((Z-u) > Thresh).and.(Load > 0.0)) )
    !Biggest error
    ErrNeg = sum( Z - u, mask=((Z-u) > Thresh).and.(Load > 0.0).and.(Diag==1)) )
    !Ice 'created'

```



```

CALL DATE_AND_TIME(ClockDate, ClockTime)

!WRITE info re this step to screen
If (PrintToScreen) then

!
      If (mod(Nsteps-1,15).eq.0) then
!          WRITE(*, 502) "Time","Stps","dT","BalMod","BInt","Volume","Z_Low",
!MaxThick","ErrNg"
!          End if
!          WRITE(*,503) Time, Nsteps, deltaT, BalMod, BalInt, Volume, Zlow, MaxThick,
ErrNeg
!          WRITE(*,505) NegAccCount, PMax, ErrNeg, BigNeg
!          WRITE(*,506) Change(LC(1),LC(2)), u(LC(1),LC(2)), Z(LC(1),LC(2)),
Load(LC(1),LC(2))
!          End if

502      FORMAT (x,a8, x,a6,x,a9, x,a10, x,a10, x,a9, x,a8, x,a8, x,a10)
503      FORMAT (x,F8.3,x,I6,x,ES9.3,x,ES10.2,x,ES10.3,x,ES9.3,x,F8.1,x,F8.3,x,ES10.3)
504      FORMAT (1000(x,F9.3))
505      FORMAT ("NgCnt=",I4," KMx=",ES10.3, " ErrNg(%)=", ES10.3, " BigNg=",
ES10.3)
506      FORMAT (ES10.3, 3x, I8, 3x, F8.3, 3x, I4, 3x, ES10.3)

!WRITE info re this step to file
If (mod(Nsteps,NPrintOutFreq).eq.0) then
      WRITE(70,503) Time, Nsteps, deltaT, BalMod, BalInt, Volume, Zlow,
MaxThick, ErrNeg
!      End if

!Periodically WRITE ICE THICKNESS to file
If (mod(Nsteps,NoutFreq) .eq. 0) then
      Where (Diag ==0)
      H = -99.00
      End where

      OPEN(unit = 80, file = ThickOutFile, form='formatted')
      write(80,('Time=", F10.3)') Time
      write(80,('Volume=", ES10.3)') Volume
      write(80,('Integrated surf bal err(%)=", F8.3)') BalInt
      write(80,('Date=",a12," Time=",a12)') ClockDate, ClockTime
      write(80,*) "Nr, Nc, xllcorner, yllcorner, deltaXY, nodataval"
      write(80,('I4,I4,ES15.8,ES15.8,I5,I7)') Nc, Nr, xllcorner,
yllcorner, DeltaXY, NoDataVal
      do irow=1, Nr
      write(80,504) ( H(irow,icol), icol=1, Nc )
      end do
      CLOSE(unit = 80)
!      End if
!End of output calculation section
.....

END DO !WHILE
!End of loop that runs forward through time
=====

Where (Diag .ne. 1)
      H = -99.00
End where

!Write the ice thickness vector to the ice thickness grid
OPEN(unit = 80,file = ThickOutFile,form='formatted')
      write(80,('Time=", F10.3)') Time
      write(80,('Volume=", ES10.3)') Volume
      write(80,('Integrated surf bal err(%)=", F8.3)') BalInt
      write(80,('Date=",a12," Time=",a12)') ClockDate, ClockTime
      write(80,*) "Nr, Nc, xllcorner, yllcorner, deltaXY, nodataval"
      write(80,('I4,I4,ES15.8,ES15.8,I5,I7)') Nc, Nr, xllcorner,
yllcorner, deltaXY, NoDataVal
      do irow=1, Nr
      write(80,504) ( H(irow,icol), icol=1,Nc )
      end do
CLOSE(unit = 80)
CLOSE(unit = 70)      !StepInfo file

```

```
!Deallocate allocated arrays; dereference pointers
DEALLOCATE (u_full, H_full, Z_full, uOld)
NULLIFY (u, H, Z )
NULLIFY (u_w, u_e, u_n, u_s)
NULLIFY (Z_w, Z_e, Z_n, Z_s)
NULLIFY (H_w, H_e, H_n, H_s)

STOP
!Error messages
1000 Print*, "Cannot find/open thickness file, ", ThickInFile
END
```